AD NUMBER: AD0804603

LIMITATION CHANGES

TO:

Approved for public release; distribution is unlimited.

FROM:

Distribution authorized to US Government Agencies only; Export Control; 1 Nov 1966. Other requests shall be referred to Air Force Flight Dynamics Laboratory, Wright-Patterson AFB, OH 45433

AUTHORITY

AFFDL ltr dtd 8 Jun 1972

AFFDL – TR – 66 – 184

SYNTHESIS OF A FLUIDIC FLIGHT CONTROL SYSTEM

L.B.Taplin
K.W.Verge
W.F.Datwyler

The Bendix Corporation

Technical Report AFFDL-TR-66-184

November 1966

Air Force Flight Dynamics Laboratory
Research and Technology Division
Air Force Systems Command
Wright - Patterson Air Force Base, Ohio 45433

NOTICES

When Government drawings, specifications, or other data are used for any purpose other than in connection with a definitely related Government procurement operation, the United States Government thereby incurs no responsibility nor any obligation whatsoever; and the fact that the Government may have formulated, furnished, or in any way supplied the said drawings, specifications, or other data, is not to be regarded by implication or otherwise as in any manner licensing the holder or any other person or corporation, or conveying any rights or permission to manufacture, use, or sell any patented invention that may in any way be related thereto.

Copies of this report should not be returned to the Research and Technology Division unless return is required by security considerations, contractual obligations, or notice on a specific document.

BLANK PAGE

SYNTHESIS OF A FLUIDIC FLIGHT CONTROL SYSTEM

L.B.Taplin
K.W.Verge
W.F.Datwyler

FOREWORD

This report, prepared by The Bendix Corporation, Research Laboratories Division, Southfield, Michigan, is the final report describing the results of an investigation of the feasibility of synthesizing a fluidic flight control system. This work was accomplished during the period April, 1964 to August, 1966 under Air Force Contract AF 33(615)-1492, Project Number 8226, Task Number 822604 sponsored by the Air Force Flight Dynamics Laboratory of the Research and Technology Division, Wright-Patterson Air Force Base, Ohio. This program was administered under the direction of Mr. James Hall, of the Air Force Flight Dynamics Laboratory, FDCL. The work was conducted at the Bendix Research Laboratories Division in the Energy Conversion and Dynamic Controls Laboratory, managed by Mr. L. B. Taplin. The project was directed by Mr. K. W. Verge, Assistant Department Head, Flight Controls Department, with W. F. Datwyler as alternate Project Supervisor.

This manuscript was released by the authors October 1966 for publication as an RTD Technical Report.

Publication of this technical report does not constitute Air Force approval of the findings or conclusions stated in the report. It is published only for the exchange and stimulation of ideas.

ABSTRACT

A program was conducted to investigate the feasibility of synthesizing a fully-pneumatic fluidic flight control system for advanced vehicle applications. A pitch axis flight stabilization system was developed to determine feasibility and to indicate achievable performance.

The system approach selected for investigation utilizes a novel pulsating vortex rate sensor, jet digital signal processing elements, an orifice-volume analog frequency shaping network, and a complete integrated rotary position servo. The position servo consists of analog vortex and venjet amplifiers, a novel vortex servovalve, a fluidic position transducer, and a rotary actuator. All components and subsystems required were designed and developed into integrated configurations suitable for operation on 1000°F air in a 1000°F environment.

Functionality was demonstrated for all components and subsystems and for the complete integrated system. The position servo operated excellently with air supply and environmental temperatures in the tested range from 70°F to 1000°F. Operation of the rate sensing componentry was limited to several hundred degrees F. Basic designs exist for all functional components and subsystems required. Subsequent effort can be directed to design refinement for enhanced performance, temperature capability and packaging as desired.

TABLE OF CONTENTS

LIST OF ILLUSTRATIONS

LIST OF ILLUSTRATIONS

LIST OF TABLES

BLANK PAGE

SECTION 1

INTRODUCTION

The requirements for control of advanced Air Force flight vehicles demand that systems be built to withstand severe compartment environmental temperatures which in some vehicles can be as high as 1400°F. Where these temperatures are to be encountered, if conventional electro-hydraulic or electro-mechanical approaches are to be used, a considerable weight and complexity penalty will be suffered in providing the necessary cooling and/or insulation. This added complexity can result in a reduction of overall weapon system reliability and performance.

One relatively new approach to solving this problem has been the realization that a hot gas flight stabilization system is feasible. Through work sponsored by the Air Force Contract 33(600)-40538, the feasibility of operating a flight stabilization system on 1300°F gases in a 1400°F environment has been shown. Gas gyros, compensation networks and servo-valves which operate rotary-type servo actuators have been tested at these temperatures with no cooling or insulation employed. The advent of fluidic technology has, of course, brought about the realization that such a hot gas system can be improved further through better reliability, increased operating temperatures, and increased capability to withstand shock and vibration. In addition, the flueric devices and circuits provide additional design flexibility in that simple compensation and gain change means are possible, and additional control functions - such as acceleration limiting - are easily added. Fluidic Technology provides still another very important degree of flexibility in that this technology is not limited to just proportional or analog devices but provides also a large inventory of digital devices and techniques. Because both digital and analog techniques are available, it was possible to consider the design of hybrid circuitry which capitalizes on the best of each of these techniques, thus leading to a system which has better signal-to-noise ratios, performance, and reliability.

For purpose of establishing a realistic set of ground rules for the "Synthesis of a Fluidic Flight Control System" the pitch axis stabilization loop of a typical advanced aircraft was selected as the framework for the development of these rules. As with most advanced aircraft, the flight

conditions vary over such a large range that large changes in the vehicle's dynamic characteristics take place requiring that the stabilization loop be adjusted in gain to compensate for these changes if proper damping and response are to be maintained. A functional block diagram of the stabilization loop is shown in Figure 1.

The system specifications for stabilizing a typical vehicle are listed in Table 1. Because flueric devices have been shown to operate over a large range of pressures, and particularly low pressures, the use of turbojet engine compressor bleed gases were selected for the sensing and compensation portions of the stabilization loop. High pressure 1000°F air was selected for operating the gas servo so as to maintain a realistic and small servo actuator size and weight. A rotary gas servo is employed in order to achieve a high static and dynamic servo stiffness. A low servo stiffness can easily aggravate and accentuate body bending modes and control surface flutter in the aircraft.

The system approach selected for investigation utilizes a novel pulsating vortex rate sensor, jet digital signal processing elements, an orifice-volume analog frequency shaping network, and a complete integrated rotary position servo. The position servo consists of analog vortex and venjet amplifiers, a novel vortex servovalve, a fluidic position transducer, and a rotary actuator. All components and subsystems required were designed and developed into integrated configurations suitable for operation on 1000°F air in a 1000°F environment.

Functionality was demonstrated for all components and subsystems and for the complete integrated system. The position servo operated excellently with air supply and environmental temperatures in the tested range from 70°F to 1000°F. Operation of the rate sensing componentry was limited to several hundred degrees F. Basic designs exist for all functional components and subsystems required. Subsequent effort can be directed to design refinement for enhanced performance, temperature capability and packaging as desired.

Table 1 - Partial Specifications for a "Fluidic Flight Control System"

Operating Media	100°F - 1000°F Air
Operating Ambient	1000°F Maximum
Rate Sensor	
Bandpass (45° Phase Shift)	>5 cps
Threshold	0.1°/Sec
Range	50°/Sec
Compensation Network	
Washout Break Frequency	0.1 Cps
Lag Break Frequency	1 Cps
Gain Change Ratio	10 To 1
Control Surface Actuator	
Supply Gas Pressure	>600 Psia
Supply Gas Temperature	100°F To 1000°F
Maximum Hinge Moment	50,000 In-Lb
Maximum Horsepower	5 Hp
Bandwidth	>5 Cps
Static Stiffness	2×10^6 Lb-In/Rad

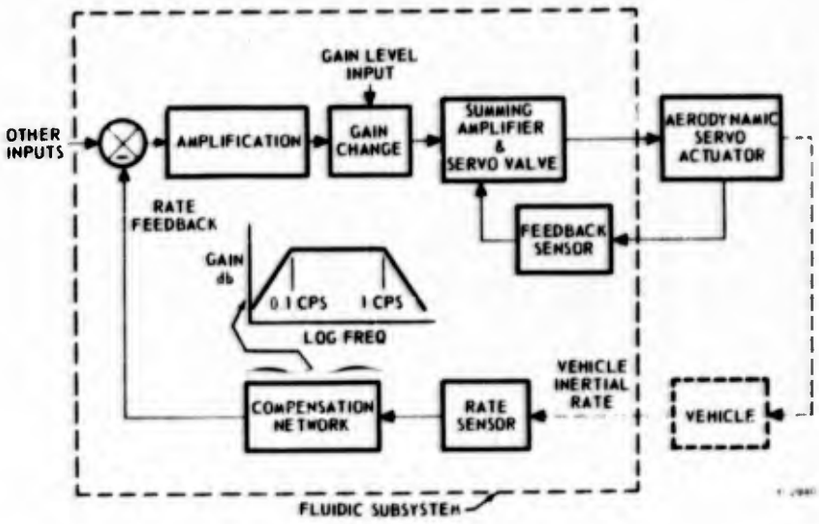

Figure 1 - Functional Block Diagram - Flight Stabilization Loop

SECTION II

DEVELOPMENT APPROACH

A. SYSTEMS CONSIDERATIONS

Many flueric components have been tested in the last few years. some demonstrating performance sufficient to allow consideration of these devices for use in control systems. In many instances, the device performance, while good as an unloaded device, has been shown to be seriously degraded when it is used to drive another flueric device. In some cases, parasitic oscillations occur when two elements are coupled; also, signal-to-noise ratios may be seriously reduced, and signal reflection may degrade circuit performance. In short, all too often, devices have been connected in which proper attention has not been paid to impedance matching, which, in turn, can result in circuit and device designs which are improperly sized. This mismatched circuit can cause excessive use of fluid, thus reducing circuit efficiency, and in some cases may require that additional elements be used to achieve the desired circuit gain.

B. SIGNAL AMPLIFICATION

In selecting circuit techniques and establishing impedance matching criteria, one must decide what figures of merit or circuit performance parameters are to be constraints on the selection. Certainly, one of the most important parameters must be a high signal-to-noise ratio if a sufficiently large operating range is to be achieved. In control applications, a ratio on the order of 500 to 1 is usually required. Also of importance are circuit response, minimum drift and null shift, and efficient circuit elements, i.e., circuit elements with the highest possible pressure, flow, and power recovery. Reasonably good linearity and a minimum threshold are also important performance parameters.

Again, probably the most difficult figure of merit to be met is that of signal-to-noise ratio, especially where pneumatic flueric devices are to be used. Noise levels are known to increase very rapidly with high Reynolds numbers in pneumatic devices; therefore, in most instances, subsonic flows are employed. It should be noted that where high velocity or supersonic flows can produce a large improvement in

signal gain, the signal-to-noise ratio may be improved, even though the absolute noise level is also much higher. It is interesting to examine a sensor and amplifier circuit in which each element introduces a noise signal N_i. The sensor gain is defined as K_i, and each amplifier has a gain, K. The circuit is shown in Figure 2. The output signal without noise is given by:

$$\theta_o = K_s K_1 K_2 \theta_i \tag{1}$$

The output noise is given by:

$$\theta_N = (N_s K_1 + N_1) K_2 + N_2 \tag{2}$$

and the signal-to-noise ratio is

$$\frac{\theta_o}{\theta_N} = \frac{\theta_i}{\frac{N_s}{K_s} + \frac{N_1}{K_s K_1} + \frac{N_2}{K_s K_1 K_2} + \cdots} \tag{3}$$

There are of course, some rather obvious facts to be learned from this simple expression: (1) if the amplifier gains are large enough, the signal-to-noise ratio is essentially that set by the sensor, (2) if all amplifiers cannot have a high gain, then the first-stage gain must be high, or, more precisely, the amplifier nearest the sensor must have a high signal-to-noise ratio.

A number of things affect the noise level N at any stage. First, the flow receiver in which the fluid is partially stagnated can cause eddies, etc., which appear as noise. Second, the power supply used to drive in the stage must be low in noise content. Third, flows in the device which pass over edges or which are split by edges can cause edge tones, and, in most cases, momentary attachments which cause noise. Fourth, - a most important factor in flight control - structural

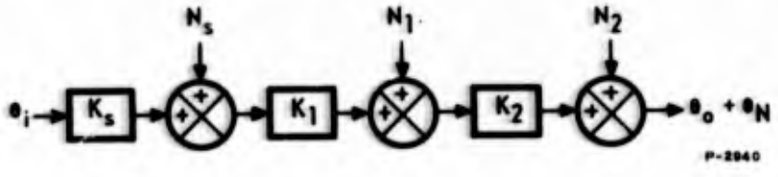

Figure 2 - Sensor and Amplifier Network with Noise Sources

resonance noise, vibration, and acoustic noise from engines may introduce noise into the flueric network; the devices and circuits must exhibit very low microphonic characteristics. As an example, a 166-db engine noise level is a pressure fluctuation level on the order of 0.6 psi. If this pressure fluctuation is introduced without attenuation at the sensor or preamplifier stages, a serious degradation in signal-to-noise ratio can result.

One technique used by electronic engineers to achieve better signal-to-noise ratios has been that of employing digital techniques for preamplification of signals; i.e., the information is handled in the time or frequency modulation domain so as to avoid picking up amplitude noise. The flight control system selected for evaluation uses a digital, or time-modulated, approach as a means of achieving the best possible signal-to-noise ratio.

As an example, assume a sensor can be developed which has a pulse rate output which is proportional to the input signal. Assume further that the signal-to-noise ratio for this sensor is equivalent to its analog counterpart. The noise, in this case, manifests itself as a variance in pulse rate or interpulse period. If it is further assumed that the information carried by the pulse frequency must be eventually converted to an analog signal after amplification, the question arises as to what type of amplification should be used. The analog signal conversion could be either in the form of a binary number or the average pressure represented by the number of pulses occurring per second. The pulses leaving the sensor could be standardized by use of a pulse stretching network, a form of amplification, which would add width to the pulse. Such networks usually add some additional noise to the signal. Further amplification could be achieved by using the standardized pulse to trip a series of flip-flops, each operating at an increased supply pressure, thus building up the amplitude of the pulse. It is, of course, obvious that any amplitude noise which adds to the output signal of any of the intermediate flip-flop stages has no effect on signal-to-noise ratio as the signal information is still being carried by the rate at which pulses occur. The final flip-flop stage can add noise if it is at this point that the average pressure corresponding to the number of pulses is to be used as the analog conversion of the information. This simple scheme using pulse stretching and flip-flops can, in many cases, provide signal amplification with less signal-to-noise degradation than when proportional analog amplification is used.

Still another method of amplifying involves counting the pulse train on a flueric up-down counter and using feedback through a D to A converter, so that a binary number corresponds to the value of the sensed variable. A circuit for this method of amplification is shown in Figure 3. A sensor capable of being biased must be used in implementing this circuit technique in order to allow for negative feedback.

If a vortex rate sensor is assumed, K_v represents the velocity gain of the vortex flow field, K_f is the feedback D to A converter gain, and K_p is the gain of the A to D converter portion of the rate sensor which converts amplified degrees per second into a pulse rate. The pulses are counted, or integrated, by the flueric up-down counter. The output, $\dot{\theta}_o$, for an input, $\dot{\theta}_i$, is given by:

$$\frac{\dot{\theta}_o}{\dot{\theta}_i} = \frac{\frac{K_v}{K_f}}{\frac{s}{K_f K_p} + 1} \qquad (4)$$

The counter uses flueric complementing flip-flops which, of course, introduce a noise, N, on the output signal. This noise signal is

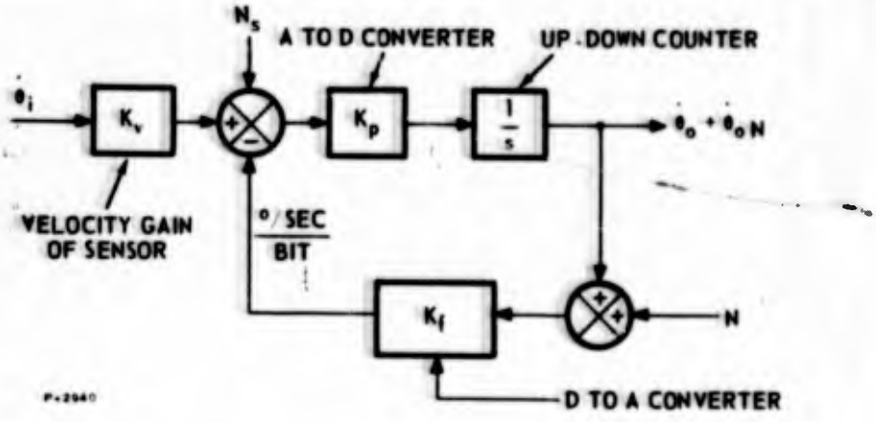

Figure 3 - Binary Digital Output Sensing Circuit

essentially proportional to the magnitude of $\dot{\theta}_o$, i.e., $N = K_N \dot{\theta}_o$. The noise content in the counter output, $\dot{\theta}_{oN}$, is given by:

$$\dot{\theta}_{oN} = \frac{N + \frac{N}{K_f} s}{\frac{s}{K_f K_p} + 1} \qquad (5)$$

The signal-to-noise ratio is given by:

$$\frac{\dot{\theta}_o}{\dot{\theta}_{oN}} = \frac{\dot{\theta}_i}{\frac{N}{K_v} s + \frac{N K_f}{K_v}} \qquad (6)$$

Here the noise output is set only by the sensor noise and the noise level on the final output stage. If flip-flops were used to amplify the pulse level so that the pulses would drive a high pressure counter, amplitude noise introduced by the interstage flip-flops would not degrade the signal-to-noise ratio.

C. IMPEDANCE MATCHING CRITERIA

In the case of proportional jet-on-jet devices and vortex devices, the controlling parameter is momentum; i.e., device operation or its output is related directly to the efflux momentum leaving the control port. To illustrate, the flueric device output is to be transmitted to the control port of a second device, as shown schematically in Figure 4. The objective, selected for illustration, is to maximize the efflux momentum delivered within the next device. An equivalent circuit can be constructed for the fluid state circuit schematic, as shown in Figure 4(b). The pressure, P_r, is taken as the stagnation pressure in the element receiver when it is blocked. This pressure is, of course, a function of the control pressure P_{c1}. When the receiver is not blocked, but rather connected to the control port of the second device, a pressure P_{c2} is developed upstream of this control port and a weight flow, W, passes through the connecting line. The pressure drop caused by the receiver impedance can be represented by an equivalent orifice of area, A_o. (If the receiver length to equivalent diameter ratio is very large, an equivalent laminar restrictor instead of an orifice must be used to

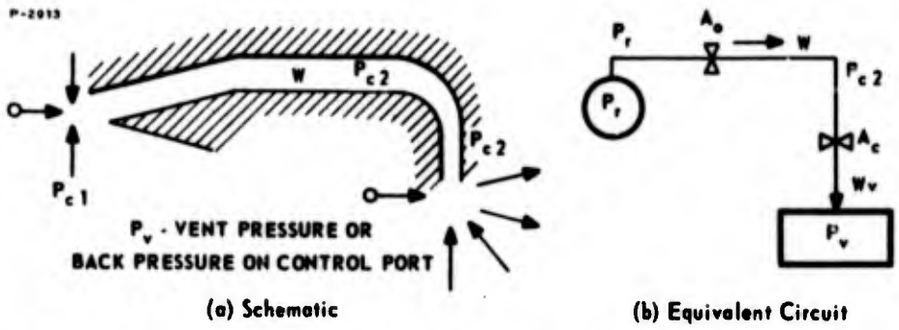

Figure 4 - Momentum Transfer Between Elements

represent the impedance characteristics of the receiver.) At high operating frequencies, the length and volume of the receiver channel will introduce amplitude attenuation and phase shift; thus the equivalent impedance will require, in addition to the orifice, a capacitance and delay function. To illustrate the impedance matching problem simply, frequencies will be assumed to be low enough that the capacitive and transport delay effects are negligible.

Two operating conditions must be examined for the control port flow and momentum: (1) the control port or orifice, A_c, is flowing sonically; (2) it is flowing subsonically.

$$W = \frac{C\, C_d\, A_c\, P_{c2}}{\sqrt{T}} \tag{7}$$

where

W = weight flow - lb/sec

C = orifice flow constant - $^\circ R^{1/2}$/sec

C_d = orifice discharge coefficient

A_c = orifice area - in^2

P_{c2} = pressure upstream of the orifice - psia

T = upstream gas temperature - $^\circ R$

P_V = back pressure on orifice - psia.

The momentum rate leaving the orifice is given by:

$$\vec{M} = W v_s \tag{8}$$

where

$\vec{M}$ = momentum rate - lb-in/sec^2

v_s = sonic velocity of gas at orifice throat - in/sec

The momentum rate is then directly proportional to the upstream pressure P_{c2}; therefore, A_c should be selected for a given A_o to maximize (P_{c2} A_c). The equivalent output impedance orifice, A_o, is assumed to be flowing subsonically, and the following flow equation can be used to a good approximation for this orifice:

$$W = \frac{2 C C_d A_o P_{c2}}{\sqrt{T}} \sqrt{\frac{P_r}{P_{c2}} - 1}\,. \tag{9}$$

Equating (7) and (9)

$$A_c = 2 A_o \sqrt{\frac{P_r}{P_{c2}} - 1}\,. \tag{10}$$

or

$$P_{c2} = \frac{P_r}{1 + \frac{A_c^2}{4 A_o^2}} \tag{11}$$

$$\vec{M} = \frac{C C_d v_s A_c P_{c2}}{\sqrt{T}} = \frac{C C_d v_s A_c P_r}{\sqrt{T}\left[1 + \frac{A_c^2}{4 A_o^2}\right]} \tag{12}$$

It is now necessary to find that value of A_c which will produce the maximum M. Taking the derivative with respect to A_c and setting it equal to zero:

$$\frac{\overrightarrow{dM}}{dA_c} = \frac{C\, C_d\, v_s\, P_r}{\sqrt{T}} \left[\frac{\left[1 + \frac{A_c^2}{4 A_o^2} \right] - \frac{A_c^2}{2 A_o^2}}{\left[1 + \frac{A_c^2}{4 A_o^2} \right]^2} \right] = 0 \qquad (13)$$

and

$$A_c = 2 A_o \qquad (14)$$

Also from equation (11):

$$\frac{P_r}{P_{c2}} = 2 \qquad (15)$$

These expressions simply state that for a sonic control port, the maximum delivered momentum rate occurs when the receiver delivers as much flow as possible. If the recovery can be represented by an equivalent orifice, A_o, then this orifice should flow sonically. Once the equivalent output impedance orifice is sonic, it does not matter what the value of P_{c2} or A_c is as long as $P_{c2}/P_V \geq 2$ or:

$$\text{for } \frac{P_r}{P_{c2}} \geq 2$$

$$2 \leq \frac{A_c}{A_o} \leq \frac{P_r}{P_{c2}} \text{ as long as } \frac{P_{c2}}{P_V} \geq 2. \qquad (16)$$

For the case where the control port is operating subsonically, the weight flow is given by:

$$W = \frac{2\, C\, C_d\, A_c\, P_v}{\sqrt{T}} \sqrt{\frac{P_{c2}}{P_V} - 1}. \qquad (17)$$

Equating (17) and (9),

$$A_c = A_o \sqrt{\frac{\frac{P_r}{P_V} - \frac{P_{c2}}{P_V}}{1 - \frac{P_V}{P_{c2}}}} \qquad (18)$$

The momentum expression for subsonic flow can now be used and derivatives taken, as was done in the sonic case, to find the area ratio A_c/A_o that produces maximum momentum rate. Plots of normalized momentum rate are shown in Figure 5 which clearly shows the pressure ratio P_{c2}/P_V for maximum $\vec{M}$ for various values of P_r/P_V. The momentum rate was normalized with respect to $\vec{M}_N$ as given by:

$$\vec{M}_N = 0.915\ C\ C_d\ A_o \sqrt{k\ g\ R}\ P_V \qquad (19)$$

Once P_{c2}/P_V is known, equation (18) can be used to find the proper control port area, A_c. A plot of P_{c2}/P_V and A_c/A_o is shown in Figure 6.

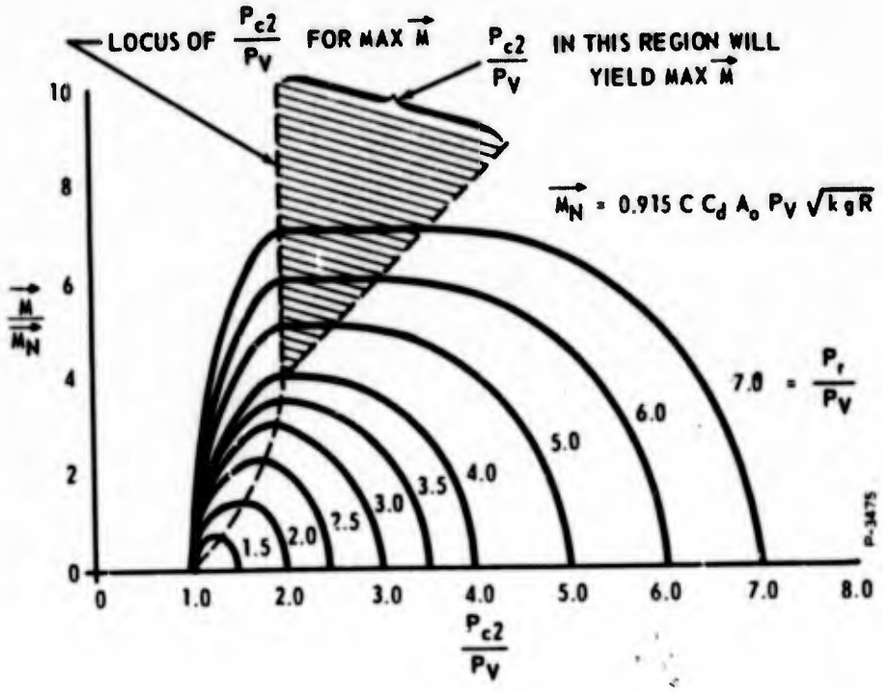

Figure 5 - Normalized Momentum Rate Characteristic Curve

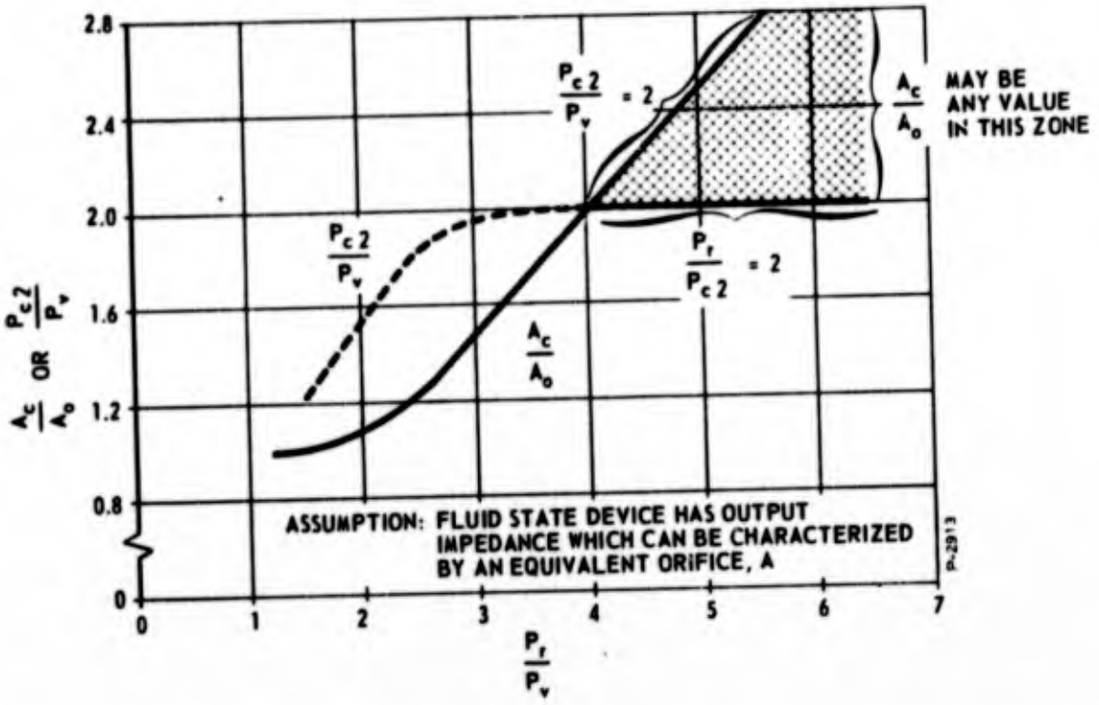

Figure 6 - Area Ratio Impedance Matching Criteria for Momentum Rates

Obviously, the control area selected should be that needed for the maximum P_r, which a device will deliver so that a maximum momentum rate will be delivered by the load orifice or control port of the next device.

Again, it should be remembered that the above criteria and area ratios plotted in Figure 6 are only good for those elements where the output impedance can be characterized by an equivalent orifice. If the weight flow-pressure relationship at the receiver of a flueric element is not characteristic of orifice flow, then the actual flow relationship should be used and the above procedure repeated to determine the proper load orifice size.

One interesting aspect of the impedance matching criteria, shown in Figure 6, is that when the available pressure ratio, P_r/P_V, is greater than 4, the load orifice can be any size within the range shown. The reason for this range of orifice sizes is that above P_r/P_V of 4, both orifices can flow sonically within a bounded range of pressures, P_{c2}.

The terminology "impedance matching" is perhaps a misnomer in that only at the low subsonic flows do the impedances literally match,

i.e., $A_c = A_o$. Again, the criteria of matching (not literal matching) is that of finding the proper load orifice to maximize momentum. Obviously, other criteria can be established based on maximizing weight flow, delivered power - a volumetric flow times differential pressure acting on a piston-cylinder actuator, and even signal-to-noise ratio. In the case of preamplification of weak signals, the best signal-to-noise criteria of matching should be used.

D. CIRCUIT TECHNIQUES

In designing flueric circuits for wide range temperature operation, care must be taken to offset the effects of temperature and pressure variations which can cause serious null shifts. One technique which tends to cancel these effects embodies the use of push-pull circuitry; that is, the circuit is in essence dual with the signal output being transmitted as a differential pressure or flow signal. A push-pull stage of amplification then has two outputs, one of which increases while the other decreases when a signal is applied at the input. The push-pull circuit is, of course, a natural technique for the jet-on-jet devices as they inherently have the necessary duality. Figure 7 shows two amplifying networks which are push-pull.

One advantage of the push-pull circuit is that it greatly attenuates or cancels the effect of power supply pressure variations. This advantage is realized if the amplifier is designed so that it has constant gain for reasonable changes in supply pressure. By constant gain, it is meant that the change in output differential pressure is a constant. When the gain is not constant, noise on the supply pressure source will modulate the differential output signal when an input signal is present. This is an important point in considering noise phenomena in that it is not enough to consider just null noise; the signal-to-noise ratios must be established with a signal applied.

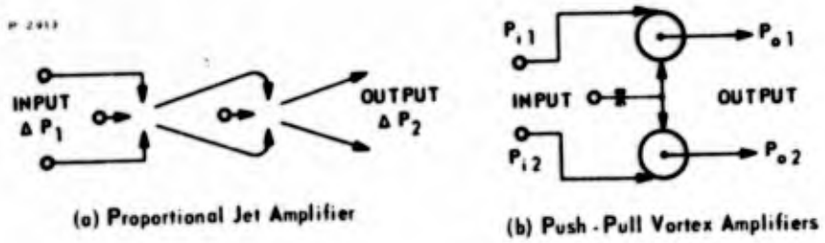

(a) Proportional Jet Amplifier

(b) Push-Pull Vortex Amplifiers

Figure 7 - Push-Pull Circuit Techniques

Another advantage of push-pull circuitry lies in the ability of the circuit to reject even harmonic distortions resulting from slight nonlinearities in the amplifying elements. Suppose the output of one of the vortex amplifiers for a sinusoidal input, $\bar{P} \sin \omega t = P$, is:

$$P_{o1} = K P + a P^2 + b P^3 + \ldots\ldots \qquad (20)$$

For the sinusoidal input, the affect of the a P^2 term is to introduce a null shift and a second harmonic term, while that of the b P^3 term is to introduce a third harmonic term. In the case of the vortex push-pull circuit using identical amplifiers, the signal $P_{o1} - P_{o2}$ with $P_{i1} = P$, and $P_{i2} = -P$ is:

$$P_{o1} - P_{o2} = 2 K P + 2 b P^3 + \ldots\ldots \qquad (21)$$

The network rejects the even harmonic terms. With a single supply jet in the jet amplifier network, it is difficult to say that such an amplifier rejects even harmonics; however, the push-pull design of the element tends to build in this effect in the sense that push-pull operation of the control jets offsets some of the nonlinearity associated with operating each control jet separately.

In the selection of an amplifier type, other parameters of extreme importance are the pressure recovery and biasing of the stage. In the case of the jet amplifiers, the bias pressure level on the control port is less than the supply, but the ratio of maximum pressure recovered in a receiver to supply can be low (20 to 50 percent of supply). Therefore, it is difficult to build up the pressure level of a signal. In the case of vortex amplifiers, the bias pressure must be higher than supply, but the maximum pressure recovered can be nearly 100 percent of supply. In cascading standard vortex amplifiers, the operating supply pressure of succeeding stages must be progressively lowered. (There are special vortex amplifiers where the control bias is lower than supply, thus eliminating this problem.) For those where the bias pressure must be greater than supply, at least four stages can be cascaded together before the maximum delivered pressure reaches 1/2 of supply. The four-stage cascade of vortex amplifiers will, in most cases, have more gain than the same number of stages of jet amplifiers. Still another consideration is amplifier response. In general, the jet amplifier has higher response and is, of course, to be preferred where this high response is required.

Compensation circuits and flueric filter networks for operation over a wide temperature range require special attention; for, as the gas temperature changes, corner frequencies of the network can shift. This shift in corner frequencies or circuit time constants must be taken into account in designing the network for a particular system. As an example of the temperature shift phenomena, the simple lag network shown in Figure 8 is analyzed.

Assuming, for the moment, that the orifices are flowing subsonically, the weight flow W_1 is given by:

$$W_1 = \frac{2 C C_d A_1 P}{\sqrt{T}} \sqrt{\frac{P_r}{P} - 1} \qquad (22)$$

This weight flow supplies the compressible flow to the volume, V, and the flow, W_2, leaving the downstream orifice.

$$W_1 = W_2 + \frac{V}{k R T} \left[\frac{d P}{d t}\right] \qquad (23)$$

and

$$W_2 = \frac{2 C C_d A_2 P_V}{\sqrt{T}} \sqrt{\frac{P}{P_V} - 1} \qquad (24)$$

Linearizing equations (15), (16), and (17); using W_o as the quiescent weight flow, P_o as the quiescent pressure between the orifices, P_{ro} as the quiescent signal pressure; and letting

$$P_{\Delta 1} = P_{ro} - P_o$$

$$P_{\Delta 2} = P_o - P_V$$

$$Q_o = \frac{W_o R T}{P_o}$$

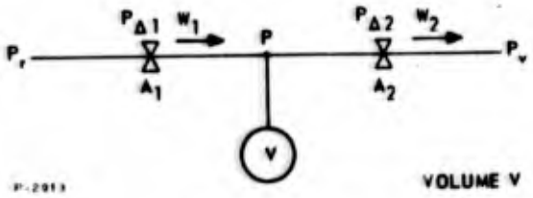

Figure 8 - Orifice - Volume Lag Network

then

$$\frac{\Delta P}{\Delta P_r} = \frac{\dfrac{1}{1 + \dfrac{P_{\Delta 1}\, P_V}{P_{\Delta 2}\, P_o}}}{\dfrac{Vs}{1 + k\, Q_o \left[\dfrac{P_o}{2\, P_{\Delta 1}} + \dfrac{P_V}{2\, P_{\Delta 2}} \right]}} \tag{25}$$

The time constant is:

$$\tau = \frac{V}{k\, Q_o} \left[\frac{1}{\dfrac{P_o}{2\, P_{\Delta 1}} + \dfrac{P_V}{2\, P_{\Delta 2}}} \right] \tag{26}$$

or

$$\tau = \frac{V}{k\, Q_o} \left[\frac{1}{\dfrac{1}{2\left[\dfrac{P_{ro}}{P_o} - 1 \right]} + \dfrac{1}{2\left[\dfrac{P_o}{P_V} - 1 \right]}} \right]$$

Also

$$\frac{\Delta P}{\Delta P_r} = \frac{\dfrac{1}{1 + \dfrac{\dfrac{P_{ro}}{P_o} - 1}{\dfrac{P_o}{P_V} - 1}}}{1 + s\tau} \qquad (27)$$

When the two orifices are flowing sonically the transfer function for $\Delta P/\Delta P_r$ is:

$$\frac{\Delta P}{\Delta P_r} = \frac{1/2}{1 + \dfrac{V}{k Q_o} s} \qquad (28)$$

The effect of a change in gas temperature can now be investigated. The pressure ratios and quiescent pressures are not affected by temperature. The quiescent volumetric flow, Q_o, between the two orifices is temperature-sensitive. Since W_o is inversely proportional to the square root of the absolute temperature, the volumetric flow, Q_o, is proportional to the square root of the temperature; therefore, as the temperature increases, the time constant will decrease. The time constant is inversely proportional to the square root of the gas temperature.

If the time constant change is too large for a given application, then it will be necessary to compensate for the change. One method employs the use of a thermally-adjustable orifice which is constructed so that its flow area decreases with increasing temperature. In some cases, a volume may be used which has a bimetallic wall so constructed that, as temperature increases, the volume increases.

The effects of temperature change on flueric amplifiers and sensors must also be recognized. Where amplifiers utilize the principle of conservation of momentum, little temperature effect is noted, as momentum is independent of temperature for a given pressure. Resultant momentum vector angles do not change with temperature, and since the jet dynamic head is proportional to the product of fluid density times its velocity squared, the stagnation pressures are unaffected. There is, of course, a slight exception, since density and viscosity changes affect Reynolds number.

SECTION III

FLUIDIC FLIGHT STABILIZATION SYSTEM DESCRIPTION

The need for a high dynamic range in rate sensing, necessitating a marked improvement in signal-to-noise ratio for pneumatic flueric sensors and amplifiers, has prompted the selection of a digital sensing technique. Although the sensor by its very nature is analog, once the signal is converted to a form which will allow digital processing, no further noise should be picked up until the signal is finally converted back to an analog signal. The system chosen, then, is shown in block diagram form in Figure 9.

As discussed above, the direct use of the rate sensor pulse rate information requires very fast computation rates and was therefore abandoned in favor of a time unbalance modulator approach. The modulator keeps the information stored in the time domain while it is amplified and converts it finally at the servo input amplifier to an analog signal with appropriate filtering as stated in the list of specifications.

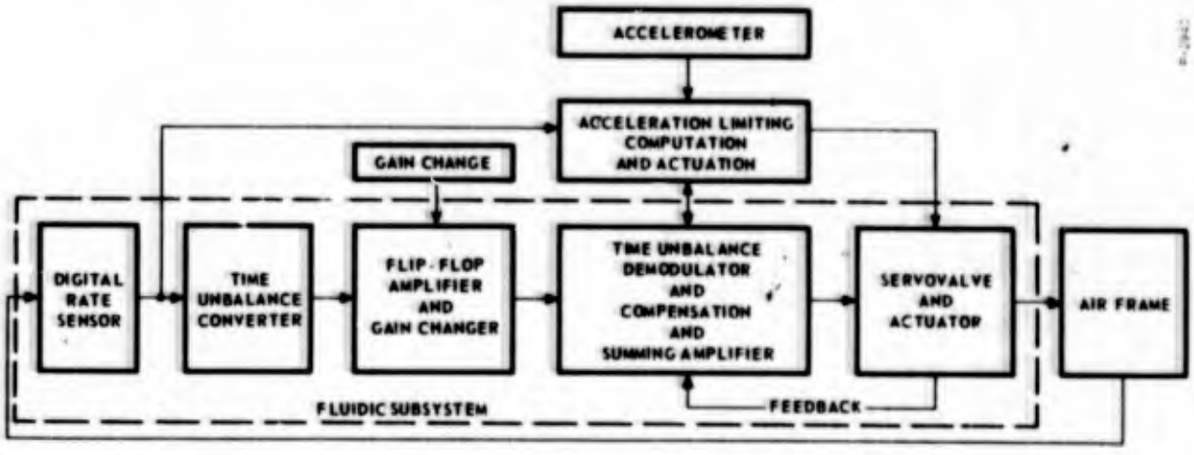

Figure 9 - Block Diagram of Fluidic Flight Stabilization System

The servovalve employs a fluidic interface which has proven to have significant merit in that no damping tanks or lead networks are needed to damp the closed loop servovalve. A loop closure which slaves the servovalve spool position to a flueric pilot stage has been achieved. The servo actuator employs a pneumatic vane motor which allows for expansion of the working gases. This technique as used in the Hot Gas Flight Stabilization System AF 33(600)-40538 has been shown to reduce fuel consumption. Servo feedback of elevon position employs a pneumatic bridge pickoff technique compatible with the flueric summing amplifier. This amplifier accepts the vehicle rate information directly from the compensation network. The rate signal is not amplified by an analog amplifier which could degrade the signal-to-noise ratio.

A. SYSTEM FORM AND OPERATION

The fluidic flight control system consists of three major subsystems, as indicated on Figure 10.

- The Rate Sensing Subsystem senses angular rate and provides a time-unbalance-modulated pulse train with average value proportional to input rate. The subsystem consists of a biased pulse-mode vortex rate sensor and a jet element bias-alternating network connected in a feedback loop to derive the desired time-unbalance modulations.
- The Signal Processing Subsystem consists of a variable-gain pulse amplifier and orifice-volume filter networks which amplify and demodulate the Rate Sensing Subsystem signal and provide requisite signal frequency shaping.
- The Servo Subsystem consists of vortex summation amplifiers, venjet amplifiers, a servovalve, a motor, and a position transducer connected in a position servo loop to convert the processed rate signal into an aerodynamic surface position.

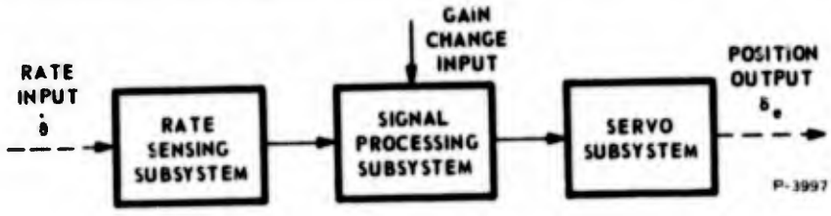

Figure 10 - Subsystem Block Diagram

B. RATE SENSOR SUBSYSTEM

The rate sensor subsystem design is based on the use of a novel flueric vortex rate sensor having a pulsating output, allowing the utilization of digital processing techniques.

The pulse rate of the basic rate sensor is a function of both angular rate and pneumatic tangential control inputs, as shown in idealized form in Figure 11. Given such a sensor, various system forms having the advantages of digital processing may be considered.

One simple approach is to convert the sensor output pulses to standard pulses (precise time duration) such that the pulse rate (hence, rate input level) is indicated by the average value of the pulse train. Another approach is to process the output pulse train by digital computation techniques wherein the output frequency is converted to a binary number by periodic count sampling. The latter approach involves considerable network complexity and requires pulse and process rates in excess of the present state-of-the-art.

A third approach was selected for implementation which avoids the complexity of the count-sample approach while having significant advantages over the simple standard-pulse-averaging approach. The approach selected utilizes the pneumatic control capability of the basic sensor in a feedback mode to convert directly the rate sensor output into a time-unbalance-modulated pulse train.

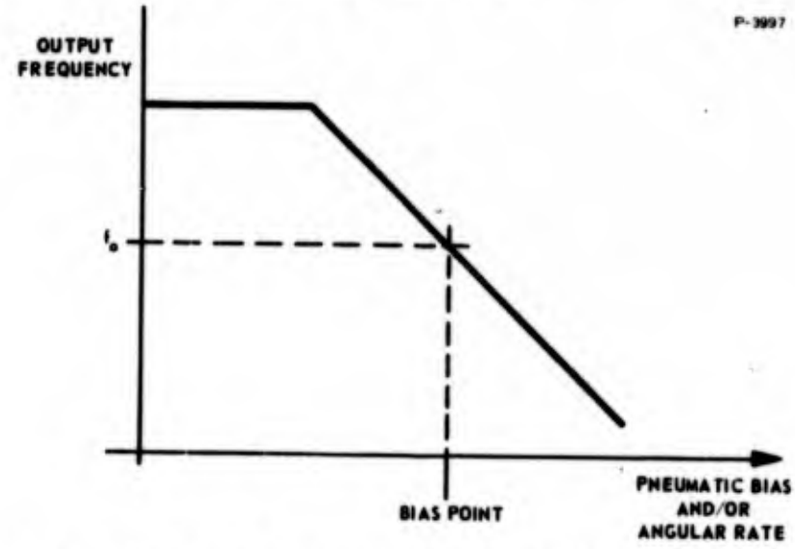

Figure 11 - Rate Sensor Idealized Characteristic

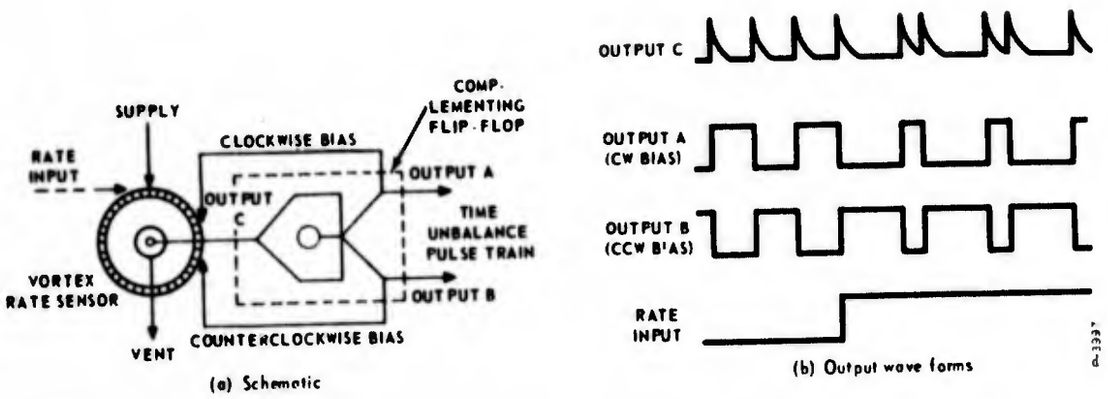

Figure 12 - Rate Sensor Subsystem-Basic Schematic and Waveforms
(a) Schematic (b) Output Waveforms

In the basic network (Figure 12(a)), each sensor pulse (output C) switches the output of the complementing flip-flop (outputs A and B). The flip-flop outputs are connected back to opposing control inputs on the sensor to establish the sensor bias direction. Since the flip-flop switches at each sensor pulse, the sensor bias direction also changes after each sensor pulse. Since the time between pulses is established by the vector sum of the bias and rate-induced angular moments, rate alternately adds to the bias for one pulse period and subtracts for the next. Only the direction of bias is alternated (the magnitude is constant) so that with zero rate, the alternate pulse durations are equal. The output of the network is the time-unbalance-modulated pulse train which exists at the flip-flop output (Figure 12(b)).

The major advantage of the selected approach over a simple standard-pulse-averaging approach is that the selected approach intrinsically compensates for changes in temperature and source pressure level, affording the advantages of push-pull techniques without requiring a pair of matched sensors.

The use of alternating bias to achieve time-unbalance modulation requires that the time for bias be short, relative to the shortest time between sensor output pulses. If the sensor output frequency has a maximum value of f_{max} for the maximum corresponding rate input, $\dot{\theta}_{max}$, the sensor bias reversal time must be short compared to

$$T_{min} = \frac{1}{f_{o\,max}} .$$

This constraint on bias reversing time requires that delays in the external network and the switching time constant of the vortex chamber be held low, consistent with the desired sensor operating frequency range. Ideally, delays and lags in the bias switching path should be zero; practically, moderate values of effective switching time merely result in reductions in modulation sensitivity and processed frequency.

C. SIGNAL PROCESSING SUBSYSTEM

1. Variable-Gain Pulse Amplifiers

The pulse amplifier chain performs two functions, the first being amplification of the time-unbalance signal by increasing the height of each pulse with negligible change in the pulse width. This is done with a series of bistable amplifiers. The second function is gain change of the system, accomplished manually using an external valve. The required gain change is 10:1; that is, the maximum gain is ten times the minimum gain.

The amplifier configuration is shown in Figure 13. Four bistable amplifiers are connected in series so that the gain of the total is the product of the individual gains. The first three stages utilize units which have a good pressure gain when working with the small signal output of the rate sensor subsystem; these will not work, however, at

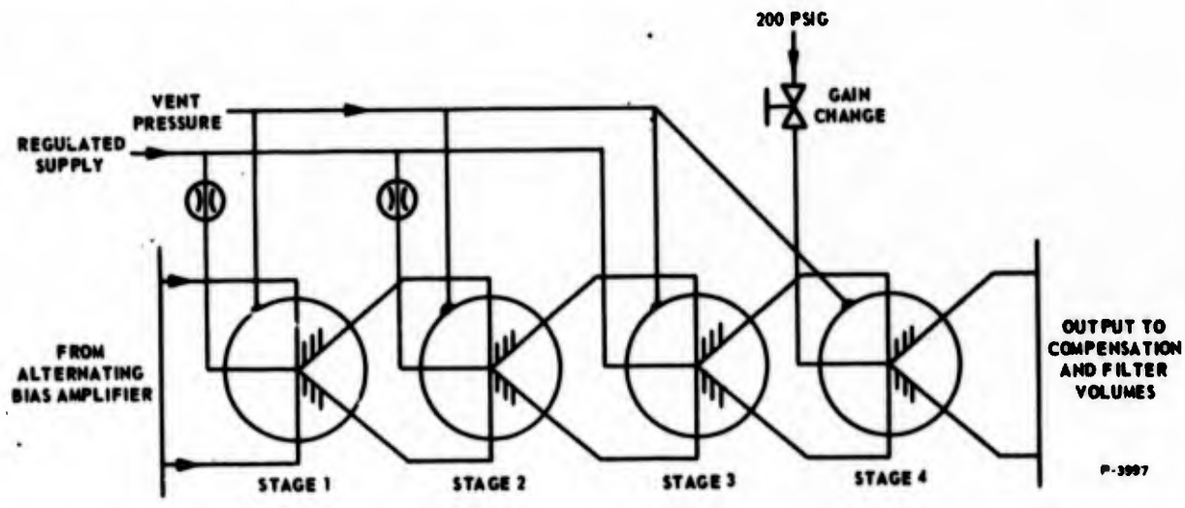

Figure 13 - Variable Gain Pulse Amplifier

the high supply pressure required by the last stage. Therefore, an amplifier with less pressure gain (i.e., better wall attachment) is used because it remains bistable at pressures above 200 psig, the maximum supply pressure to the fourth stage. As with the alternating bias amplifier, these amplifiers operate at 25 psig back pressure.

The gain of the entire amplifier chain is controlled by the supply pressure to the fourth stage. The first three stages are set up in such a way that the output pressure of the third stage is sufficient to switch the fourth amplifier for all supply pressures to the fourth amplifier. The output pressure of the fourth stage depends on the supply pressure to this stage; and the gain of the amplifier chain is the ratio of the output to the input pressures. Therefore, when the supply pressure to the fourth stage is varied, the gain can be varied without affecting performance. In effect, the gain is changed by changing the gain of the last stage.

2. Filter Shaping Network

The function of the filter compensation network is to convert an amplified time-unbalance pulse-train input to a time-varying average signal (by filtering) and to form a "washed-out" time varying signal by subtraction of two differentially lagged functions of the time-varying average signal.

Filtering is achieved by passing the time-unbalanced pulse-train through a first-order filter comprising an orifice-volume combination. The "wash-out" function is achieved by passing the same time-unbalanced pulse-train through a second first-order filter (with break frequency lower than the first filter) and subtracting the two filtered time-varying signals. The difference of the two signals is formed by injecting the signals from the two filters into a summation vortex amplifier (in opposing control ports) such that the output of the vortex amplifier is the desired time-varying difference signal. Figure 14 is a block diagram of the network and Figure 15 is a schematic of the network.

The filtering volumes used consist of two 50 in^3 volumes and two 5 in^3 volumes. They are coupled in such a way that there are two filtering paths, each connected to one 50 in^3 volume and one 5 in^3 volume.

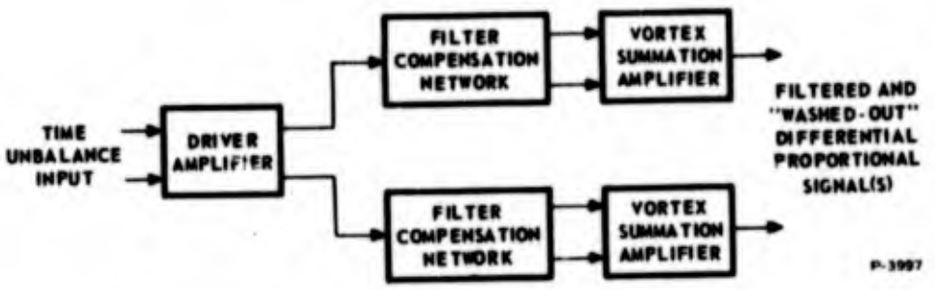

Figure 14 - Filter Compensation Network - Block Diagram

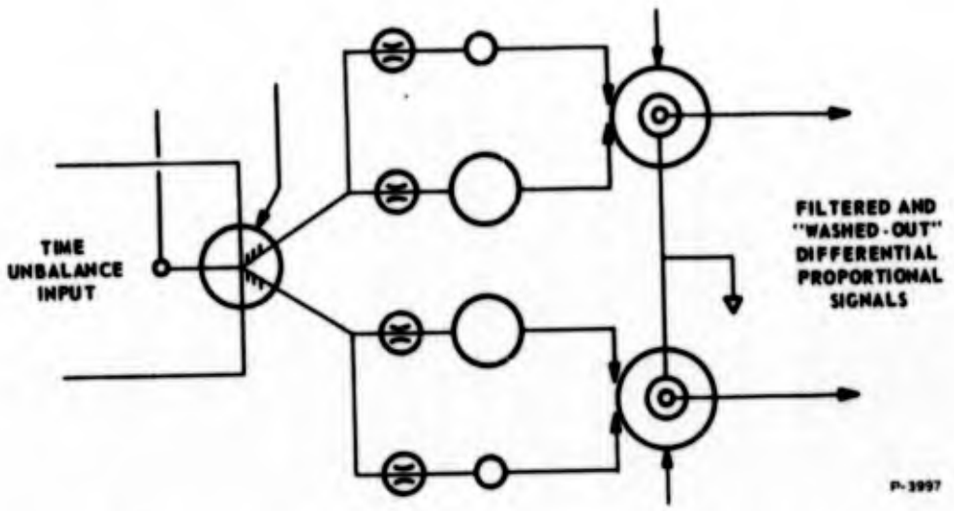

Figure 15 - Schematic - Basic Configuration of Filter Network

D. SERVO SUBSYSTEM

The servo subsystem is shown assembled in Figure 16 and expanded in Figure 17. The system includes the servo amplifier, servovalve, motor and position transducer. The processed rate signal from the compensation network enters the servo amplifier as a position command signal for the servo. The signal is compared to the position feedback signal from the position transducer and a position error is determined. This error signal is amplified by a two-stage amplifier and directed to the servovalve. The valve in turn provides flow to the motor in proportion to the magnitude of the error signal. The sign of the error signal (plus or minus) determines to which motor port the flow is metered and hence the motor direction. The motor proceeds

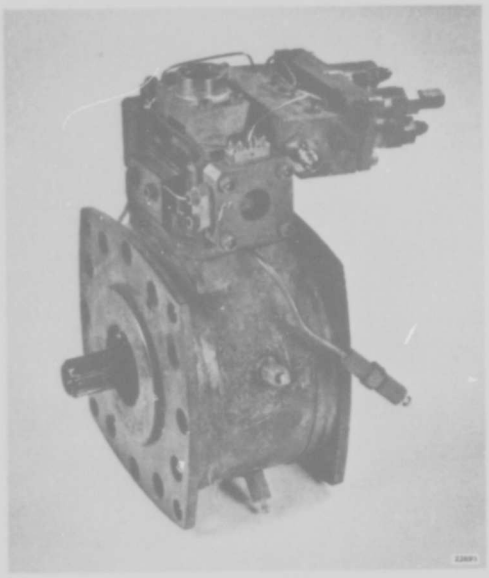

Figure 16 - Assembled Servo Subsystem

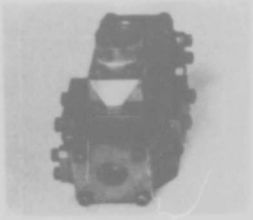

SERVOVALVE

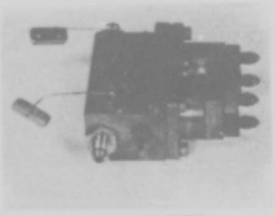

SERVOAMPLIFIER

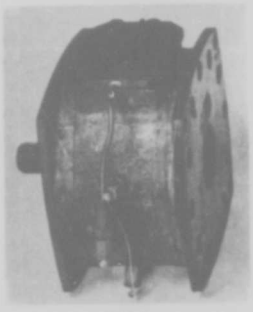

MOTOR

Figure 17 - Disassembled View of Servo Subsystem

to move and drive the position transducer through a small transmission that represents the ratio required in a typical application. When the position error reaches zero, the amplifier and servovalve null themselves and the servo stops until the demand signal changes.

The individual components are described in detail in the following sections. The servo requirements derived from the system studies are listed in Table 2.

The servo block diagram is shown in Figure 18.

The nomenclature for this block diagram is as follows:

P = Amplifier output (psid)

a = Feedback pot output (psid)

Y_a = Servovalve position (in.)

p = Filter network (psid)

K_a = Amplifier gain (psi/psi)

K_s = Servovalve gain (in/psi)

K_f = Feedback point gain (psi/rad)

G_s = Servovalve transfer function

G_a = Amplifier transfer function

Table 2 - Servo Subsystem Specifications

Linearity	5% or better
Hysteresis	3%
Null Shift	Less than 10% for a 1000°F temperature rise
Frequency Response	Less than -3db at 5 cps Less than 90 deg. phase at 5 cps
Transient Response	Maximum overshoot - 25%
Static and Dynamic Resolution	0.05 deg.
Static Stiffness	2.24×10^6 in-lb/rad min.
Saturation Velocity	30°/sec min.
Travel	±35 deg.

P-3997

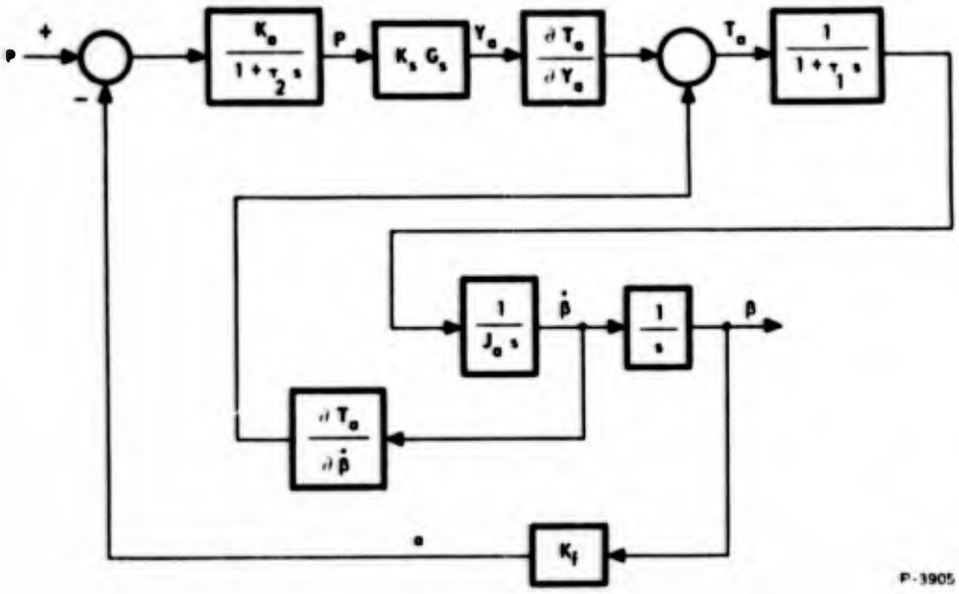

Figure 18 - Servo Subsystem Block Diagram

τ_1 = Pressurization time constant (sec)

J_a = Actuator moment of inertia (in-lb-sec^2)

β = Actuator position (rad)

$\dot{\beta}$ = Actuator velocity (rad/sec)

T_a = Actuator torque (in-lb)

$\frac{\partial T_a}{\partial Y_a}$ = Actuator torque gain at operating point $\frac{\text{in-lb}}{\text{in.}}$

$\frac{\partial T_a}{\partial \dot{\beta}}$ = Actuator torque-speed slope at operating point $\frac{\text{in-lb}}{\text{rad/sec}}$

The servovalve transfer function is given by,

$$\frac{Y_a}{S} = \frac{K_v}{\frac{S^3}{\beta \omega_{nv}} + \frac{\alpha S^2}{\beta \omega_{nv}^2} + \frac{S}{\beta \omega_{nv}} + 1}$$

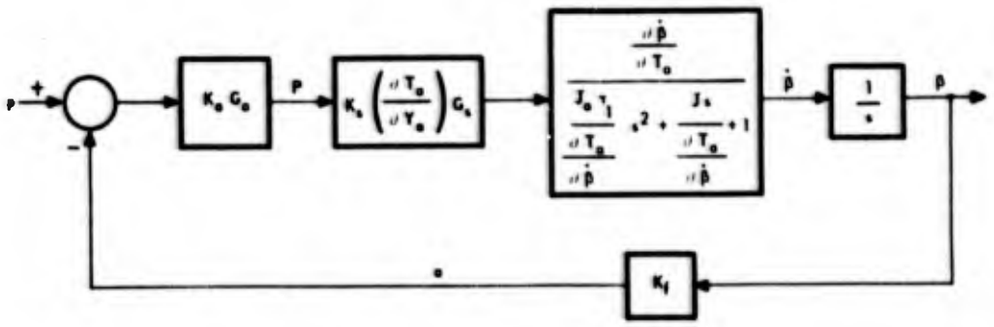

Figure 19 - Reduced Servo Subsystem Block Diagram

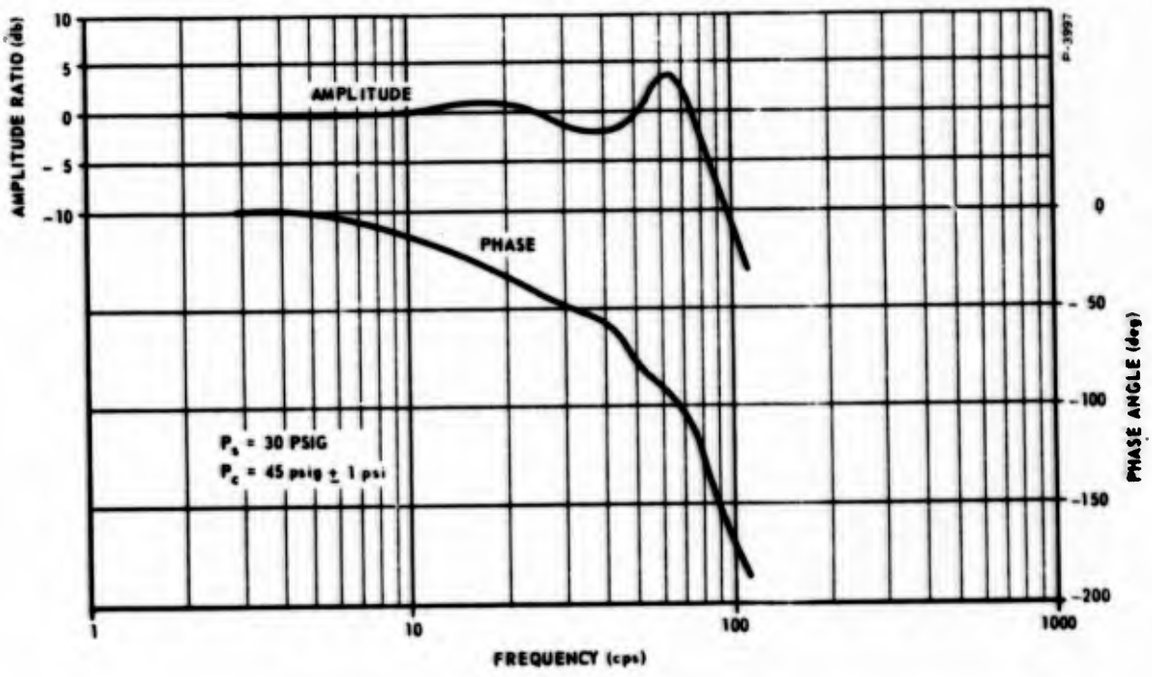

Figure 20 - Servo Amplifier Response Curve

and,

$$\omega_{nv}^2 = \frac{2 A^2 k P_o}{MV}$$

where

M = spool mass (lb-sec^2/in)

V = end chamber volume (in^3)

k = 1.4 for air

P_o = end chamber quiescent pressure

A = spool end area

The block diagram of Figure 18 may be reduced to the form shown in Figure 19 where the first block represents the servo amplifier gain and transfer function. The second block represents the servovalve transfer function, and servovalve-motor gain and the third block diagram represents the motor transfer function.

Figures 20, 21 and 22 are the dynamic response curves of these three blocks and:

$$\frac{\partial \beta}{\partial T_a} = 0.000018 \text{ rad-sec/in-lb}$$

$$\frac{\partial T_a}{\partial Y_a} = 6{,}000{,}000 \text{ in-lb/in}$$

$$K_s = 0.0003 \text{ in/psid}$$

$$K_f = 10 \text{ psid/rad}$$

Figure 23 is the open loop response of the servo obtained by summing Figures 20, 21 and 22.

Setting the loop gain such that an 8-db gain margin exists in Figure 8 yields the closed loop response curve shown in Figure 24. The required K_a amplifier gain is 36 db or 31 psi/psi.

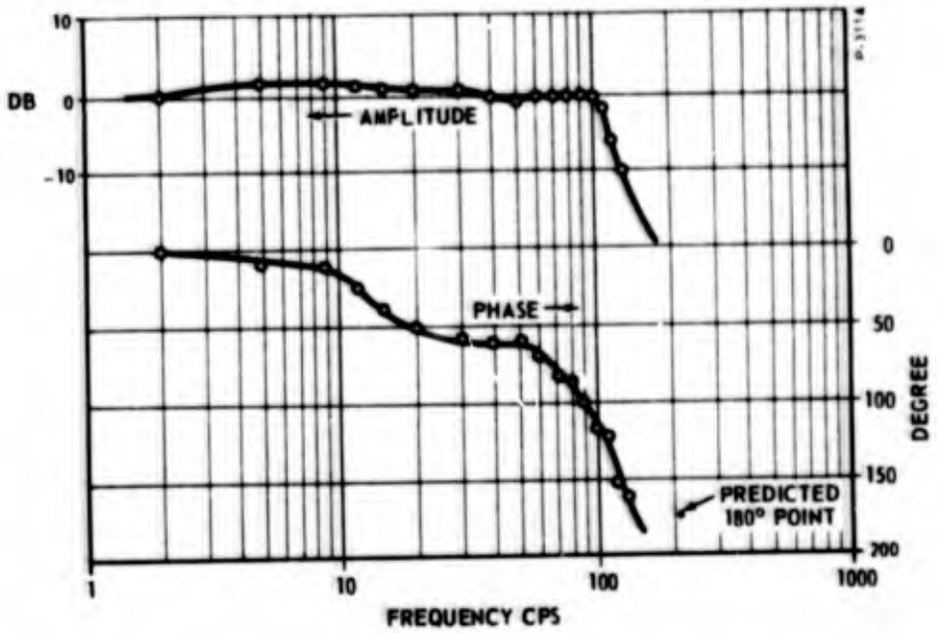

Figure 21 - Servovalve Response Curve

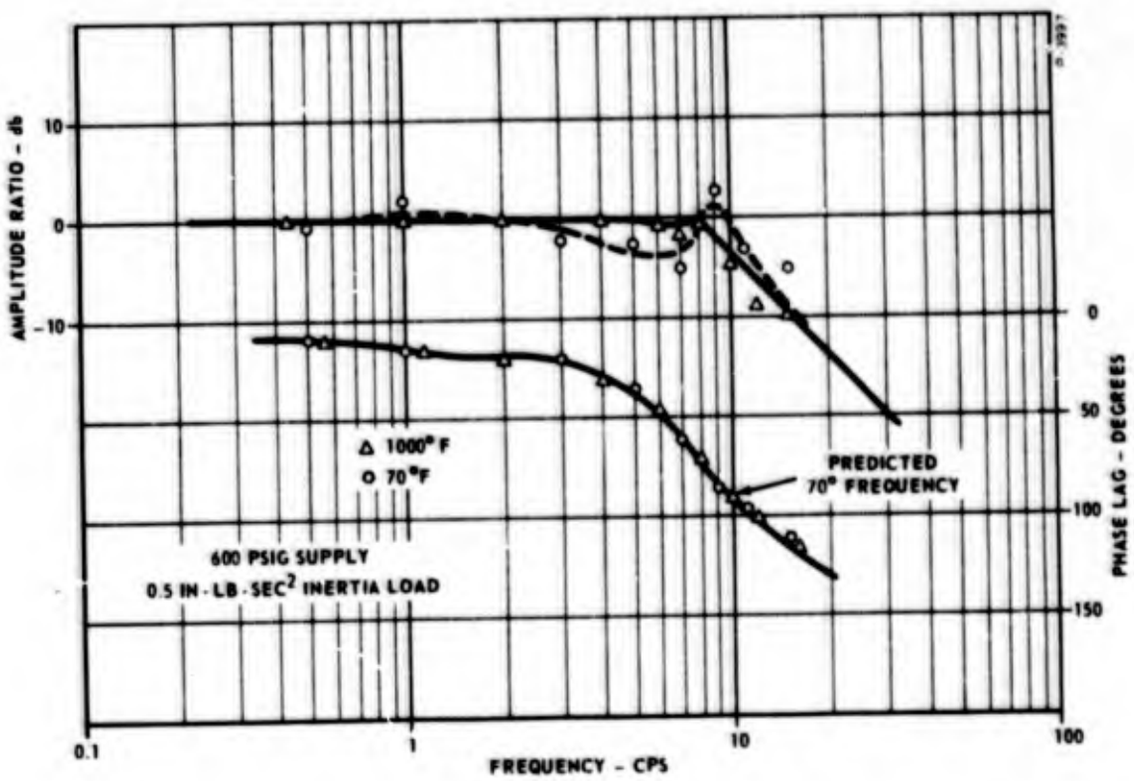

Figure 22 - High Temperature Actuator and Servovalve Frequency Response

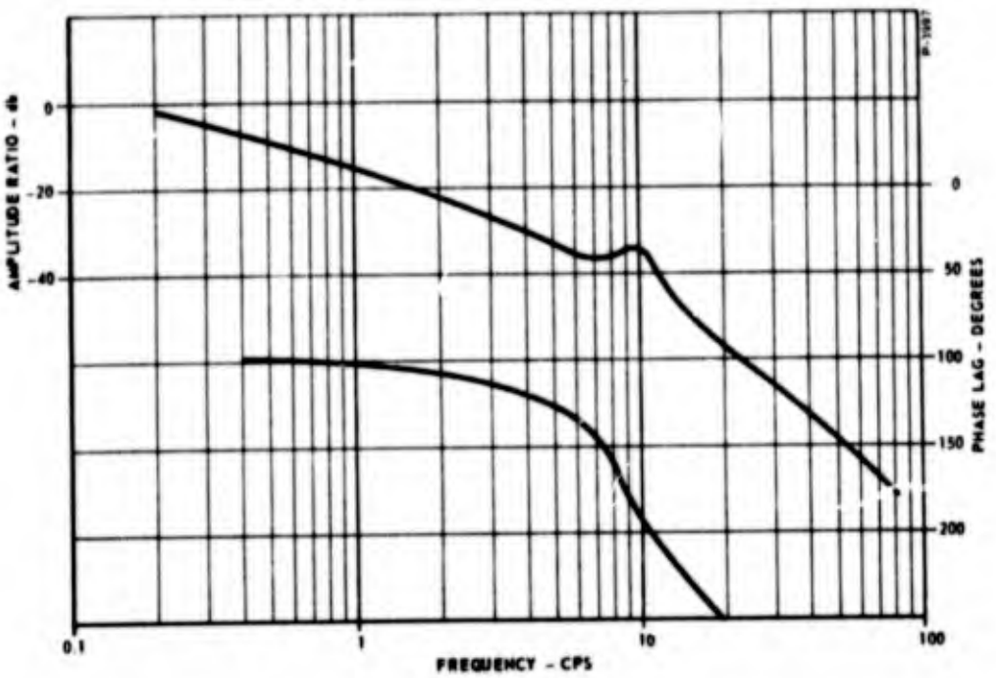

Figure 23 - Servo Subsystem Open Loop Frequency Response

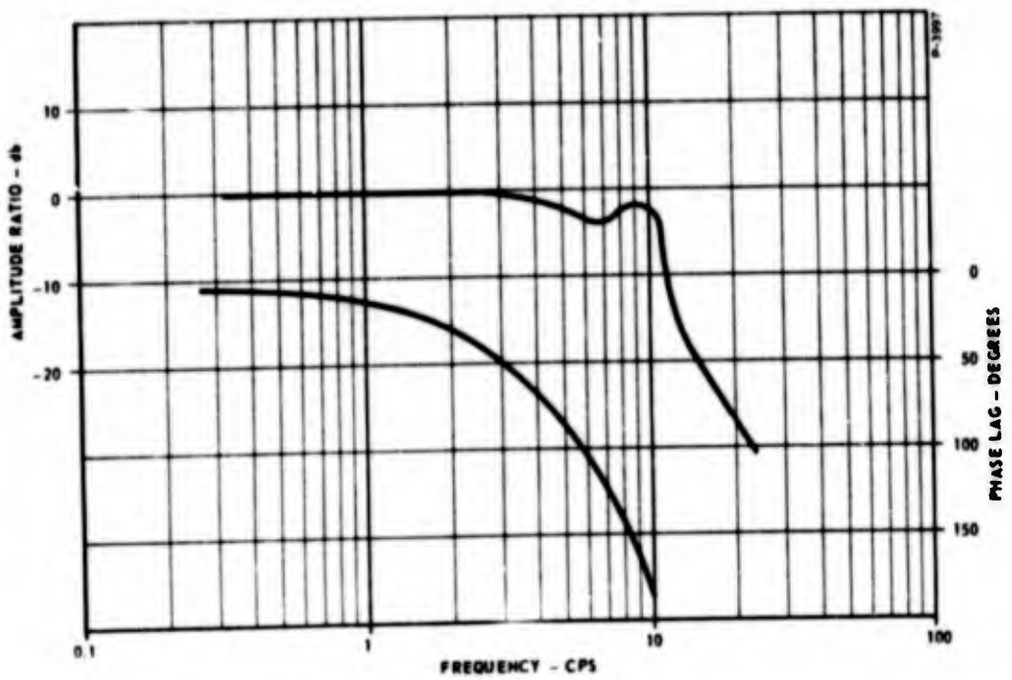

Figure 24 - Servo Subsystem Closed Loop Frequency Response

The fluidic servo amplifier provides the signal summation function and amplifies the error signal to a level appropriate for operating the flueric pilot stage of the servovalve. The amplifier consists of a vortex summation amplifier stage and two stages of venjet pressure and level amplification. Each stage contains two elements operating in push-pull with all signals being push-pull orientated.

A schematic of the amplifier is shown in Figure 25. The inputs are push-pull pressure signals and include a compensated vehicle rate signal, a servo angular position signal and an addition signal or bias pressure. The output signal is the amplified servo position error signal and operates the servovalve pilot stage. Two supply pressures, one at 600 psig supplied to the high pressure port and one at 30 psig supplied to the low pressure port are required to operate the amplifier.

The unit is designed to mount on the servo housing and has internally manifolded ports as well as external ports. It is fabricated from stainless steel and will operate at 1000°F gas temperatures. The assembly consists of three parts which include a manifold assembly containing the four venjet amplifiers, all internal connections and two

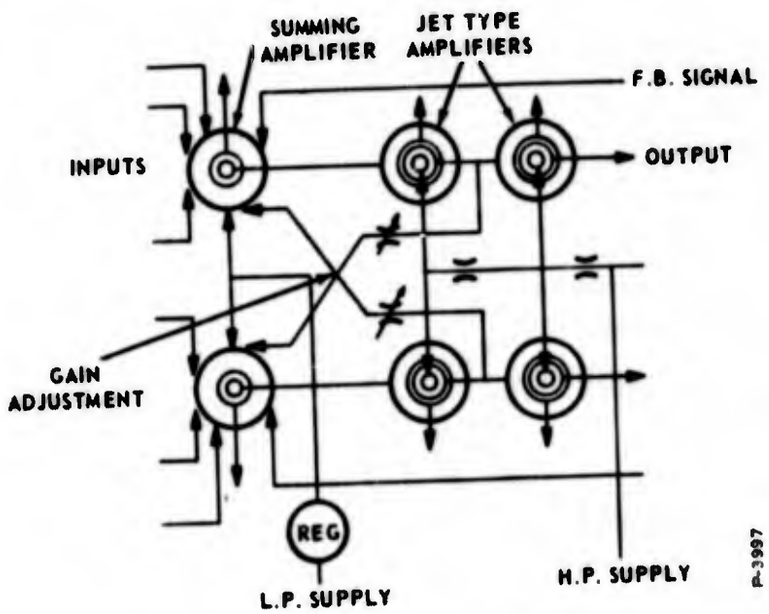

Figure 25 - Servo Amplifier Schematic

vortex summation amplifiers. All joints in the three subassemblies are diffusion bonded or high temperature brazed to eliminate use of seals. The summing amplifiers are connected to the manifold assembly with metal seals. These can be removed or replaced with a modified amplifier if required. The venjets are located in the manifold block. They are fixed assemblies brazed together using high temperature brazing alloys. However, the supply manifold is accessible. Supply orifices can be modified if the high pressure supply requirement is changed to the servomotor. Two adjustable orifices are located on the sides of the manifold assembly for the specific purpose of adjusting the servo amplifier gain.

The rate signal from the compensation volume is supplied to the amplifier through the servo housing and enters the manifold assembly. The position feedback signals are supplied directly to the summing amplifiers through external ports located on their ends. The output signal is supplied to the servovalve by two small stainless steel tubing lines that are part of the manifold assembly. The assembly bolts to the servo housing with three Number 10-24NC screws which also clamp the venjet supply manifold cover. The cover cannot be removed, however, without removing the small flathead screws on its face. The summing amplifiers are bolted to the manifold by four screws. A seal spacer plate and five seals must be placed between the amplifiers and manifold prior to assembly. The summing amplifiers are right and left hand assemblies. Installation must be performed in such a manner as to line up the supply ports characterized by the single large seal. A photograph of the complete servo amplifier is shown in Figure 26.

A gain adjustment function is provided in the servo amplifier by a feedback path from the first venjet stage to the summing amplifier. The feedback loop is a regenerative loop in that it increases the original gain by a given amount determined by an orifice adjustment. As the summing amplifier pressure output increases, the venjet output is increased. The venjet output is fed back to further increase the summing amplifier output. The gain of the feedback path is always less than one; thus, the loop cannot become unstable. The output pressure of the venjet is set at the proper pressure to be introduced into the summing amplifier.

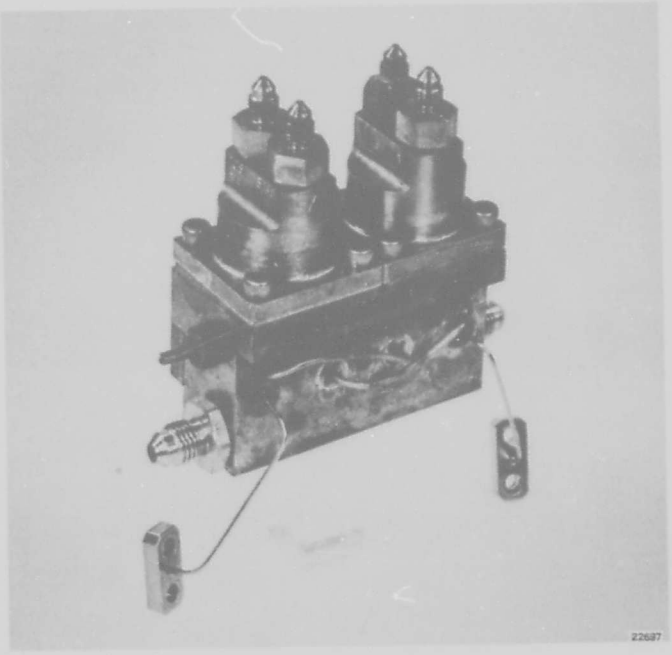

Figure 26 - Servo Amplifier

SECTION IV

COMPONENT DESIGN AND DEVELOPMENT

A. RATE SENSOR

The vortex rate sensor is similar to a vortex valve in that it uses conservation of momentum in a vortex field to amplify the rate input. However, the interior of the vortex chamber has two outstanding differences from the interior of a vortex valve or a vortex pressure amplifier. The supply flow enters around the button through a porous ring known as a coupling element instead of coming directly in from a supply plenum. Secondly, the ratio of the outer diameter to the outlet hole diameter is larger than that for a vortex valve, being 60:1 compared to 10:1 for the valve. The rate sensor is shown in cross-section in Figure 27.

The coupling element couples angular rate around the axis perpendicular to the plane of the vortex chamber to the gas entering the

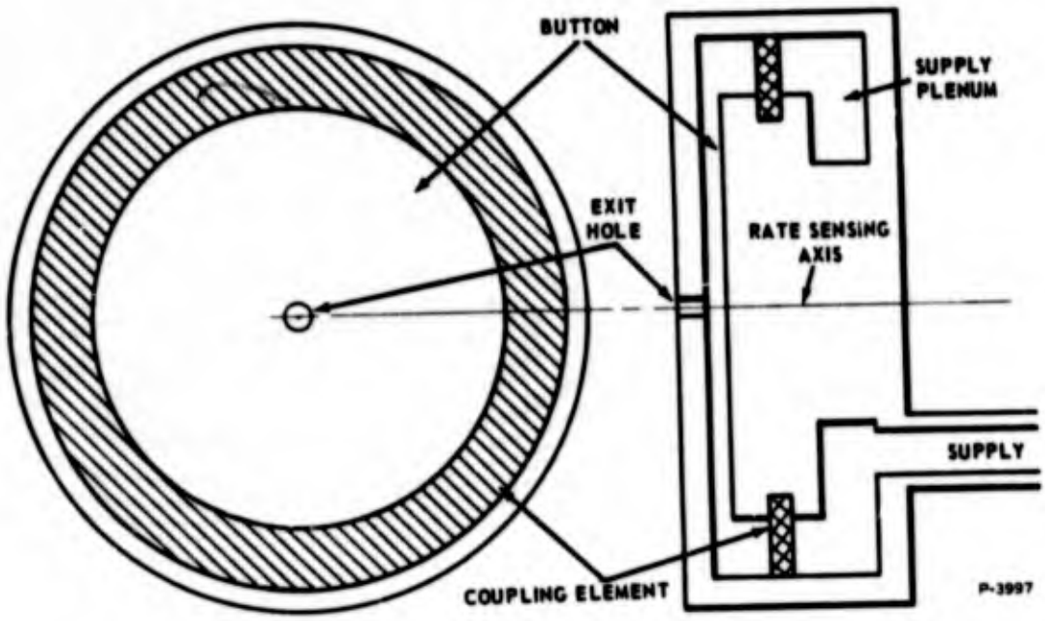

Figure 27 - Rate Sensor Vortex Chamber

chamber. This tangential velocity, V_{to}, which is equal to the chamber radius, r_o, times the angular rate of rotation, $\dot{\theta}$, is extremely small for normal values of $\dot{\theta}$. As the flow proceeds towards the center of the vortex chamber, the principle of conservation of angular momentum says that the product of the tangential velocity and the radius must remain constant, neglecting viscosity. This means that the tangential velocity is amplified by the ratio of the outer diameter to the outlet hole diameter which is 60. This shows why the outlet hole is small compared to the size of the vortex chamber.

The swirling flow spreads out as it leaves the vortex chamber, the angle of spreading being proportional to the tangential velocity of the flow in the exit hole. For large amounts of swirl the flow pattern will be conical with a hollow core.

A probe, similar to a pitot tube is placed on the axis of the exit hole as shown in Figure 28. The pressure sensed by this tube is related to the spreading angle of the jet; therefore, this pressure is related to the angular rate of the sensor. The pressure output versus angular rate is shown in Figure 29. Notice that there is almost no turndown until a point is reached where the pressure drops rapidly with increasing rate. The rate sensor is biased to this sensitive region by adding tangential flow through slots in the outer edge of the vortex chamber.

Biasing also provides a sense of direction in that the rate sensor is biased to the middle of the high gain region so that the pressure increases when the input rate opposes the bias and decreases when the input rate adds to the bias swirl. Since the bias swirl direction is known, the direction of rotation is shown by the output pressure rising or falling.

If two sets of bias injectors facing in opposite directions are provided, and if they are alternately turned on, then part of the time the input rate is bucked, and part of the time it is reinforced causing the output pressure to fluctuate. The difference between the output pressures for the two bias states would then be a function of the input rate if the bias pressure is kept constant while alternating sign.

If the probe has some internal volume and a slender neck leading to this volume the internal pressure will oscillate for certain distances between the probe tip and the vortex chamber exit hole. The frequency of the probe oscillation is related to the pressure that the probe sees,

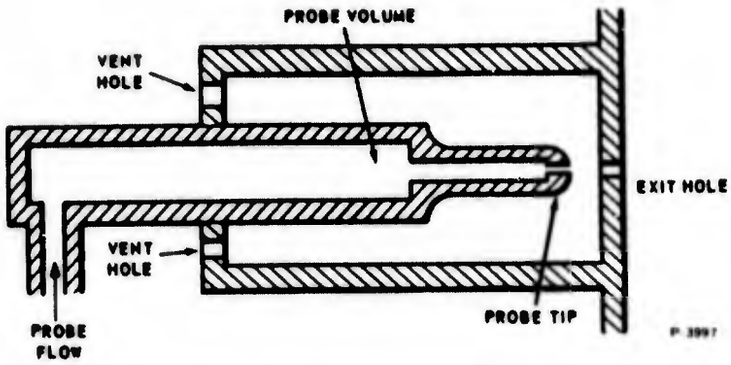

Figure 28 - Rate Sensor Pickoff

Figure 29 - Output Characteristic of Rate Sensor

a fact which makes the frequency proportional to the input angular rate and/or the bias flow.

The output pulses are triangular and symmetrical, but by blowing flow into the back end of the probe as shown in Figure 30, the pulse becomes nonsymmetrical, characterized by a sharp rise and a slow decay shown by Figure 30. The flow rate entering the back of the probe controls the discharge time constant which increases with increased flow. (See Figure 31.)

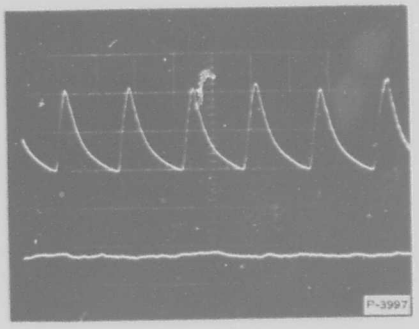

Figure 30 - Probe Output Pulse with Blowing Flow

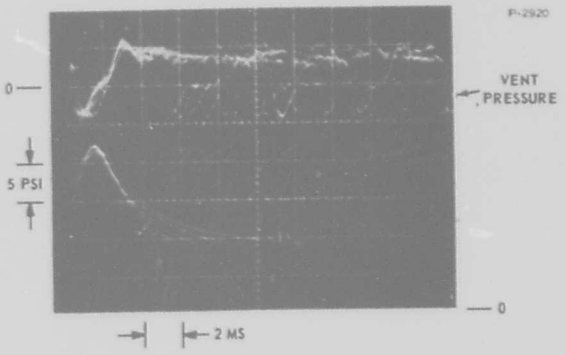

Figure 31 - Effect of Changing Blowing Flow

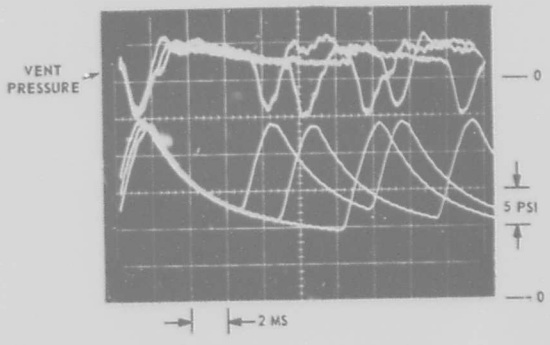

Figure 32 - Effect of Changing Swirl

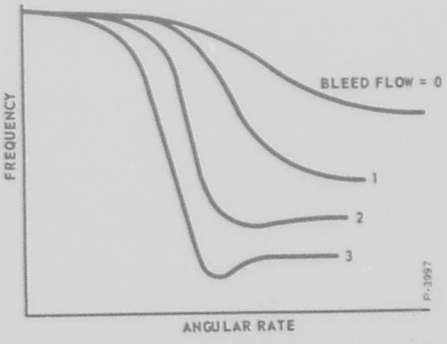

Figure 33 - Output of Pulsing Rate Sensor

The frequency variation with changing swirl in the vortex chamber is due to the threshold pressure of the pulse which allows the probe to discharge for a longer time as shown by Figure 32.

Figure 33 shows the probe frequency versus bias pressure curves which are similar to that of Figure 29 showing that the frequency is mainly controlled by the pressure that exists outside the probe tip. Here again, one can see that pneumatic biasing improves sensitivity and provides a sense of direction. The different curves are obtained by bleeding flow from a hole in the button opposite to the exit hole of the vortex chamber which improves the sensitivity many times.

Linearity is achieved somewhat by biasing to the middle of the sensitive region, but assuring linearity to the limits of saturation can

only be obtained by systematically adjusting the probe-to-exit hole distance and the flow rate into the back of the probe.

Range and sensitivity are linked by an empirical relationship which is that the total frequency range of the probe is equal to two thirds of its frequency when no swirl is present. This means that a probe pulsing at 150 pps can be turned down to 50 pps before it saturates. Therefore, the product of sensitivity and range is fixed by the geometry of the probe, increased sensitivity results in reduced range in swirl input and vice-versa.

The response of the rate sensor is critical to the operation of the time-unbalance-modulated system. If the probe can recycle before the bias is completely switched within the chamber, the probe will give out spurious pulses at the no-swirl frequency, and it is possible for the rate sensor to lock onto either the no-swirl frequency or a frequency with a period equal to the response time of the chamber.

The response time of the sensor to a change in input is directly proportional to the vortex chamber volume and inversely proportional to the size of the outlet hole. This implies that the response requirements are contrary to the requirements of sensing angular rate, which is true except for the bleeding of flow from the button which improves sensitivity while decreasing the response time by increasing the flow rate through the vortex chamber.

Since the input from the angular rate is so weak, flow noise in the vortex chamber or in the exit flow can easily swamp this signal. Some sources of noise are:

(1) Porosity of the coupling element not sufficient to produce well distributed flow.

(2) Turbulent mixing of supply and bias flow.

(3) Irregularities in vortex chamber walls.

(4) Nicks or burrs on the inside surfaces of the exit hole.

(5) Excessive turbulence of the outlet flow, due to improper venting or misalignment of the probe.

(6) Any variation in pressure being fed to the rate sensor.

Testing indicates that noise can be reduced by smooth uninterrupted introduction of flow into the vortex chamber and by a good surface finish on all wetted surfaces.

B. BIAS ALTERNATING NETWORK

The required function of the jet network used in conjunction with the pulsating rate sensor is to reverse the direction of the sensor bias after each sensor output pulse. Alternating the sensor bias direction on a pulse-to-pulse basis converts the basic frequency-modulation output to a time-unbalance modulation form.

In the rate sensor subsystem, the bias alternating function is performed by an advanced design flueric complementing flip-flop (CF). The output of such a component changes state every time an input pulse is introduced. The two outputs of the CF are connected back to opposing tangential inputs of the rate sensor, providing the bias reversing function.

On a functional basis, the rate sensor subsystem could be implemented using only the CF to close the bias-reversing loop around the rate sensor, as shown in Figure 12. Because of signal bias level considerations, the basic network form of Figure 12 must be modified slightly as shown in Figure 34.

As indicated in Figure 35, the bias input to rate sensor alternates between P_s and $P_s + \Delta P_B$, whereas the peak rate sensor output pressure is less than P_s. So that the jet network output has the proper minimum (inactive) pressure level, the jet elements are vented to a pressure equal to the rate sensor P_s. With such a jet element vent pressure level, the rate sensor peak output is inadequate to drive the complementing flip-flop, requiring elevation of the sensor output pressure.

Since the rate sensor pulse has a larger peak-to-peak swing than is required to switch the CF component, it is possible to elevate the sensor output by a simple orifice-divider network. Such an approach is analogous to using a resistance-divider network to elevate dc voltage bias levels in an electronic dc amplifier.

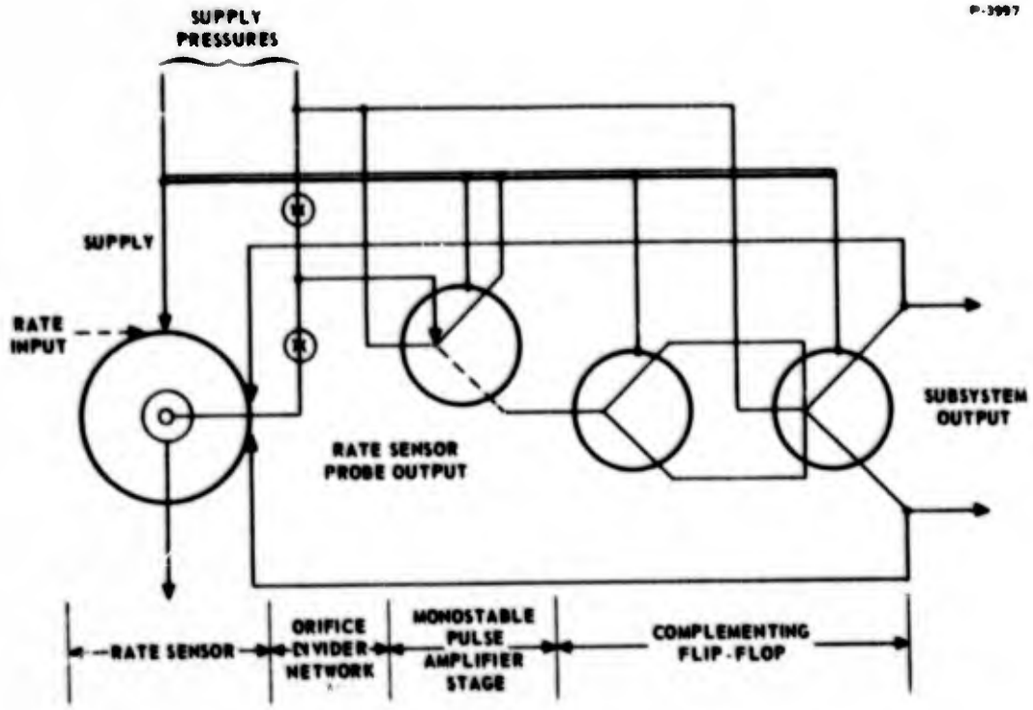

Figure 34 - Rate Sensor Subsystem Schematic

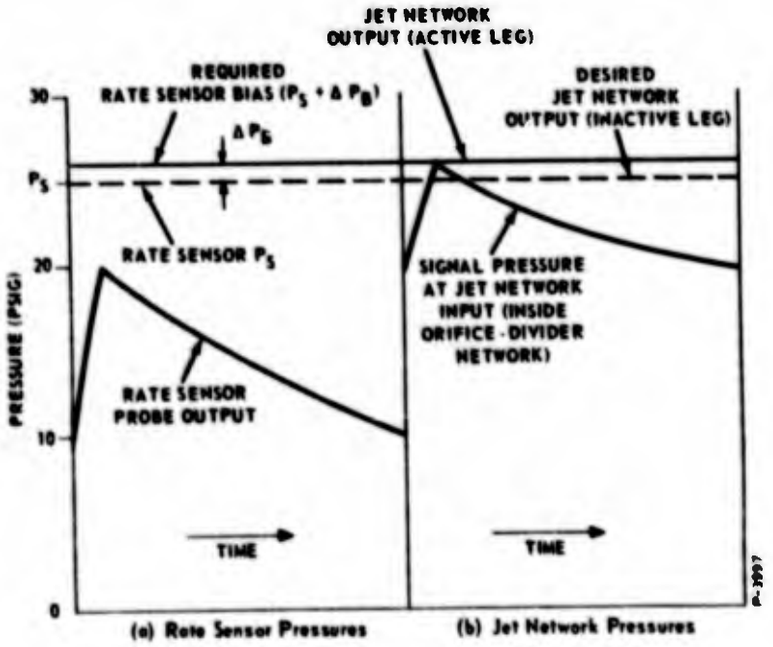

Figure 35 - Rate Sensor Subsystem - Jet Network Signal and Bias Considerations

Since the rate sensor as a component operates best with a slight amount of external flow into the probe, the orifice-divider approach is particularly suitable in that the connection from a higher pressure to the probe through an orifice normally exists and introduction of the orifice-divider network does not in any way alter or degrade the basic rate sensor operation. Care must of course be taken to hold the effective volume at the center of the orifice divider to a very low value to minimize degradation of the output pulse waveform due to orifice-volume filtering action.

The monostable amplifier stage shown in Figure 34 was added to provide a suitable excess (reserve) of signal level at the CF input to maximize network reliability under varying operating conditions.

Venting of the CF to the same pressure level as the rate sensor supply ensures that flow from the inactive bias port will be nominally zero, eliminating the inactive input as a potential noise source. In addition, the higher vent pressure minimizes the supply pressure requirements of the CF and monostable flip-flop (MF) elements.

C. FILTER COMPENSATION NETWORK

A pulse-train comprised of rectangular pulses (Figure 36) has a theoretical average value which depends upon the ratio of the "on" time (T_1) to the total pulse period (T_o). For the train of Figure 36, the ideal average value is

$$P_{avg} = \rho_1 \left[\frac{T_1}{T_1 + T_2}\right] = P_1 \left[\frac{T_1}{T_o}\right] = k\, P_1$$

where

$$k = \frac{T_1}{T_o} = \text{modulation fraction}$$

Given a pneumatic pressure pulse-train of the form of Figure 36, it is desired to process the pulse train to derive the average value in the form of a constant pressure. The approach used for investigation utilizes a simple orifice-volume combination for first-order filtering of the pulse-train to remove high frequency components, leaving the direct component.

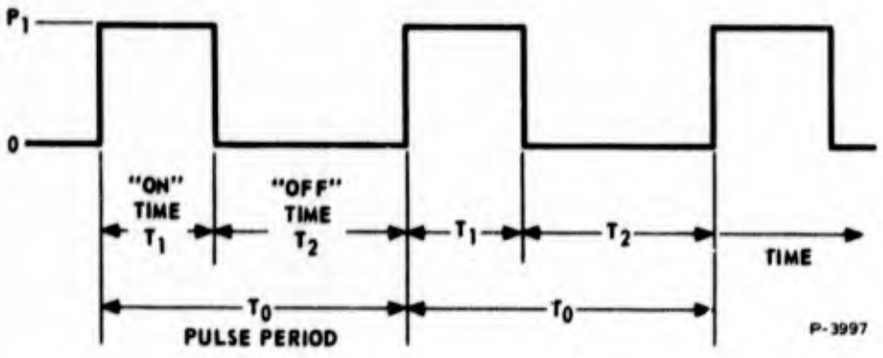

Figure 36 - Rectangular Pulse Train

Experimental Tests

To verify the equation for the ideal average pressure, the investigation encompassed the following objectives:

(1) To develop a flueric test network which derives the average value of a time-duration modulated pulse-train.

(2) To determine the comparison between the ideal and actual values of the average output pressure.

(3) To develop a mathematical model and compare the actual and theoretical performance.

(4) To determine the effect of variation of significant parameters.

(5) To investigate methods of improving performance.

(6) To consider alternate flueric networks.

The test schematic is shown in Figure 37. The test pulse-train was produced by rotating a perforated disc (siren) containing eight slots sized to give a pulse-duration equal to 75 percent of the period. The modulation fraction was varied by masking portions of the slots. Constant pulse-duration was obtained by adjusting the wheel speed at each modulation fraction for a 3 millisecond pulse-duration. The pulse-duration and modulation fractions were appropriately combined for test pulse rates from 50 to 250 pps.

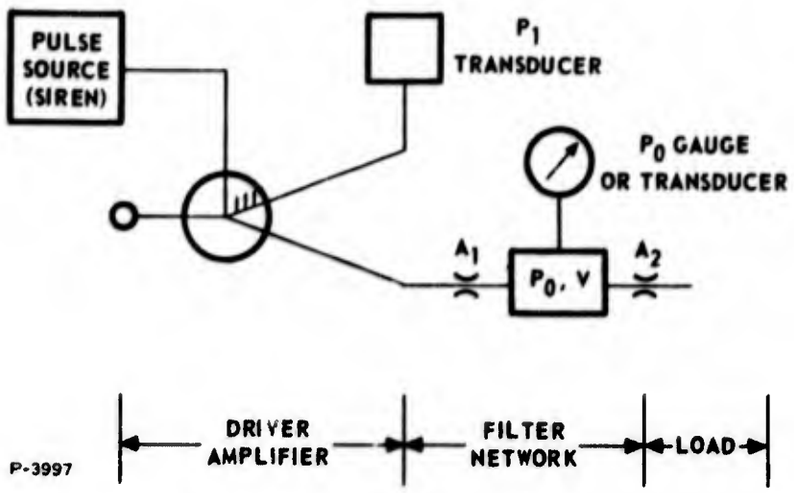

Figure 37 - Test Configuration

Supply pressures to the disc input of 10 psig and to the driver amplifier source of 25 psig were found to give most satisfactory input wave forms.

The input wave form was monitored by connecting a Kistler pressure transducer (Type 601A) to the NOT side of the driver amplifier and displaying the wave form on an oscilloscope. The output wave form was monitored at a tap at the center of the volume with a Kistler transducer. A 0-15 psi pressure gage was used to measure the average output pressure, also measured at the center of the volume. Wave forms were recorded on Polaroid film.

Test runs were as listed in Table 3.

Table 3 - Filter Network Test Conditions

	Run Number				
	1	2	3	4	5
Filter inlet orifice area (in^2)	0.000300	0.000300	0.000300	0	0
Load orifice (in^2)	0.000300	0.000158	0	0.000300	0.000158

For each run, the following values of k were used:

k = 0.15, 0.30, 0.45, 0.60, 0.75.

At each value of k, P_o was recorded at the following pulse ratio:

50, 100, 150, 200, 250 pulses per second.

Step inputs were used to determine the variation of filter time constants with input amplitude. The step inputs were provided by manually turning the slotted wheel. The output from the slotted wheel was coupled directly to the filter input orifice with the drive amplifier omitted. Several values of input pressure were used, since the time constant varies with the pressure level and magnitude of pressure change.

The average output pressure test data and the ideal and theoretical curves are shown in Figures 38 and 39. The relationship between average output pressure and modulation fraction was nonlinear. There was, however, an intermediate range of k, in which the curves were reasonably linear.

The output pressure was considerably greater when there was no orifice between the driver amplifier and the volume; but the ripple was also much greater.

The variation of P_o with pulse rate is shown in Figure 40 for the 0.0003 in^2 discharge orifice and in Figure 41 for the 0.000158 in^2 orifice. The inlet orifice area was 0.0003 in^2 for Figures 40 and 41. There was no noticeable variation in P_o with pulse rate when the input orifices was omitted.

Figure 42 shows the effect of input pressure level variation. The linear zone was shorter for the lower pressure level.

The input pulse-train is shown in Figure 43 for several values of k with speed adjusted to give a pulse duration of 3 milliseconds in each case. There was some distortion of the wave form at higher frequencies. Examination of the wave form, however, indicated that the actual time-unbalance corresponded very closely to the desired modulation fraction.

Figure 44 shows the ripple amplitude at two pulse rates. The amplitude was 0.2 psi at 150 pps and 0.09 psi at 250 pps.

The response to step inputs with various input pressure is shown in Figure 45. The time constants were measured from these pictures and were taken as the time required to reach 63 percent of the final value.

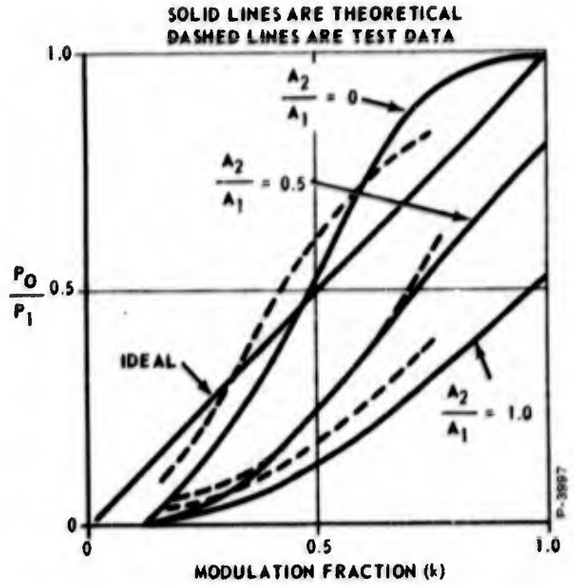

Figure 38 - Average Output Pressure Versus Modulation Fraction

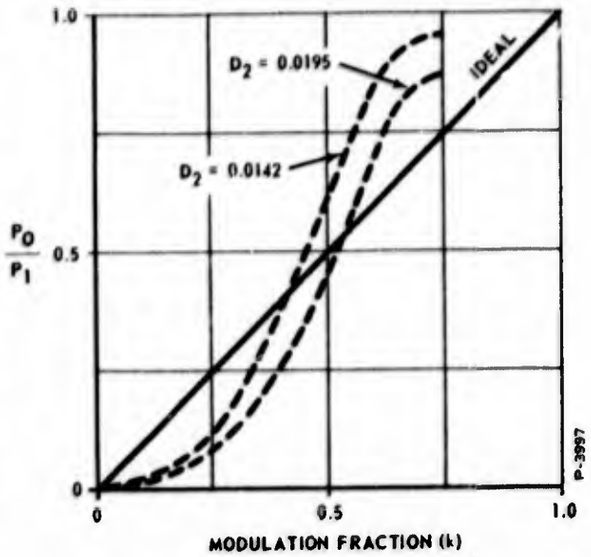

Figure 39 - Average Output Pressure Versus Modulation Fraction with No Filter Input Orifice

The filter time constant was shown to vary from 0.13 second with 20 psig input pressure to 0.03 second at 2 psig input with the input and discharge areas equal to 0.0003 in^2. Assuming a first-order linear network model, the filter break frequency was calculated to be 1.2 cps at 20 psig input pressure to 5.3 cps at 2 psig input pressure for the two cases.

Refer to schematic in Figure 46. The theoretical average output pressure is determined by steady-state analysis in which the inlet and discharge flows are equated, with the effect of compressibility omitted.

The volume is being charged through the inlet orifice for a fraction of time, k, and discharged through the inlet orifice for a fraction of time, 1 - k. The filter is discharging through the outlet orifice all of the time. Equating the inlet and discharge flow gives

$$k\, C_1 A_1 \sqrt{P_1(P_1 - P_o)} = (1 - k)\, C_1 A_1 \sqrt{P_o (P_o - P_A)}$$

$$+ C_1 A_2 \sqrt{P_o (P_o - P_A)}$$

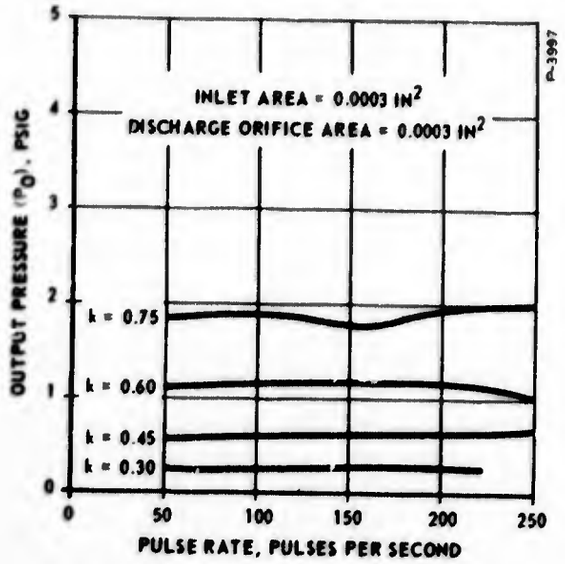

Figure 40 - Variation of Output Pressure With Pulse Rate

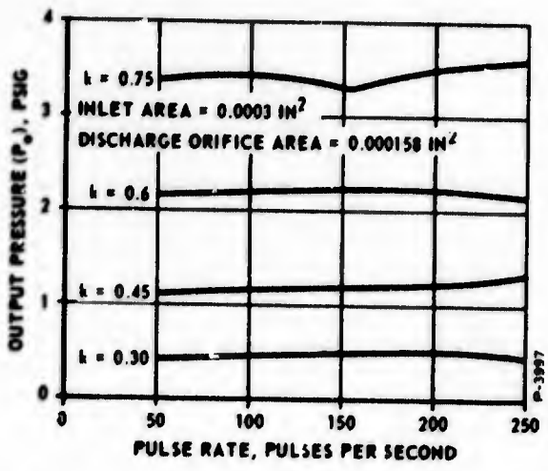

Figure 41 - Variation of Output Pressure With Pulse Rate

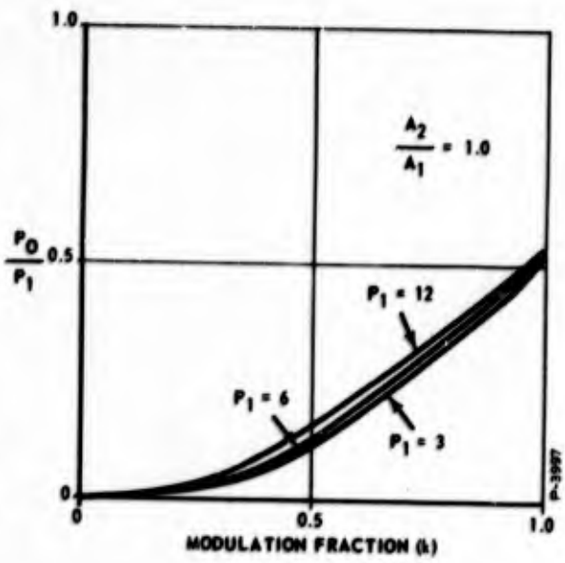

Figure 42 - Average Output Pressure Versus Modulation Fraction for Various Input Pressures

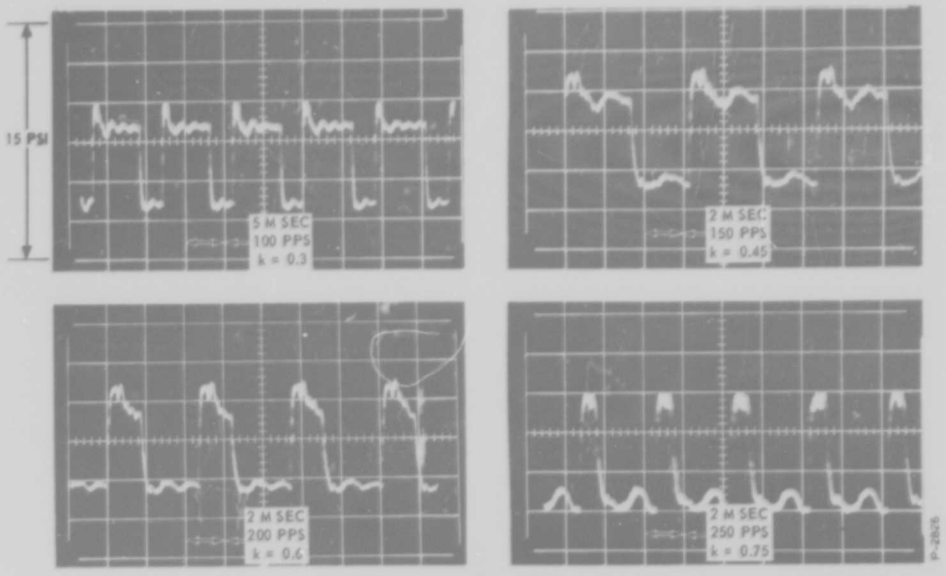

Figure 43 - Input Pulse Train

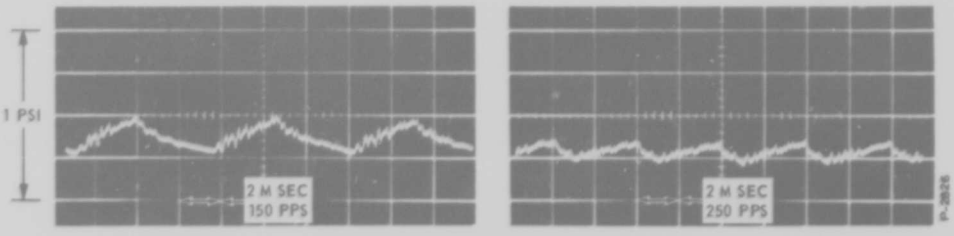

Figure 44 - Ripple at Filter Output

where

$$C_1 = C_d \sqrt{\frac{2g}{RT}}$$

Simplifying

$$k\sqrt{P_1(P_1 - P_o)} = \sqrt{P_o(P_o - P_A)}$$

where

$$k = \frac{k}{1 - k + \frac{A_2}{A_1}}$$

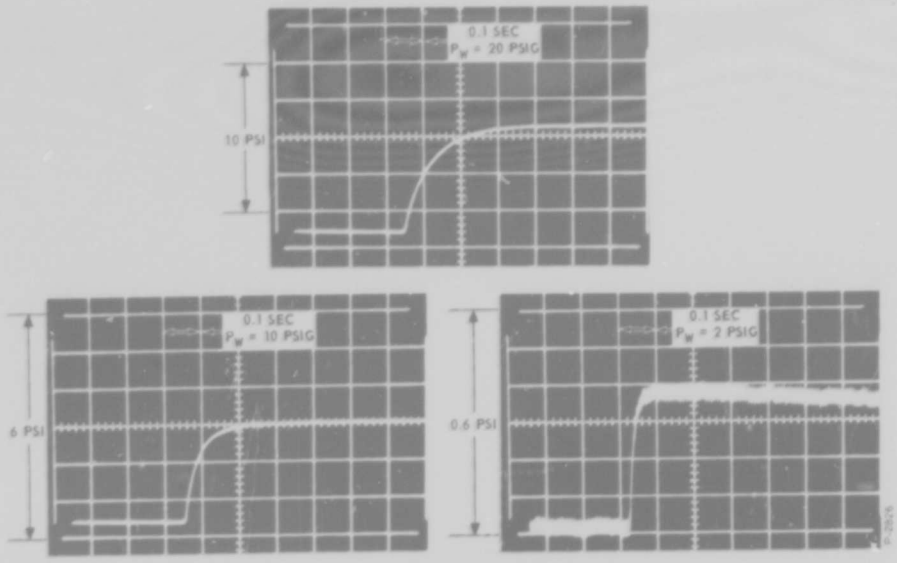

Figure 45 - Filter Step Response

Squaring both sides and solving for P_o,

$$P_o = \frac{1}{2}\left[P_a - k^2 P_1 + \sqrt{(P_A - k^2 P_1)^2 + 4 k^2 P_1^2}\right]$$

This equation gives the theoretical average filter output pressure.

The time constant for charging and discharging a volume between two orifices at low subsonic flow is

$$\tau = \frac{V}{k' Q_o} \qquad \frac{\Delta P}{P_o^*}$$

where the parameters are defined as follows:

k' = specific heat ratio

ΔP = difference between the (psi) initial and final values of the filter pressure

P_o^* = $P_a + 0.7\ P$ (psia)

V = filter volume (in^3)

$$Q_o = k C_1 A_1 R \sqrt{T} \; f_1\left(\frac{P_o^*}{P_1}\right) \; (in^3/sec) \; .$$

P_o^* is the effective value of P_o. P_o^* is a constant while P_o is varying during the step response. The relationship between P_o^* and P_o could be determined by the use of nonlinear techniques; however, it is much simpler to derive an empirical relationship. During the step response, P_o varies from P_a to $P_a + \Delta P$; therefore, P_o must be within these limits. The expression for P_o^* is shown to give the correct time constant for the three cases presented. Q_o is the flow rate that would exist if the filter pressure were held constant at P_o^*.

The correlation between this expression for the time constant and responses shown in Figure 45 are shown below.

Figure 45(a).

P_w = 20 psig (given for reference only)

ΔP = 7.1 psi

τ = 0.13 sec (observed)

$P_o = P_a + 0.7\,\Delta P = 14.7 + 5.0 = 19.7$ psia

$Q_o = 0.45 \times 0.0003 \times 640 \times 23 \times 0.89$

$= 1.76\ in^3/sec$

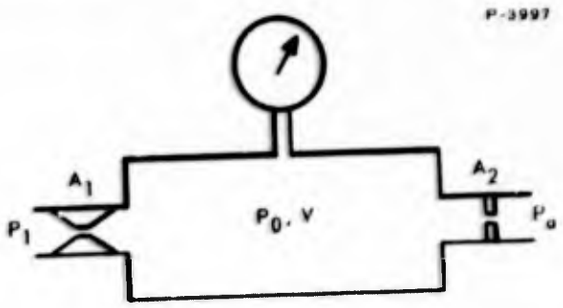

Figure 46 - Model for Analysis

$$\tau = \frac{0.92}{1.4 \times 1.76} \times \frac{7.1}{19.7} = 0.13 \text{ sec (theoretical)}$$

Figure 45 (b)

P_w = 10 psig

ΔP = 2.8 psi

τ = 0.08 sec (observed)

P_o = 14.7 + 2.0 - 16.7 psia

$Q_o = 1.75 \times \frac{0.67}{0.89} = 1.32 \text{ in}^3/\text{sec}$

$$\tau = \frac{0.92}{1.4 \times 1.32} \times \frac{2.8}{16.7} = 0.08 \text{ sec (theoretical)}$$

Figure 45(c)

P_w = 2 psig

ΔP = 0.4 psi

τ = 0.03 sec (observed)

P_o = 15.0

$Q_o = 1.76 \times \frac{0.28}{0.89} = 0.56$

$$= \frac{0.92}{1.4 \times 0.56} \times \frac{0.4}{15.0} = 0.03 \text{ sec (theoretical)}$$

Thus, the correlation between the theoretical and actual values of time constant is good.

The ripple at two speeds is shown in Figure 44. The theoretical ripple amplitude at 150 pps is now determined and compared with the actual value.

At 150 pps the on and off times are approximately equal. The input amplitude is 6 psi. The amplitude of the fundamental component of a square wave is $4/\pi$ times the square wave amplitude. Thus, the amplitude of the fundamental component of the input is

$$6\left(\frac{4}{\pi}\right) = 7.65 \text{ psi}$$

The average flow through the filter is

$$Q_o = kC\,A_1\,R\,\sqrt{T}\,f_1\left(\frac{P_o}{P_1}\right) = 0.45 \times 0.45 \times 0.0003 \times 640\sqrt{530}\,f_1\left(\frac{1.59}{20.7}\right)$$

$$= 0.77 \text{ in}^3/\text{sec}$$

The time constant is

$$\tau = \frac{V}{k' Q_o}\,\frac{\Delta P}{P_o} = \frac{0.92}{1.4 \times 0.77} \times \frac{1.2}{15.9} = 0.064 \text{ sec}$$

The output should then be

$$\frac{7.65}{1 + j\,\omega\tau} = \frac{7.65}{1 + j\,2\,\pi \times 150 \times 0.064} = 0.13 \text{ psi}$$

The ripple wave form is triangular with an amplitude of 0.20 psi. The amplitude of the fundamental component is then

$$\frac{8}{\pi}\ 2 \times 0.20 \text{ psi} = 0.16 \text{ psi}$$

Thus, the actual and theoretical values of the ripple amplitude agree very closely.

D. SUMMING AMPLIFIER

The summing amplifier shown in Figure 47 serves as the summation point for all the servo signals and provides the error signal. The error signal represents a servo position error and causes the servo to accelerate and move to the correct position in order to nullify the error. The error signal is actually zero when the amplifier outputs are equal (no differential pressure).

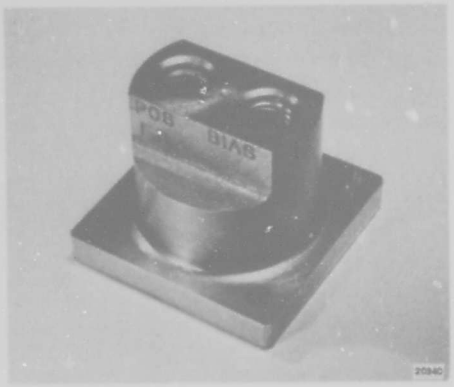

Figure 47 - Vortex Summing Amplifier

P-3997

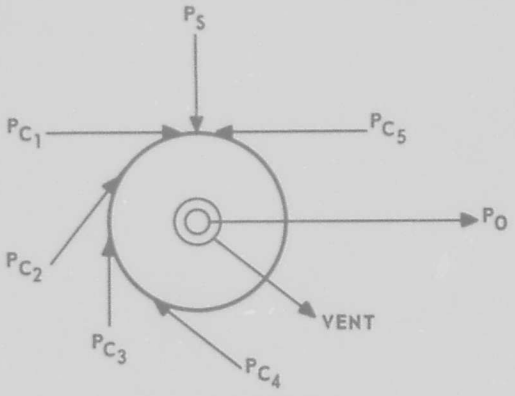

Figure 48 - Summing Amplifier Schematic

A schematic of the summing amplifier is shown in Figure 48. The amplifier operates on a constant supply pressure of 30 psig and accepts input signals from 30 to 60 psig. Its output can vary from approximately 28 psig to 5 psig and normally operates at approximately 15 psig. The absolute pressure gain of each input port is about one. Four of the input ports have a negative sign; that is, the output pressure decreases for an increase in input pressure. The fifth port has a positive sign.

The primary requirement of the servo amplifier is to provide a summation point for the various signals. First, the rate signal must be subtracted from its "lagged" signal to provide the washout function. Secondly, the demand signal, or compensated rate input, must be compared to the servo position feedback and a position error signal must be formed. A device uniquely suited for these functions is the vortex amplifier shown schematically in Figure 49. A regulated supply pressure is supplied to the "P_s" port and a signal is obtained from the "P_o" port. The output signal or pressure is controlled by the "P_c", or control port, which is the tangential input to the vortex chamber. It is possible to have many separate tangential input holes around the vortex chamber periphery, each one being completely isolated from the others. Therefore, each port becomes an input to a summing junction which is the vortex chamber. The output of the vortex amplifier then becomes the summation of all the inputs. Subtraction and/or addition can be accomplished by the tangential direction of the input ports. If two ports oppose each other as they enter the chamber, they will subtract their

respective pressures. If both are equal they may be any value without any output signal. On the other hand, if two ports aid each other or enter the chamber in the same direction they will add their respective signals to give an output equal to their sum.

Another consideration is that push-pull operation is required in the servo amplifier; two amplifiers are necessary as shown in Figure 50.

An addition sign change can be introduced by this circuit. If the push-pull signal is connected to P_{c1} and P_{c2} the output sign can be reversed by simply interchanging P_{c1} with P_{c2}. Also, if a signal is to be fed back to the summing amplifier, its sign can easily be changed by changing the side to which it is to be fed back.

Considering the many possible combinations of input signs possible, as described above, the final configuration was chosen as shown in Figure 48. All inputs except one are of the same sign and all add to the amplifier's null state. That is, the swirl direction corresponds to the P_c input's direction.

One of the P_c inputs (P_{cs}) is used as a subtraction input to complete the rate signal washout function. This allows the compensated rate signals to be at any level without affecting the amplifier bias. This is very advantageous, as it allows a gain change to be accomplished outside of the servo loop without affecting the servo loop gain.

E. VENJET AMPLIFIER

The venjet amplifiers take the summation amplifier output or error signal and perform two operations upon it. First, the venjet amplifiers provide a pressure signal amplification required by the servo loop. To provide sufficient gain, two of the amplifiers are cascaded together so that the output of the first one drives the input of the second. Secondly, the signal level is raised from the 15 psig input to the first stage to about 200 psig of the second-stage output. This function is necessary to provide the proper quiescent pressure to the servovalve pilot stage.

The first-stage venjets are supplied through a fixed pressure reducing orifice with their inputs at approximately 70 psig. Since the venjets represent a fixed sonic orifice to the supply line, the input pressure remains constant. The second stage is supplied with another fixed orifice and its input pressure is approximately 300 psig. Both

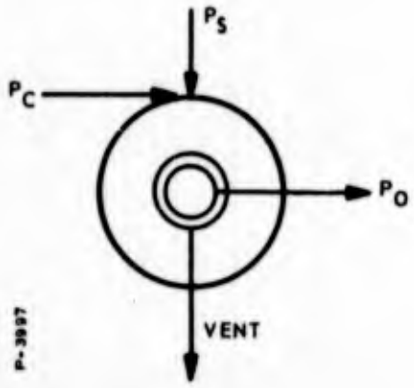

Figure 49 - Vortex Amplifier Schematic

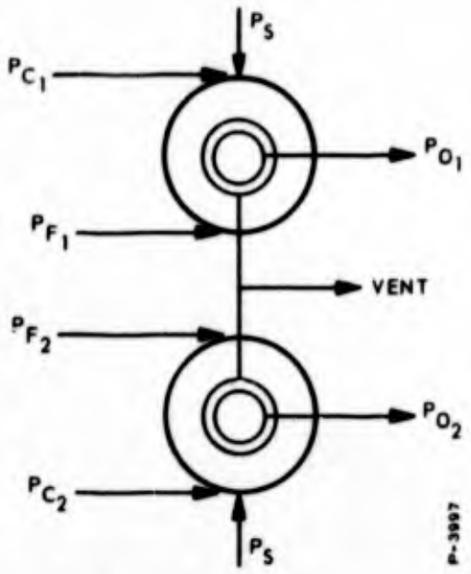

Figure 50 - Push-Pull Vortex Amplifier Operation

fixed orifices are utililized to drop the 600 psig supply pressure from the high pressure supply port and must be sized to provide proper supply pressures.

The venjets are especially designed to accept a control signal from the summing amplifier or another venjet. This input pressure supplies flow to a chamber formed around the upstream portion of the jet. A wall, with a hole about two diameters larger than the jet, forms the downstream part of this chamber. The output pressure is recovered from the jet with a conventional pickoff and varies from 40 percent to 80 percent of the supply pressure as a function of the control pressure. The control pressure is set by the geometry of the chamber and the pickoff position. Control pressure is 20 percent of the supply pressure.

The output signal of the summing amplifier is the servo position error which must be amplified to provide the proper servo loop gain. An amplification of about 20 to 40 psi per psi is required before entering the servovalve.

The output signal quiescent pressure at null is about 15 psig; whereas, the valve input quiescent level is at about 200 psig, thus a level amplification is needed. An element that gives both pressure gain and level amplification is the "venjet" shown schematically in

Figure 51. Supply pressure enters a concentric hole or nozzle to form a concentric jet. The jet is recovered by a receiver similar to a vortex amplifier receiver and becomes the output port. The cavity around the jet is closed off and connected to a vent port. The vent pressure in this cavity determines the recovery pressure of the receiver, or the output pressure. By controlling this vent pressure, which is about one-fourth the supply pressure, the output pressure of the device can be controlled from 50 to 90 percent of the supply pressure. Gains between 1 and 25 are realizable between change in vent pressure and change in output pressure. Therefore, the device serves both as a pressure amplifier and a level amplifier.

The conventional method of controlling the vent pressure is to place a throttling element in the vent line. This would require a vortex valve or equivalent throttling flueric element. On the other hand, it is possible to fix the vent orifice at a desired minimum output point and introduce a flow to the vent cavity to raise its pressure. The main problem with this method is one of inefficiency, since a considerable control flow is required. Several designs were investigated to improve the efficiency, because this would eliminate the use of a vortex valve in the circuit which represents an additional element. A design shown in Figure 52 was tested and found to be as efficient as a vortex valve controlled venjet. The control flow is equivalent to that required by a vortex valve in the vent line.

A typical output curve of the amplifier is shown in Figure 53. The gain is approximately 5 psi per psi. By changing the receiver design, the gain can be increased to 25 psi per psi as shown in Figure 54. Output impedance curves were obtained and are exactly equivalent to those of a similar sized vortex amplifier receiver and can thus be considered equal.

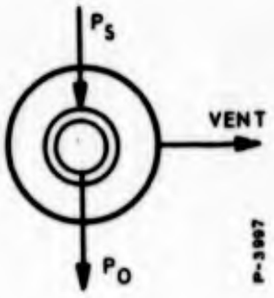

Figure 51 - Venjet Amplifier Schematic

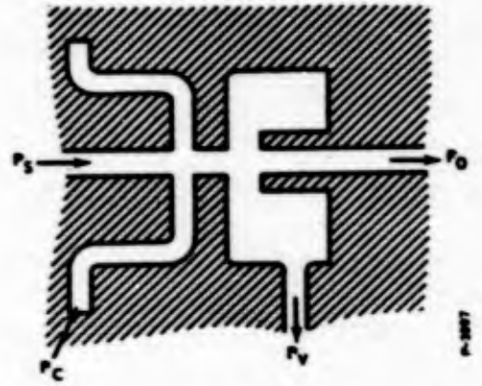

Figure 52 - Venjet Design

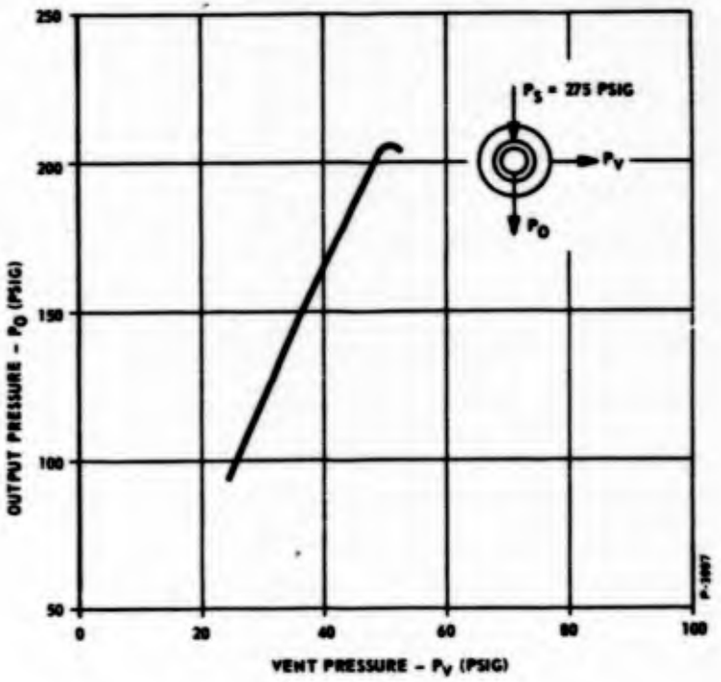

Figure 53 - Venjet Characteristic Curve

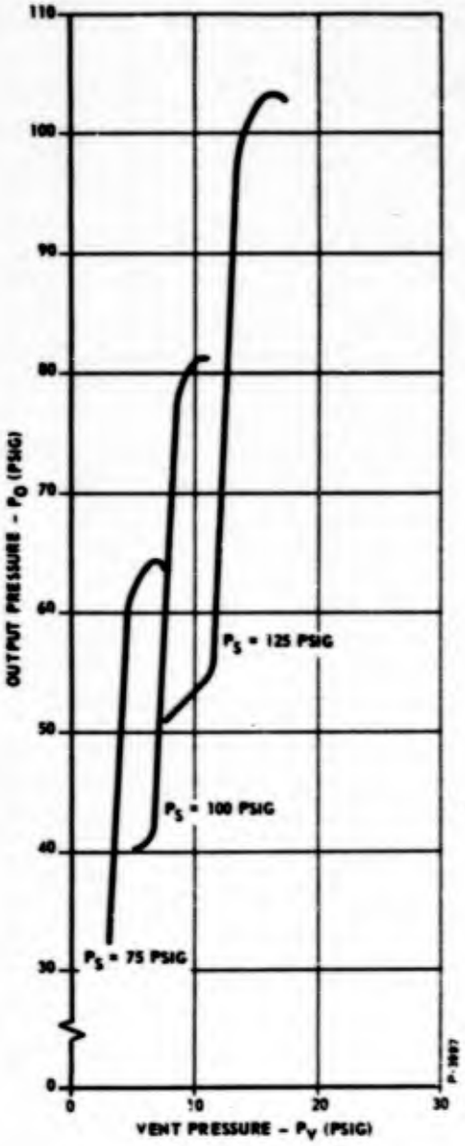

Figure 54 - High Gain Venjet Characteristics

This allows the units to be designed in the same manner as vortex amplifiers with respect to output impedance.

The final manifold assembly, containing both venjet amplification stages is shown in Figure 26. The high pressure supply port supplies all four venjets through individual orifices which are sized to provide the proper supply pressures. The outputs of the first stage are internally connected to the inputs of the second stage. The four venjets were individually adjusted to the proper operating levels and welded together. This ensures a trouble-free assembly tolerant to the temperature extremes associated with the environment. The manifold block also provides the internal connection required by the servo amplifier.

F. SERVOVALVE

The servovalve (shown in Figures 55 and 56) is a pneumatic four-way spool valve actuated by a ± 50 psid pressure signal applied to a fluid state input. A ± 40 psid signal displaces the 0.625-diameter spool ± 0.015 inch in a direction dependent on the differential pressure in the system. The maximum spool supply area is 0.0186 square inch; the maximum exhaust area is 0.0294 square inch. The valve is designed to operate within a temperature range of 70°F to 1000°F. The valve spool and body are made of Stellite 6B.

The schematic diagram (Figure 57) shows the internal mechanism of the servovalve. The basic concept for stroking the spool using vortex flow in the ram chambers was chosen for simplicity. The end lands of the spool become the buttons of vortex valves. The annular clearance between the spool and body provides the supply flow from the supply pressure land. Control flows are injected tangentially into this clearance area while flow exits from the center of the end caps.

Because the valve is a flow control valve, spool position must be a function of the input signal. This requirement was met by a spool position feedback signal which is summed with the input signal at the vortex valves. A tapered ramp on the spool varies a nozzle area which provides a pressure signal that is a function of spool position for the feedback signal.

The vortex flow also provides the necessary damping of spool motion, eliminating the need for conventional damping tanks.

Lubrication is provided by a black oxide film applied to the spool and bore by preheating the parts in an oxidizing atmosphere. The end caps and manifolds are fabricated from 440C stainless steel, since they serve only as static components, not requiring lubricant.

The four-way flueric input valve was selected because its characteristics are low fuel consumption and minimum flow of less than 20 percent of the maximum rated flow. Of the many types of valves considered, a spool valve was decided upon because it has virtually no unbalanced loading condition or highly stressed part.

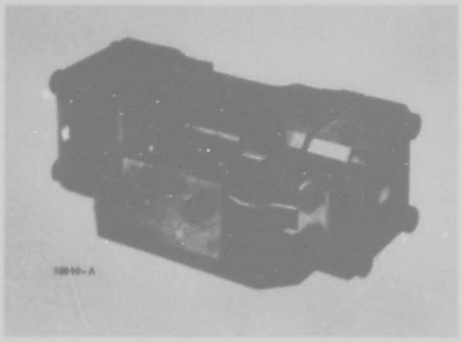

Figure 55 - Fluidic Pilot Operated Servovalve

During the development, it was of fundamental importance to find a differential ram pressure signal.

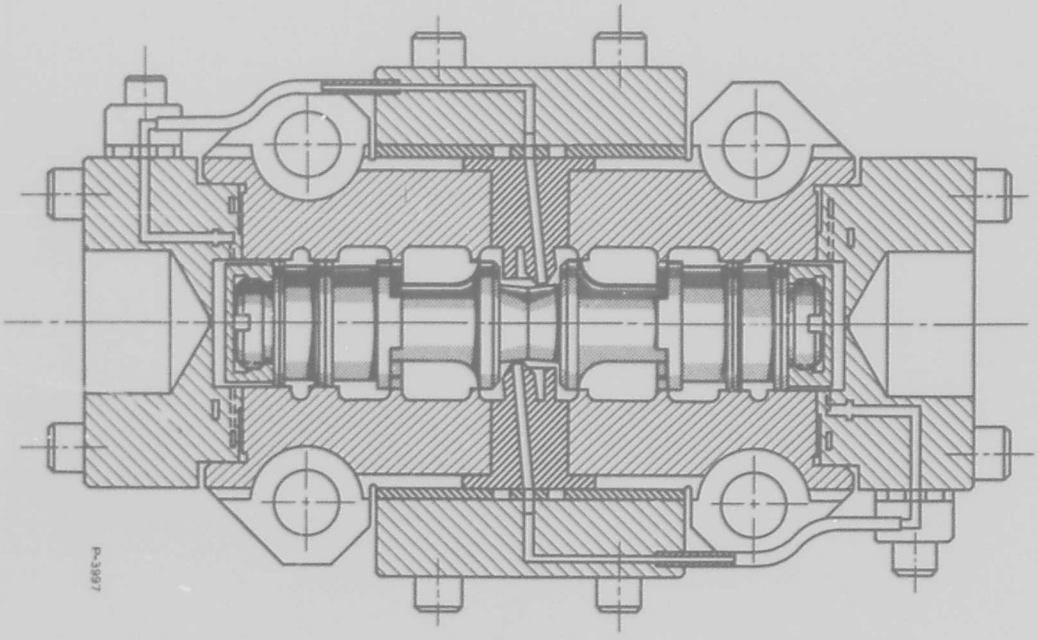

Figure 56 - Vortex Servovalve Assembly

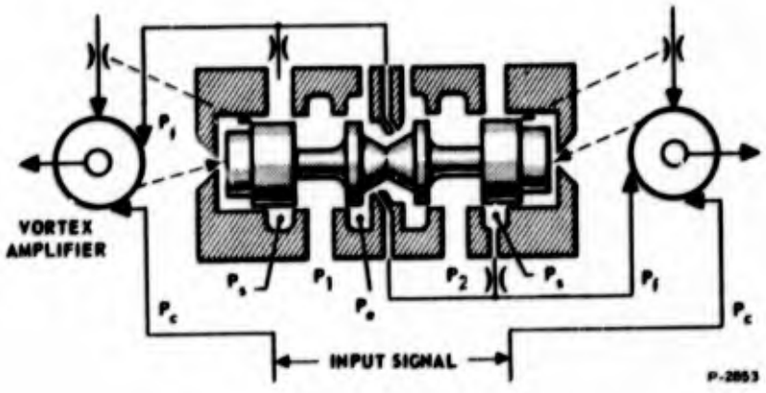

Figure 57 - Servovalve Schematic

Vortex flow in the ram chamber of the valve was selected for the simplicity of the total valve concept and ease of introducing various pressure inputs into the valve. This type of flow was also introduced because it eliminated the need for damping volumes. The mathematical analysis used for development of the servovalve appears in Appendix II.

A study was made of the pilot stage configurations shown in Figures 58, 59 and 60 to determine the best design. The configuration in Figure 58 was undesirable because the ram pressure gain for stroking a sticky spool was too low for reasonable quiescent pressure levels. The configuration in Figure 59 was not feasible because it was considered too complex for system requirements. Analysis indicated that the ram pressure gain of the configuration in Figure 60 could be brought up to the required limit. Experimental tests verified this. The final design is shown in the schematic in Figure 57.

The power stage of the servovalve is a 0.625-inch diameter spool, with a supply metering area of 0.0186 square inch and an exhaust area of 0.0294 square inch, at a rated spool stroke of $\pm$0.015 inch.

The exhaust area was made larger than the supply area to minimize the exhaust back pressure on the motor. This was accomplished with a single diameter spool by utilizing the full circumference for the exhaust area and only a portion of the circumference for the supply area. The supply area consists of three equally-spread 76 degree angular openings.

Should it be desirable to increase the supply area, the angular openings can be increased from the present 228 degrees to the full 360 degrees, thus utilizing the full circumference.

The material selected for the valve spool and body was Stellite 6B. Lubrication was provided by a black oxide film which was applied to the spool and bore by preheating the parts in an oxidizing atmosphere. The end caps and manifolds were fabricated from 440 C stainless steel, since they serve only as static components, not necessitating the need for lubricant.

A temperature stabilization technique was applied to the body and spool. The stabilization consisted of cycling the valve parts before final fitting several times through a temperature range greater than the expected operational temperature range. This technique minimizes subsequent valve distortion due to temperature extremes.

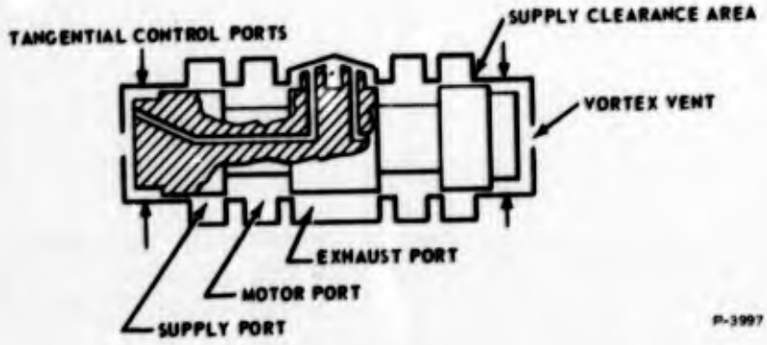

Figure 58 - Vortex Ram Chambers with Bleed Position Feedback

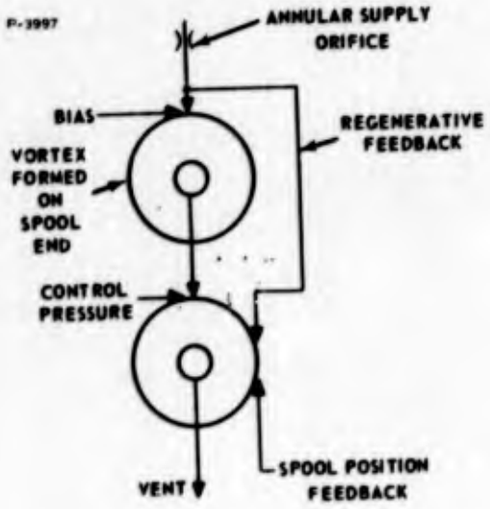

Figure 59 - Cascode Pilot Stage Configuration

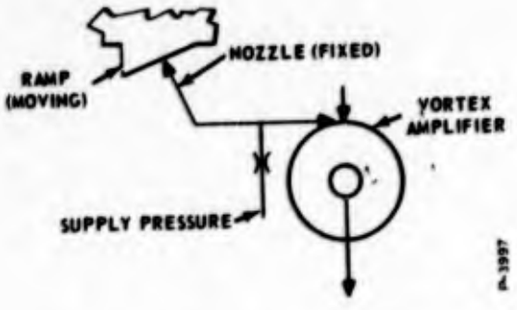

Figure 60 - Feedback Line Schematic

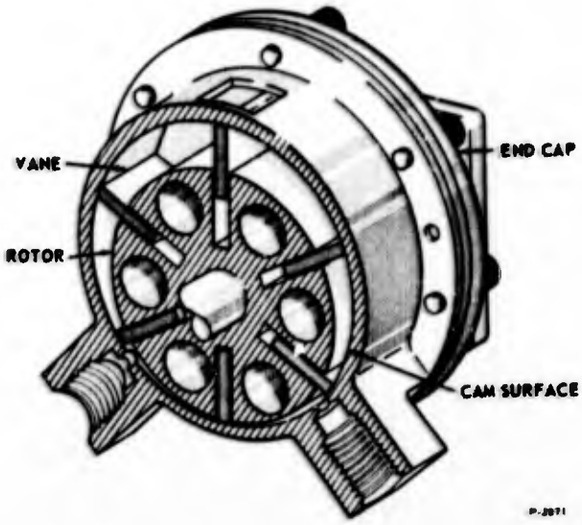

Figure 61 - Reversible Vane Motor - Schematic

The valve seals used were commercial metallic static seals fabricated from Inconel "X". They are silver plated, with special care being taken to lap the sealing surfaces to a fine finish.

G. VANE MOTOR

The vane motor is composed of four basic parts - the rotor, the housing or cam surface, the vanes and the end caps.

The rotor is the output member and also serves to retain the vanes in proper geometric position. The housing (or cam) surface serves to guide the vanes in their inward or outward motion. The vanes (in this case there are six) divide the motor into variable volumes, and the end caps are used to contain the gas in the chambers formed by the vanes.

Gas under high pressure is metered from the inlet port to a chamber formed by two vanes, the rotor, the housing and the end caps. The pressure gradient across the vanes then causes a force unbalance with rotation resulting. As each vane chamber rotates into position, it is filled with high pressure gas flow at essentially supply conditions. This charging process continues until the trailing vane of that chamber acts off the inlet port.

An expansion-type motor was selected to provide greater fuel economy. This type of motor allows the gas to expand before exhausting, therefore utilizing a portion of the internal energy of the gas. The rotor is offset in the housing as shown in Figure 61, creating an increase in chamber volume during rotation through the power stroke. As the leading vane of the chamber "uncovers" the exhaust port, the gas escapes to ambient with the final pressure in that chamber being nearly atmospheric.

With further rotation, the trailing vane "cuts off" the exhaust port and the trapped volume or residual gas must be compressed. Work must be expanded to compress this gas; therefore, work is lost through recompression. The compression process continues until the leading vane uncovers the inlet port. At this time, the gas escapes to what is essentially ambient pressure. The motor has then completed one cycle with a network output. In a unidirectional vane motor, recompression work can be eliminated by porting one side of the motor to ambient conditions.

The mechanical design for this motor program is based upon the experience gained from previous extreme environment expansion vane motor development efforts at Bendix Research Laboratories. For the immediate discussion, the description and analysis will be confined to the areas where deviations have been made from basic vane motor design and to investigation imperative for understanding the theoretical model.

Pneumatic vane motors have been restricted by several problems. Most significant of these were:

(1) Vane tip wear

(2) Vane chatter (bounce)

(3) Deadband caused by high breakout friction

(4) Inadequate lubrication in extreme temperature environments.

Vane materials have, in part, been selected on the basis of tensile stresses (encountered during bending under load) and vane tip wear. This necessarily eliminated many materials that had either excellent wearing qualities or could withstand severe impact, but could not combine both qualities. As can be readily surmised, one of the major

development areas of this program was provision for a reliable combination of optimum vane tip properties with structural integrity. The result was a rod-shaped vane tip insert with hard, brittle characteristics held rigidly in the vane in all but the axial direction. This provided for relative axial motion between vane and insert, due to differences in thermal expansion coefficients as well as differential heating rates.

A secondary problem was that of vane tip fracture due to an unstable heating phenomenon. The tips, in continuous rubbing contact with the cam surface, developed intense heat. Leakage past the ends of the vanes cooled them leaving the center tip areas hot and expanded. As thermal gradients increased, the friction heat generated became increasingly concentrated in the center of the tips, resulting in severe thermal growth of the vane center tip area which caused subsequent tip failure from either bending or impacting port edges. The primary solution of this problem was to provide small leakage paths across the vanes (located immediately under tip inserts for convective insert cooling) and to reduce heat generated in the center tip area by reducing the period of vane tip surface contact. Crossport leakage was not increased by the leakage paths because the paths were sealed off in the vane slots as they passed the pressure ports. Period of vane tip contact was reduced by relieving the housing for approximately 60 degrees of arc away from the inlet ports in the direction of expansion in the center area only. As a result, no heat was generated in the center of each vane tip during one-third of each revolution. During this period, tips were cooled by leakage over them.

Keeping the vanes in close proximity to the cam surface has been of vital concern in all efforts to design pneumatic vane motors. The vanes tried to stick in the slots at lower speeds as the result of differential pressure across the vane and friction between the vane and rotor. When sticking occurs on the expansion side, a leak path will open over the vane tip, reducing the differential pressure and, subsequently, the slot friction. The vane returns to the cam surface, and the cycle begins anew. This process results in excessive leakage and considerable power loss.

By separating opposite vanes by rods, the vanes remain close to the cam surface during all operating conditions. These rods which push the vanes against the surface on the expansion stroke, necessitated other changes; however, the cam surface could not be a circle because the

dimension over opposite vane tips must be constant while the rotor is placed eccentrically to the center of the cam surface.

Possible differences in temperature of the motor parts could cause interference of the vane stockup in the cam contour. The effects of this situation were reduced by addition of Bellville spring stacks in series with the push rods to limit the compressive loads on the vanes and push rods.

As a result of this program, starting reliability was improved and high temperature deadband decreased. Essentially, four factors accounted for this.

The first was the increase of low speed torque derived by cooling leakage paths. This made the motor operate much like a non-expansion motor at low speeds. The second was reduction of recompression work at low speeds (also due to cooling leakage paths). Thirdly, vane tip materials were utilized that did not gall. Finally, the cam surface was able to be kept cooler because of reduction of vane tip chatter.

Previous experience and testing indicates Hi-T-Lube, General Magnaplate Corporation, to have a superior product for extreme temperatures. During development effort, however, this process can often be time consuming and costly; thus, a substitute was sought. Worthwhile results were obtained from a gold flash followed by approximately 0.00015 silver plating on sliding parts subsequently run in with molybdenum disulfide powder suspended in mineral oil. The molybdenum disulfide would permeate the oil and remain after the oil was driven off.

The specified motor performance characteristics are that the motor shall develop five horsepower output power and through the transmission provide a hinge moment of 50,000 in-lb and a maximum angular velocity of 1 rad/sec. The required motor output torque to provide the maximum hinge moment is:

$$T_m = \frac{\text{max hinge moment}}{N_T \times R}$$

where

N_T = the transmission efficiency (assume 80%)

R = the transmission ratio (assume 640/1)

$$T_m = \frac{50{,}000 \text{ in-lb}}{0.80 \times 640} = 97.5 \text{ in-lb}$$

The required maximum motor speed with only the friction load is:

$$N_s = \frac{60 \text{ rad/min}}{2\pi} \times 640 = 6{,}100 \text{ rpm}$$

However, the torque-speed curve for pneumatic motors approximates a straight line and, therefore, it can be shown by taking the half speed point that the motor would not provide 5 horsepower:

$$HP = \frac{T\,N}{63{,}000} = \frac{48.75 \times 3{,}050}{63{,}000} = 2.36 \text{ HP}$$

To meet the 5 horsepower specification, it is necessary to increase the maximum torque and thus raise the entire torque-speed curve.

$$T_m = \frac{2 \text{ HP} \times 63{,}000}{3{,}050} = 207 \text{ in-lb}$$

The relationship between the displacement of the motor and torque is as follows:

$$T_m = \left(\frac{D \times \Delta p}{2\pi} \right) N_m$$

or,

$$D = \frac{2\pi T_m}{\Delta p \times N_m}$$

Based upon previous experience with pneumatic vane motors and servovalves for extreme environment applications, a differential pressure of approximately 66 percent of the supply pressure to the valve can be expected at the motor. The overall motor torque efficiency is approximately 50 percent.

Thus;

$$D = \frac{2\pi \times 207 \text{ in-lb}}{400 \times 0.5} = 6.5 \text{ in}^3/\text{rev}$$

The displacement of an expansion vane motor having six vanes is approximately

$$1.8 \left[A_H - A_R\right] \ell_R \quad \frac{\text{in}}{\text{Rev}}$$

where

A_H = the cross-sectional area of the housing

A_R = the cross-sectional area of the rotor

ℓ_R = the length of the rotor.

If we assume that the rotor will be approximately square, that is that ratio of diameter to length is approximately one,

$$D_{isp} = \left(\frac{1.8 \times \pi}{4}\right) \left[(D_R + 2e)^2 - D_R^2\right] D_R$$

$$6.5 \text{ in}^3/\text{rev} = \left(\frac{1.8 \times \pi}{4}\right) \left[D_R^2 + 4 D_{Re} + 4 e^2 = D_R^2\right] D_R$$

$$1.15 = D_R^2 e + D_R e^2$$

From a practical view as to design, the maximum e is in the range of $D_R/16$.

Therefore:

$$\frac{D_R^3}{16} + \frac{D_R^3}{257} = 1.15$$

$$\frac{256\, D_R^3 + 16\, D_R^3}{16 + 256} = 1.15$$

$$D_R^3 = \frac{1.15 + 16 \times 256}{272} = 1.73$$

$$D_R = 2.6 \text{ in.}$$

After laying out the motor, the various design parameters were adjusted slightly, due to other design considerations. The final design has the following design parameters:

Rotor Diameter	2.640 in.
Rotor Length	2.174 in.
Eccentricity	0.180 in.
Dimension over opposite vanes	3.000 in.
Displacement	6.40 in^3/rev

H. POSITION TRANSDUCER

A position transducer was needed which would perform reliably without drift or permanent changes when exposed to high temperatures. A rotary position transducer is required to convert the angular position to a flueric signal.

Figure 62 is an assembly drawing of the transducer. It is a differential output rotary transducer with a $\pm$40-degree stroke. Two ducts shown in Figure 63 illustrating view of the transducer with the cover off. The ducts are used to provide the differential output. Flow enters through a supply port and flows around and behind a rotor. This

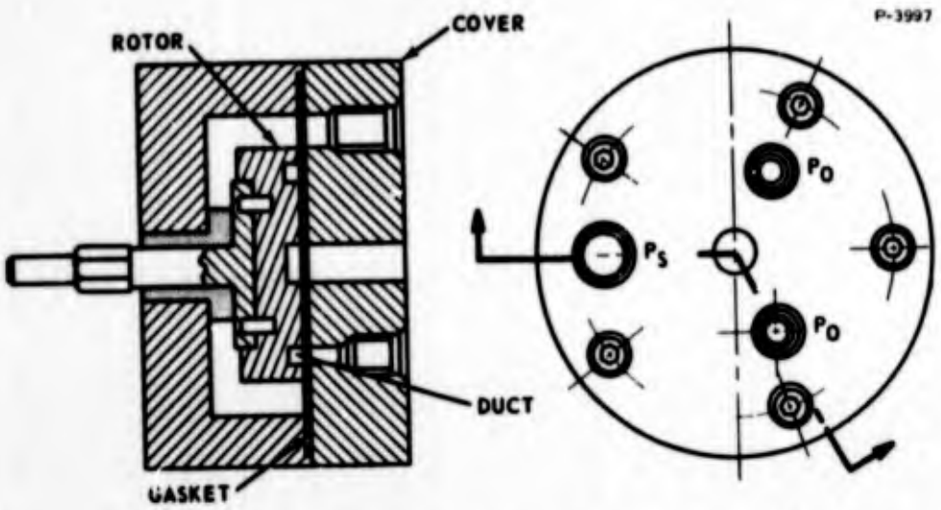

Figure 62 - Rotary Position Sensor Assembly

flow enters the two ducts and flows out a center hole in the cover. The pressure differential thus set up across the rotor forces it against a teflon gasket on the cover face, sealing the duct. The two static pressure taps in the cover remain stationary while the duct moves with the rotor. Figures 64 and 65 are assembled and disassembled views of the transducer.

Several position sensing devices were considered before selection of the final unit. Included were a flapper nozzle arrangement, a jet-on-jet oscillator and several analog configurations with static pressure taps sensing a pressure gradient that is a function of position.

The main disadvantage of a flapper nozzle arrangement is that a torsion tube in the arrangement is too highly stressed at stroke limits. A jet-on-jet device is unsatisfactory because it cannot sense large position changes.

Figure 66 is a schematic of the first analog device which was studied. The pickoff tube extends past the duct entrance so its motion will not vary the duct area.

Figure 67 is a schematic of the selected unit. The pickoff method used was to provide a static pressure tap on one of the duct walls and move this wall with respect to the duct itself.

Figure 63 - View of the Transducer Showing the Rotor Ducts

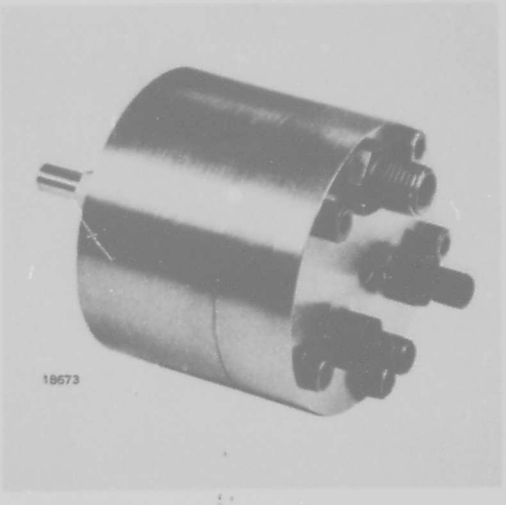

Figure 64 - Assembled View of the Position Transducer

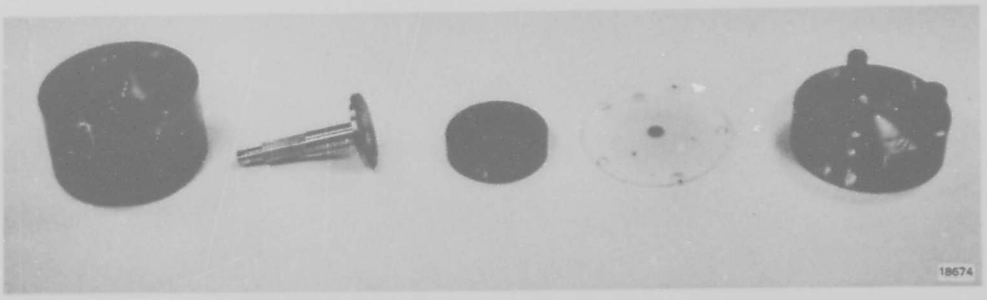

Figure 65 - Disassembled View of Position Transducer

To determine the required duct area distribution, the continuity equation for a perfect gas flowing adiabatically and reversibly was used.

$$A_x = \frac{W V_x}{u_x}$$

Where W is the flow rate through the duct (a constant along the duct), V is the specific volume of the gas at section x, u is the velocity of the gas at section x and A is the area at section x.

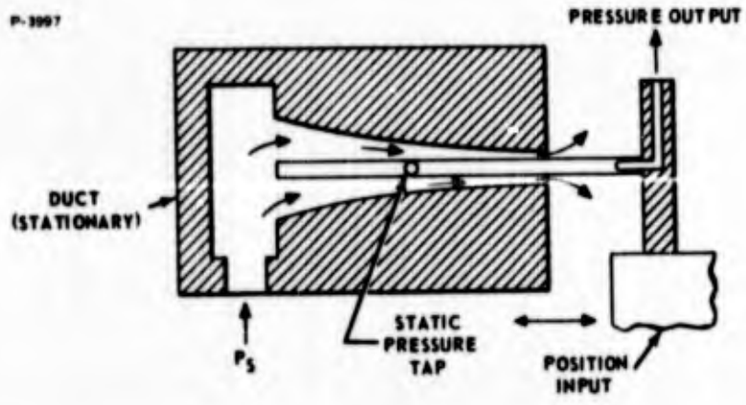

Figure 66 - Linear Position Transducer Schematic

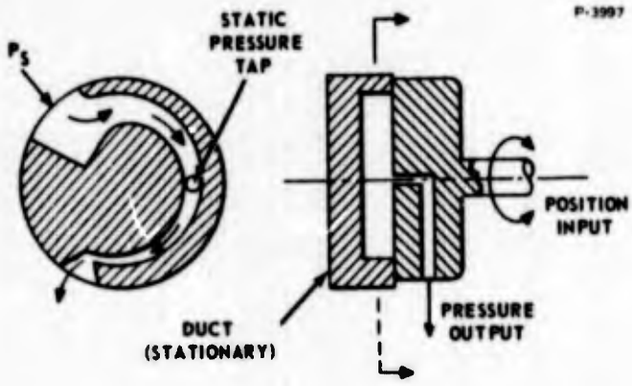

Figure 67 - Rotary Position Transducer Schematic

For a convergent duct, it was convenient to normalize the specific volume and velocity equations as functions of the specific volume and velocity at the exit area of the duct. It was also convenient to specify the equations in terms of the desired pressure at position "x" as a ratio of the supply pressure. This could be utilized, however, only if the entrance velocity was negligible. From standard texts on compressible flow, these equations were found to be

$$\frac{u_x}{u^*} = \sqrt{\frac{1 - \left(\frac{P_x}{P_s}\right)^{\frac{a-1}{a}}}{1 - \left(\frac{P}{P_s}\right)^{\frac{a-1}{a}}}}$$

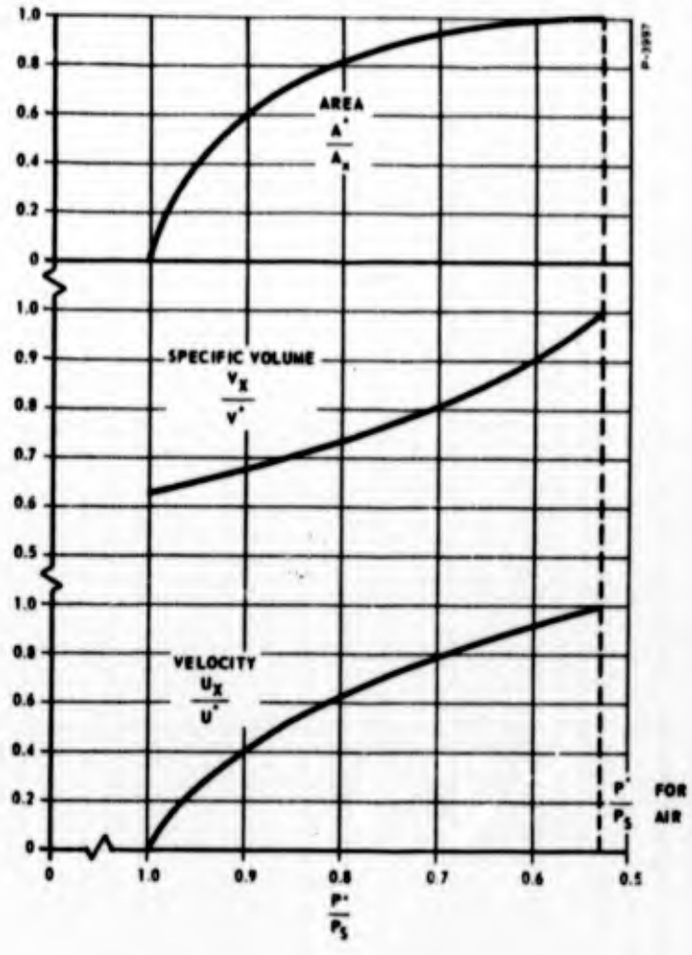

Figure 68 - Velocity, Specific Volume, Area, Versus Functions of Throat Conditions

$$\frac{V_x}{V} = \frac{P^*}{P_x} \quad \frac{1}{a}$$

where P^* is the critical supply gas pressure, and u^* and v^* are the throat velocity and specific volume.

The velocity, specific volume and cross-sectional area are plotted in Figure 68 as functions of throat velocity, specific volume and cross-section area for a linear pressure drop along the duct. The area increases to infinity at the inlet for truly zero inlet velocity. However, an area of ten times the throat velocity presents an almost zero velocity condition.

SECTION V

CRITICAL TESTS AND EVALUATION

This section presents the results of critical testing relating to design optimization and/or performance evaluation of major components and subsystems and of the combined system.

A. RATE SENSING AND SIGNAL PROCESSING SUBSYSTEMS

1. Rate Sensor

The detailed performance of the pulsating rate sensor depends upon phenomena too complex for mathematical prediction, and a variable-geometry test model sensor was therefore built to determine the effects of the various dimensions and shapes on sensitivity, range, noise and frequency response.

The outer diameter of the rate sensor was held fixed at 1-1/2 inches while the exit hole diameter, probe shape, diameter, and spacing, and chamber length were varied. Figure 69 shows the general test model configuration. A schematic of the test setup is shown in Figure 70.

Initial tests showed that the probe diameter had to be about 25 percent less than the outlet hole diameter to be able to modulate the probe frequency with varying swirl. The spacing between the probe and the exit hole was also found to be crucial for good modulation sensitivity. When the spacing was two exit-hole diameters, the probe pulsed regularly and exhibited some rate sensitivity. When the spacing was 1-1/2 diameters, the pulsing shifted to a higher frequency and the rate sensitivity was twice what it had been at the two-diameter position.

The shape of the probe tip is important for minimizing noise in that it influences the stability of the triggering pressure level for each new pulse. A straight-sided conical shape allows the jet to attach to the tip, making it harder for the probe to discharge and tending to counteract the spreading of the jet when the flow is swirling. A blunted cone shape was tried and proved successful for exit holes and probe tips larger than 0.035 diameter, but the flat area produced by blunting the cone appeared to reduce attachment excessively with smaller probe sizes.

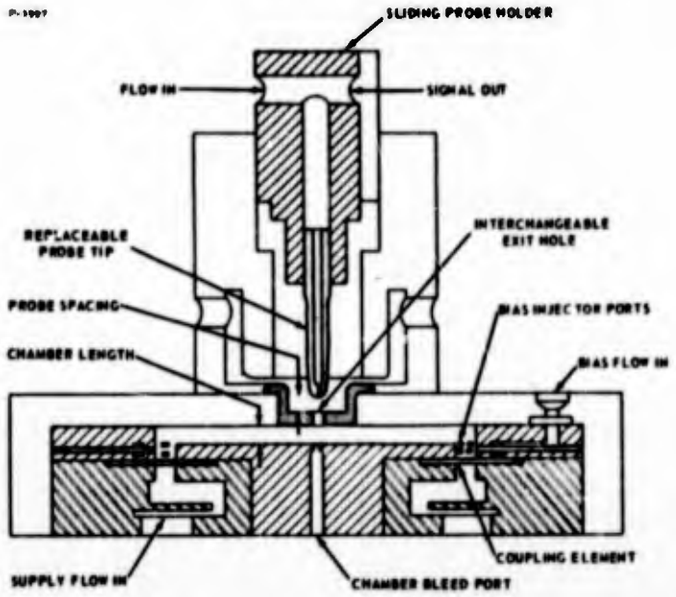

Figure 69 - Rate Sensor Test Model - Section Diagram

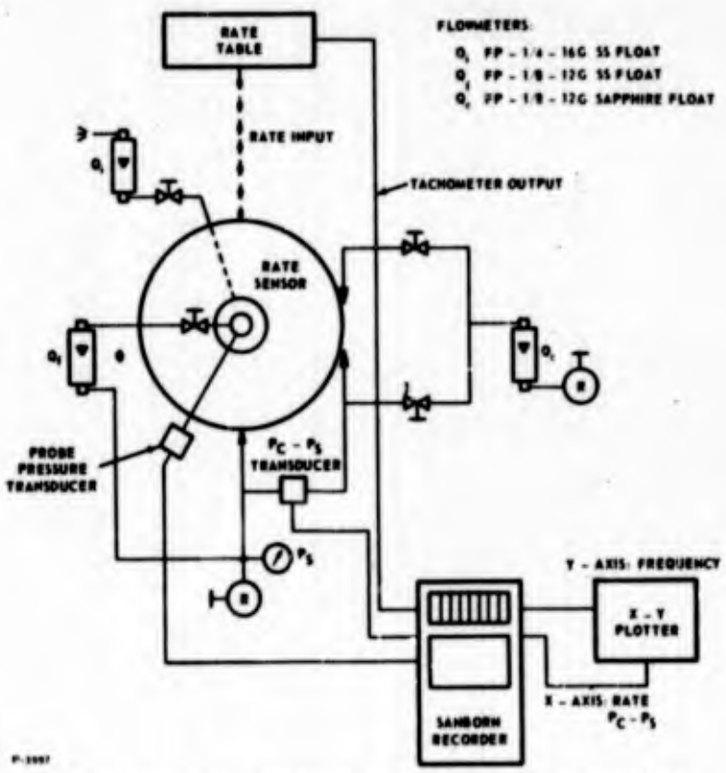

Figure 70 - Rate Sensor Test Schematic

The design finally selected has an ogive shape similar to the tip of a bullet, with a sharp edge around the hole in the tip. The hole at the probe tip is 0.020 inches in diameter and opens to 0.050 inches at a depth of 0.080 inches in order to reduce friction losses in the tip.

Exit hole sizes from 0.027 inch to 0.050 inch diameter were tested. The range was narrowed to between 0.027 and 0.030 inch diameter because the larger sizes resulted in reduced modulation sensitivity.

Figure 71 shows curves of frequency versus control pressure minus supply pressure for the 0.027 inch exit hole with a 0.020 inch probe. The sensitivity to control pressure, which is analogous to rate sensitivity, is greatly increased by bleeding flow, Q_i, from the internal pickoff (chamber bleed port of Figure 69). The curve for a bleed of 5 showed good linearity and a rate sensitivity of 30 pps for 100 deg/sec. When the bleed was increased to 14.5 the gain increased but the linear range virtually disappeared. A compromise bleed setting of 7 was selected, giving a rate sensitivity of 50 pps for 100 degrees per second and an adequate linear range.

The chamber length was then cut from 0.050 to 0.025 inches in order to improve the chamber switching response by decreasing the filling time and to improve the linearity of the output. Figure 72 shows the resulting frequency-versus-rate curve with a nominal sensitivity of 50 pps for 100 deg/sec rotation. Performance with the reduced chamber length thus was satisfactory, and the basic geometry of that model was selected for the final sensor configuration.

Figure 73 shows the effect of control bias on the sensor frequency-versus-rate characteristics. As indicated, quiescent (zero rate) frequency and rate range-about-quiescent can be modified by varying the amount of bias swirl in the chamber.

Early tests on frequency-versus-rate with and without pneumatic bias indicated that the bias injector can be a significant noise source if bias flow is not introduced uniformly around the diameter of the chamber. In the course of developing the final sensor, two bias injector configurations were fabricated and used in sensor testing. The importance of injection uniformity was first noted with a bias injector having only four parallel injection ports. Unfiltered noise (experienced as output frequency "jitter") was equivalent to approximately 20 degree/second of rate. With a new bias injector having twice the flow

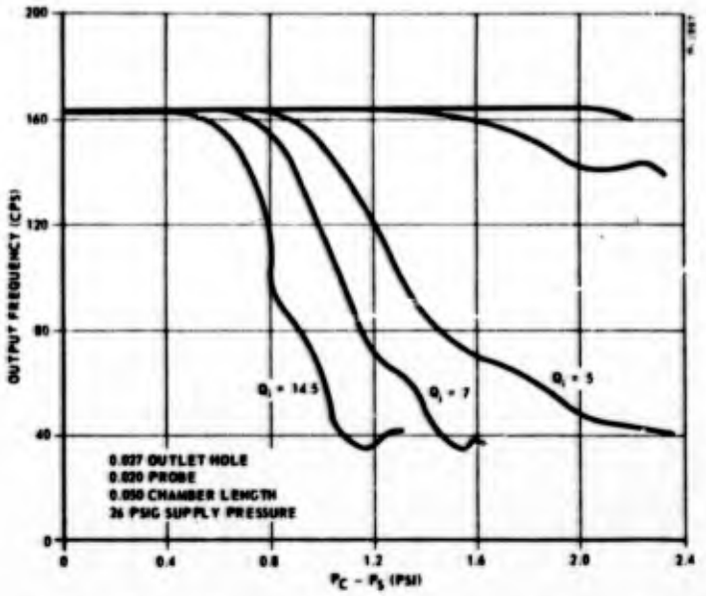

Figure 71 - Rate Sensor Sensitivity to Bias Pressure

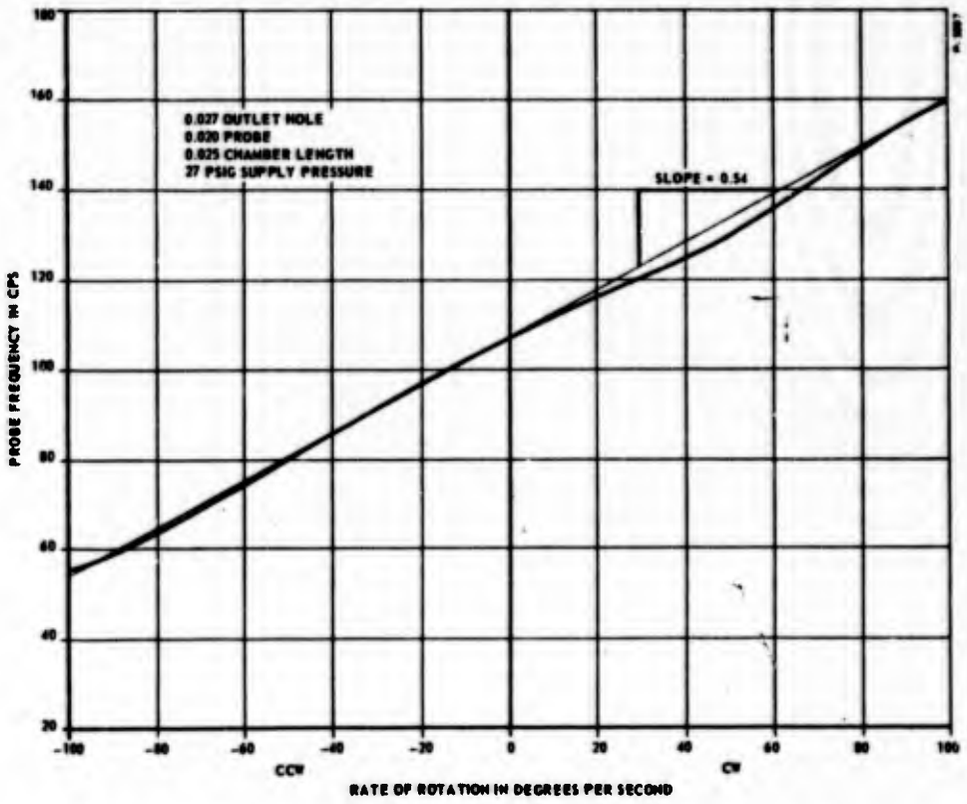

Figure 72 - Frequency Versus Rate for Final Test Model Basic Geometry

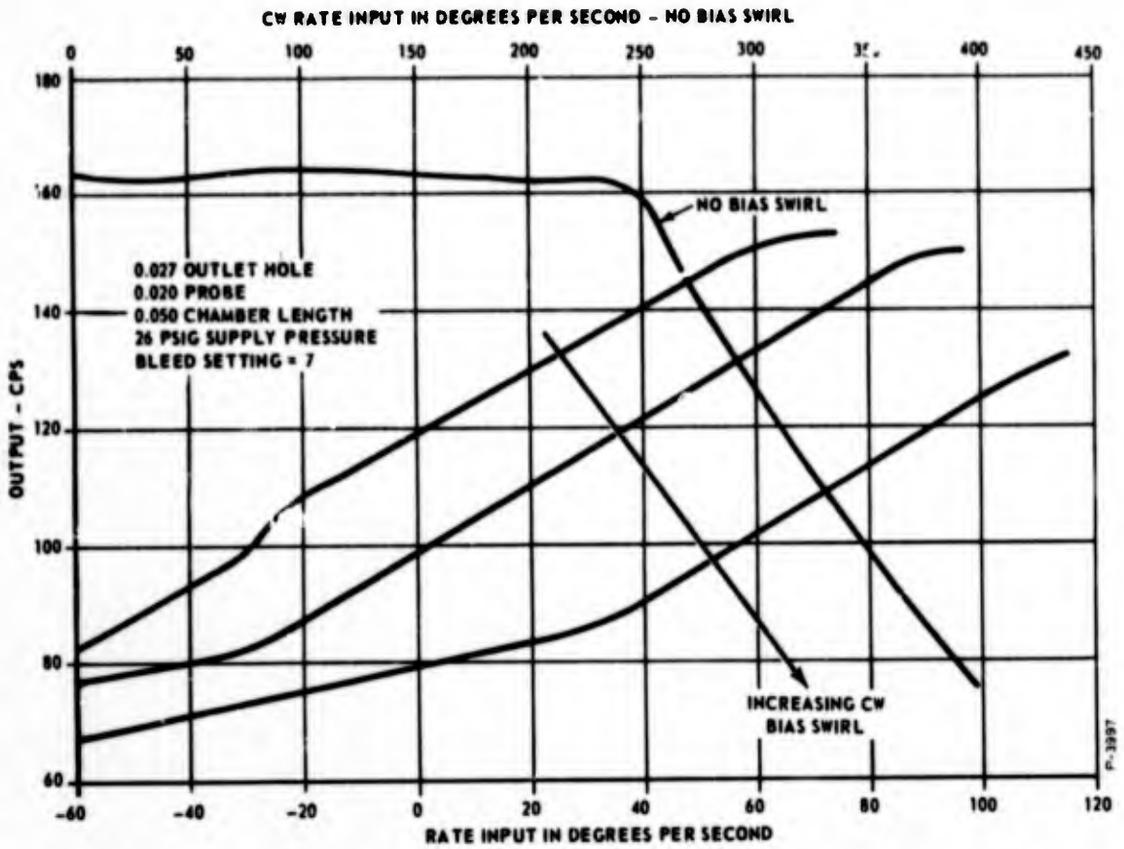

Figure 73 - Rate Sensitivity with Varying Bias Swirl

area of the old one distributed over six times as many holes, the unfiltered noise was reduced to 2-1/2 degrees per second. With first-order filtering of the processed output, the noise measured 1 deg/sec with a 5 cps filter and 0.5 deg/sec with a 0.5 cps filter, the latter being representative of required system bandwidth. The second bias injector was incorporated in the final design.

The final configuration rate sensor was fabricated entirely from Type-416 stainless steel. All of the seals except for the seals on the bias injector inlet are Hydrodine metal bellows. The bias injector seals are specially-made serrated copper rings which were required by space restrictions.

Some of the detailed changes in the final rate sensor configuration increased the chamber gain to the point where it became sensitive to pulses reflected from the pulsating probe back into the vortex chamber which resonated at certain frequencies. At the resonant points the supply

flow and pressure fluctuated enough to run the output frequency up and down the gain curve, resulting in disallowed regions on the frequency versus P_c-P_s curve as shown in Figure 74. The fluctuations were diminished by adding damping in the form of a choked orifice in the supply line, constraining the variation of supply flow to the chamber. Figure 75 shows the improved turndown curve.

Further minor adjustments in probe spacing and supply pressure were required to optimize range and rate sensitivity before the rate sensor was sealed up. Data on the final configuration shows a reasonable linear range in (Figure 76) and a rate sensitivity of approximately 40 pps for 100 degrees per second as indicated in the response to a sinusoidal rate input of Figure 77.

The most significant dimensions for the final configurations are summarized in Table 4.

2. Signal Processing Networks

A schematic of the signal processing network is shown in Figure 78 and the actual amplifier profile as etched in stainless steel is shown in Figure 79. The jet elements are arranged to integrate with the top of the rate sensor to minimize the path lengths between the 10CF-14 and the bias injector and between the probe and the inlet to the 10MF1.

To test the feasibility of this circuit prior to fabrication, the feedback loop consisting of a 10MF1 and a 10CF14 was breadboarded and tested. The divider tee was formed in a small brass block with adjustable orifices to set the pressure in the tee and the flow to the rate sensor probe. A schematic of this arrangement is shown in Figure 80.

Figure 81 shows the signal waveforms at various points in the circuit. In Figure 81(a) the pressure inside the divider tee is shown compared to the rate sensor pulse, with the tee pressure scale being 1 psi/cm and the probe pressure scale being 5 psi/cm. The attenuation of the signal is about 1/5, and the upper peak is rounded off, but otherwise the shape of the wave going into the 10MF1 is identical with the probe pulse. In Figure 81(b) the output of the 10MF1 is compared with the probe signal showing that the 10MF1 lags the rate sensor by 2 ms. In Figure 81(c) the output of the 10CF14 and the 10MF1 are shown. The sensor has a continuous rate input to illustrate the appearance of a time unbalance signal, i.e., the "on" time is shorter than the "off" time.

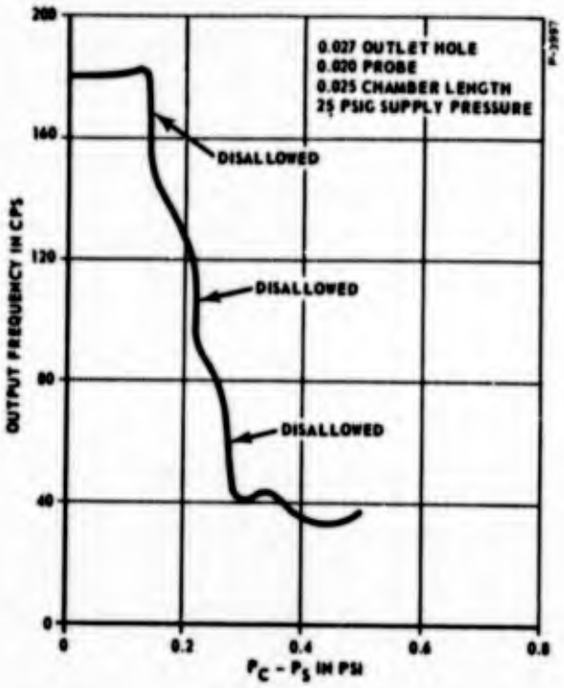

Figure 74 - Rate Sensor Sensitivity to Reflected Probe Pulses

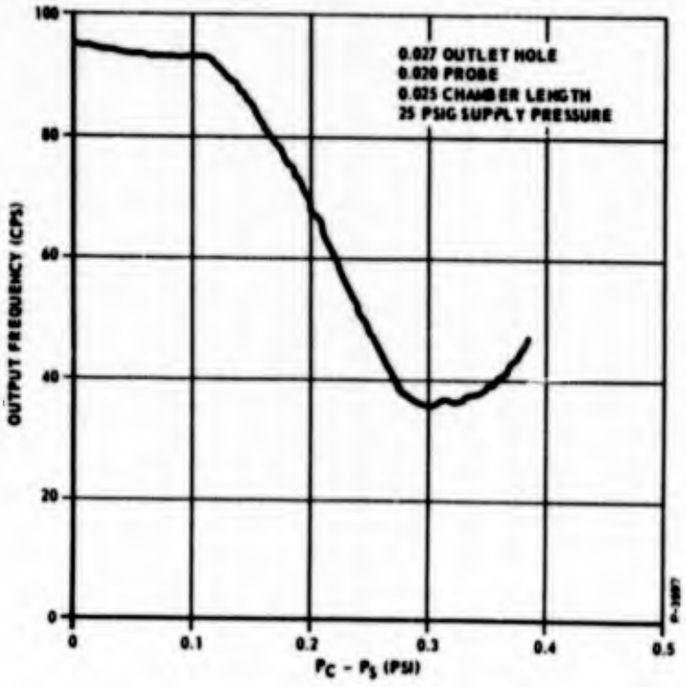

Figure 75 - Rate Sensor Turndown with Choked Orifice in Supply Line

Table 4 - Summary of Final Rate Sensor Dimensions

Vortex Chamber:	Diameter	1 1/2 inch
	Exit	0.027 inch
	Length	0.025 inch
	Bleed	3800 cc/min
Bias Injector:	Number of Holes	2 sets of 24
	Hole Size	0.005 x 0.005 inch
Probe:	Spacing	0.039 inch
	Tip Diameter	0.020 inch
	Internal Volume	0.0254 inch^3
Coupling Element:	Stainless Steel Wire Mesh	400 x 400 wire/inch
Supply Pressure =	26 psig	

P-3997

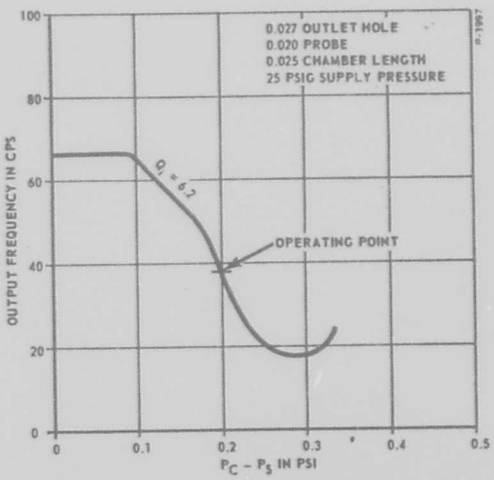

Figure 76 - Frequency Versus Bias for Final Rate Sensor Configuration

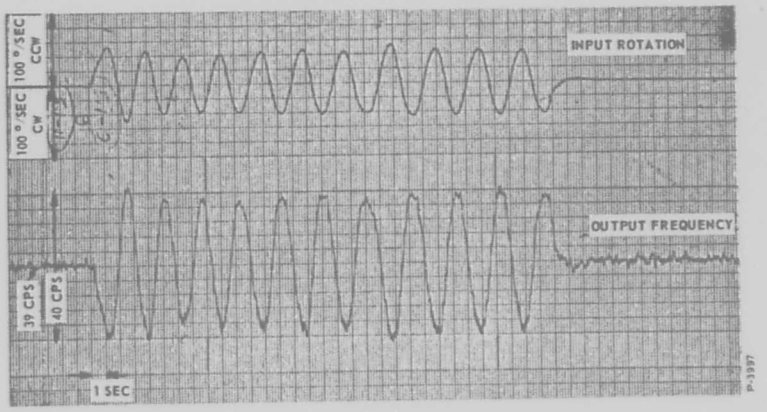

Figure 77 - Rate Response of Final Rate Sensor Configuration

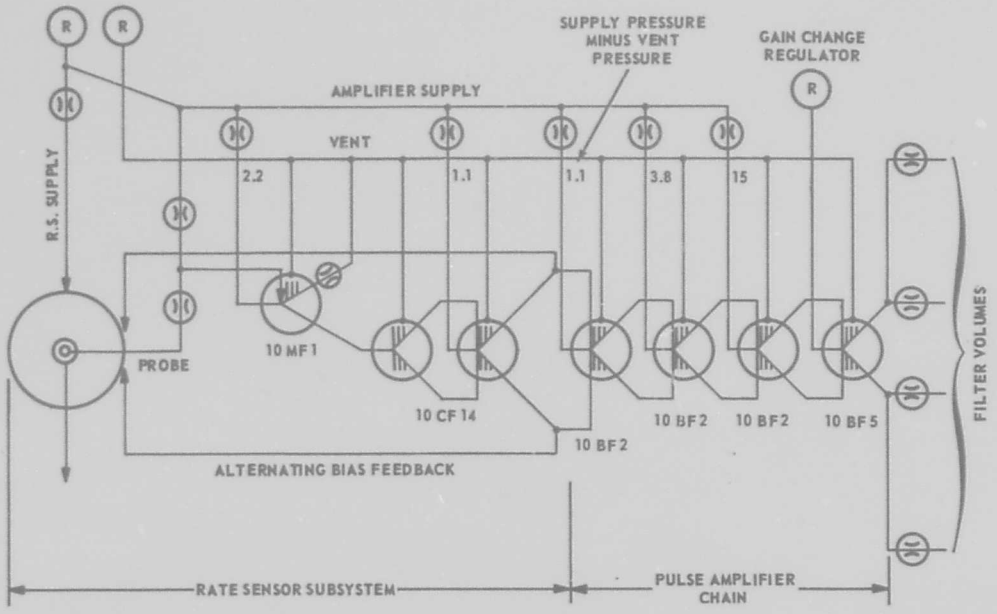

Figure 78 - Rate Sensor and Signal Processing Network - Combined Schematic

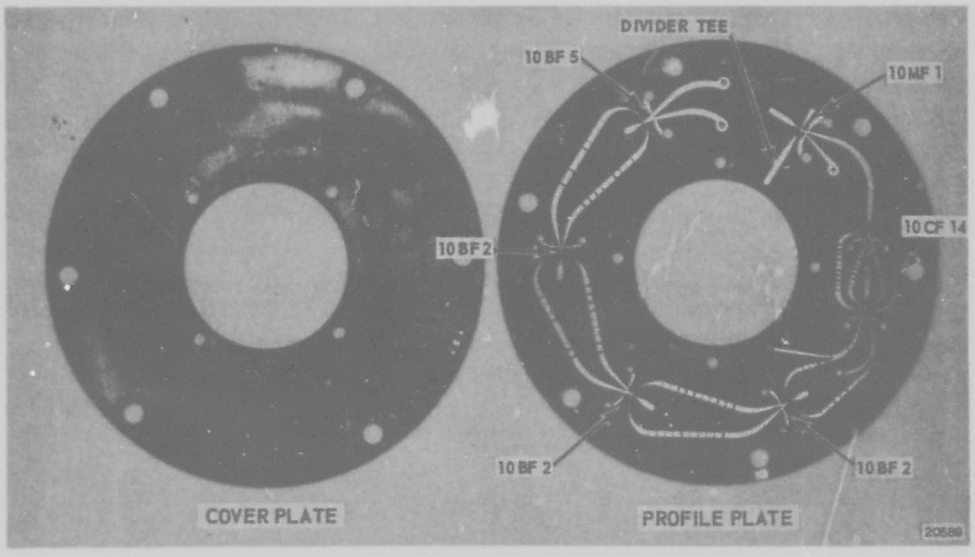

Figure 79 - Signal Processing Network and Cover Plate

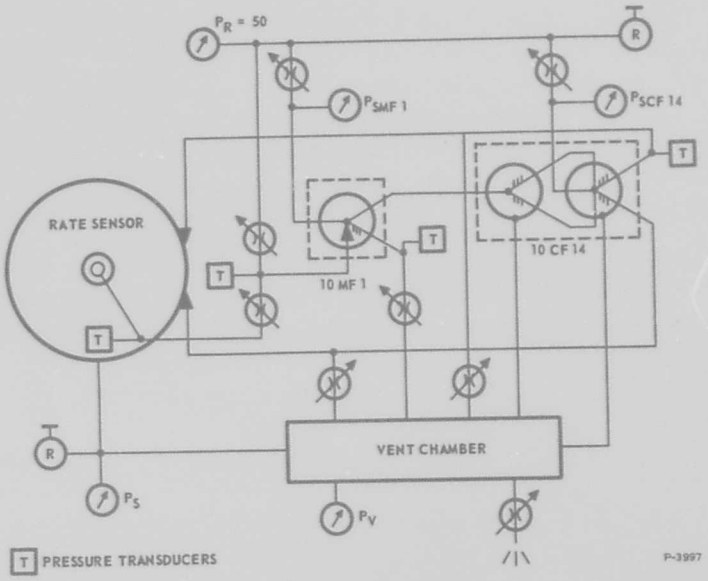

Figure 80 - Breadboard Rate Sensor Subsystem Schematic

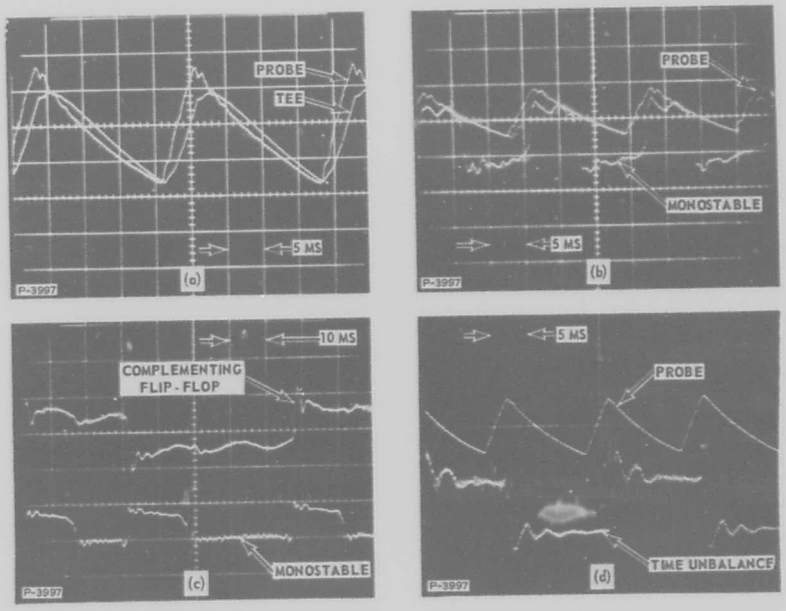

Figure 81 - Signal Waveforms in the Alternating Bias Amplifier

Figure 81(d) shows the probe signal and the feedback signal from the 10CF14, which lags the probe pulse by 4 milliseconds. The combined lag through the alternating bias amplifier and the rate sensor limited the maximum frequency for the breadboard to 60 cps. If the rate sensor probe pulsed faster, the feedback signal could not switch the bias before the probe emitted another pulse, resulting in abnormal operation.

The feedback loop of the integrated amplifier assembly of Figure 78 was designed on the basis of the breadboard testing; the pulse amplifier chain was designed using test data on bistable amplifiers in a 25 psig atmosphere. Data on a 10BF5 used in the design of the pulse amplifier chain are summarized in Figures 82, 83 and 84 showing the critical switching pressure and recovery as functions of supply pressure. The critical switching pressure is the minimum pressure necessary to switch the supply flow for a given supply pressure. In Figures 83 and 84 the performance at 25 psig vent pressure is compared with performance at 0 psig vent pressure, illustrating the increase in range obtained by increasing the vent pressure.

The curve in Figure 82 is important in the design of the variable gain pulse amplifier chain because it defines the required input to the last amplifier in the chain which has a supply pressure varying from 35 to 200 psig as the gain is changed over a range of 1:10. The output of the preceding amplifier must be at least 6 psi above the vent in order to switch the last stage over the stated supply pressure range.

The number of elements in the pulse amplifier chain was determined by starting with the 10CF14 output pressure, which is the bias pressure to the rate sensor of nominal 0.19 psi above vent, and computing the pressure increase through each element until an output pressure of 6 psi is reached. Examination of curves of available amplifiers resulted in the selection of the 10BF2 profile and the design of a three-stage pulse amplifying chain. The comparison curves of Figures 83 and 84 were used to get the estimated characteristics of the 10BF2 at 25 psig vent as in Figures 85 and 86.

The initial slope of the critical switching curve in Figure 85 is 16, while the initial slope of the recovery curve in Figure 86 is 0.385 giving a gain of 16 x 0.385 = 6. With a gain of 4, a 50 percent safety margin is obtained and a chain of 3 stages gives 12 psi at the output. Since this is more switching pressure than necessary, the 10BF2 supply pressures were lowered to those shown in Figure 78 to give 6.5 psi output.

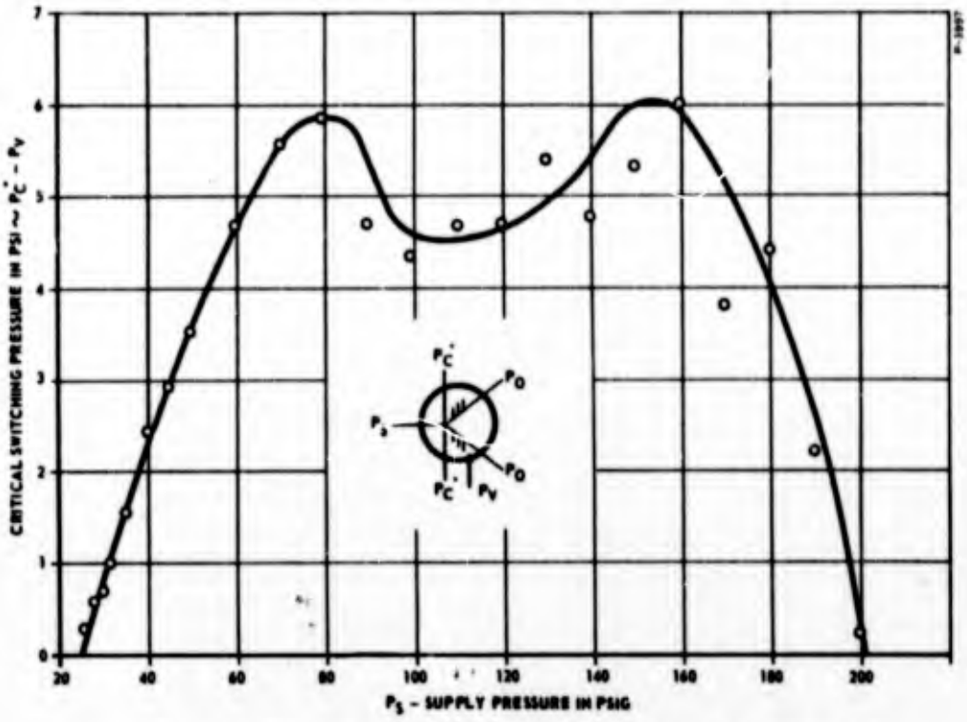

Figure 82 - Switching Characteristics of 10BF5

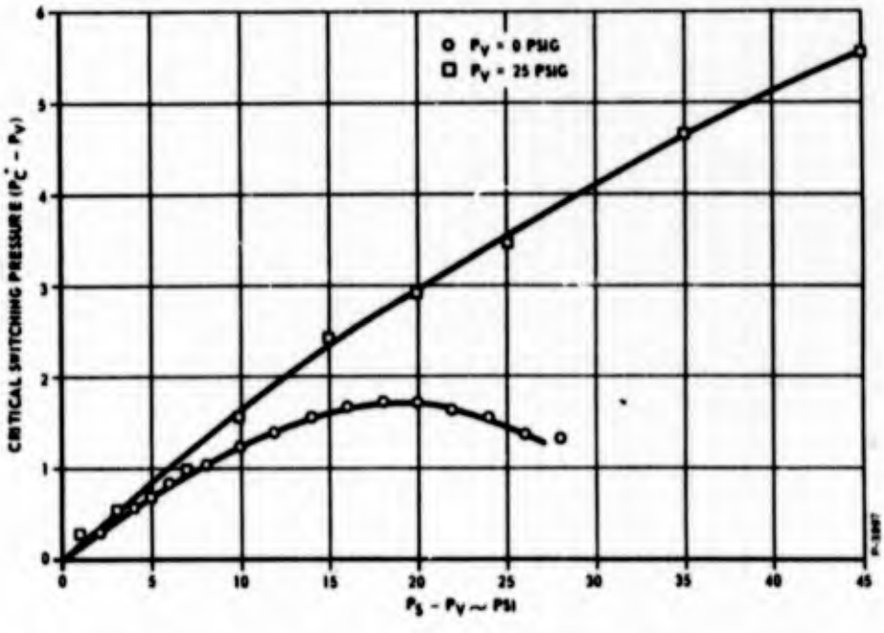

Figure 83 - Switching Pressure Versus Supply Pressure for Two Back Pressure Levels

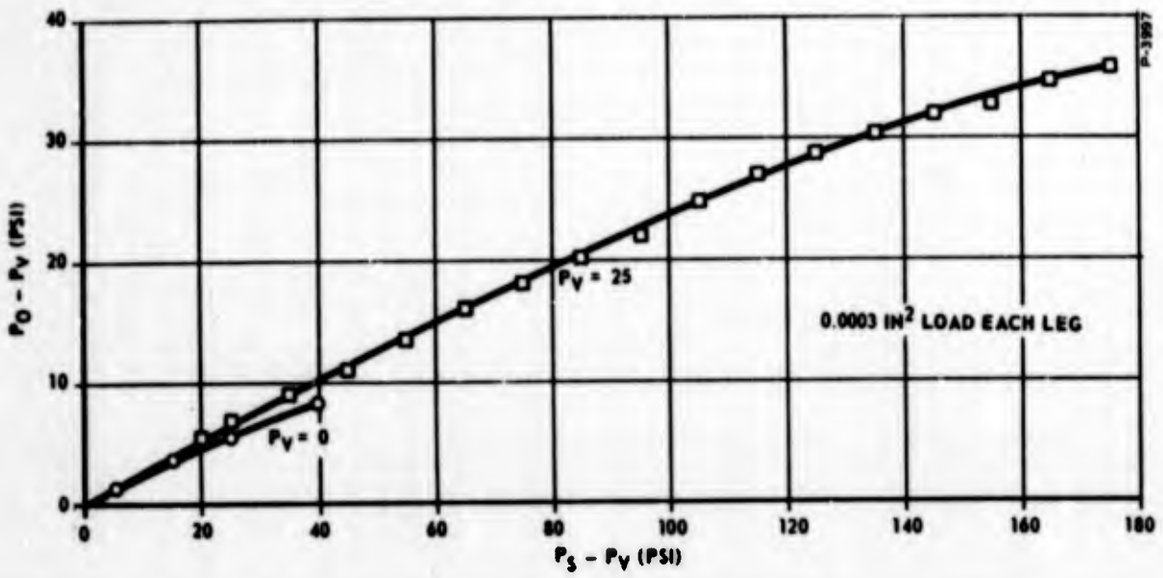

Figure 84 - Pressure Recovery of 10BF5 with Two Vent Pressures

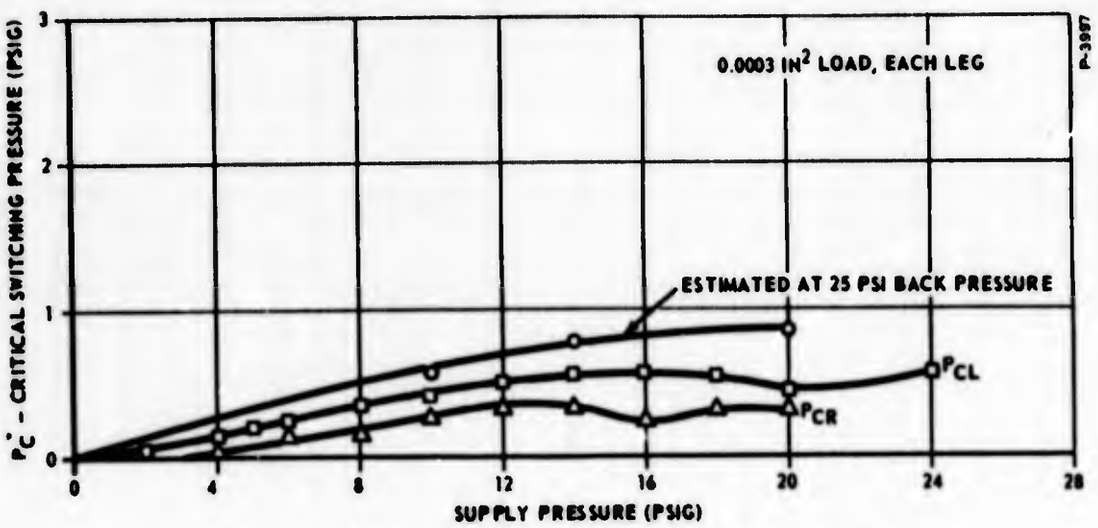

Figure 85 - Switching Characteristics of 10BF2

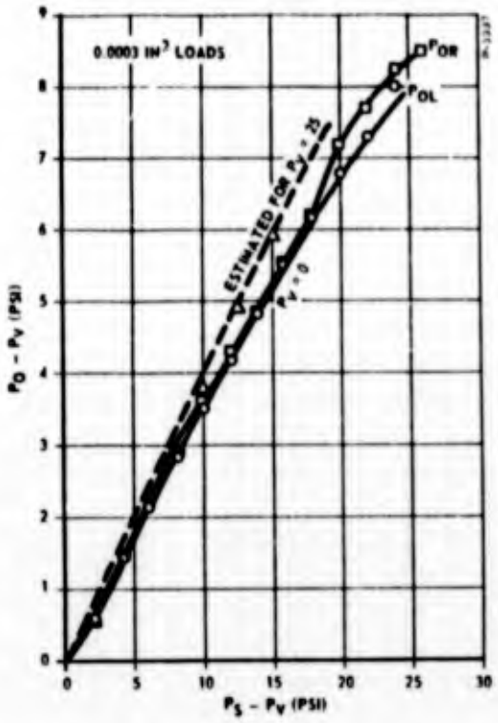

Figure 86 - Output Pressure Versus Supply Pressure for 10BF2

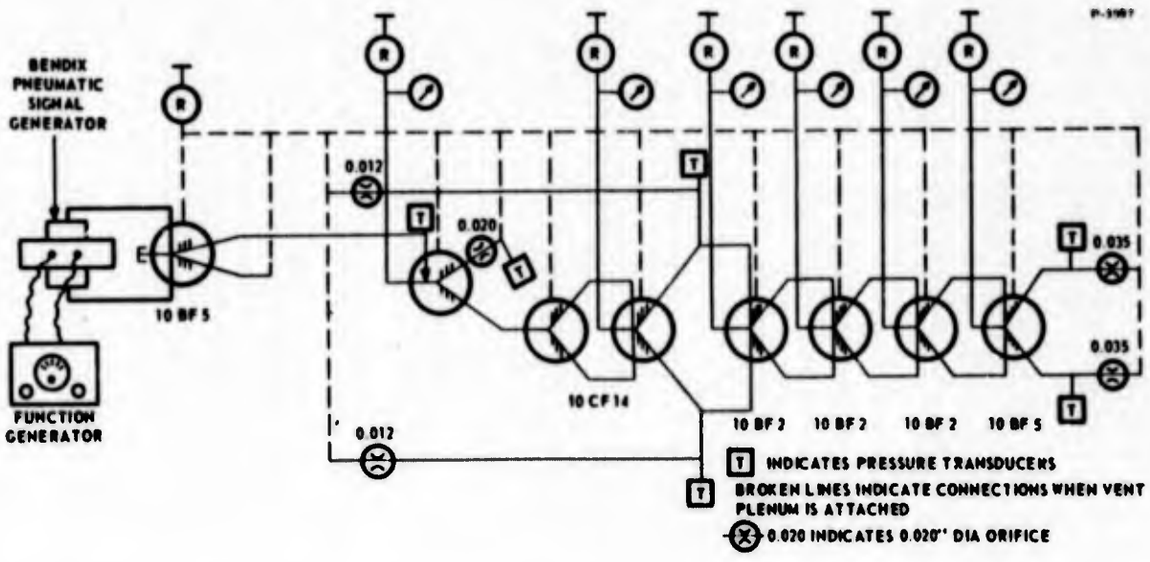

Figure 87 - Test Schematic for Integrated Rate Sensor and Signal Processing Network

Two models of the signal processing network were etched in stainless steel. Both models were tested with zero vent pressure using a rectangular wave from a 10BF5 activated by a Bendix Pneumatic Signal Generator as shown in the schematic of Figure 87. The supply pressure to each stage was scaled down from the previously calculated pressures by a factor of 14.7/(25 + 14.7). Figure 88 shows the input and output waveforms. The decision of which model to use was based on the performance of the 10CF14 which must perform with high precision and reliability on a very small supply pressure. One model showed a slightly different recovery between the two output legs of the 10CF14 which would result in different bias levels in the rate sensor and a time unbalance signal for zero rate input, making that model unacceptable.

The selected signal processing network was bonded to the vent plenum, an annular shaped chamber that covers all the amplifier vents and supplies the 25 psig vent pressure. The signal processing network was again tested using a test signal input following assembly to the vent, and adequate behavior was achieved.

3. Subsystem Integration

To facilitate orifice sizing and general integration testing, a test plate was used having provisions for needle valves to set the supply pressures to the various elements, test points for mounting transducers to observe the signals at each amplifier, and special holes for inserting interchangeable test orifices into the divider tee while retaining the minimum tee volume. Specially made silastic seals were used to eliminate leaks in the test configuration.

Orifice Divider Tee

The divider tee is the critical interface between the rate sensor and the signal processing network. It is connected between the rate sensor probe, the common supply, and the control port of the 10MF1 as shown by Figure 89. The probe pulse repetition rate is dependent on the flow rate and volume at the back of the probe as well as the input rate of rotation and bias pressure. Therefore, the probe orifice, A_p, is uniquely determined by the probe geometry and the divider tee pressure, P_T. Tests of the rate sensor alone were performed with a needle valve for A_p, and this valve was then flow checked and determined to be equivalent to a 0.020 inch diameter orifice.

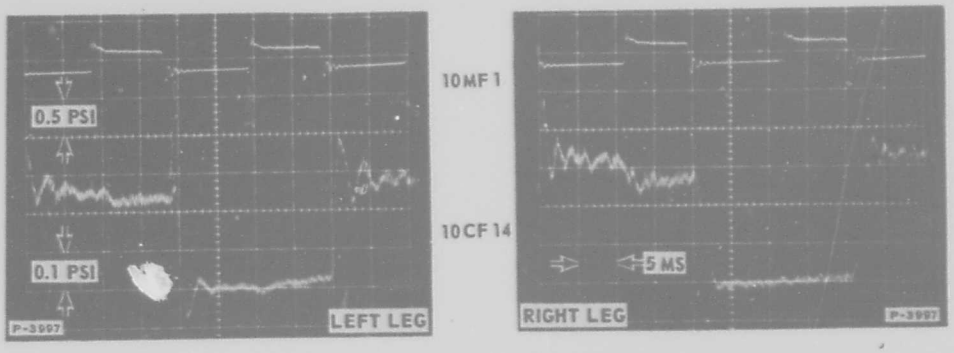

Figure 88 - Outputs of 10MF1 and 10CF14 - Waveforms

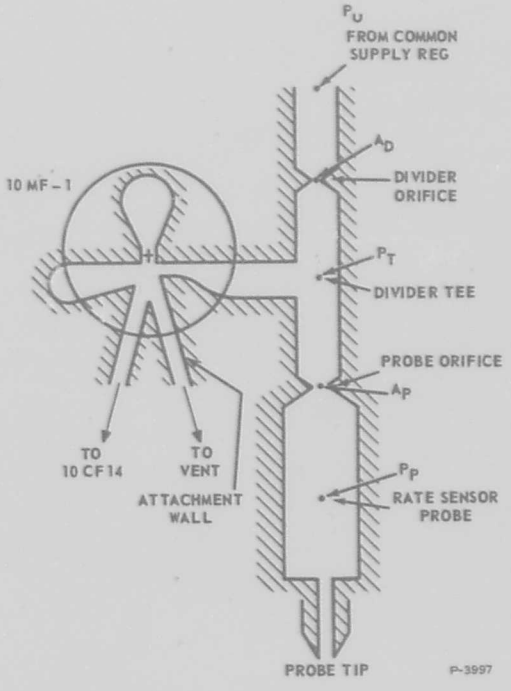

Figure 89 - Orifice-Divider Tee

The probe frequency varies generally as the reciprocal of the product of probe volume and flow. The total probe volume in the integrated configuration is about 33 percent larger than the volume used for the rate sensor alone; so in order to preserve the desired sensor frequency, the probe flow rate was reduced by accordingly reducing A_p. As an approximation, A_p was reduced by 33 percent by reducing the diameter to 0.0172 inch. Final further adjustments of the integrated sensor frequency were made by attaching various lengths of tubing to the side of the probe to adjust its volume until the desired frequency was obtained.

The assumptions used in calculating an approximate value for the upstream or divider orifice, A_D, were:

(1) There is no net flow from the tee to the 10MF1.

(2) The flow through the orifices is determined by the average pressure in the tee and in the probe, i.e., 24 psig in the tee and 15 psig in the probe.

(3) The upstream pressure would be regulated at 63 psig which is sufficient to provide choked flow for the rate sensor supply.

Based on those assumptions, the divider orifice diameter was calculated as 0.0112 inch. When this was tried, the 10MF1 would not detach from the attachment wall until the rate sensor supply pressure was increased, thereby increasing the average probe pressure and decreasing the probe flow. This indicated that the divider orifice was too small. Increasing the orifice diameter to 0.0122 inch resulted in proper operation as shown by the scope traces of Figure 90.

Jet Amplifying Network

The supply pressures to the jet elements in the test configuration were set by small needle valves fed from the 63 psig common supply. The supply pressures were measured by a differential pressure gauge with one side connected to the vent plenum and were set to the values shown in Figure 78.

Figure 91(a) shows the 10MF1 output waveforms when the 10BF5 is shut off. Notice that the waves are rectangular and that the 10CF14 off and on times are essentially equal. The pulse from the 10MF1 has a squiggle on its trailing edge due to the gradual slope of the trailing edge of the probe pulse which causes the control pressure of the 10MF1 to decrease slowly, preventing the 10MF1 jet from returning quickly to the attachment wall.

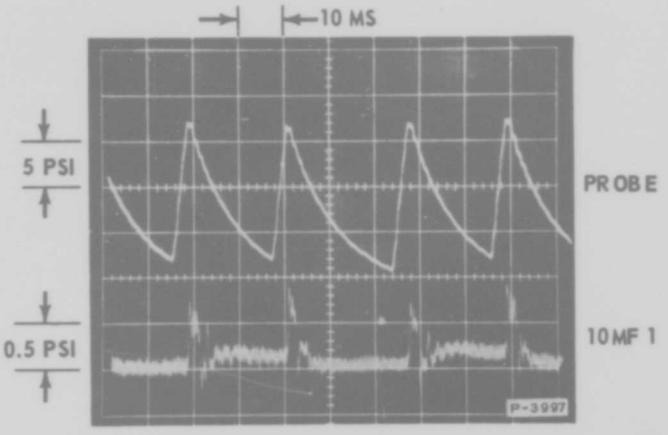

Figure 90 - Probe Signal and 10MF-1 Output Waveforms

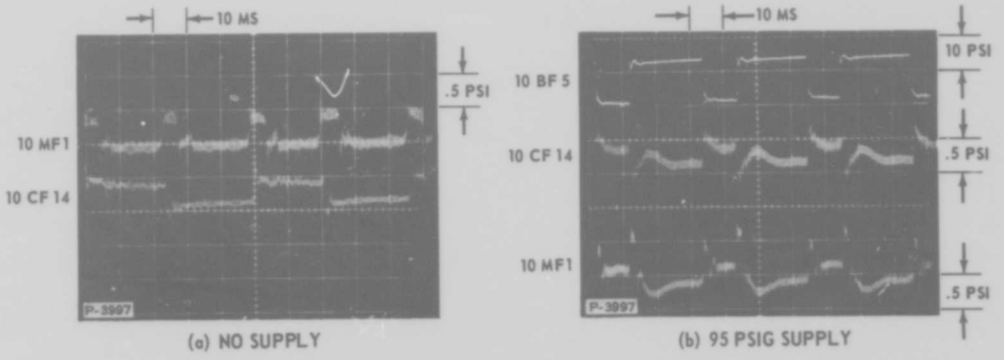

Figure 91 - Effect of 10BF5 Supply Pressure on Alternating Bias Amplifier

When the supply to the 10BF5 was increased to about 100, the 10CF14 and 10BF15 signals became time-unbalanced and otherwise distorted (Figure 91), apparently due to interaction between the high-pressure and low-pressure stages through the vent plenum. One way for the 10BF5 to influence the vent pressure in this manner is to have unequal loads on its two output legs. If one leg is restricted more than the other it will cause an unbalanced flow to be dumped into the vent plenum, causing periodic fluctuations in net vent flow and a resultant vent pressure modulation. The loading orifices of the 10BF5 stage were removed, flow checked and reset to 0.030 inch diameter. The operation improved, but a slight time unbalance remained due to residual asymmetry in the 10BF5 configuration.

Rate Sensitivity of the Test Configuration

A first order electronic filter with a 0.5 cps break frequency was connected to the transducer on the 10BF5 to simulate the averaging of the signal by the filter-compensation network. Figure 92 shows data obtained and indicates the general test procedure. The output signal was first recorded unfiltered to get the peak to peak value, which is 7 psi in this case. The filter was then connected to derive the average value of the signal, which is 3.8 psi above vent pressure. The rate table was then given a sinusoidal rate input and the average value of the output signal follows this. For the test shown, the output is saturating at about +80 degree/second, and the sensitivity is 1.43 psi for 100 degree/second.

Sizing of Orifice Plugs

The settings of the needle valves were used to size the orifice plugs to be pressed into the common supply plenum of the final integrated configuration. The needle valves were removed from the test plate and their positions noted. An upstream pressure of 60 psig was applied to each one and the flow was measured by a Fisher-Porter rotameter type flowmeter exhausting to atmosphere. The measurements indicated that the following sizes were needed:

10 MF-1	0.0115 inch
10 CF-14	0.094 inch
10 BF-2, first stage	0.0088 inch

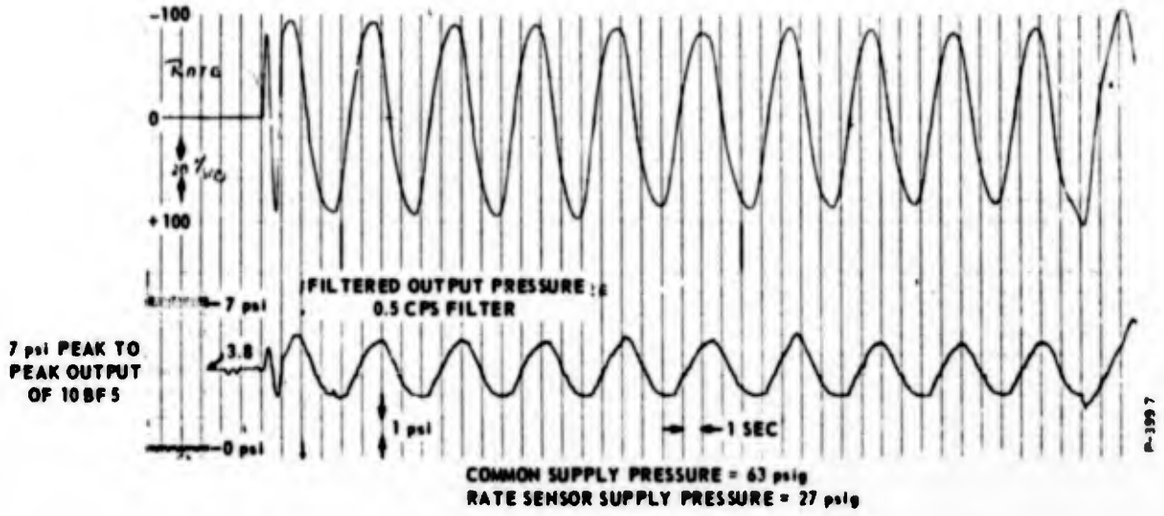

Figure 92 - Rate Response of Rate Sensor Subsystem - Test Configuration

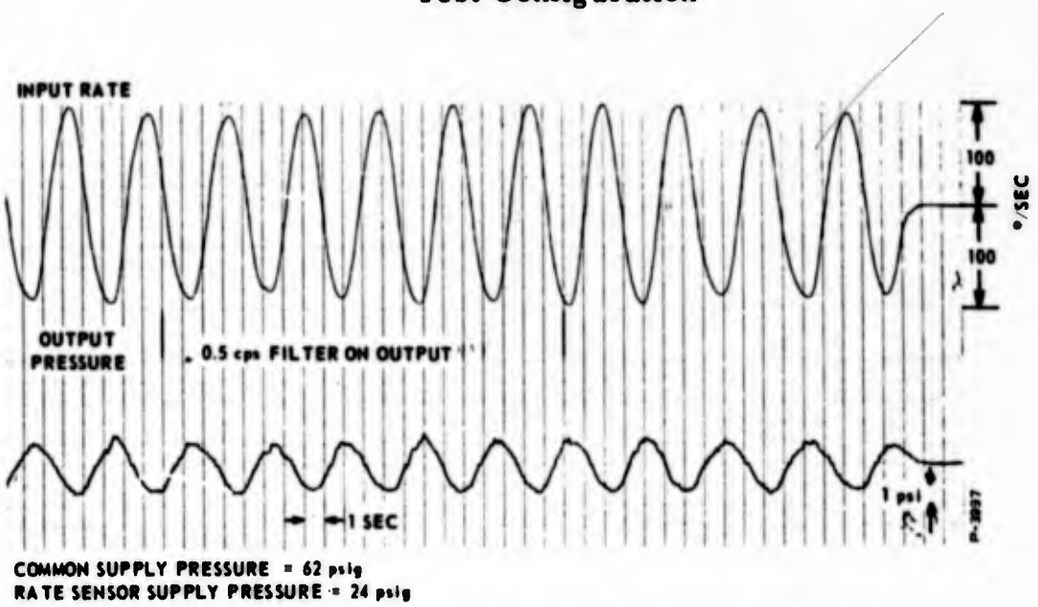

Figure 93 - Rate Response of Rate Sensor Subsystem - Final Configuration

10 BF-2, second stage	0.0131 inch
10 BF-2, third stage	0.0157 inch

Final Assembly Integration

The subsystem did not function properly when first assembled with the orifice plugs and the metal seals. Leaky seals were suspected, and the sealing surfaces were reground and lapped to an 8 microinch finish. No leaks were found after this was done, but the subsystem still would not function.

All orifices were then checked and found to be flowing within 4 percent of the prescribed values except for the two which formed the divider tee network. To get the required accuracy, new orifices were drilled undersize and lapped to match the previously measured flow rates. When this was done the subsystem began to operate but frequently skipped pulses.

It was then decided to return briefly to the test configuration using the test plate to check the operation of the alternating bias amplifier. Tests showed that the 10MF-1 was not functioning properly. This was remedied by ultrasonically cleaning the jet network in a freon bath, apparently removing an impurity picked up in the assembly process.

The final configuration was then reassembled and functioned adequately. The operating point was off the optimum point of the rate sensitivity curve apparently because of slight oversize of the supply orifice for the 10CF14. However, the combined performance was judged adequate for system integration. The final rate sensitivity traces obtained before integration into the complete system are shown in Figure 93. The rate sensitivity is 1.22 psi for 100 degrees per second. The unfiltered signal is 7 psi so that the modulation for the trace shown is 34 percent. The irregularity at the extreme upper peaks of the filtered output curves is due to the rate sensor being driven to an abnormally low frequency and missing pulses as a result of being slightly off the optimum bias point.

4. Filter-Compensation Network

The filter-compensation network shown schematically in Figure 94 and mounted on the servo package in Figure 153(b) consists of two 50 cubic inch volumes, two 5 cubic inch volumes and four 0.020 inch

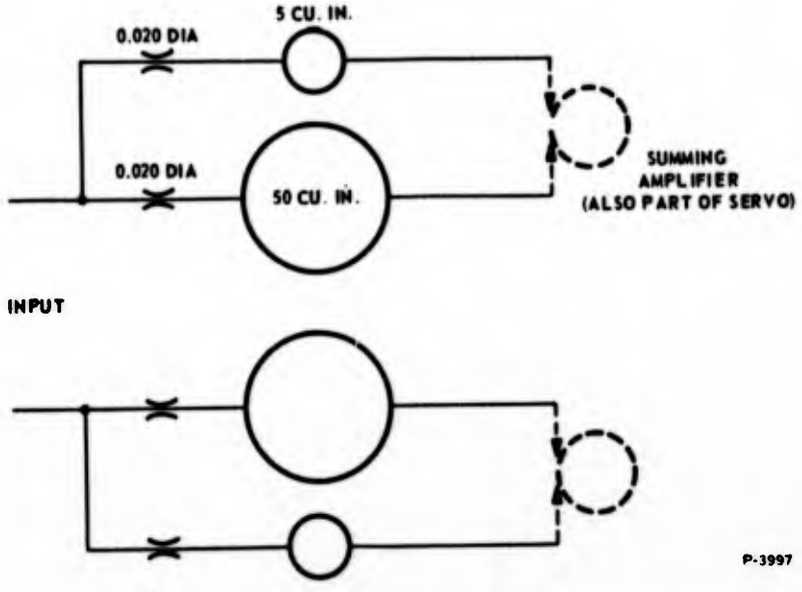

Figure 94 - Compensation Network Schematic

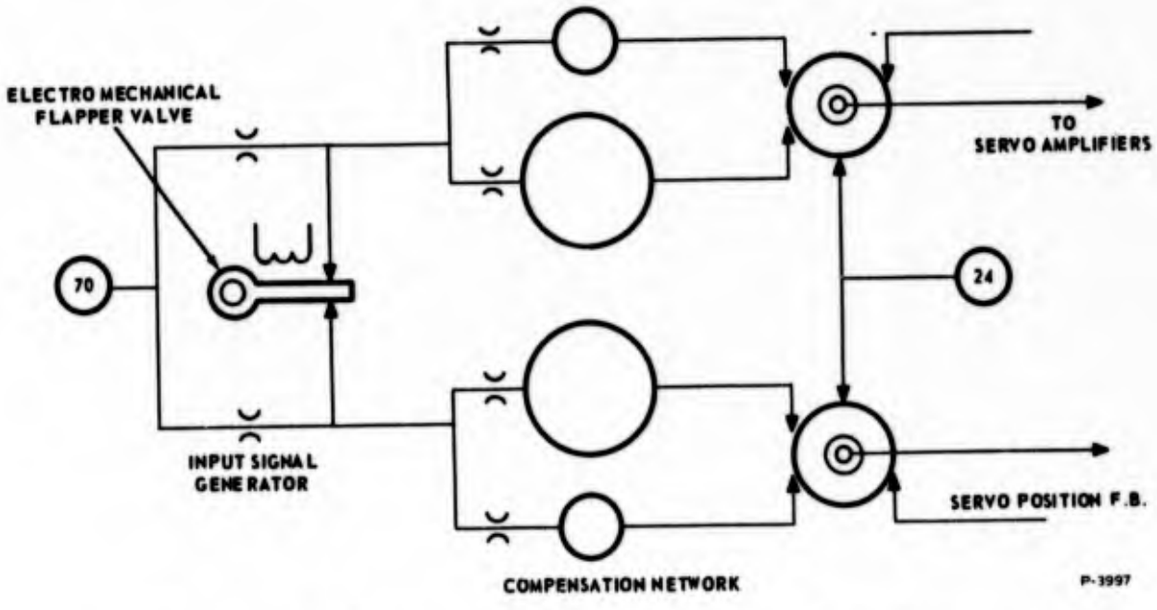

Figure 95 - Compensation Network Test Schematic

diameter input orifices. The unit was tested in conjunction with the servo subsystem package because the summing amplifiers at the servo input are necessary for the low-frequency shaping function of the circuit. Figure 95 shows the test schematic used.

The first test consisted of providing a step input signal to the network and recording the servo output position as a function of time. The results of this test are shown in Figure 96. As indicated, the required washout function is properly achieved.

The next test consisted of obtaining a frequency response of the network to determine its break points. A sinusoidal signal was introduced into the filter-compensation network inputs and the combined network and servo response were recorded. The results are presented in the response plot of Figure 97. The measured breakpoints are approximately 0.065 cps and 0.65 cps. The washout at very low frequencies deviates slightly from the desired values due to inaccurate subtraction in the summation amplifiers. The overall results are quite adequate, however.

B. SERVO SUBSYSTEM

1. Servo Amplifier

Summation Amplifier

To determine the required amplifier parameters, a breadboard model was developed. The critical parameters, such as exit hole size, receiver size, chamber dimensions, and receiver position, were flexible and an optimization study was made on the proper combinations.

Figure 98 is a set of curves for different external receiver positions showing the effect on output range and pressure. Although this dimension is not extremely critical, an optimum position does exist beyond which recovery begins to deteriorate. In this test and in the following studies, the control port area remained constant at 0.0003 square inches. Figure 99 indicates the effect of different exit hole sizes for the same receiver size. As indicated this parameter primarily affects amplifier gain, since gain is proportional to control to exit area ratio.

Another area of optimization was output impedance. It is desirable to obtain as much flow as possible from the output without

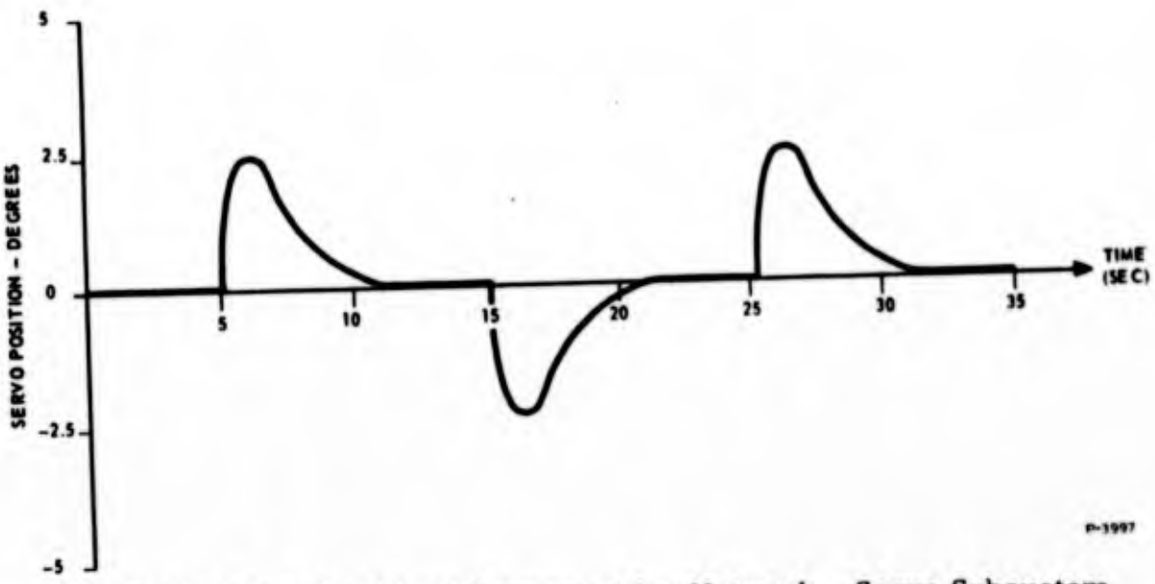

Figure 96 - Combined Compensation Network - Servo Subsystem Step Response

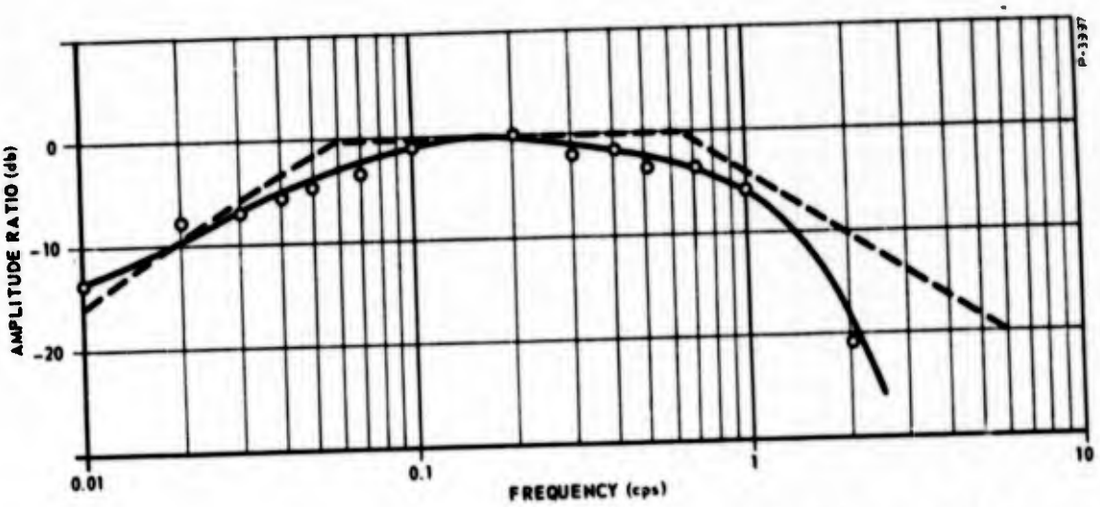

Figure 97 - Combined Compensation Network - Servo Subsystem Frequency Response

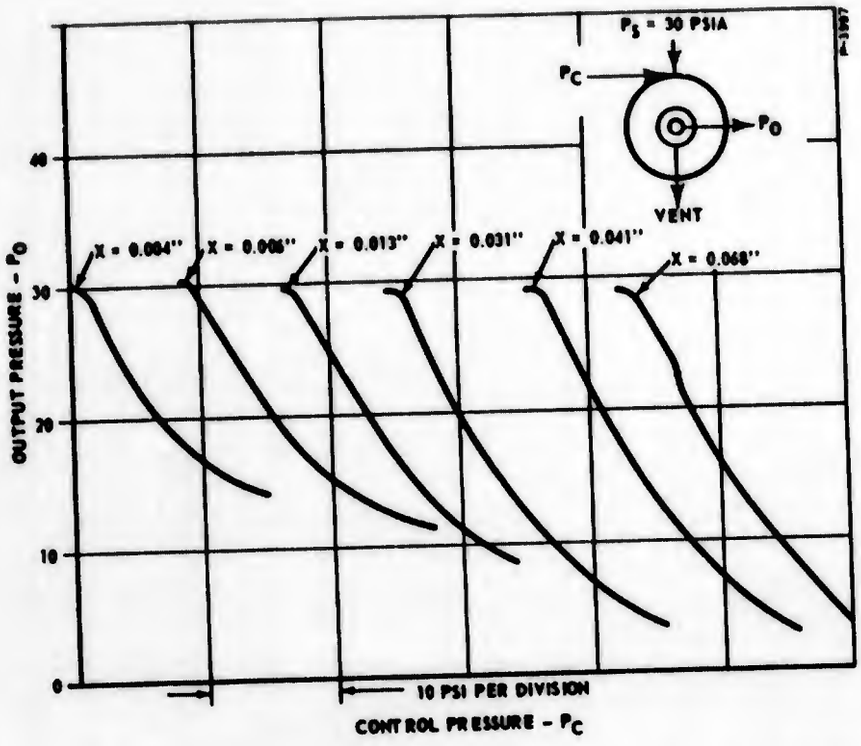

Figure 98 - Vortex Amplifier Characteristics for Various Receiver Positions

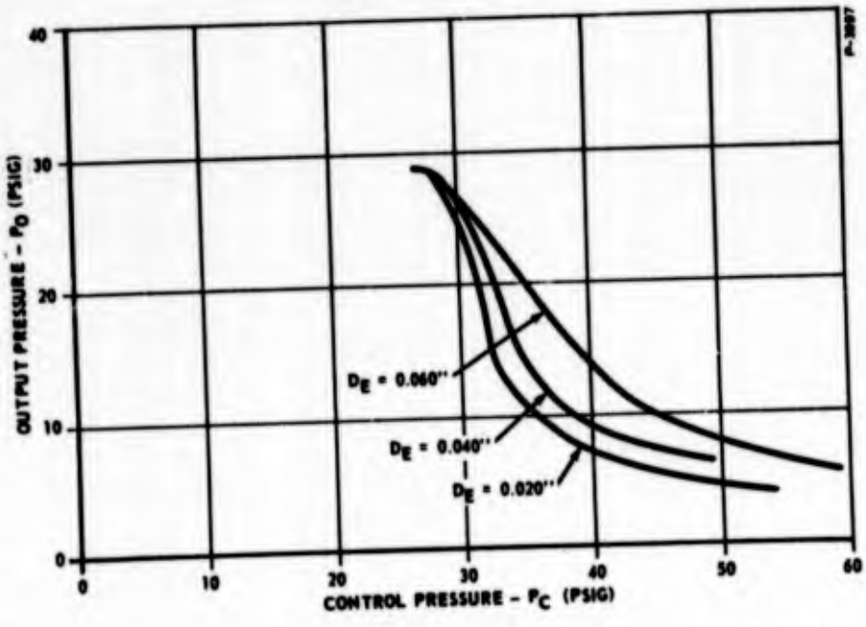

Figure 99 - Vortex Amplifier Characteristics for Various Exit Hole Diameters

gain loss. Figure 100 shows a set of output impedance curves for the external and internal receiver combinations. It was determined that these two receivers could be completely interconnected without any significant change in input-output characteristic as shown by Figure 101. The complete output impedance curve is shown in Figure 102. The summing amplifier as designed for high-temperature use is shown in Figure 103. The assembly is a diffusion bonded assembly without internal joints and seals. The amplifier has two external input ports for the position feedback signal and a bias signal. The remaining inputs as well as the supply and vent ports are located in the flanges base and connected to the servo amplifier manifold. The characteristic curves of the amplifier are shown in Figures 104 through 107.

Venjet Amplifiers

Two stages of venjet amplifiers are required to raise the summing amplifier output pressure of 10 to 20 psig to the servovalve input pressure of 175 to 225 psig, and to provide the necessary pressure gain. These two push-pull stages are built into a manifold block as shown in Figure 108. The manifold also serves as the manifold for the vortex summing amplifiers and interconnects them with the venjets.

The input-output pressure characteristic of the low pressure venjet stage is shown in Figure 109 and the high pressure stage is shown in Figure 110. The input impedance curves are shown in Figures 111 and 112, and the output impedance curves are presented in Figures 113 and 114.

Figure 115 is the input-output pressure characteristic of two combined stages where the input is the low pressure amplifier input and the output is the high pressure amplifier output. The venjet manifold combined with the summing amplifiers form the servo amplifier as shown in the diagram of Figure 116. The unit was tested using the test schematic of Figure 116 and the results for various summing amplifier supply pressures are shown in Figure 117. The pressure gain with no positive feedback was 8 and, with various amounts of positive feedback, could be increased up to 30 psi per psi. The amplifier's input impedance is that of the summing amplifiers shown in Figure 118. Its output impedance is that of the 2nd stage venjet which was presented in Figure 114.

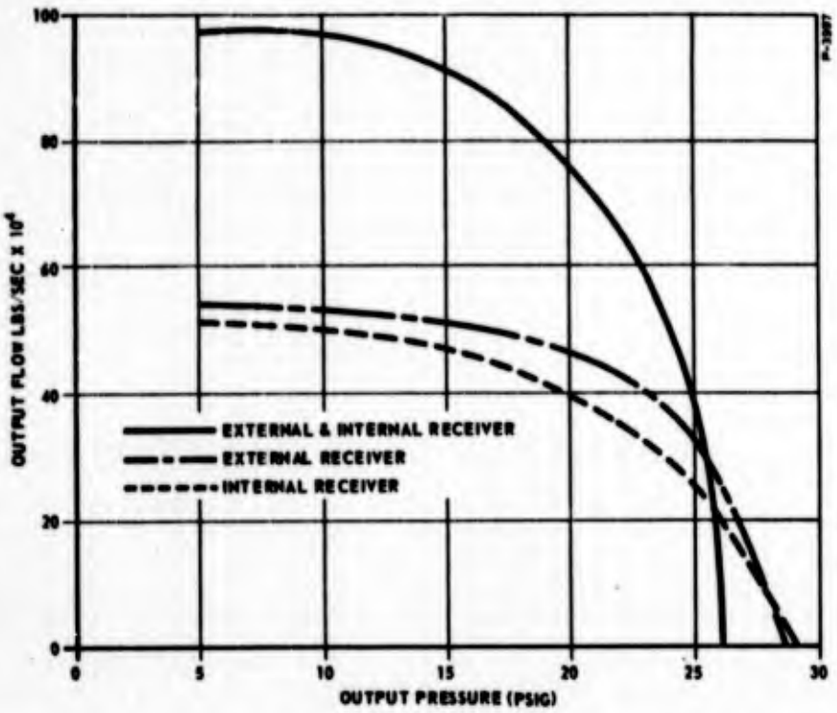

Figure 100 - Vortex Amplifier Output Impedance - Internal and External Receiver Combinations

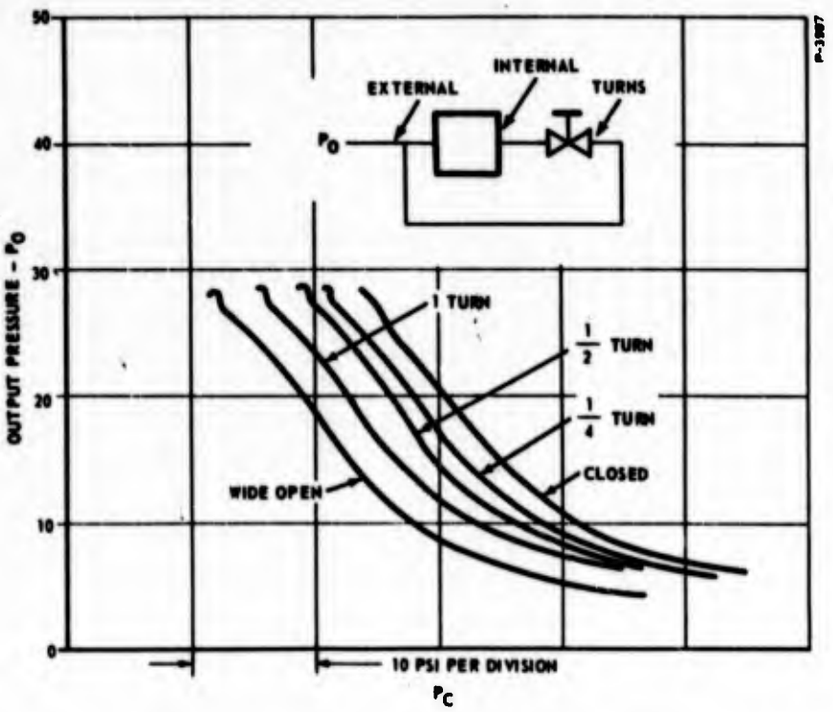

Figure 101 - Effect of Interconnecting Internal and External Pickoffs

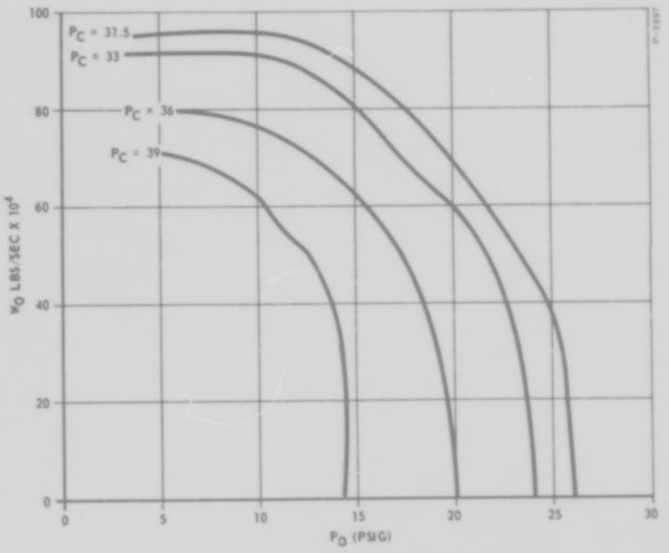

Figure 102 - Vortex Amplifier Output Impedance as Function of Control

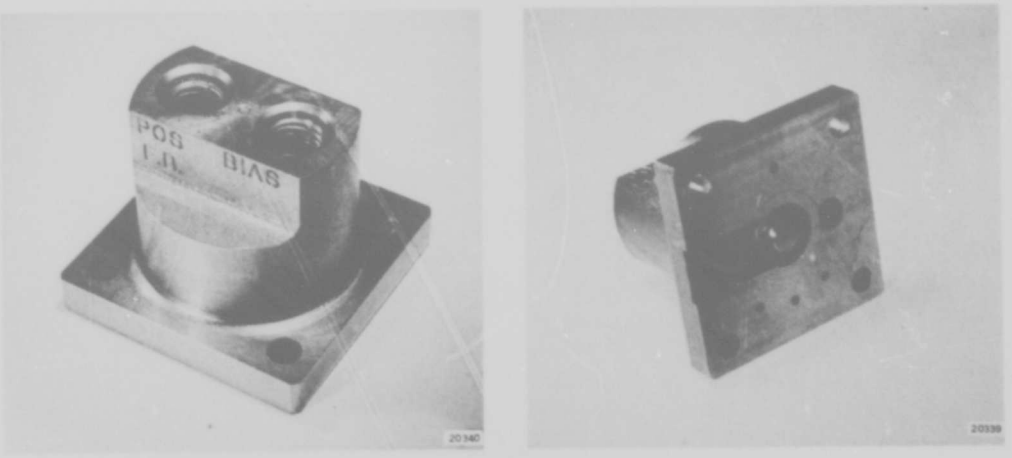

Figure 103 - Vortex Summing Amplifier Assembly

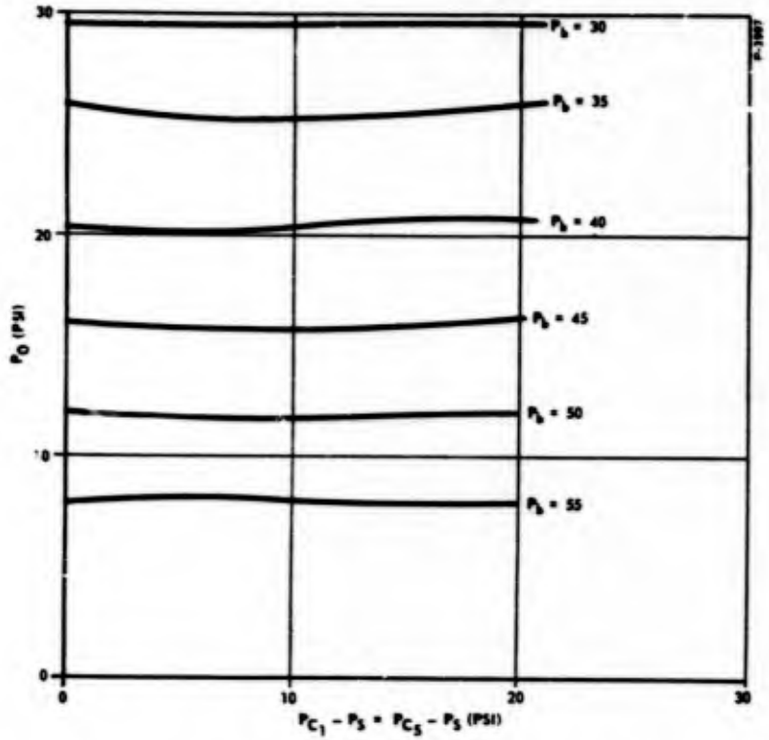

Figure 104 - Summing Amplifier - Subtraction Characteristics

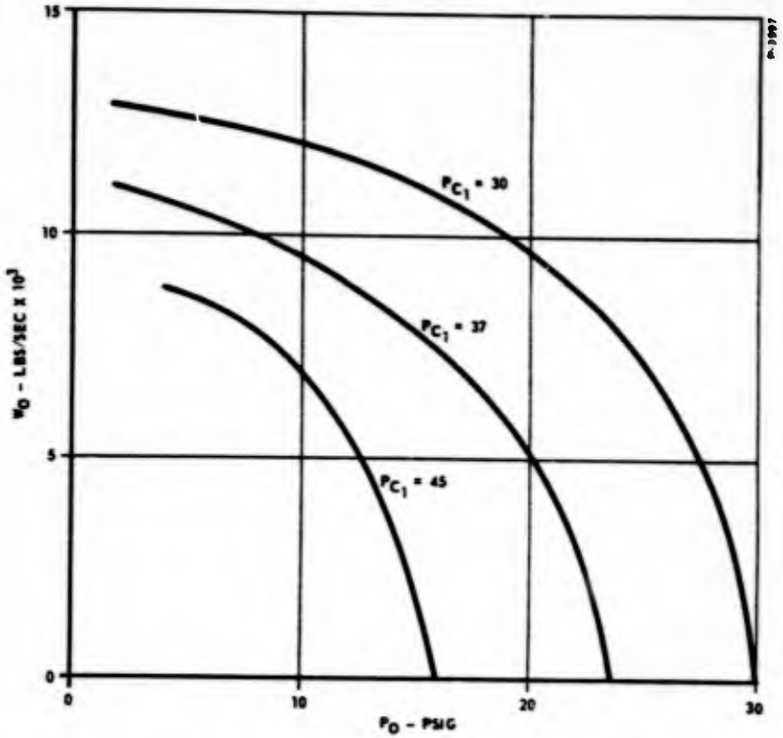

Figure 105 - Summing Amplifier - Output Impedance Characteristics

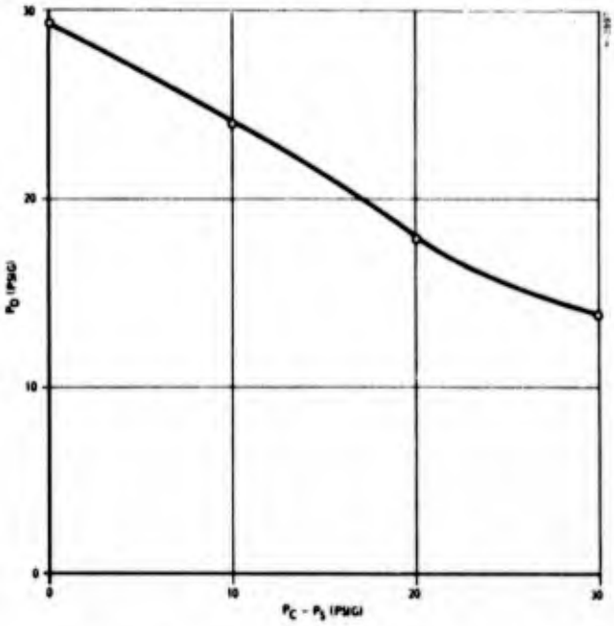

Figure 106 - Summing Amplifier - Input-Output Characteristics

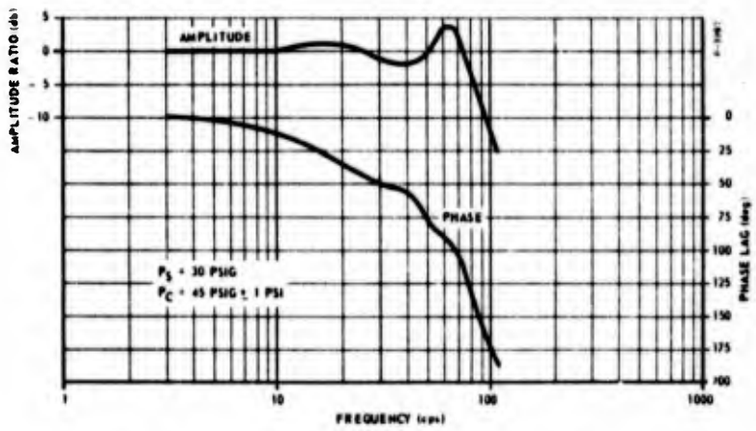

Figure 107 - Summing Amplifier - Frequency Response

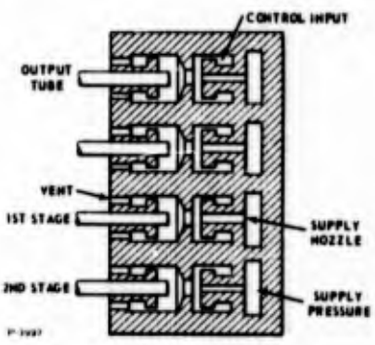

Figure 108 - Venjet Manifold Assembly

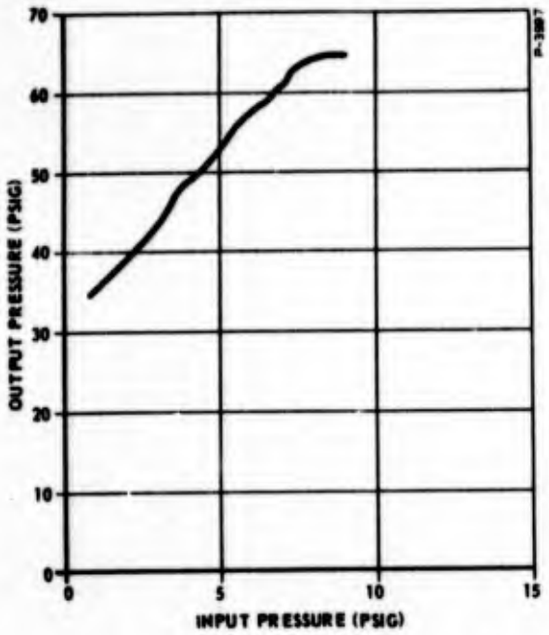

Figure 109 - First-Stage Venjet Pressure Gain

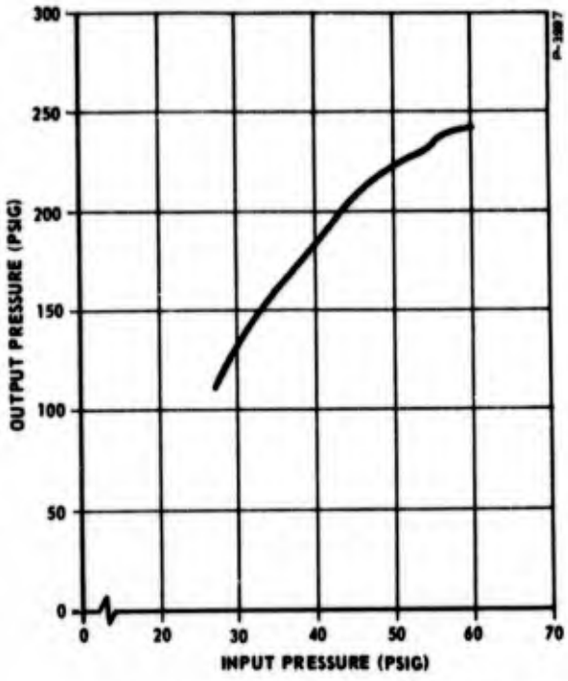

Figure 110 - Second-Stage Venjet Pressure Gain

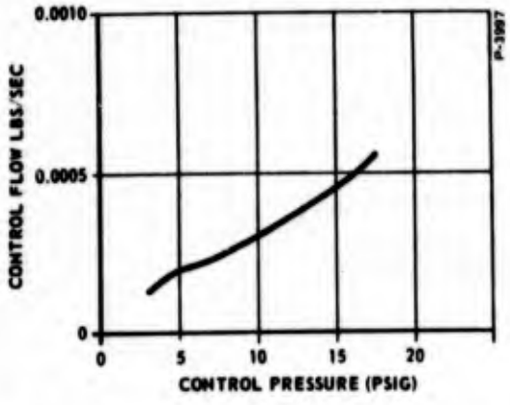

Figure 111 - First-Stage Venjet Input Impedance

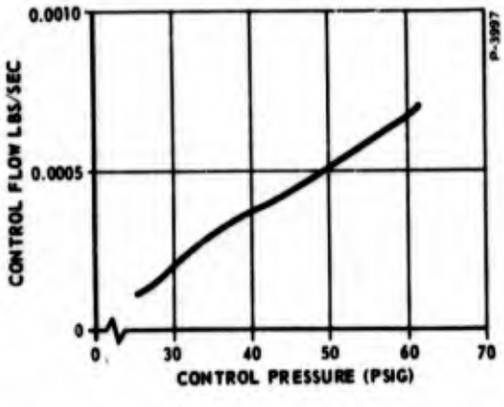

Figure 112 - Second-Stage Venjet Input Impedance

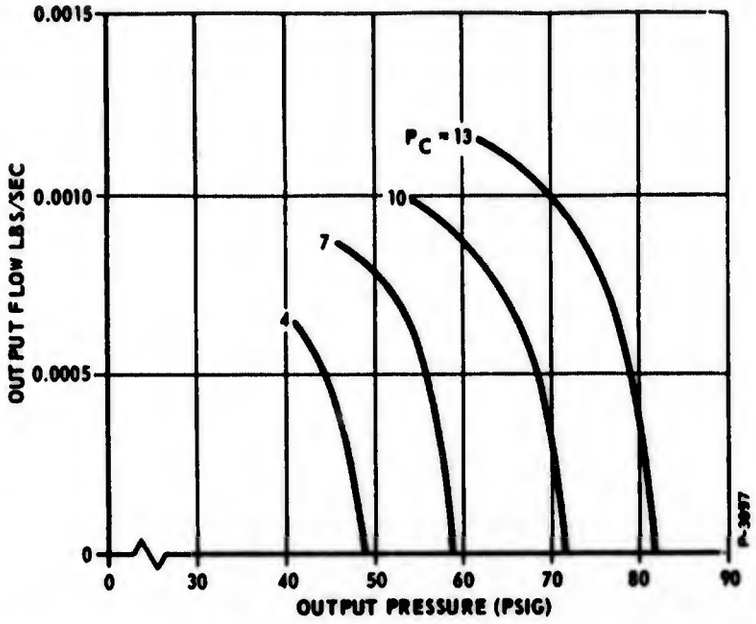

Figure 113 - First-Stage Venjet Output Impedance

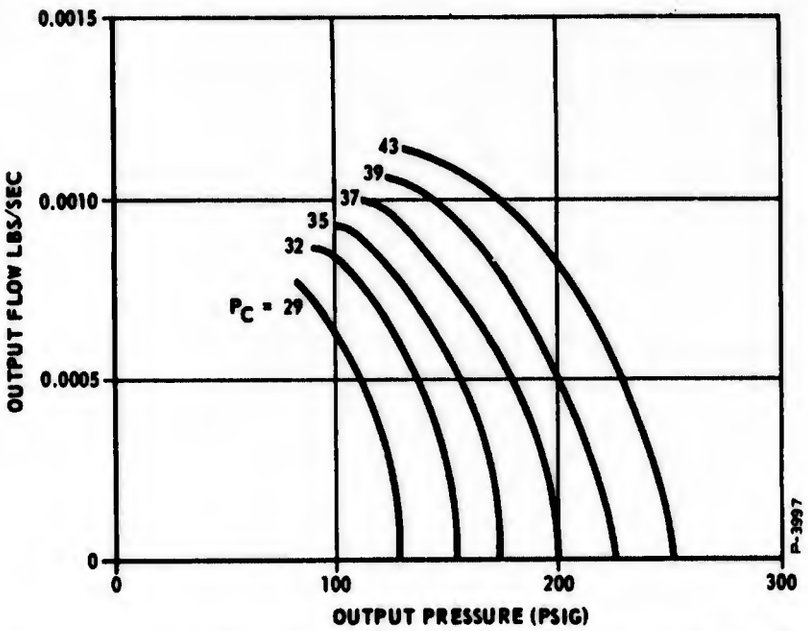

Figure 114 - Second-Stage Venjet Output Impedance

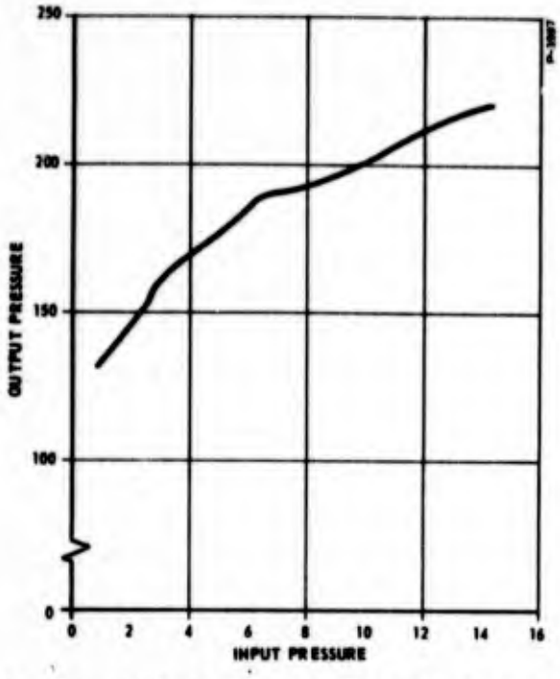

Figure 115 - Two-Stage Venjet Pressure Characteristics

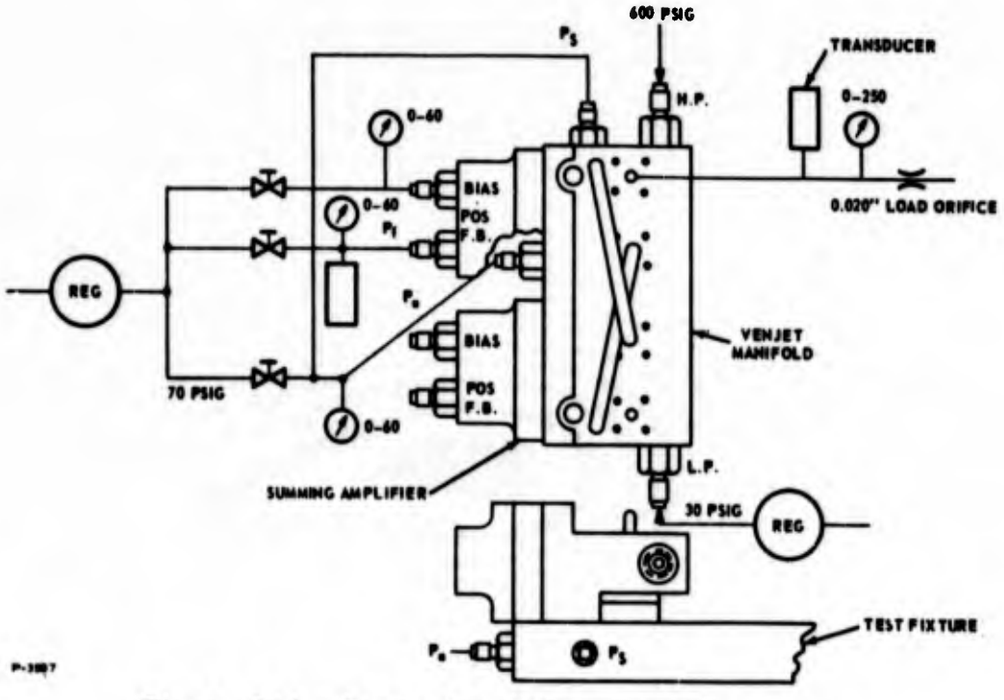

Figure 116 - Servo Amplifier Test Schematic

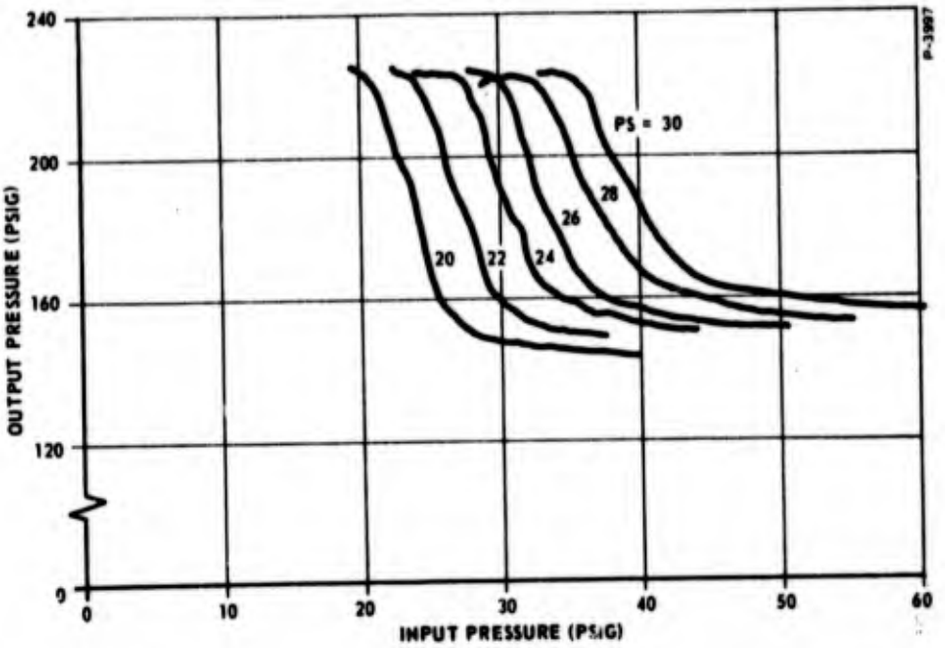

Figure 117 - Servo Amplifier Input-Output Characteristics

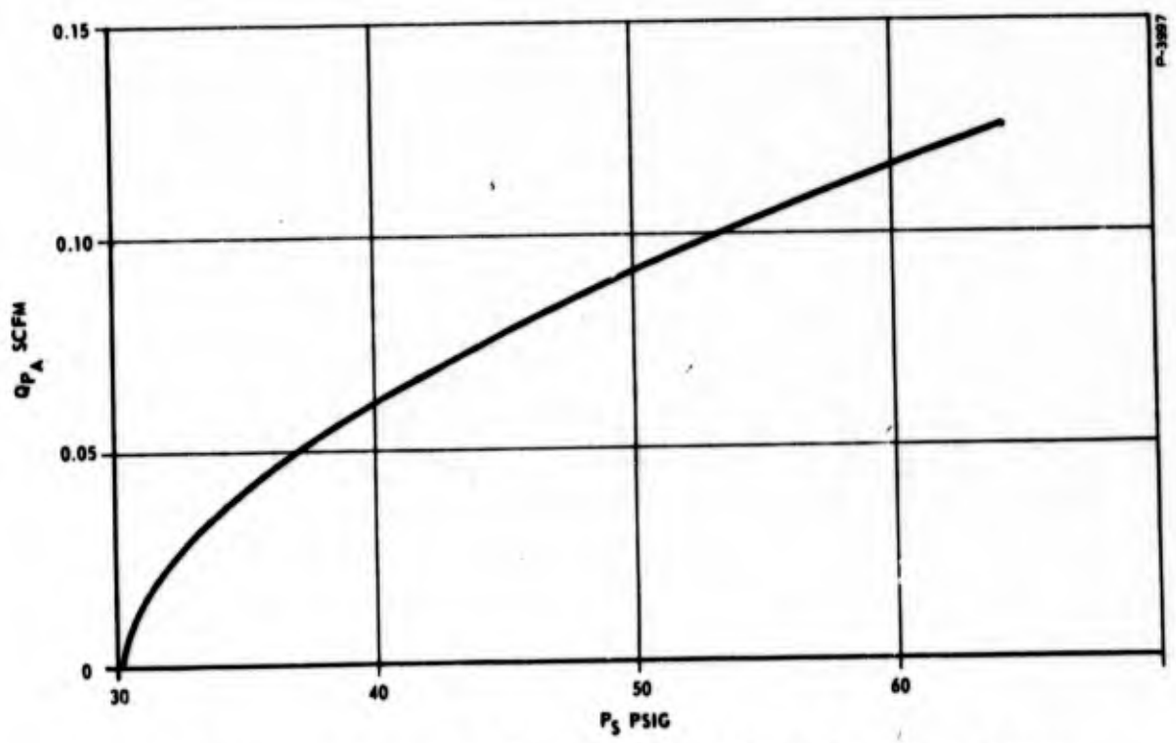

Figure 118 - No. 1 Summing Amplifier Input Impedance

2. Servovalve

The test schematic of the valve is shown in Figure 119. Frequency response and spool position sensitivity were measured only at room temperature, while motor port characteristics were measured at both room temperature and 1000°F.

The valve performance specifications obtained from the tests are listed in Table 5.

Power Stage

Valve static performance was evaluated by placing load orifices in the valve motor ports, applying a command signal and observing motor port pressure fluctuations. Proper orifice size selection enables a good approximation of servo valve vane motor performance.

The block motor port sensitivity is shown in Figures 120 and 121. The data in Figure 120 was taken before the spool was stabilized by inserting a guide pin to prevent rotation or spinning of the spool. The improvement is easily seen in Figure 121.

The loaded port pressure sensitivity is shown in Figures 122 and 123. The load orifices approximate the flow requirements of the motor. Figure 124 indicates the corresponding flow sensitivity. The quiescent flow used by the vortex pilot stage is about 20 percent of the total null quiescent leakage. The remaining leakage is past the supply land to exhaust.

Pilot Stage

A breadboard model of a 5/8 inch diameter servovalve was fabricated for testing the design. The stroke was limited to ± 0.015 inches from null, and the spool was of standard configuration.

The test schematic is shown in Figure 125. A small pin screwed into the spool extends through one of the motor ports. A Bentley proximity transducer senses spool position from the pin. A conventional electropneumatic flapper valve is used to provide the differential control pressure, a transducer used to monitor this signal. The model had all external manifolding, thus the feedback supply flow was easily changed by varying supply pressure.

Table 5 - Servovalve Performance Specifications from Test

Working Fluid		Air, Nitrogen
Working Pressure		600 psig
Operating Temperature Range		70°F to 1000°F
Input Characteristics		
(a)	Signal	Differential pressure
(b)	Quiescent pressure	150 psig
(c)	Rated input	± 60 psid
(d)	Rated flow	1 scfm N_2 at 70°F
Output Characteristics		
(a)	Blocked Port pressure gain	40 psid per percent rated input
(b)	Rated no load flow	140 scfm N_2 at 70°F
Input-Output Characteristics		
(a)	Quiescent flow	20 scfm N_2 at 70°F
(b)	Hysteresis	1 percent
(c)	Linearity	5 percent
(d)	Frequency Response	
	-3 db Amplitude	110 cps
	90° Phase Shift	80 cps

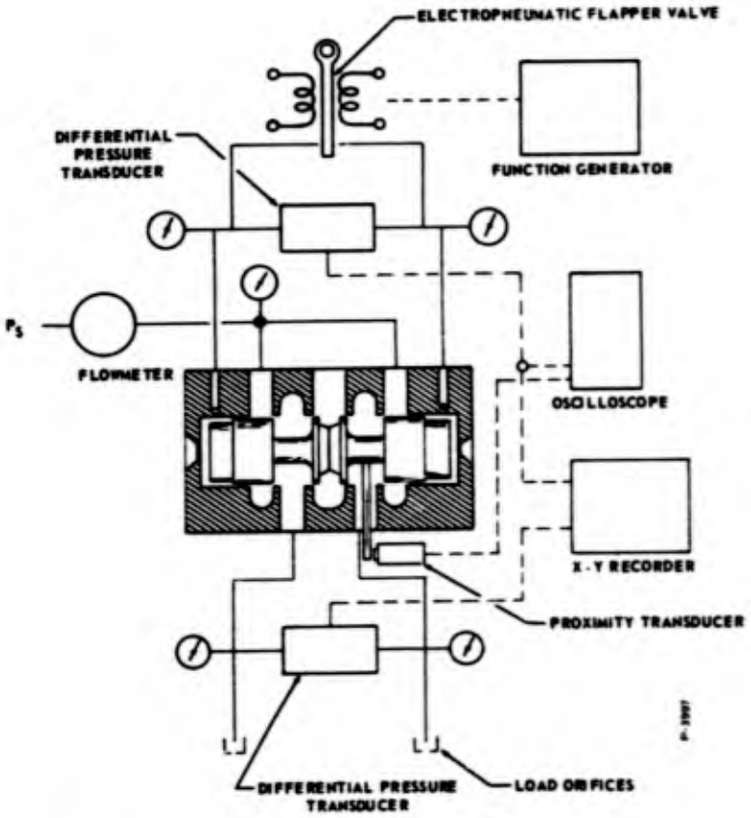

Figure 119 - Pneumatic Interface Servovalve Test Schematic

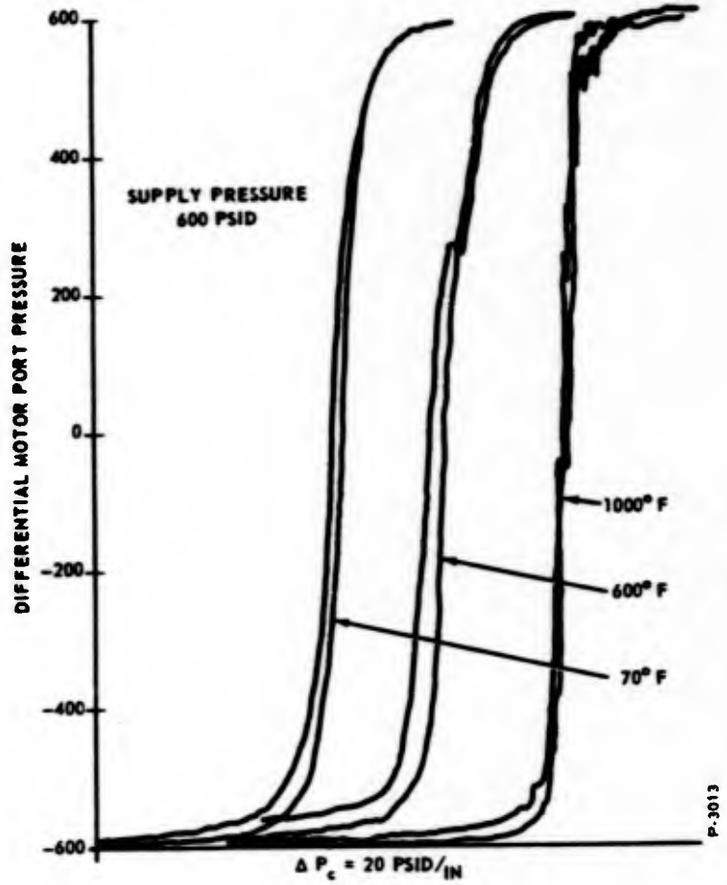

Figure 120 - Servovalve Blocked Motor Port Pressure Sensitivity at Various Temperatures

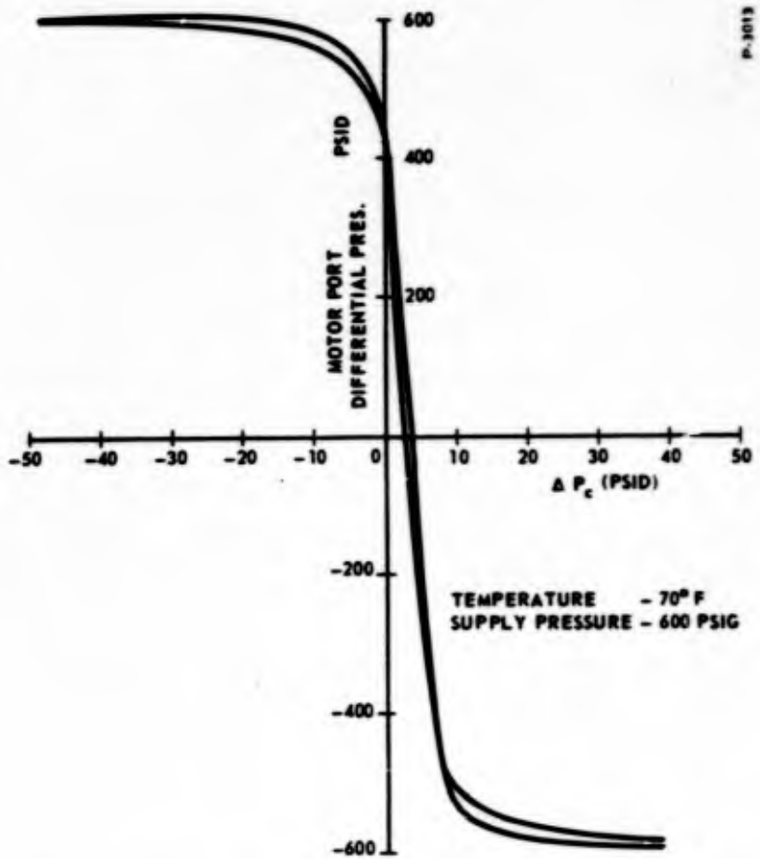

Figure 121 - Servovalve Blocked Motor Port Pressure Sensitivity

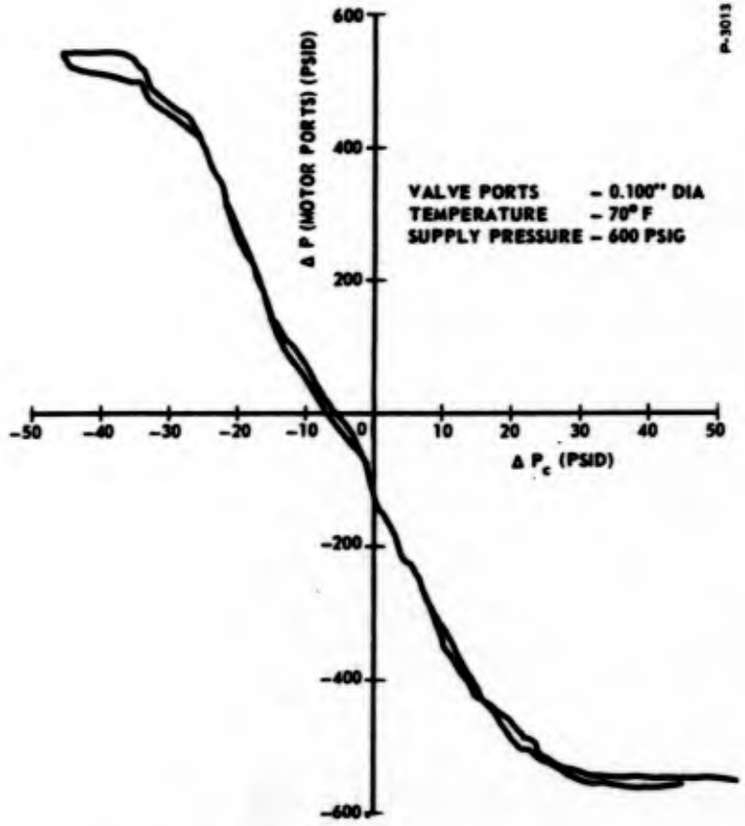

Figure 122 - Servovalve Loaded Motor Port Pressure Sensitivity

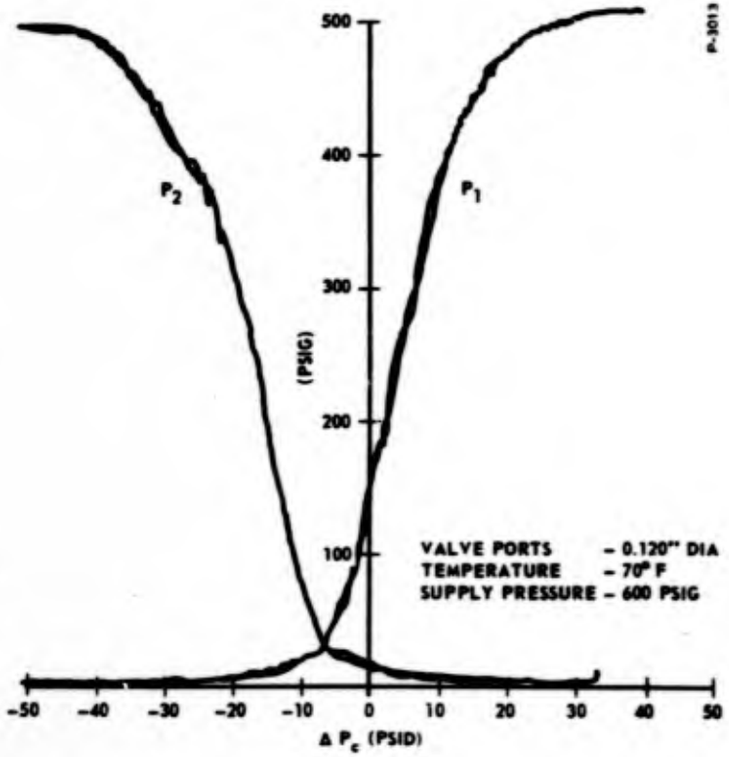

Figure 123 - Servovalve Loaded Motor Port Pressure Sensitivity

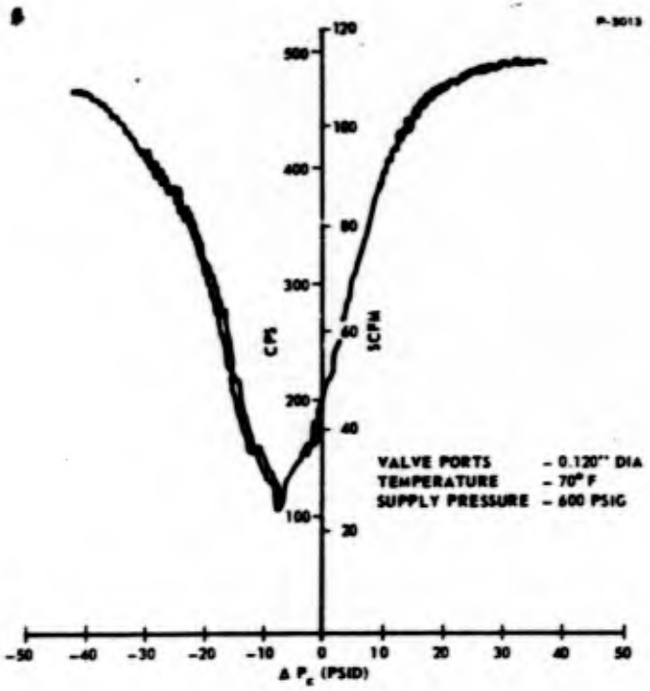

Figure 124 - Servovalve Flow Characteristics

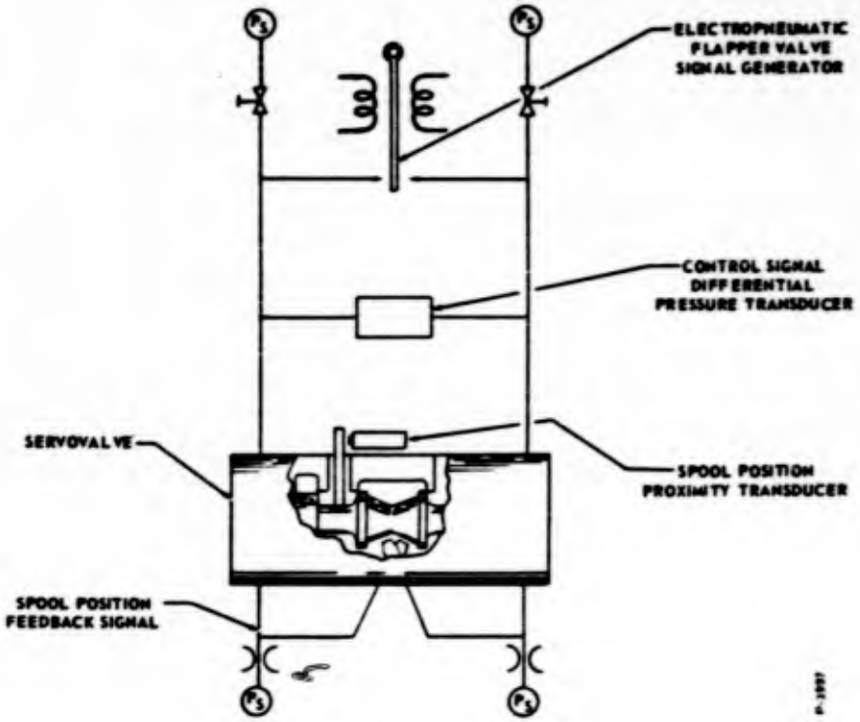

Figure 125 - Pneumatic Servovalve with Vortex Pitot Stage - Test Schematic

Vortex characteristics were determined and are shown in Figure 126. Losses seemed to be at a minimum, indicating that operation would agree with the assumed analytical model. On closing the position loop, the valve was unstable or erratic at times, making control of the spool position almost impossible. The problem was traced to excessive ram chamber volume due to instrumentation. The erratic or unstable behavior was caused by a large damping factor due to a 1/16 inch line connecting a static pressure tap on the ram chamber wall to a Bourdon tube pressure gage. A plot of spool position as a function of differential control pressure is shown in Figure 127. The slight deviation from linearity was caused by a damaged nozzle.

Valve frequency response was found to be approximately 30 cps. This was considerably lower than the natural frequency which indicated an α of over 3. An increase in pressure ratio at the tangential control ports should reduce α. This was attempted experimentally by reducing the area of the port width with no apparent change of response.

A possible cause for the low response was found to be a large lag found in the position feedback loop. Volumes and line lengths were studied. An analytical analysis of the volume in the feedback line (originally neglected) indicating that the lag was proportional to the pressure ratio across the tangential feedback port. This ratio was decreased by enlarging the feedback port area with a 30 cps increase in response resulting.

Further reduction of this volume was not feasible because of the necessary line length needed on the breadboard to connect the nozzle with the control port. The final valve pilot stage was fabricated and the line and volume lengths were kept to a minimum. Figure 128 is a plot of the valve frequency response measured at room temperature. The input signal was 10 percent of the rated input pressure. A typical trace of spool position response is shown in Figure 129. The frequency of the signal is 60 cps and as can be seen, the noise level is very low.

3. Vane Motor

Motor Acceptance Test

The test schematic for the motor is shown in Figure 130. The motor was tested completely at room temperature and,with the exception of the maximum speed attained, all performance specifications were met.

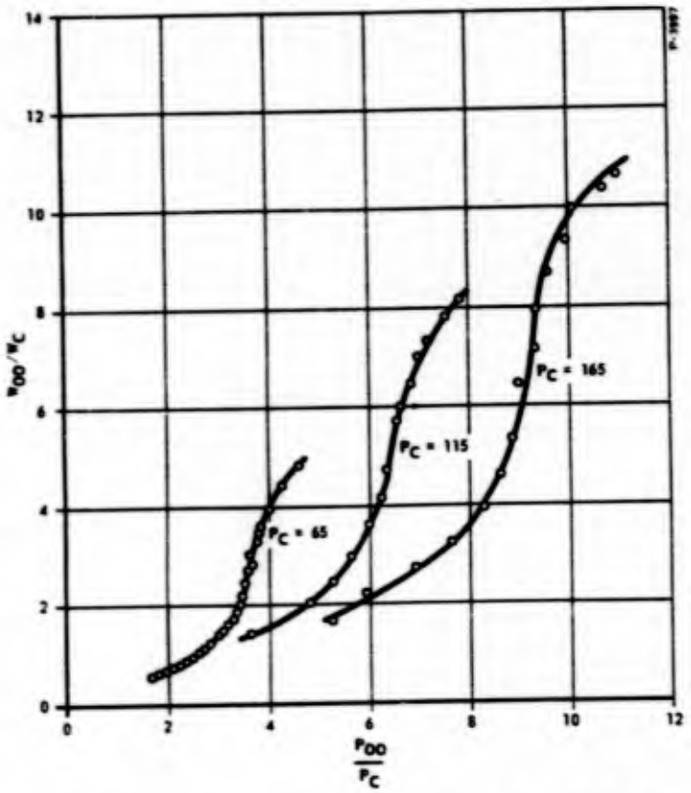

Figure 126 - Servovalve Vortex Amplifier Characteristics

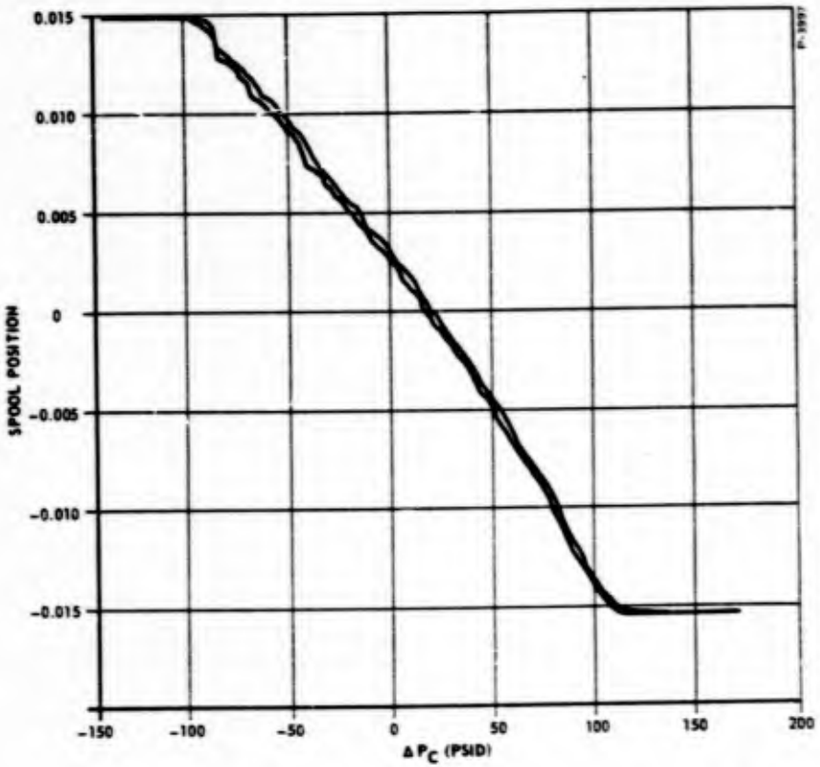

Figure 127 - Servovalve Spool Position Sensitivity

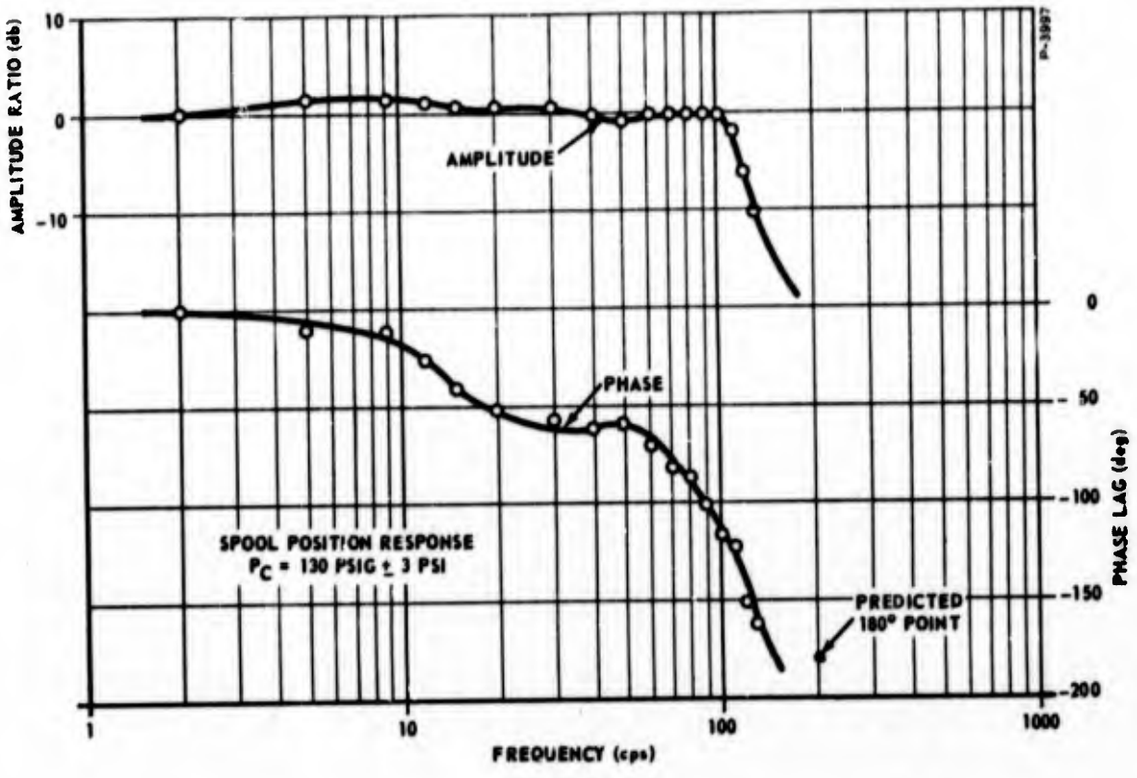

Figure 128 - Servovalve Spool Position Frequency Response

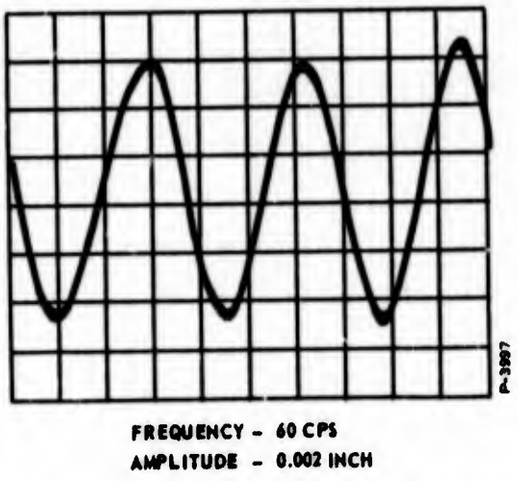

Figure 129 - Spool Position Response to a Sinusoidal Input Signal

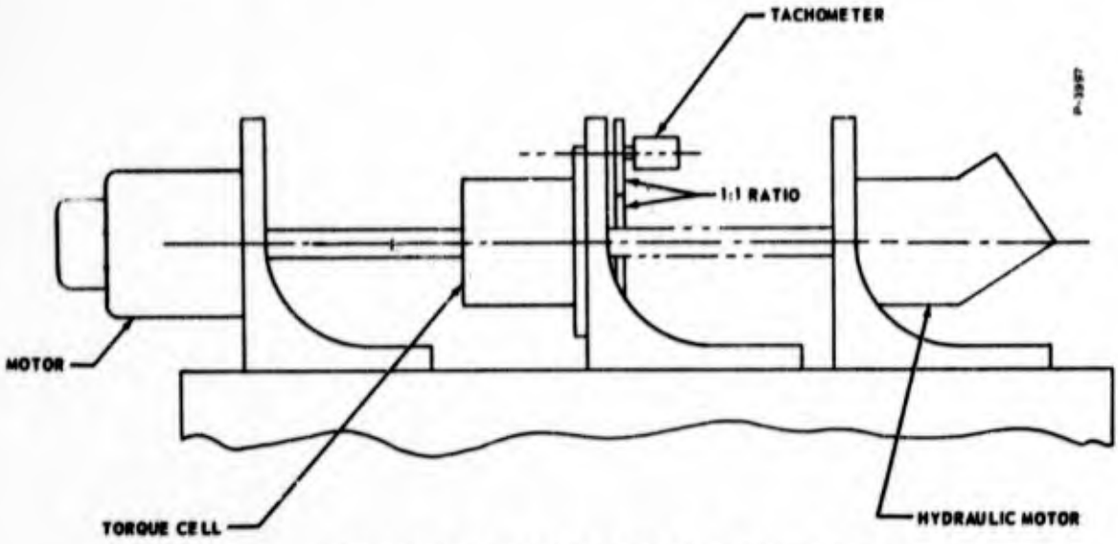

Figure 130 - Motor Test Schematic

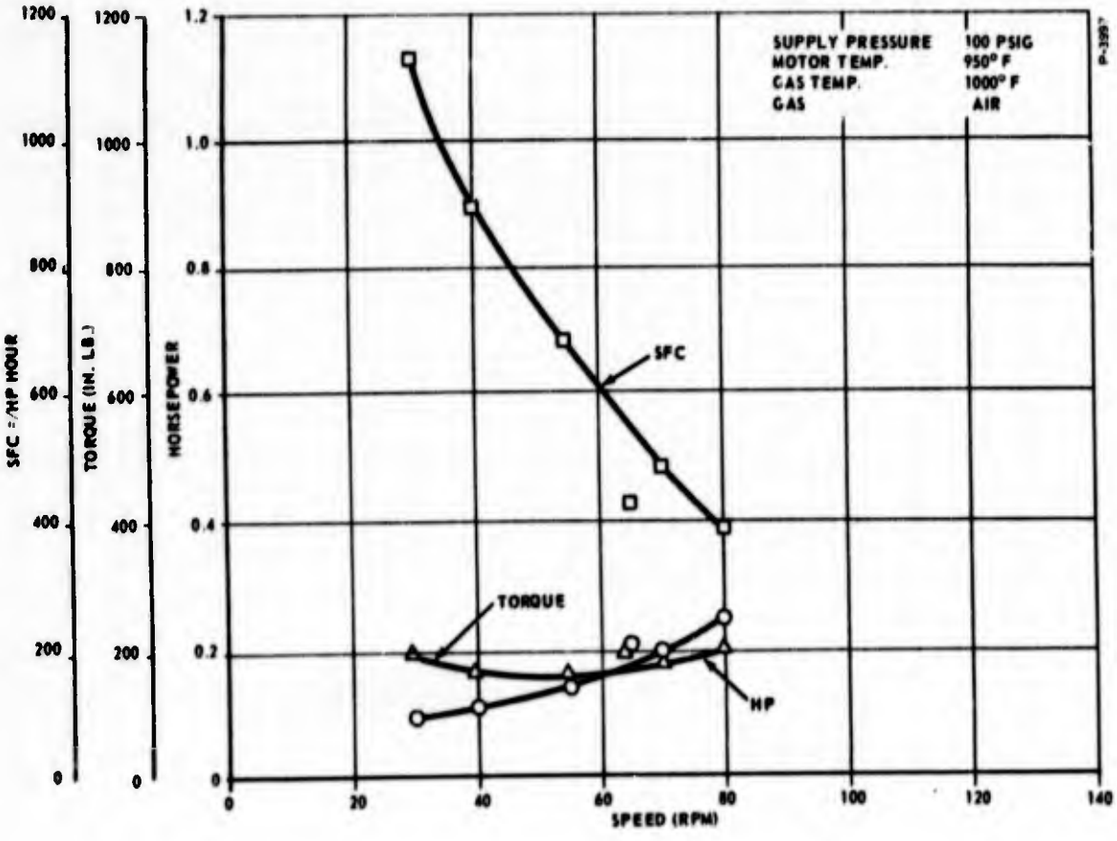

Figure 131 - Motor Performance at 100 Psig Supply

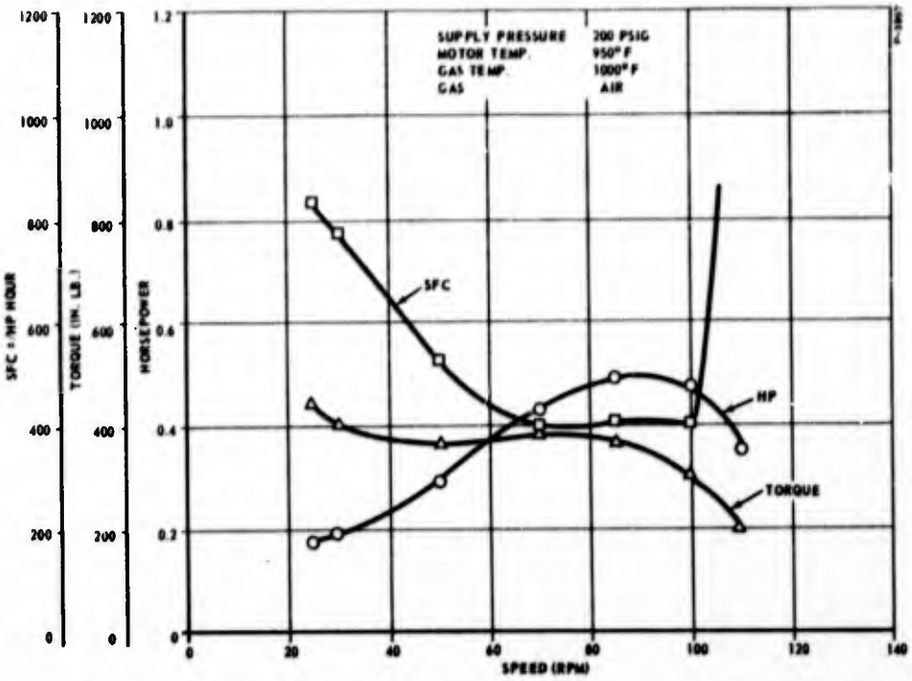

Figure 132 - Motor Performance at 200 Psig Supply

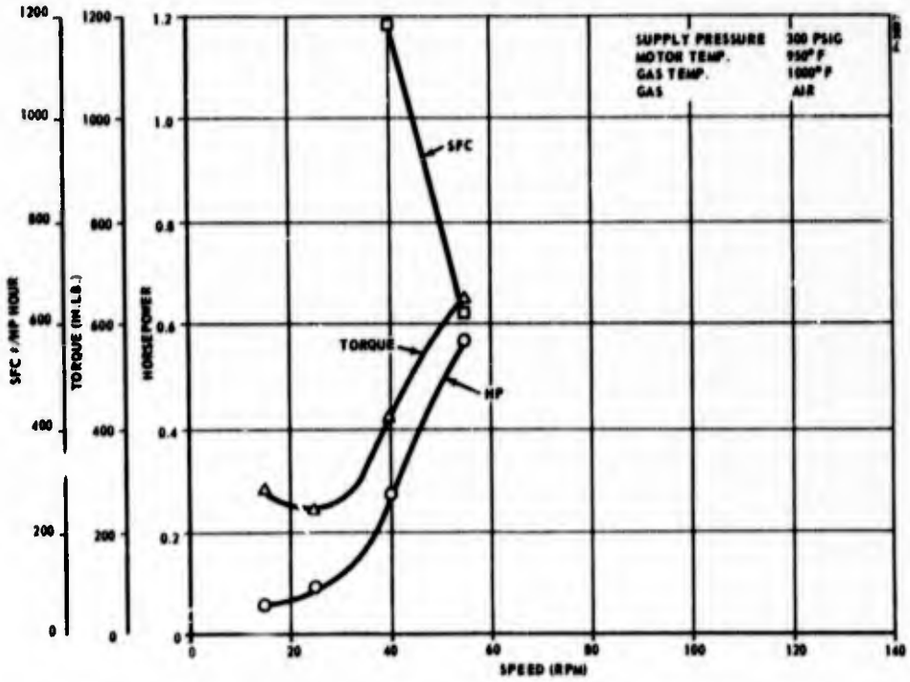

Figure 133 - Motor Performance at 300 Psig Supply

Performance tests on the motor were conducted at 750°F where the molybdenum disulfide provided some dry film lubrication. Although performance at 750°F is not specified, the motor does meet predicted levels.

Tests at 1000°F indicated a high level of internal friction due to inadequate lubrication. At 1000°F the metal oxides form too slowly to provide lubrication effects and the temperature is beyond the range of available wet or dry film lubricants.

Graphs depicting the motor performance at 1000°F at supply pressures of 100, 200, 300 and 400 psi are shown in Figures 131 through 134.

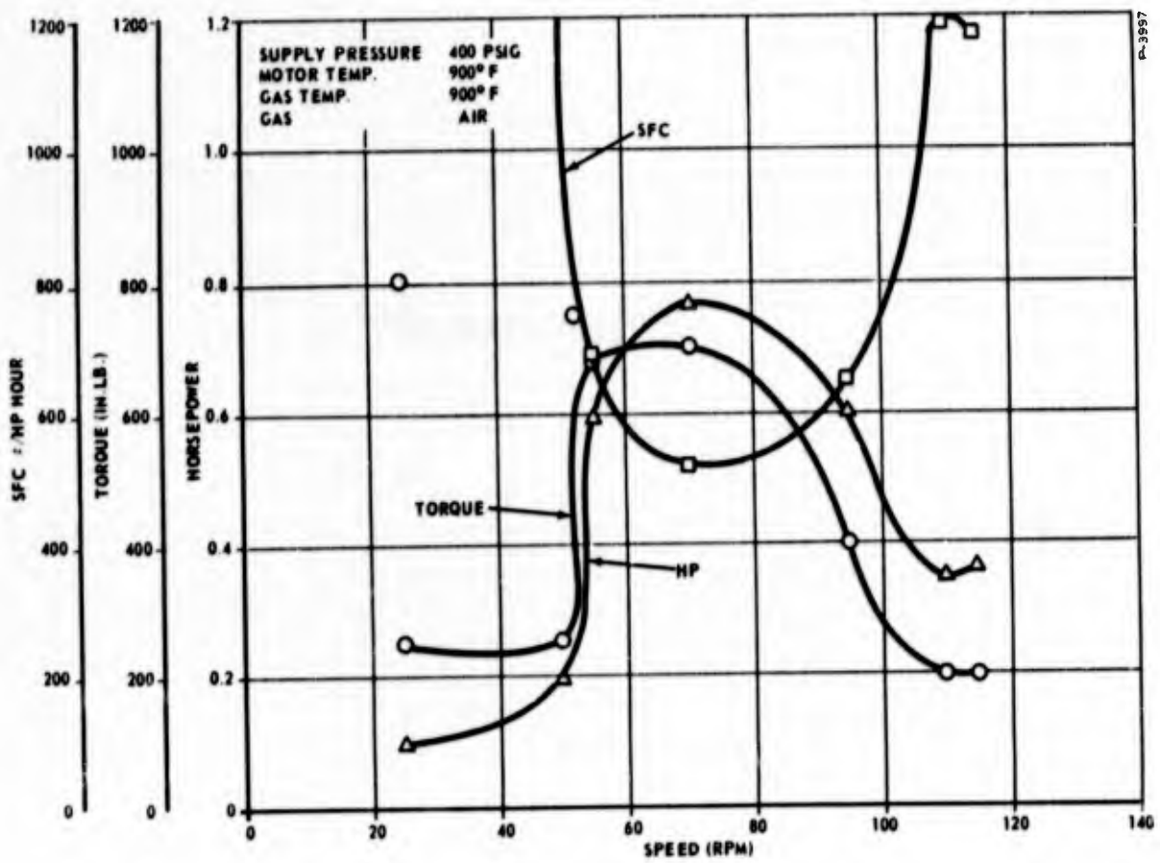

Figure 134 - Motor Performance at 400 Psig Supply

Development Tests

The major development area was with the synthetic sapphire vane tip inserts. After a short duration of running, the inserts would fail by cracking near the center of the vane and then subsequently fretting or chipping until total failure occurred. Consideration of this problem led to the belief that the vanes were heating unevenly. Friction at the vane tips would generate heat in the vane. As the supply gas leaked past the ends of the vanes cooling them, the center portion would remain relatively expanded, resulting in more concentrated loading near the centers of the vane tips. This condition, being unstable, worsened until failure occurred due to fracture of the tips. The problem was remedied by first porting some gas beneath the tips for cooling and by relieving the center portion of the cam surface for approximately sixty degrees of arc beyond the inlet ports. This reduced the total heat generated in the center of the tips and air-cooled them when they did not contact the cam surface.

Although the vane distortion was virtually eliminated, the synthetic sapphire vane tip inserts proved unsatisfactory due to impact resistance. Tungsten carbide rods were substituted and proved to be much more durable.

The leakage over the vanes, in addition to cooling them, resulted in a significant improvement in the performance characteristics of the motor. At low speeds, the supply gas can charge the preceding vane chamber through the relief in the cam surface, increasing the effective motor displacement.

At high speeds, the housing relief does not provide the total displacement flow into the preceding chamber. Thus, expansion takes place and the advantage of the expansion motors is retained.

4. Position Transducer

In order to investigate the effect of removing flow through the static pressure tap and verify the predicted operation of the transducer, an experimental model was constructed to obtain test data.

Figure 135 is a test schematic used with the test model. The supply pressure was regulated at 50 psig. The output flow was varied from zero to the maximum amount with a pair of hand valves.

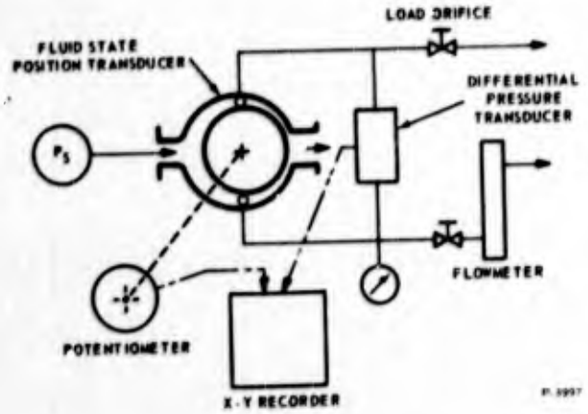

Figure 135 - Position Transducer Test Schematic

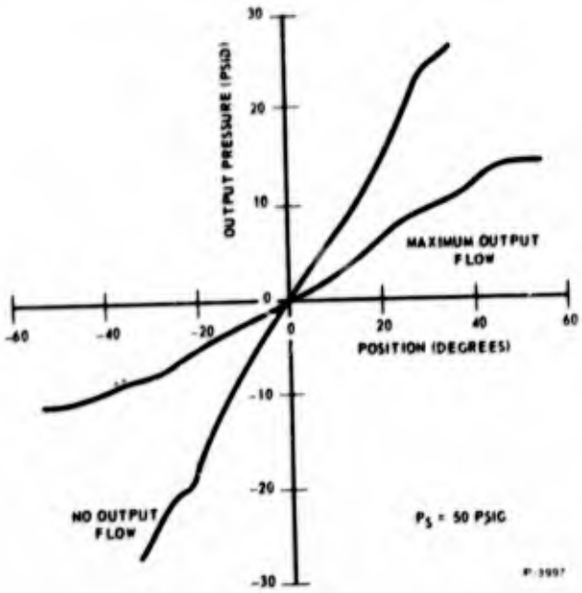

Figure 136 - Position Transducer Input-Output Characteristic - Loaded and Unloaded

Figure 136 shows the no-load output curve for the transducer. The nonlinearity at -20° was caused by machining errors in the duct. A slight high spot exists and a crude attempt was made to reduce it. A considerable improvement was noticed; it was concluded that a nearly linear curve was possible using ordinary machine tolerances as long as an attempt was made to keep the duct walls continuous. A series of radii, instead of the point to point machining used, should improve the linearity without increased fabrication costs.

The load orifices were fully opened and the recovered flow measured. This maximum flow corresponded exactly to the maximum orifice flow rate through the static tap diameter. The loaded curve of Figure 136 indicates that the linearity remains adequate under this maximum load condition. The maximum flow from one side at this condition was 40 percent of the supply flow at the high pressure end of the duct and 20 percent of the supply flow at the low pressure end. This corresponded to the static tap area-to-duct exit area ratio.

5. Servo Subsystem Performance

Servovalve-Motor Integration

The servovalve was first integrated with the servomotor and tested at both room temperature and 1000°F.

Figure 137 shows stall torque as a function of valve input signal. Figure 138 shows the motor torque-speed characteristic when coupled with the servovalve, and Figures 139 and 140 show additional stall characteristics.

The valve-motor frequency response with a full inertia load is shown in Figure 141 for room temperature and 1000°F. As indicated, the frequency response if essentially independent of temperature.

Servoamplifier-Servovalve Integration - The servovalve was next integrated with the servoamplifier. This was accomplished as shown in the test schematic of Figure 142. Test results are shown in Figure 143.

Closed Loop Servo Subsystem - The position transducer was added to the servomotor and the feedback loop was closed. The input circuit is shown in Figure 144. The quiescent pressures were adjusted to bias each amplifier stage at its null point and appropriate biases were added to the summing amplifiers to null the servo. The following tests were performed.

Hysteresis - Figure 145 shows the input-output hysteresis loop. The approximate one degree of hysteresis shown is essentially all traceable to the transmission backlash indicating that the fluid state part of the subsystem contributes negligible hysteresis, as expected.

Resolution - Figure 146 shows resolution trace indicating a resolution envelope of 1.0 degrees.

Threshold - Figure 147 is a threshold trace indicating a threshold of 1 psid.

Step Response - Figure 148 is a step response trace for a 4 degree step input.

Frequency Response - The closed loop frequency response is plotted in Figure 149.

Repeatability - A repeatability trace is shown in Figure 150. The repeatability is within the noise of the measurement.

Linearity - The linearity achieved is illustrated in Figure 151.

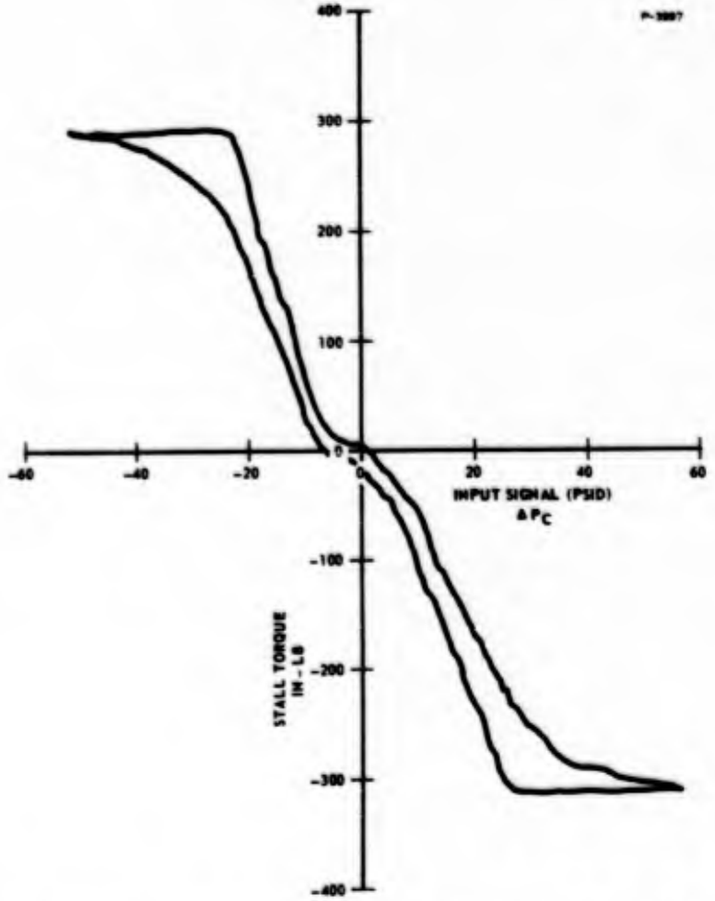

Figure 137 - Servovalve - Servomotor Stall Torque Characteristic

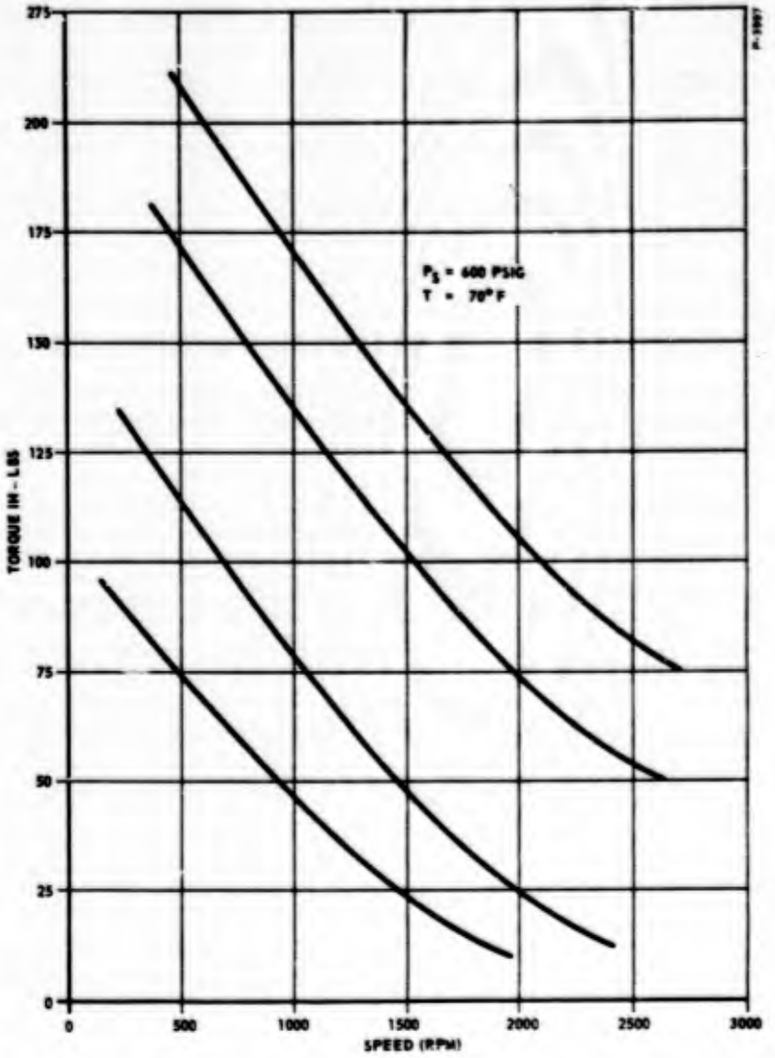

Figure 138 - Servovalve - Servomotor Torque-Speed Characteristic

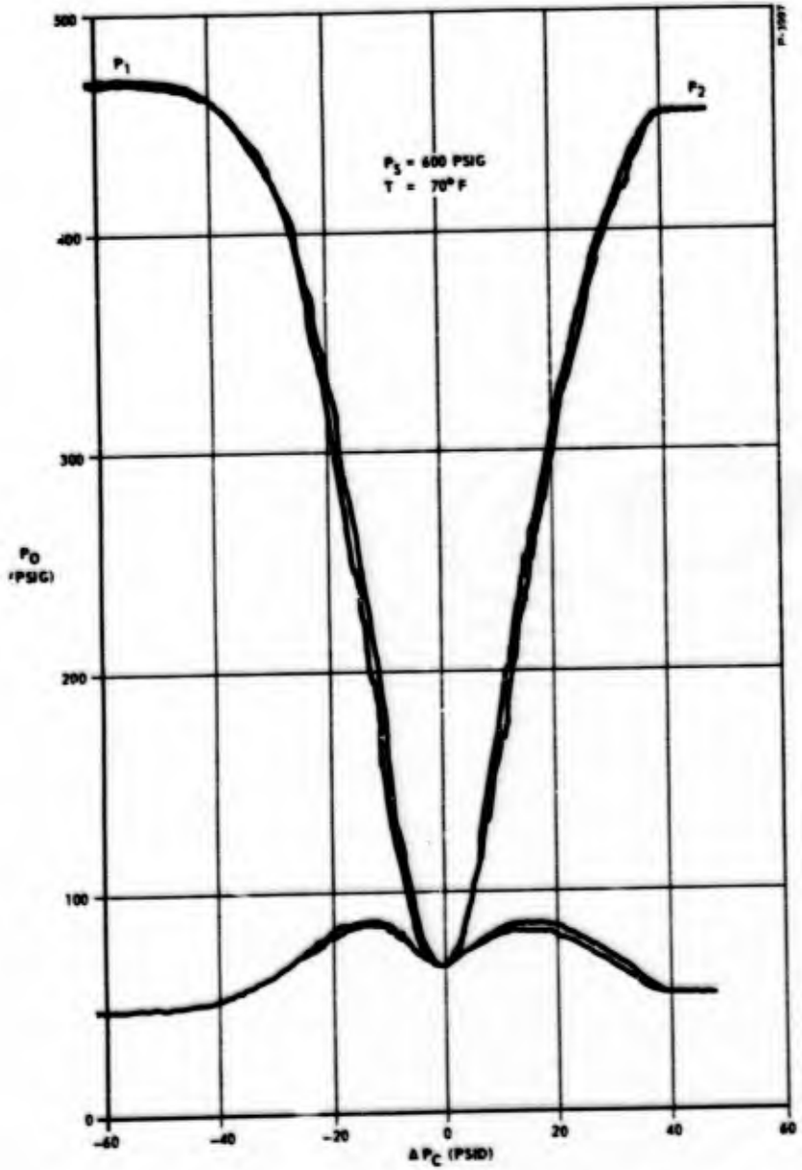

Figure 139 - Servovalve - Servomotor Stall Pressure Characteristics - Room Temperature

Figure 140 - Servovalve - Servomotor Stall Pressure Characteristics - 1000°F

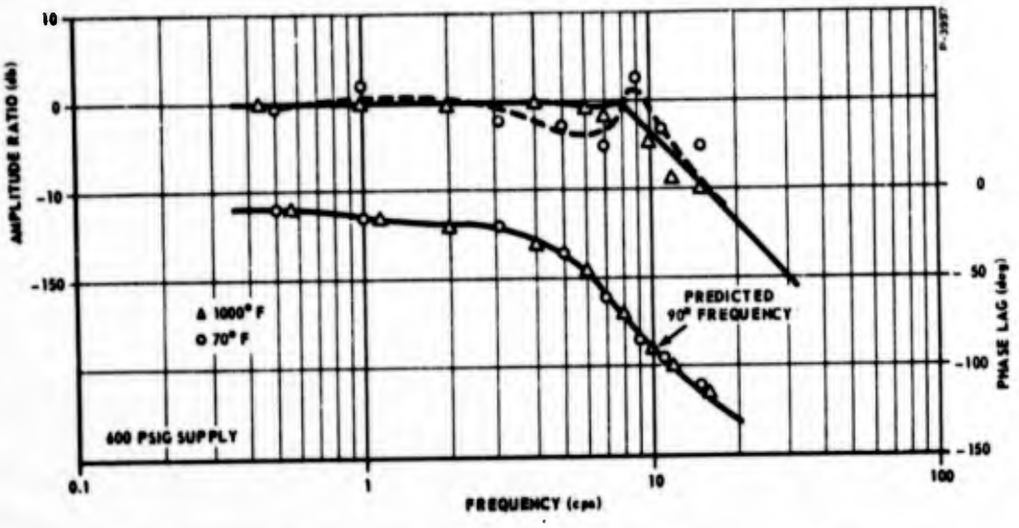

Figure 141 - Servovalve - Servomotor Frequency Response (70°F and 1000°F)

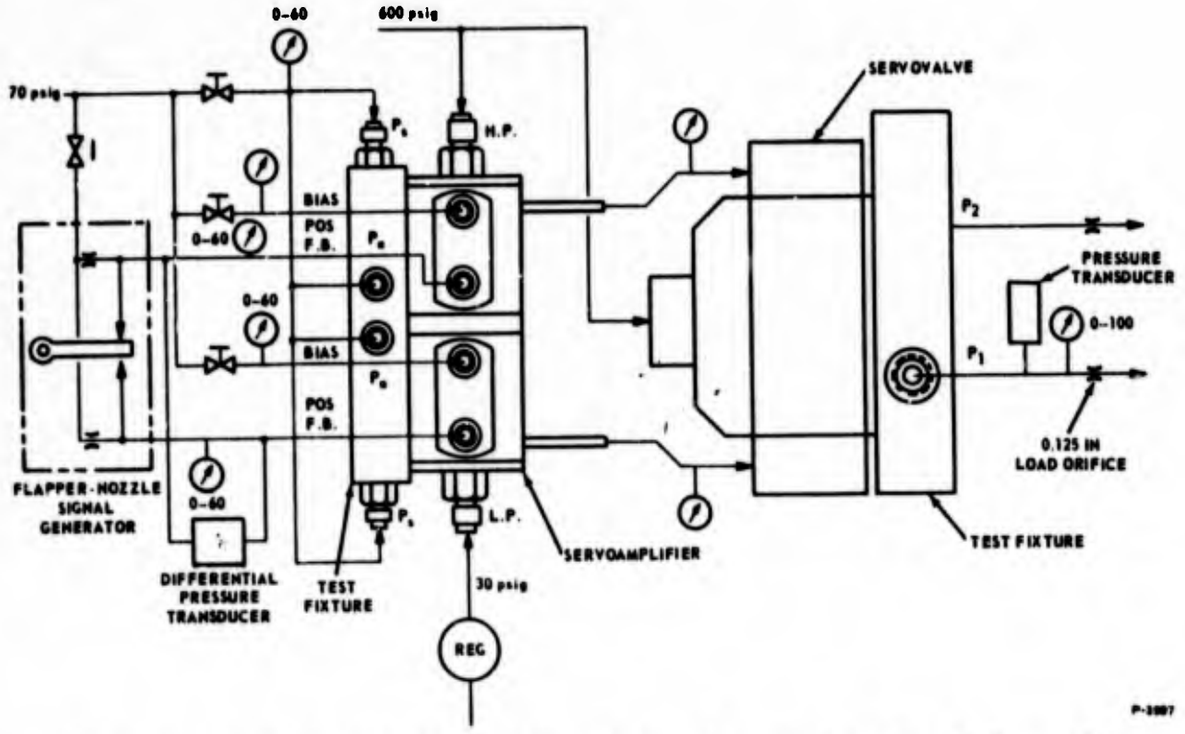

Figure 142 - Integrated Servoamplifier - Servovalve Test Schematic

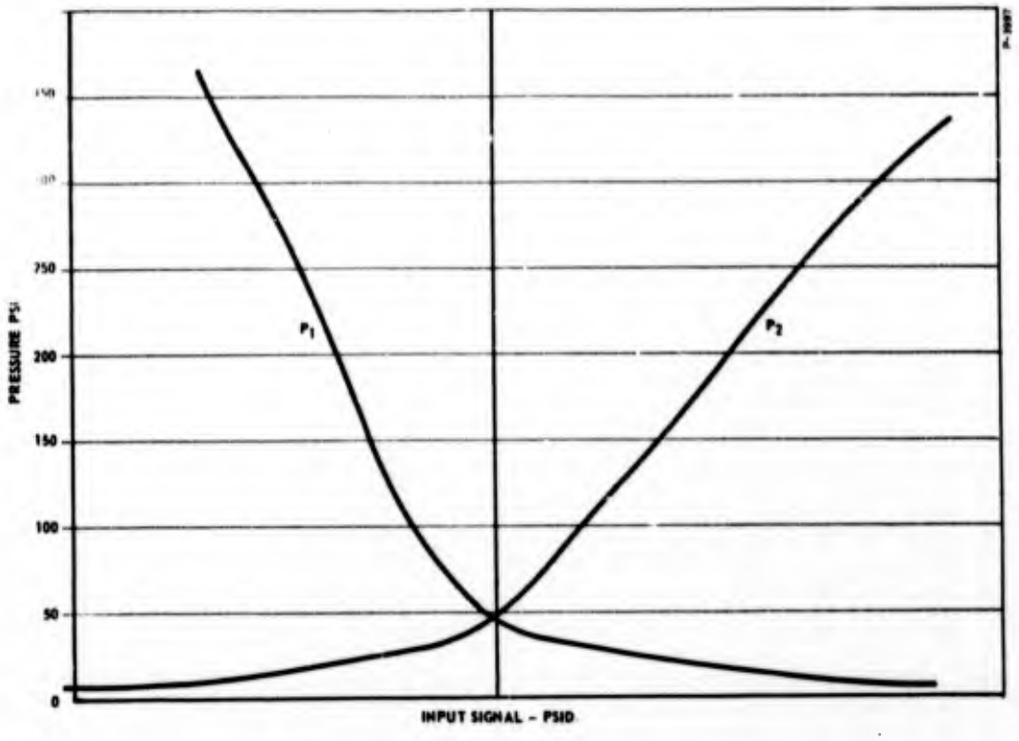

Figure 143 - Integrated Servoamplifier - Servovalve - Input-Output Data

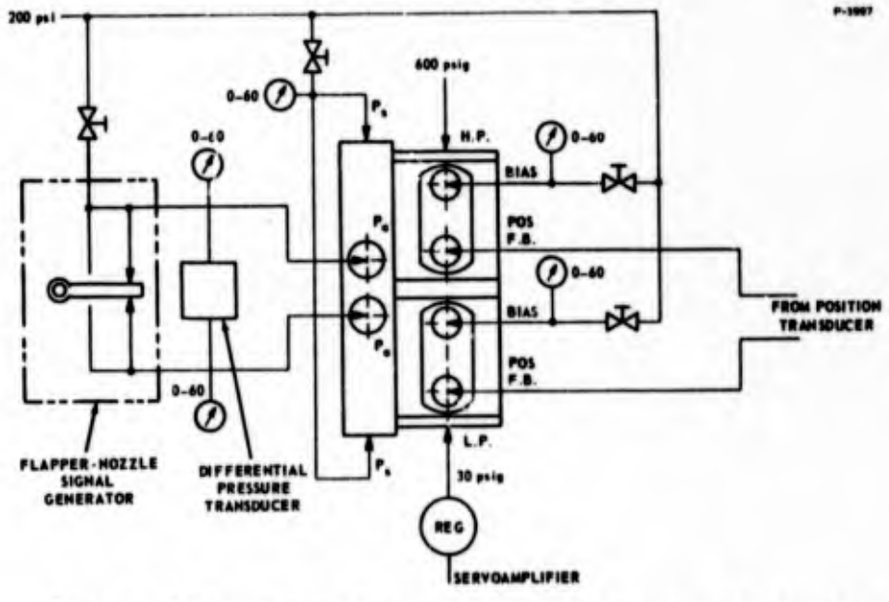

Figure 144 - Servo Subsystem Input Circuit Schematic

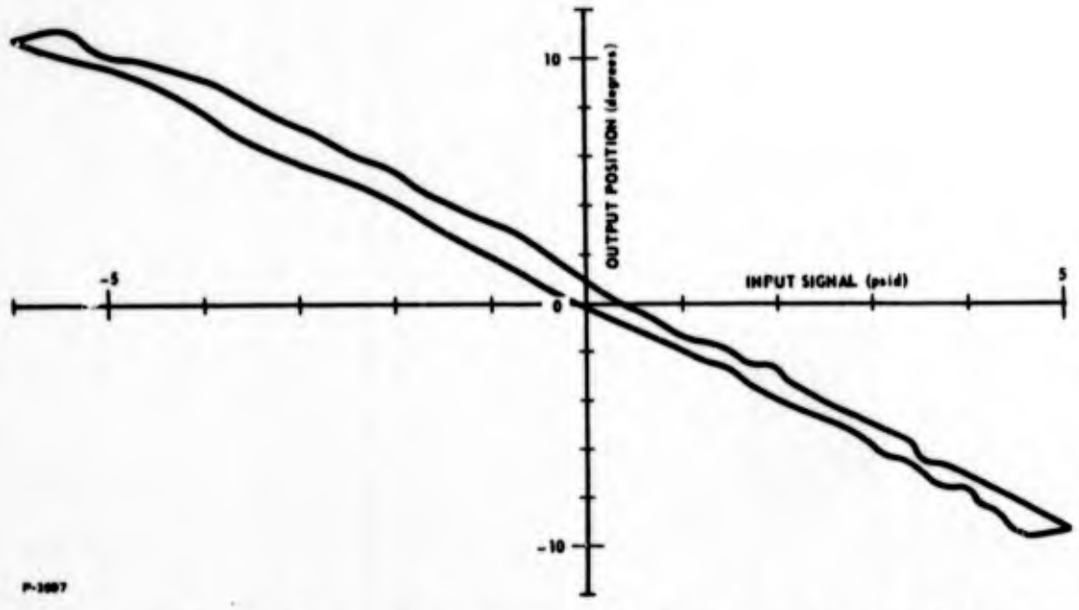

Figure 145 - Servo Subsystem Input-Output Hysteresis Loop

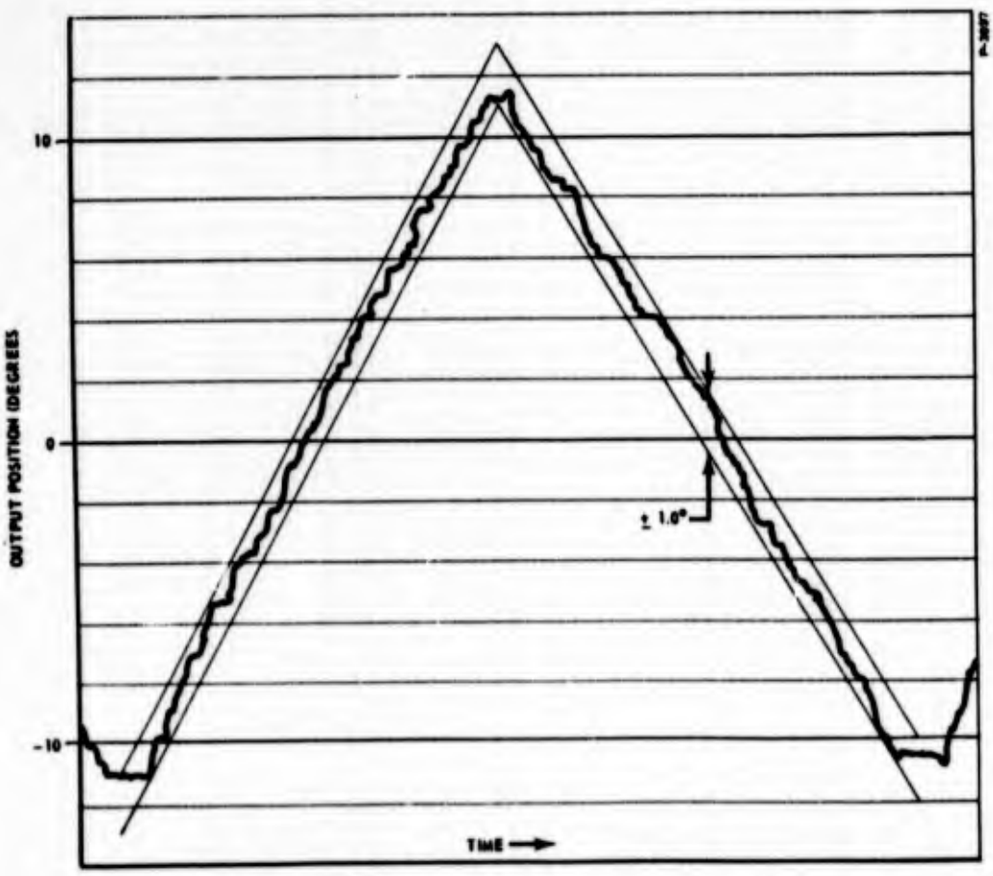

Figure 146 - Servo Subsystem Resolution

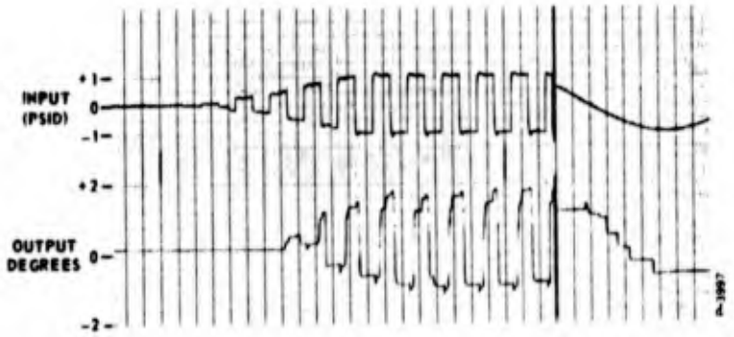

Figure 147 - Servo Subsystem Threshold

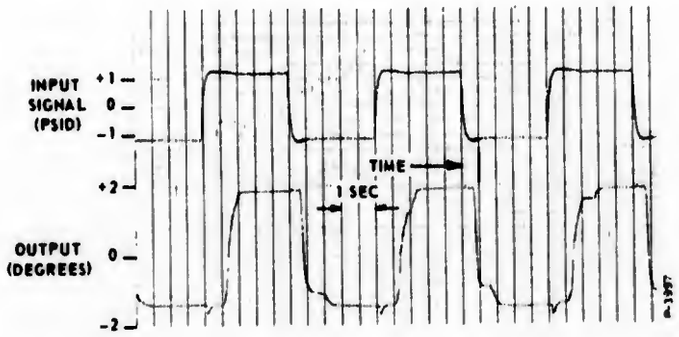

Figure 148 - Servo Subsystem Step Response

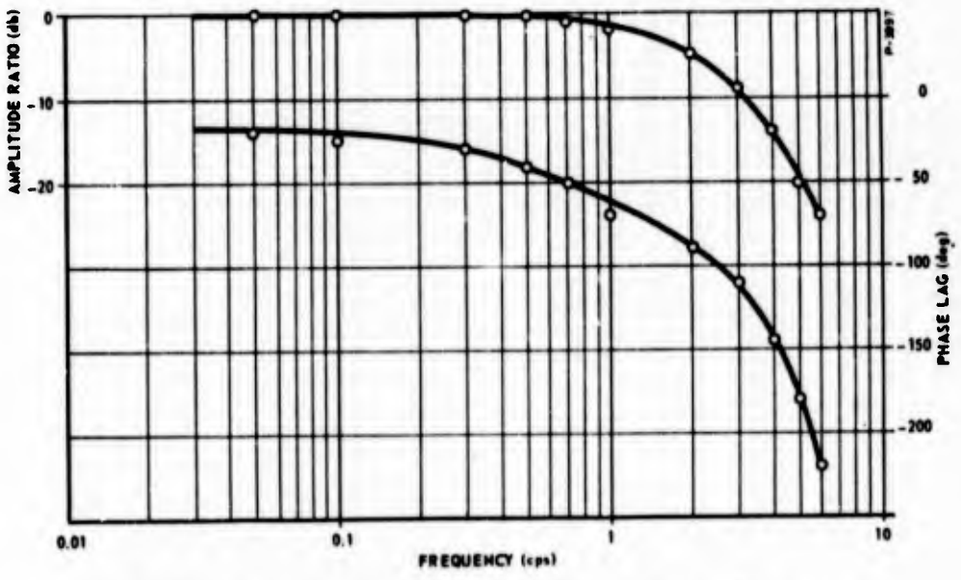

Figure 149 - Servo Subsystem Frequency Response

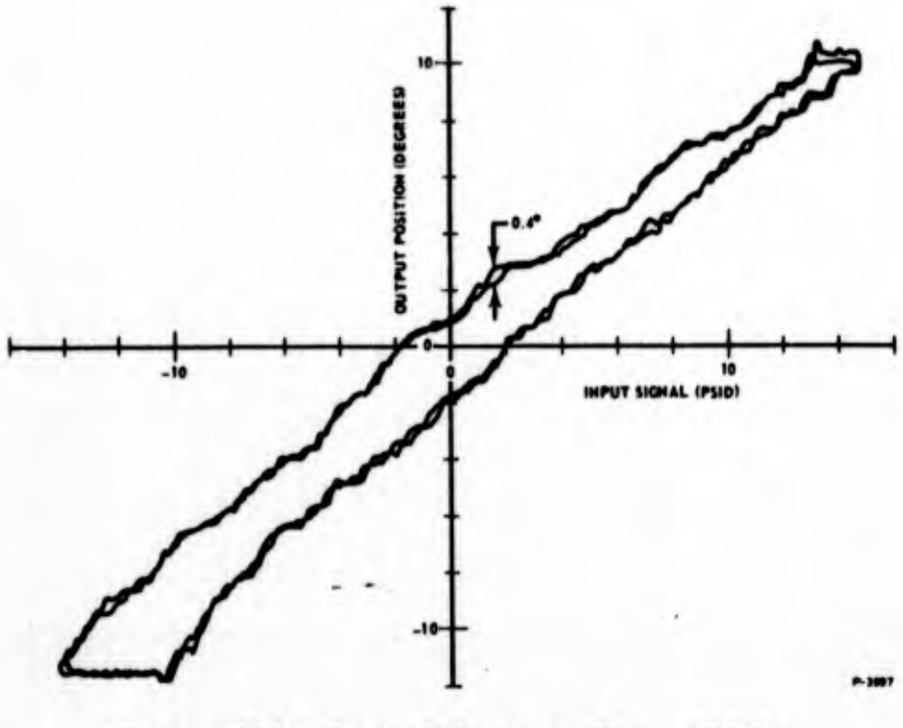

Figure 150 - Servo Subsystem Repeatibility

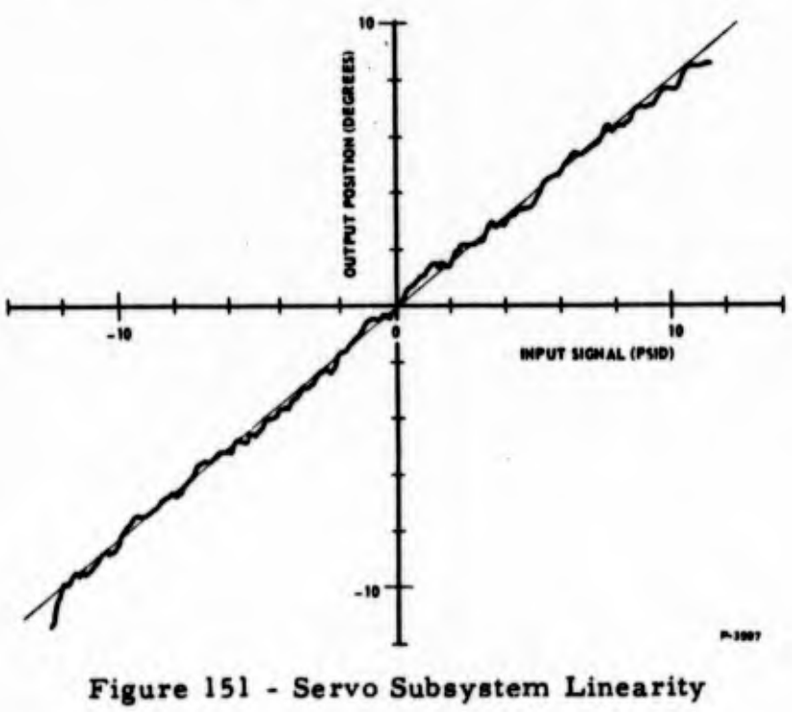

Figure 151 - Servo Subsystem Linearity

C. System Integration and Test

1. System Test Configuration

The final component hardware was designed to integrate into a compact unit as shown in Figure 152. All components were fabricated from materials suitable for 1000°F operation. The two major subsystem groupings, the Rate Sensor and Signal Processing Subsystem and the Servo Subsystem with Compensation Network Volumes are shown in Figure 153 (a) and (b).

The Rate Sensor and Signal Processing Subsystem consists of the rate sensor, alternating bias amplifier, and variable-gain pulse

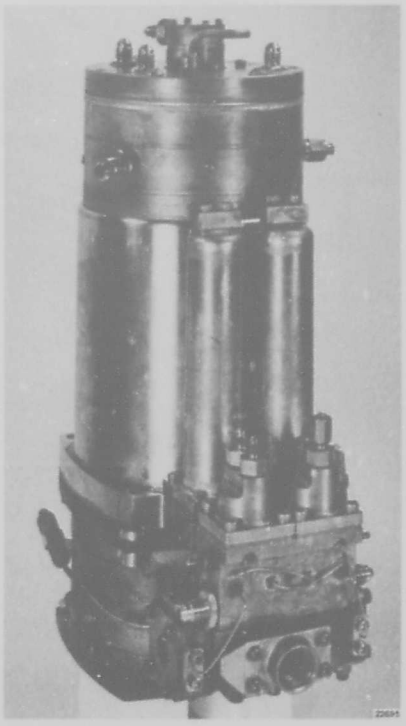

Figure 152 - Fluidic Flight Control System - Integrated Final Configuration

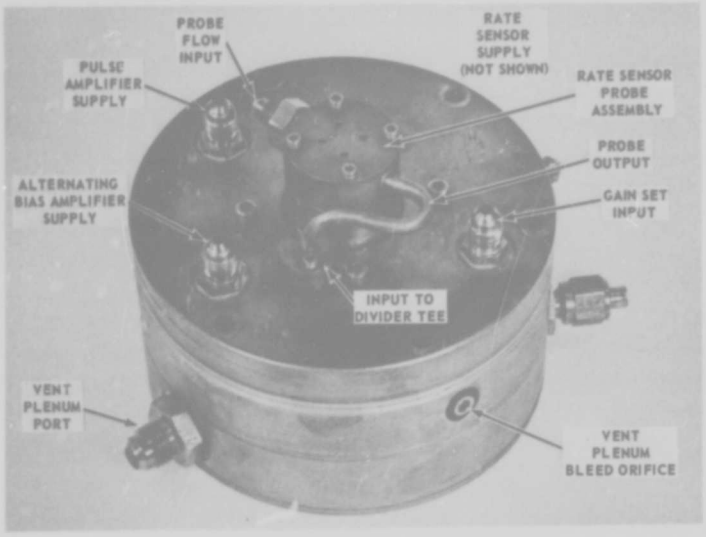

(a) Integrated Rate Sensing and Signal Processing Subsystems

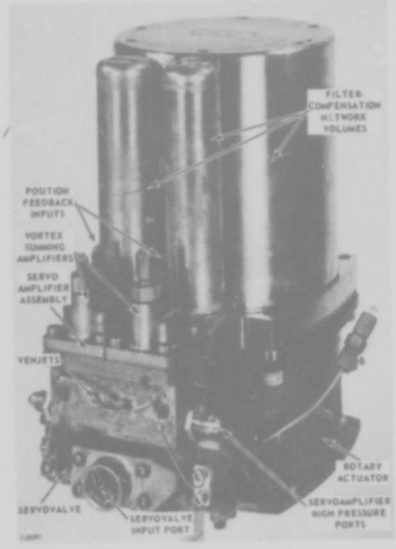

(b) Servo Subsystem and Compensation Network Volumes

Figure 153 - Fluidic Flight Control Subsystem

amplifier in an integrated assembly. The subsystem is interconnected solely with internal manifolding and has as its output the pulsating time-unbalanced signals to the compensation network volumes. All supply and vent lines are terminated in readily accessible fittings for external hookup.

The Servo Subsystem consists of the rotary actuator, the servovalve, the servoamplifier (with 4 venjet and 2 vortex amplifying elements), the position transducer, and a manifold plate. For packaging convenience, the volumes used in the system filter-compensation network were attached to the Servo Subsystem package as shown in Figure 153(b).

The servovalve mounts directly to a pad located on the motor. The manifold is attached to the motor flange and secures the compensation network volumes and the servoamplifier, consisting of the venjets and vortex amplifiers. The servoamplifier output is connected to the servovalve by two small lines as shown in Figure 153(b).

The integrated combination of the two (2) subsystems is shown in Figure 152. The rate sensing and signal processing components are shown attached to the filter compensation volumes. The only system component not shown is the position transducer, which mounts to the motor output shaft through a small instrument transmission and closes the position loop with the requisite gain. The position transducer push-pull outputs are fed back to the vortex summing amplifiers with two small pneumatic lines.

2. Test Setup

The complete system was mounted on an oscillating rate table especially built for the system tests. The rate table supported the system at the motor flange and rotated it about the rate sensor-motor shaft axes. Pneumatic power was fed into the rate table through a pneumatic slip ring and electrical instrumentation signals were returned through an electrical slip ring. This allowed continuous rotation of the rate table at any frequency or rate without angular displacement limitations.

Figure 154 is a schematic of the test setup. Supply pressure of 600 psig was brought directly through the slip ring to the servovalve supply port and the venjet manifold assembly high pressure port as shown. This pressure was also supplied to a bank of pressure regulators

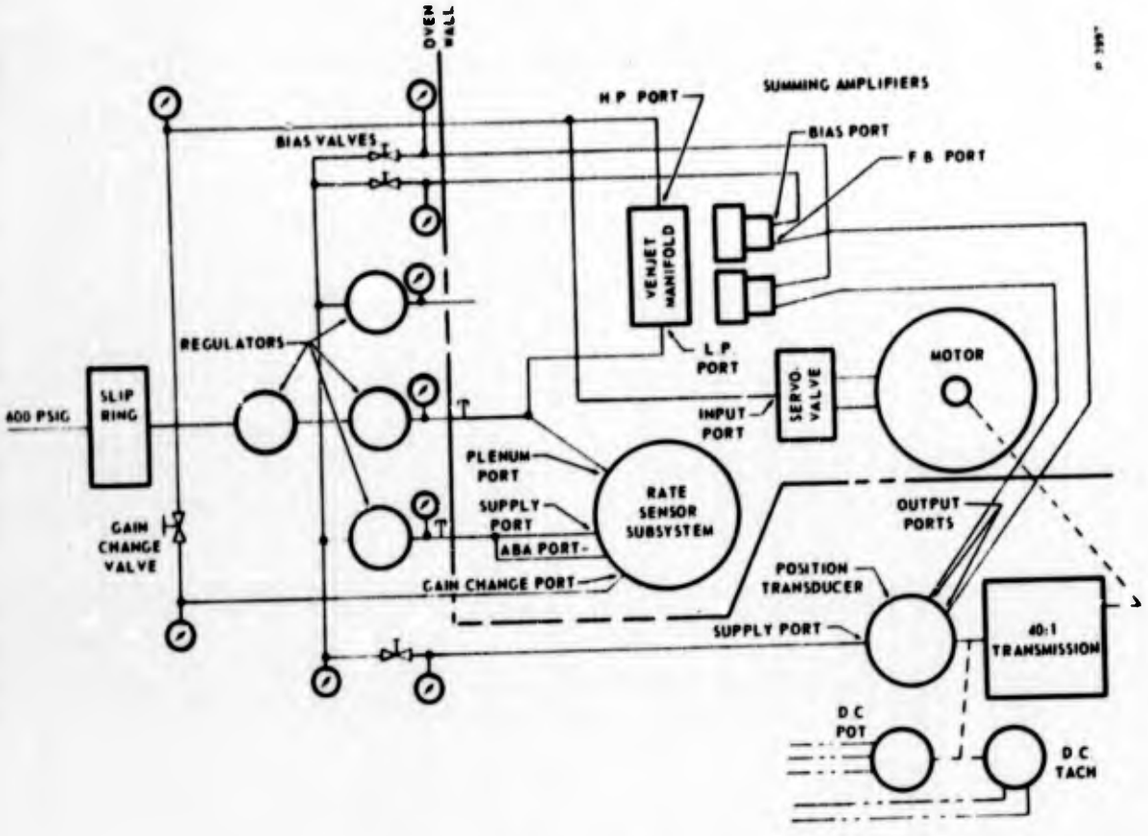

Figure 154 - Servo Subsystem Test Schematic

set to provide the required subsystem supply pressures. The following pressures were provided to the listed supply ports.

Servovalve Supply	600 psig
Servoamplifier High Pressure	600 psig
Servoamplifier Low Pressure	24 psig
Summing Amplifier Bias Valves	60 psid
Pneumatic Position Transducer	49 psig
Gain Change Valve	200 psig
Rate Sensor Supply Port	75 psig
Plenum Port	24 psig

The system outputs (servo position and velocity) were measured by a potentiometer and tachometer, respectively. These signals were carried from the table through the electrical slip ring to the recording equipment. The following items were recorded:

(1) Servo Position

(2) Servo Velocity

(3) Rate Input (Rate Table Rate)

(4) Motor Temperature

(5) Compensation Volumes Temperature

(6) Rate Sensor Temperature

Pressure gages were provided to observe all supply pressures.

A radiant oven was installed around the system to establish and control the requisite ambient temperature. Pneumatic supply lines were coiled around the system to provide gas heating area for the radiant oven. The ambient and gas temperatures were maintained essentially equal at all times by this method. The table platform was thermally isolated from the rest of the rate table by a heat shield and a low conduction path, minimizing undesirable temperature gradients.

A Sanborn strip chart recorder was used to record and monitor the items listed above during all tests. The rate table was driven by a pneumatic high performance servo and had a 0.01 deg/sec to 200 deg/sec capability from continuous rate to sinusoidal frequencies of 5 cps.

3. Test Description

System frequency and transient responses were obtained to evaluate and demonstrate functionality. Sinusoidal peak-to-peak rates of 50 deg/sec and 100 deg/sec were introduced at the following frequencies: 0.01, 0.02, 0.03, 0.05, 0.07, 0.10, 0.20, 0.30, 0.50, 0.70, 1.0, 2.0, and 3.0 cps. Step changes in steady-state rates of 10 deg/sec, 20 deg/sec, 40 deg/sec and 100 deg/sec were introduced using square wave rate at a frequency of 0.01 cps to observe transient response. The ambient temperature was increased using the radiant oven and servo response to rate changes was observed and recorded.

4. Test Results and Comments

The system frequency response with 70°F gas and ambient is shown in Figure 155. Step response traces similar to those of Figure 95 with a rate input to the system also verified the functionality of the integrated system.

Testing of performance at elevated temperature was conducted by gradually increasing temperature while continuously applying a sinusoidal rate of 100 degrees/second peak at a frequency of 0.2 cycles per second.

Servo performance was essentially unchanged as temperature was increased from 70°F to 1000°F, as also indicated by previous subsystem high temperature testing. Operation of the overall system was limited to below 200°F because of changes in rate sensing and signal processing performance. In particular, degradation of performance with temperature was attributed by subsequent subsystem testing to resultant changes in certain bias pressure levels within the jet processing network.

The rate sensor exhibited normal basic pulsation action except for changes in quiescent frequency from room temperature to approximately 500°F. Sensor quiescent (zero rate input) frequency was constant within ± 8 percent in the range from 70°F to 275°F, and then increased rapidly as the temperature was elevated to 475°F. Such behavior of the

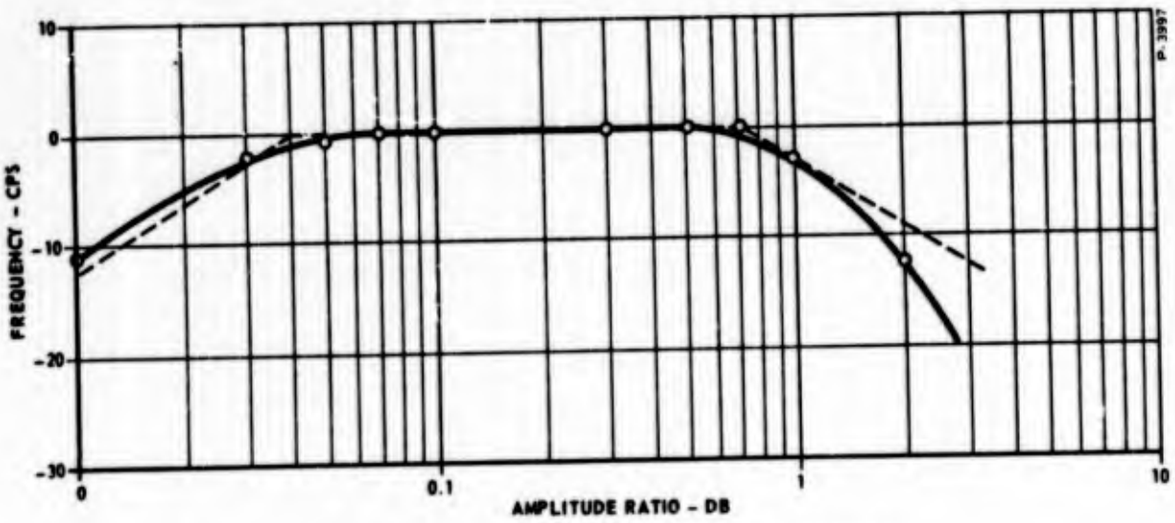

Figure 155 - System Frequency Response

sensor frequency is consistent with a continuously decreasing sensor bias pressure level in conjunction with cessation of the alternating bias function. Only a minor change in frequency is predicted due to changes in gas temperature alone, with otherwise invariant geometry and pressure conditions.

In addition, the breakdown of the alternating bias function as temperature was increased is explainable by a slight but critical bias change at the divider-tee, where the sensor probe output triggers a monostable jet amplifier to drive the network bias alternating flip-flop.

It should be noted that minor changes in sensor quiescent frequency do not in themselves result in changes (e.g., offset) at the system output. As explained in Section III B, reversing the sensor bias direction after each pulse converts the sensor output signal form from frequency to time-unbalance modulation in a manner that eliminates the quiescent frequency. The significance of a gross change in frequency as noted as temperature approaches 500°F is that it implies a significant change in the sensor bias point, which, in general, will be accompanied by an undesired reduction in sensor rate sensitivity and possible disruption of processing network biasing.

Observations of general sensing and processing network behavior during the hot tests suggest that the system would function at 1000°F with the existing configuration if slight adjustments of pressure levels were made; that is, if the network were trimmed to the high-temperature condition. The integrated nature of the design and constraints of testing and adjusting with a hot oven did not permit such trimming without disassembly, making trimming to the higher temperature condition impractical during the current effort.

5. Conclusions and Recommendations

A complete functional system was designed, developed, integrated, and tested utilizing a pulsating vortex rate sensor, jet digital processing elements, an orifice-volume analog frequency shaping network, and a complete integrated rotary position servo. The position servo consists of analog vortex and venjet amplifiers, a vortex servovalve, a fluidic position transducer, and a rotary actuator.

The complete system was successfully integrated and tested at room temperature. Performance of the integrated position servo subsystem was excellent. Functionality of the combined rate sensor and jet signal processing network was demonstrated, but improvements are

required in rate sensitivity and noise level in the pulsating vortex rate sensor. Performance of the jet networks (for alternating bias and variable gain pulse amplification) is generally satisfactory except for a requirement for better decoupling of the low-level and high-level jet stage vents in the combined vent manifold.

Evaluation of system performance at elevated temperatures indicated that:

(1) the integrated position servo functions well with negligible temperature effect throughout the complete range from 70°F through 1000°F, as tested, and

(2) the integrated rate sensor and jet signal processing networks experience variations with temperature of critical bias levels, resulting in changes of sensor operating point and eventual malfunction (through a mismatch of interstage bias) of the alternating bias amplifier.

In addition to improving the general performance of the rate sensor (in particular, rate sensitivity and noise), subsequent investigation and development effort should identify the specific sources of temperature sensitivity and strive to eliminate them. The temperature sensitivity of the bias levels appears to be mainly due to geometric variations rather than to changes in fluid characteristics, so that the problem is related to the detailed physical design rather than to the fundamental approach. With the general functional design available, it is probable that significant improvements in temperature resistance can be achieved with minor revisions in the network design.

As indicated in Figures 152 and 153, a significant portion of the hardware envelope is chargeable to the volumes used in the frequency shaping network. In the interest of expedition, the sizes shown were selected and committed to hardware before the signal processing network design was finalized. The design of the filter-compensation network, including source and load amplifiers, and final required break frequencies, should be reviewed in subsequent investigation with a view to reducing the filter volumes for a lighter, more-compact system configuration.

APPENDIX I

MATHEMATICAL ANALYSIS OF FILTER-SHAPING NETWORK

APPENDIX I

LIST OF ILLUSTRATIONS

Table A-1 - Nomenclature

		Units
A	= Orifice area	in^2
C	= Flow equation constant	$(°R)^{1/2}/sec$
C_D	= Orifice loss coefficient	
C_V	= Velocity of approach coefficient	
C_1 to C_6	= Analytical constants	
D	= Orifice diameter	in.
f	= Frequency	$(sec)^{-1}$
f_1	= Flow equation function	
f'_1	= Differentiated flow equation function	$(sec)^{-1}$
G	= Pressure gain of the vortex summing amplifier	
g	= Gravitational constant	in/sec^2
h	= Enthalpy	Btu/lb
J	= Mechanical equivalent of heat	in-lb/Btu
k	= Specific heat ratio	
K	= Analytical constant	
P	= A designated pressure	psig
$p(t)$	= Dynamic portion of designated pressure, P	psi
P_o	= Steady-state portion of designated pressure, P	psig
R	= Gas constant	in/°R
T	= Temperature	°R
t	= Time	sec
u	= Internal energy	Btu/lb
V	= Velocity	in/sec
$\mathcal{V}$	= Volume	in^3
$\dot{w}$	= Weight flow rate	lb/sec
z	= A height above an arbitrarily designated datum	in.
Δ	= A finite differential	
ρ	= Weight density	lb/in^3
τ	= Time constant	sec

Subscripts

A	= Upper circuit loop
B	= Lower circuit loop
o	= Output
i	= Input
u	= Upstream
d	= Downstream

APPENDIX I

MATHEMATICAL ANALYSIS OF FILTER-SHAPING NETWORK

A. PRELIMINARY ANALYTICAL PROCEDURES

Consider the open system in Figure A-1 where energy, E, enters and leaves the system at stations (i) and (k), respectively. The transfer of energy takes place adiabatically, and no work is done by or on the system.

From the conservation of energy

$$\dot{E}_i - \dot{E}_k = \left(\frac{dE}{dt}\right)_{system} \qquad (A\text{-}1)$$

where in general

$$\dot{E} = \dot{w}\left(u + \frac{P}{\rho J} + \frac{V^2}{2gJ} + \frac{z}{J} + \text{, etc.}\right) \qquad (A\text{-}2)$$

and

u = internal energy per pound of flowing fluid

$\frac{P}{\rho J}$ = flow energy per pound of flowing fluid

$\frac{V^2}{2gJ}$ = kinetic energy per pound of flowing fluid

$\frac{z}{J}$ = potential energy per pound of flowing fluid

Carrying only the predominate energy terms, equation (A-1) becomes

$$\dot{w}_i\left(h_i + \frac{V_i^2}{2gJ}\right) - \dot{w}_k\left(h_k + \frac{V_k^2}{2gJ}\right) = \frac{d}{dt}(\dot{wu})_{system} \qquad (A\text{-}3)$$

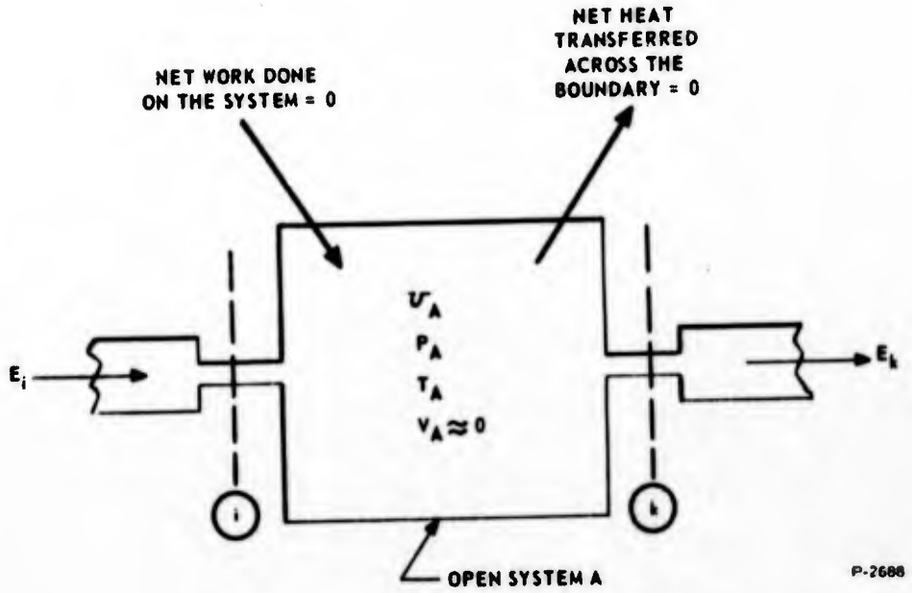

Figure A-1 - A Typical Open System

Assuming the flowing media is a perfect gas, equation (A-3) is expressed as

$$w_i \left(T_i + \frac{V_i^2}{2gJc_p} \right) - w_k \left(T_k + \frac{V_k^2}{2gJc_p} \right) = \frac{T_A}{k} \frac{dw}{dt} + \frac{w}{k} \frac{dT_A}{dt} \qquad \text{(A-4)}$$

For adiabatic, workless, flow of a perfect gas through a system, the stagnation enthalpy is constant or

$$H_o = c_p T_o = c_p \left(T_i + \frac{V_i^2}{2gJc_p} \right) = c_p \left(T_k + \frac{V_k^2}{2gJc_p} \right). \qquad \text{(A-5)}$$

If the open system velocity, V_A, is assumed zero, then $H_A = H_o$, and

$$T_o = T_A = \left(T_i + \frac{V_i^2}{2gJc_p} \right) = \left(T_k + \frac{V_k^2}{2gJc_p} \right) = \text{constant}. \qquad \text{(A-6)}$$

Equation (A-4) now simplifies to

$$\dot{w}_i - \dot{w}_k = \frac{1}{k}\left(\frac{d\dot{w}}{dt}\right)_{system} \qquad (A-7)$$

Substituting the equation of state into (A-7) and noting that v_A and T_A are constant

$$\dot{w}_i - \dot{w}_k = \left[\frac{v_A}{kRT_A}\right]\frac{dP_A}{dt} \quad . \qquad (A-8)$$

The isentropic flow of a perfect gas across an orifice (with a flow coefficient, $C_V C_D$, to compensate for losses) is expressed by the general equation

$$w = \frac{P_u A C}{\sqrt{T_u}} f_1\left(\frac{P_d}{P_u}\right) \qquad (A-9)$$

where

$$C = \frac{C_V C_D \sqrt{\frac{kg}{R}}}{\left(\frac{k+1}{2}\right)^{\frac{k+1}{2(k-1)}}} \qquad (A-10)$$

and

$$f_1\left(\frac{P_d}{P_u}\right) = \frac{\left(\frac{P_d}{P_u}\right)^{\frac{1}{k}}\sqrt{1-\left(\frac{P_d}{P_u}\right)^{\frac{k-1}{k}}}}{\left[\left(\frac{P_d}{P_u}\right)^{\frac{1}{k}}\sqrt{1-\left(\frac{P_d}{P_u}\right)^{\frac{k-1}{k}}}\right]_{critical}} \qquad (A-11)$$

u = station upstream of the orifice

d = station downstream of the orifice.

Let equation (A-9) describe the flow across the orifices at stations (i) and (k). Also let $A_i = A_1$ and $A_k = A_2$. Equation (A-8) now becomes

$$\frac{P_i A_1 C_1}{\sqrt{T_A}} f_1\left(\frac{P_A}{P_i}\right) - \frac{P_A A_2 C_2}{\sqrt{T_A}} f_1\left(\frac{P_k}{P_A}\right) = \left[\frac{\nu_A}{kRT_A}\right]\frac{dP_A}{dt} \qquad \text{(A-12)}$$

Consider the situation where P_i and P_A vary with time, but P_k does not. By writing the differential (implicitly) of equation (A-12), allowing, for example, dP_A to be approximately ΔP_A for small changes in P_A

$$\frac{C_1}{\sqrt{T_A}}\left| A_1 f_1\left(\frac{P_A}{P_i}\right)\Delta P_i - A_1 \frac{P_A}{P_i} f_1'\left(\frac{P_A}{P_i}\right)\Delta P_i + A_1 f_1'\left(\frac{P_A}{P_i}\right)\Delta P_A\right| -$$

$$\frac{C_2}{\sqrt{T_A}}\left| A_2 f_1\left(\frac{P_k}{P_A}\right)\Delta P_A - A_2 \frac{P_k}{P_A} f_1'\left(\frac{P_k}{P_A}\right)\Delta P_A\right| = \left|\frac{\nu_A}{kRT_A}\right|\Delta\left(\frac{dp_A}{dt}\right) . \qquad \text{(A-13)}$$

The final term may be rewritten as

$$\left|\frac{\nu_A}{kRT_A}\right|\frac{d}{dt}(\Delta P_A) . \qquad \text{(A-14)}$$

ΔP_i (t) and ΔP_A (t) are the new time dependent variables operating about some steady-state value P_i and P_A.

Equation (A-13) is now in linear form. Let the time dependent variables

$$\Delta P_i (t) = p_i \qquad \text{(A-15)}$$

and

$$\Delta P_A (t) = p_A . \qquad \text{(A-16)}$$

Also let the steady-state values

$$P_i = P_{oi} \qquad \text{(A-17)}$$

and

$$P_A = P_{oA} \qquad \text{(A-18)}$$

Combining the above expressions into equation (A-13) and writing in Laplace operator form (where C_1 is assumed equal to C_2)

$$\left| \frac{A_1}{A_2} f_1\left(\frac{P_{oA}}{P_{oi}}\right) - \frac{A_1}{A_2} f_1'\left(\frac{P_{oA}}{P_{oi}}\right) \right| p_i - \left| f_1\left(\frac{P_k}{P_{oA}}\right) - \frac{P_k}{P_{oA}} f_1'\left(\frac{P_k}{P_{oA}}\right) - \frac{A_1}{A_2} f_1'\left(\frac{P_{oA}}{P_{oi}}\right) \right| p_A = \frac{\nu_A}{kRC\sqrt{T_A}} A_2 (sp_A) \quad . \tag{A-19}$$

Note that equation (A-19) represents only the linearized dynamic portion of nonlinear equation (A-12).

B. ALTERNATE ANALYTICAL METHOD

From the energy balance equation (A-8)

$$w_i - w_k = \left| \frac{\nu_A}{kRT_A} \right| \left(\frac{dP_A}{dt} \right)_{\text{system}} .$$

The flow across the orifices (See Figure A-1) at stations(i) and (k) can be expressed by the combination of the continuity and Bernoulli equation or

$$\dot{w} = C_V C_D A \sqrt{\frac{2g\bar{P}}{RT} (P_u - P_d)} \tag{A-20}$$

where

P_u = pressure upstream of the orifice

P_d = pressure downstream of the orifice

$\bar{P}$ = average pressure between P_u and P_d.

For flowing gases, where $(P_u - P_d) / \bar{P}$ is less than 10 percent, equation (A-20) closely approximates the compressible flow expression (see equation A-9).

For simplicity assume that

$$\bar{P} = \frac{P_u + P_d}{2} . \tag{A-21}$$

Combining equations (A-20) and (A-21)

$$\dot{w} = C_V C_D A \sqrt{\frac{g}{RT}} \sqrt{P_u^2 - P_d^2} \qquad \text{(A-22)}$$

The flows across orifices (i) and (k) are respectively

$$\dot{w}_i = (C_V C_D)_i A_1 \sqrt{\frac{g}{RT_A}} \sqrt{P_i^2 - P_A^2} \qquad \text{(A-23)}$$

and

$$\dot{w}_k = (C_V C_D)_k A_2 \sqrt{\frac{g}{RT_A}} \sqrt{P_A^2 - P_k^2} \; . \qquad \text{(A-24)}$$

Assuming that

$$(C_V C_d)_i = (C_V C_D)_k \; , \qquad \text{(A-25)}$$

Equation (A-7) may be rewritten as

$$\frac{A_1}{A_2} \sqrt{P_i^2 - P_A^2} - \sqrt{P_A^2 - P_k^2} = \left| \frac{\nu_A}{C_V C_D A_2 k \; gRT_A} \right| \frac{dP_A}{dt} \; . \qquad \text{(A-26)}$$

Consider the case where P_i and P_A vary with time, but P_k does not. By writing the differential (implicitly) of equation (A-26), allowing, for example, dP_A to be approximately ΔP_A for small changes in P_A

$$\frac{A_1}{A_2} \frac{P_i \Delta P_i}{\sqrt{P_i^2 - P_A^2}} - \frac{A_1}{A_2} \frac{P_A \Delta P_A}{\sqrt{P_i^2 - P_A^2}} - \frac{P_A \Delta P_A}{\sqrt{P_A^2 - P_k^2}} =$$

$$\left| \frac{\nu_A}{C_V C_D A_2 k \sqrt{gRT_A}} \right| \Delta \left(\frac{dP_A}{dt} \right) \; . \qquad \text{(A-27)}$$

The final term may be rewritten as

$$\left| \frac{\nu_A}{C_V C_D A_2 \sqrt{k \, C_A}} \right| \frac{d}{dt} (\Delta P_A) \qquad \text{(A-28)}$$

where

$$C_A = \sqrt{kg\ R\ T_A} \tag{A-29}$$

ΔP_i (t) and ΔP_A (t) are the new time dependent variables operating about some steady-state values P_i and P_A.

Equation (A-27) is now in linear form. Let the time dependent variables

$$\Delta P_i\ (t) = p_i \tag{A-30}$$

and

$$\Delta P_A\ (t) = p_A \quad . \tag{A-31}$$

Also let the steady-state values

$$P_i = P_{oi} \tag{A-32}$$

and

$$P_A = P_{oA} \quad . \tag{A-33}$$

Combining the above expression into equation (A-27), and writing in Laplace operator form

$$P_i \left[\frac{\frac{A_1}{A_2}}{\sqrt{1 - \left(\frac{P_{oA}}{P_{oi}}\right)^2}} \right] - P_A \left[\frac{\frac{A_1}{A_2}}{\sqrt{\left(\frac{P_{oi}}{P_{oA}}\right)^2 - 1}} + \frac{1}{\sqrt{1 - \left(\frac{P_k}{P_{oA}}\right)^2}} \right] = \left| \frac{\nu_A}{C_V C_D A_2 C_A \sqrt{k}} \right| (sp_A) \quad . \tag{A-34}$$

Note that equation (A-34) represents only the linearized dynamic portion of nonlinear equation (A-26).

C. ANALYSIS OF FILTER AND COMPENSATION NETWORK

Let the fluid-state filter under consideration be approximated by the lumped parameter network shown schematically in Figure A-2. The steady-state flow impedance of the upper and lower loops is assumed to be identical. If the fixed orifice areas A_2 and A_4 are equal, then so also are the variable orifice areas A_1 and A_3.

The energy expression relating P_i (t) and P_A (t) in the upper loop is derived as

$$\frac{P_i A_1 C}{\sqrt{T_A}} f_1\left(\frac{P_A}{P_i}\right) - \frac{P_A A_2 C}{\sqrt{T_A}} f_1\left(\frac{P_k}{P_A}\right) = \left[\frac{\nu_A}{kRT_A}\right]\frac{dP_A}{dt} \tag{A-35}$$

where

$$C = \frac{C_V C_D \sqrt{\frac{kg}{R}}}{\left(\frac{k+1}{2}\right)^{\frac{k+1}{2(k-1)}}} \tag{A-36}$$

and

$$f_1\left(\frac{P_A}{P_i}\right) = \left[\frac{\left(\frac{P_A}{P_i}\right)^{\frac{1}{k}} \sqrt{1 - \left(\frac{P_A}{P_i}\right)^{\frac{k-1}{k}}}}{\left(\frac{P_A}{P_i}\right)^{\frac{1}{k}} \sqrt{1 - \left(\frac{P_A}{P_i}\right)^{\frac{k-1}{k}}}}\right]_{\text{critical}} \tag{A-37}$$

Similarly for the lower loop

$$\frac{P_i A_3 C}{\sqrt{T_B}} f_1\left(\frac{P_B}{P_i}\right) - \frac{P_B A_4 C}{T_B} f_1\left(\frac{P_k}{P_B}\right) = \left[\frac{\nu_B}{kRT_B}\right]\frac{dP_B}{dt} \tag{A-38}$$

Equations (A-35) and (A-38) may be linearized when the time varying signals P_i (t), P_A (t) and P_B (t) are small. For such cases

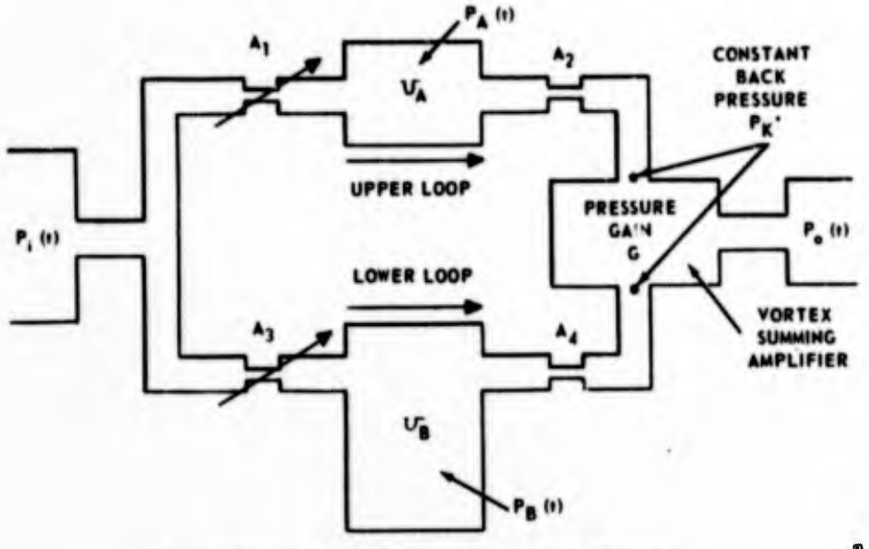

Figure A-2 - Equivalent Lumped Parameter Circuit

P (t) may be divided into a dynamic term, p (t), and a steady-state or quiescent term, P_o, or

$$P(t) = P_o + p(t) \tag{A-39}$$

Referring to the linearization technique shown in subsection A (note the alternate technique in subsection B) equation (A-39) becomes

$$\frac{C}{\sqrt{T_A}}\left| A_1 f_1\left(\frac{P_{oA}}{P_{oi}}\right) - A_1 \frac{P_{oA}}{P_{oi}} f_1'\left(\frac{P_{oA}}{P_{oi}}\right)\right| p_i + \frac{C}{\sqrt{T_A}} A_1 f_1'\left(\frac{P_{oA}}{P_{oi}}\right) p_A - \frac{C}{\sqrt{T_A}}\left| A_2 f_1\left(\frac{P_k}{P_{oA}}\right) - A_2 \frac{P_k}{P_{oA}} f_1'\left(\frac{P_k}{P_{oA}}\right)\right| p_A = \left[\frac{\nu_A}{kRT_A}\right](sp_A) \quad . \tag{A-40}$$

Collecting coefficients of the dynamic variables p_A and p_i, let

$$C_1 = \frac{A_1}{A_2} f_1\left(\frac{P_{oA}}{P_{oi}}\right) - \frac{A_1}{A_2}\frac{P_{oA}}{P_{oi}} f_1'\left(\frac{P_{oA}}{P_{oi}}\right) \tag{A-41}$$

$$C_2 = f_1\left(\frac{P_k}{P_{oA}}\right) - \frac{P_k}{P_{oA}} f_1'\left(\frac{P_k}{P_{oA}}\right) - \frac{A_1}{A_2} f_1'\left(\frac{P_{oA}}{P_{oi}}\right) \tag{A-42}$$

$$C_3 = \frac{\nu_A}{C A_2 kR\sqrt{T_A}} \tag{A-43}$$

The area ratio, A_1/A_2, may be expressed in terms of steady-state pressure ratios by noting that the flow through orifices A_1 and A_2 is identical or

$$\dot{w} = P_{oi} C A_1 f_1\left(\frac{P_{oA}}{P_{oi}}\right) = P_{oA} C A_2 f_1\left(\frac{P_k}{P_{oA}}\right) \tag{A-44}$$

or

$$\frac{A_1}{A_2} = \frac{P_{oA}}{P_{oi}} \frac{f_1\left(\frac{P_k}{P_{oA}}\right)}{f_1\left(\frac{P_{oA}}{P_{oi}}\right)} \tag{A-45}$$

Equation (A-40) now simplifies to

$$C_1 p_i = p_A (C_2 + C_3 s) = C_2 p_A \left(1 - \frac{C_3}{C_2} s\right) \tag{A-46}$$

or

$$\frac{P_A}{P_i}(s) = \frac{\frac{C_1}{C_2}}{1 + \frac{C_3}{C_2}s} = \frac{K_A}{1 + \tau_A s} \tag{A-47}$$

where

$$K_A = \frac{C_1}{C_2} \tag{A-48}$$

$$\tau_A = \frac{C_3}{C_2} \tag{A-49}$$

The lower loop transfer function is evaluated in a similar manner, or

$$\frac{P_B}{P_i}(s) = \frac{\frac{C_4}{C_5}}{1 + \frac{C_6}{C_5}s} = \frac{K_B}{1 + \tau_B s} \tag{A-50}$$

where

$$K_B = \frac{C_4}{C_5} \tag{A-51}$$

$$\tau_B = \frac{C_6}{C_5} \tag{A-52}$$

and

$$C_4 = \frac{A_3}{A_4} f_1\left(\frac{P_{oB}}{P_{oi}}\right) - \frac{A_3}{A_4}\frac{P_{oB}}{P_{oi}} f_1'\left(\frac{P_{oB}}{P_{oi}}\right) \tag{A-53}$$

$$C_5 = f_1\left(\frac{P_k}{P_{oB}}\right) - \frac{P_k}{P_{oB}}\, f_1'\left(\frac{P_k}{P_{oB}}\right) - \frac{A_3}{A_4} f_1'\left(\frac{P_{oB}}{P_{oi}}\right) \tag{A-54}$$

$$C_6 = \frac{\nu_B}{C\, A_4\, kR\sqrt{T_B}} \tag{A-55}$$

Also

$$\frac{A_3}{A_4} = \frac{P_{oB}}{P_{oi}} \frac{f_1\left(\frac{P_k}{P_{oB}}\right)}{f_1\left(\frac{P_{oB}}{P_{oi}}\right)} \tag{A-56}$$

As illustrated in Figure A-2, the individual loop signals p_A and p_B are summed (subtracted) in the vortex summing amplifier. Assuming that the summing amplifier has a pure gain, G, the circuit transfer function is

$$\frac{\nu_o}{p_i}(s) = G\left[\frac{p_B}{p_i} - \frac{p_B}{p_i}\right] \tag{A-57}$$

Note, however, when the steady-state flow is equally divided between the upper and lower circuit loop, as is the case when $A_1 = A_3$, and $A_2 = A_4$, then

$$P_{oA} = P_{oB} \tag{A-58}$$

$$C_1 = C_4 \tag{A-59}$$

$$C_2 = C_5 \tag{A-60}$$

$$K_A = K_B = K \quad . \tag{A-61}$$

Finally, by substituting equations (A-47), A-50), and (A-61) into (A-57) results in the bandpass filter network transfer function

$$\frac{p_o}{p_i}(s) = \frac{G\,K\,(\tau_B - \tau_A)s}{(1 + \tau_A s)(1 + \tau_B s)} \qquad \text{(A-62)}$$

A Summary of the Equations

The bandpass filter network equation is

$$\frac{p_o}{p_i}(s) = \frac{G\,K\,(\tau_B - \tau_A)\,s}{(1 + \tau_A s)(1 + \tau_B s)} \qquad \text{(A-63)}$$

where

G = pressure gain of the vortex summing amplifier

$$K = \frac{\frac{A_1}{A_2} f_1\left(\frac{P_{oA}}{P_{oi}}\right) - \frac{A_1}{A_2}\frac{P_{oA}}{P_{oi}} f_1'\left(\frac{P_{oA}}{P_{oi}}\right)}{f_1\left(\frac{P_k}{P_{oA}}\right) - \frac{P_k}{P_{oA}} f_1'\left(\frac{P_k}{P_{oA}}\right) - \frac{A_1}{A_2} f_1'\left(\frac{P_{oA}}{P_{oi}}\right)} \qquad \text{(A-64)}$$

$$\tau_A = \frac{\nu_A}{C\,A_2\,kR\sqrt{T_A}}\left[\frac{1}{f_1\left(\frac{P_k}{P_{oA}}\right) - \frac{P_k}{P_{oA}} f_1'\left(\frac{P_k}{P_{oA}}\right) - \frac{A_1}{A_2} f_1'\left(\frac{P_{oA}}{P_{oi}}\right)}\right] \qquad \text{(A-65)}$$

$$\tau_B = \frac{\nu_B}{C\,A_4\,kR\sqrt{T_B}}\left[\frac{1}{f_1\left(\frac{P_k}{P_{oB}}\right) - \frac{P_k}{P_{oB}} f_1'\left(\frac{P_k}{P_{oB}}\right) - \frac{A_3}{A_4} f_1'\left(\frac{P_{oB}}{P_{oi}}\right)}\right] \qquad \text{(A-66)}$$

and

$$\text{equation (A-45)}\quad \frac{A_1}{A_2} = \frac{P_{oA}}{P_{oi}}\,\frac{f_1\left(\frac{P_k}{P_{oA}}\right)}{f_1\left(\frac{P_{oA}}{P_{oi}}\right)}$$

$$\text{equation (A-56)} \quad \frac{A_3}{A_4} = \frac{P_{oB}}{P_{oi}} \frac{f_1\left(\frac{P_k}{P_{oB}}\right)}{f_1\left(\frac{P_{oB}}{P_{oi}}\right)} .$$

APPENDIX II

MATHEMATICAL ANALYSIS OF SERVOVALVE

APPENDIX II

LIST OF ILLUSTRATIONS

APPENDIX II

MATHEMATICAL ANALYSIS OF SERVOVALVE

A. NOMENCLATURE

The complete analysis used for the dynamic model of the valve, including the position feedback, follows. The nomenclature used is listed in Table B-1.

Table B-1 - Nomenclature

A = Area of end of spool - in^2

A_c = Control port throat area - in^2

A_e = Exit hole area - in^2

A_f = Feedback port throat area - in^2

A_n = Nozzle ramp annular area - in^2

A_s = Annular area between spool and bore - in^2

C_d = Discharge coefficient

k = Ratio of specific heat of gas

K = Vortex gain factor

M = Spool mass - $lb\text{-}sec^2/in$

M_c = Mach number of control flow entering vortex chamber

M_f = Mach number of feedback flow entering vortex chamber

M_{to} = Tangential velocity of fluid at outer wall of chamber - Mach number

P_c = Control pressure - psia

P_e = Ambient pressure - psia

P_f = Feedback pressure - psia

P_i = Pressure at inside periphery of exit hole - psia

P_o = Pressure at outer wall of vortex chamber - psia

P_s = Supply pressure - psia

R = Gas constant - in/lbf/lbm°R

s = Laplace operation or d/dt

ϕ = Swirl factor = $\frac{W_c M_c}{W_N}$ - nondimensional

T = Gas Temperature - °R

V = Volume under compression at spool end - in^3

W_c = Control flow entering control port, A_c, lb/sec

W_D = Weight flow displaced by spool - lb/sec

W_o = Exit flow leaving exit hole - lb/sec

W_n = Weight flow leaving nozzle-ramp area A_n - lb/sec

W_P = Pressurization weight flow - lb/sec

W_s = Supply flow entering annular chamber $A_{s'}$ - lb/sec

$W_{s'}$ = Supply flow entering feedback line through area

X_o = Quiescent normal clearance between nozzle and ramp surface - in.

y = Spool position - in.

δ = Nozzle gain parameter = $\frac{\theta}{X}$ in^{-1}

θ = Ramp angle - radians

"o" = The presence of a subscript zero or additional subscript zero implies the quiescent value of the variable. When subscript zeros appear in equations the variable without subscript zeros are changes about the quiescent values.

$f_1\left[\frac{P_o}{P_c}\right]$ = Ratio subsonic to sonic gas flow for pressure ratio P_o/P_c

$f_2\left[\frac{P_e}{P_i}\right]$ = Ratio subsonic to sonic gas flow for pressure ratio P_e/P_i multiplied by pressure ratio P_i/P_e

$f_3\left[\frac{P_o}{P_c}\right]$ = Ratio of subsonic control momentum to sonic control momentum at pressure ratio P_o/P_c

$$K_c = \frac{-f_1'\left[\frac{P_{oo}}{P_{co}}\right]}{f_1\left[\frac{P_{oo}}{P_{co}}\right]}$$

Control port back pressure sensitivity coefficient

$$K_s = \frac{-f_1'\left[\frac{P_{oo}}{P_s}\right]}{f_1\left[\frac{P_{oo}}{P_s}\right]}$$

Supply annulus back pressure sensitivity coefficient

$$K_m = \frac{-f_3'\left[\frac{P_{oo}}{P_{co}}\right]}{f_3\left[\frac{P_{oo}}{P_{co}}\right]}$$

Control momentum back pressure sensitivity coefficient

$$K_i = -\frac{P_{eo}}{P_{io}} \frac{f_2'\left[\frac{P_{eo}}{P_{io}}\right]}{f_2\left[\frac{P_{eo}}{P_{io}}\right]}$$

Exit hole gain parameter

K_i = 1 if exit hole is flowed sonically.

B. ANALYSIS

Referring to Figure B-1, the vortex chamber is considered to be a volume, V, at a chamber pressure, P_o. The exit hole is considered to be a fixed orifice with an upstream pressure, tangential Mach number. For normalization, the following defined quantity will be used.

$$W_N = \frac{C A_e P_e}{\sqrt{T}} \tag{B-1}$$

The flow equations for the vortex chamber are:

Supply Flow;

$$\frac{W_s}{W_N} = \frac{A_s P_s}{A_e P_e} f_1\left[\frac{P_o}{P_s}\right] \tag{B-2}$$

Control Flow;

$$\frac{W_c}{W_N} = \frac{A_c P_c}{A_e P_e} f_1\left[\frac{P_o}{P_c}\right] \tag{B-3}$$

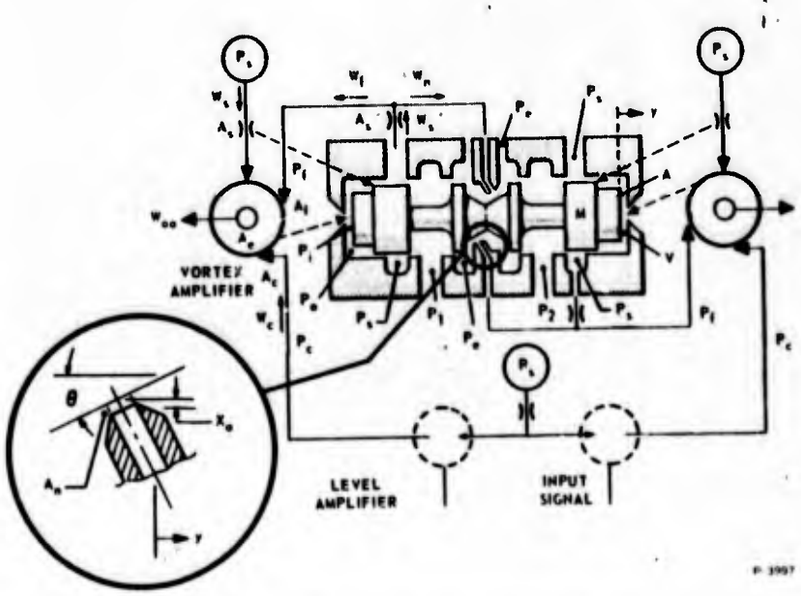

Figure B-1 - Final Valve Configuration

Feedback Control Flow;

$$\frac{W_f}{W_N} = \frac{A_f P_f}{A_e P_e} f_1\left[\frac{P_o}{P_f}\right] \qquad \text{(B-4)}$$

Displacement Flow;

$$\frac{W_D}{W_N} = \frac{A\, s\, y\, P_o}{W_N RT} \qquad \text{(B-5)}$$

Pressurization Flow;

$$\frac{W_P}{W_N} = \frac{V}{W_N k RT}\, s\, P_o \qquad \text{(B-6)}$$

Exit Flow;

$$\frac{W_o}{W_N} = C_d f_2\left[\frac{P_e}{P_i}\right] = \frac{W_s}{W_N} + \frac{W_c}{W_N} + \frac{W_f}{W_N} - \frac{W_D}{W_N} - \frac{W_P}{W_N} \qquad \text{(B-7)}$$

The flow equations for the feedback flow line, assuming negligible volume under compression, are:

Supply Flow;

$$\frac{W_{s'}}{W_N} = \frac{A_{s'} P_s}{A_e P_e} f_1\left[\frac{P_f}{P_s}\right] \qquad \text{(B-8)}$$

Nozzle Flow;

$$\frac{W_n}{W_N} = \frac{A_n P_f}{A_e P_e} f_1\left[\frac{P_e}{P_f}\right] \qquad \text{(B-9)}$$

The relationship of the exit orifice upstream pressure, P_i, to chamber pressure, P_o, and tangential Mach number, M_{to}, is given by,

$$\frac{P_o}{P_e} = \frac{P_i}{P_e}^{K (M_{to})^2} \qquad \text{(B-10)}$$

where for perfect mixing of supply and control flows,

$$M_{to} = \frac{\mathscr{S}}{\frac{W_s}{W_N} + \frac{W_c}{W_N} + \frac{W_f}{W_N}} \tag{B-11}$$

$$\mathscr{S} = \frac{W_c M_c}{W_N} + \frac{W_f M_f}{W_N} \quad . \tag{B-12}$$

The nozzle flow area is given by

$$A_n = A_{no} (1 + \delta y) \tag{B-13}$$

where

$$\delta = \frac{\theta}{X_o}$$

for small ramp angles.

Substitution of equations (B-3) and (B-4) into equation (B-12) gives

$$\mathscr{S} = \frac{A_c P_c}{A_e P_e} f_3\left[\frac{P_o}{P_c}\right] + \frac{A_f P_f}{A_e P_e} f_3\left[\frac{P_o}{P_f}\right] \tag{B-14}$$

Linearizing the above equations with P_s and P_e constant yields,

$$\frac{W_s}{W_N} = \frac{A_e P_{so}}{A_e P_e} f_1'\left[\frac{P_{oo}}{P_{so}}\right] \frac{P_o}{P_{so}}$$

but

$$\frac{W_{so}}{W_N} = \frac{A_s P_{so}}{A_e P_{eo}} f_1\left[\frac{P_{oo}}{P_{so}}\right] \tag{B-15}$$

$$\frac{W_s}{W_{so}} = \frac{f_1'\left[\frac{P_{oo}}{P_{so}}\right]}{f_1\left[\frac{P_{oo}}{P_{so}}\right]} \frac{P_o}{P_{so}} \quad .$$

Let

$$K_s = \frac{-f_1' \left[\frac{P_{oo}}{P_{so}}\right]}{f_1 \left[\frac{P_{oo}}{P_{so}}\right]} \qquad \text{(B-16)}$$

$$\frac{W_s}{W_{so}} = -K_s \frac{P_o}{P_{so}} \qquad \text{(B-17)}$$

$$\frac{W_c}{W_N} = \frac{A_c P_c}{A_e P_e} f_1 \left[\frac{P_{oo}}{P_{co}}\right] + \frac{A_c P_{co}}{A_e P_e} f_1' \left[\frac{P_{oo}}{P_{co}}\right]\left[\frac{P_o}{P_{co}} - \frac{P_{oo} P_c}{P_{co}^2}\right]$$

but

$$\frac{W_{co}}{W_N} = \frac{A_c P_{co}}{A_e P_{eo}} f_1 \frac{P_{oo}}{P_{co}}$$

$$\frac{W_c}{W_N} = \frac{W_{co}}{W_N}\left[\frac{P_c}{P_{co}}\right] + \frac{W_{co}}{W_N} \frac{f_1' \left[\frac{P_{oo}}{P_{co}}\right]}{f_1 \left[\frac{P_{oo}}{P_{co}}\right]}\left[\frac{P_o}{P_{co}} - \frac{P_{oo}}{P_{co}} \frac{P_c}{P_{co}}\right]$$

$$\frac{W_c}{W_{co}} = \left[1 + K_c \frac{P_{oo}}{P_{co}}\right] \frac{P_c}{P_{co}} - K_c \frac{P_o}{P_{co}}$$

where

$$K_c = \frac{-f_1' \left[\frac{P_{oo}}{P_{co}}\right]}{f_1 \left[\frac{P_{oo}}{P_{co}}\right]} \qquad \text{(B-18)}$$

Similarly

$$\frac{W_f}{W_{fo}} = \left[1 + K_f \frac{P_{oo}}{P_{fo}}\right] \frac{P_f}{P_{fo}} - K_f \frac{P_f}{P_{fo}}$$

where

$$K_f = \frac{-f_1'\left[\frac{P_{oo}}{P_{fo}}\right]}{f_1\left[\frac{P_{oo}}{P_{fo}}\right]} \qquad \text{(B-19)}$$

$$\frac{W_o}{W_N} = C_d - \left[\frac{P_{eo}}{P_{io}}\right]\left[f_2'\left[\frac{P_{eo}}{P_{io}}\right]\right]\frac{P_i}{P_{io}}$$

$$= \frac{W_s}{W_N} + \frac{W_c}{W_N} + \frac{W_f}{W_N} - \frac{W_D}{W_N} - \frac{W_P}{W_N} \qquad \text{(B-20)}$$

but

$$\frac{W_{oo}}{W_N} = C_d f_2\left[\frac{P_{eo}}{P_{io}}\right] \qquad \text{(B-21)}$$

$$\frac{W_o}{W_N} = \frac{W_{oo}}{W_N} \frac{f_2'\left[\frac{P_{eo}}{P_{io}}\right]}{f_2\left[\frac{P_{eo}}{P_{io}}\right]} \left(-\frac{P_{eo}}{(P_{io})^2} P_i\right)$$

$$\frac{W_o}{W_{oo}} = K_i \frac{P_i}{P_{io}} \quad \text{where } K_i = -\frac{P_{eo}}{P_{io}} \frac{f_2'\left[\frac{P_{eo}}{P_{io}}\right]}{f_2\left[\frac{P_{eo}}{P_{io}}\right]}. \qquad \text{(B-22)}$$

Similarly,

$$\frac{W_{s'}}{W_{so'}} = -K_{s'}\frac{P_f}{P_{so'}} \quad \text{where } K_{s'} = \frac{f_1'\left[\frac{P_{fo}}{P_{io}}\right]}{f_1\left[\frac{P_{fo}}{P_{so}}\right]} \quad . \qquad \text{(B-23)}$$

From equations (B-9) and (B-13)

$$\frac{W_n}{W_N} = \frac{A_{no}\,(1+\delta y)}{A_e}\,\frac{P_f}{P_e}\,f_1\left[\frac{P_e}{P_f}\right] \quad \text{but } f_1 = 1 \quad .$$

$$\frac{W_n}{W_N} = \frac{A_{no}\,P_{fo}}{A_e\,P_{eo}}\,\delta y + \frac{A_{no}\,P_f}{A_e\,P_e}\,, \quad \frac{W_n}{W_{no}} = \delta y\,\frac{P_f}{P_{fo}}$$

where

$$\frac{W_{no}}{W_N} = \frac{A_{no}\,P_{fo}}{A_e\,P_{eo}} \qquad \text{(B-24)}$$

$$P_o = \frac{P_i}{P_{io}}\,(P_{io}\,\epsilon^{K M_{too}^2}) + 2K M_{too}\,P_{io}\,\epsilon^{K(M_{too})^2}\,M_{to}$$

but

$$P_{io}\,\epsilon^{K(M_{too})^2} = P_{oo} \qquad \text{(B-25)}$$

$$\frac{P_o}{P_{oo}} = \frac{P_i}{P_{io}} + 2K M_{too}\,(M_{to}) \qquad \text{(B-26)}$$

$$M_{to} = \frac{\mathscr{S}}{\frac{W_{so}}{W_N} + \frac{W_{co}}{W_N} + \frac{W_{fo}}{W_N}} - \frac{\mathscr{S}_o\left[\frac{W_s}{W_N} + \frac{W_c}{W_N} + \frac{W_f}{W_N}\right]}{\left[\frac{W_{so}}{W_N} + \frac{W_{co}}{W_N} + \frac{W_{fo}}{W_N}\right]^2}$$

$$\frac{M_{to}}{M_{too}} = \frac{\mathscr{I}}{\mathscr{I}_o} - \frac{W_s + W_e + W_f}{W_{oo}} \qquad \text{(B-27)}$$

$$\mathscr{I} = \frac{A_c P_c}{A_e P_e} f_3\left[\frac{P_{oo}}{P_{co}}\right] + \frac{A_c P_{co}}{A_e P_{eo}} f_3'\left[\frac{P_{oo}}{P_{co}}\right]\left[\frac{P_o}{P_{co}} - \frac{P_{oo} P_c}{P_{co}^2}\right] + \cdots$$

$$\cdots + \frac{A_f P_f}{A_e P_e} f_3\left[\frac{P_{oo}}{P_{fo}}\right] + \frac{A_f P_{fo}}{A_e P_{eo}} f_3'\left[\frac{P_{oo}}{P_{fo}}\right]\left[\frac{P_o}{P_{fo}} - \frac{P_{oo} P_f}{P_{fo}^2}\right]$$

Let

$$f = \frac{A_f P_{fo} f_3\left[\frac{P_{oo}}{P_{fo}}\right]}{A_c P_{co} f_3\left[\frac{P_{oo}}{P_{co}}\right]} \qquad \text{(B-28)}$$

$$K_{m_c} = \frac{-f_3'\left[\frac{P_{oo}}{P_{co}}\right]}{f_3\left[\frac{P_{oo}}{P_{co}}\right]} \qquad \text{(B-29)}$$

and

$$K_{m_f} = \frac{-f_3'\left[\frac{P_{oo}}{P_{fo}}\right]}{f_3\left[\frac{P_{oo}}{P_{fo}}\right]} \qquad \text{(B-30)}$$

$$\frac{\mathscr{I}}{\mathscr{I}_o} = \frac{1}{1+f}\left(1 + K_{m_c}\frac{P_{oo}}{P_{co}}\right)\frac{P_c}{P_{co}} - \frac{1}{1+f}\left(K_{m_c}\frac{P_o}{P_{co}}\right) + \cdots$$

$$\cdots + \frac{f}{1+f}\left(1 + K_{m_f}\frac{P_{oo}}{P_{fo}}\right)\frac{P_f}{P_{fo}} - \frac{f}{1+f}\left(K_{m_f}\frac{P_o}{P_{fo}}\right) \qquad \text{(B-31)}$$

The above linearized equations along with,

$$W_D = \frac{P_{oo} A s y}{RT} \qquad \text{(B-32)}$$

$$W_P = \frac{V}{k RT} s P_o \qquad \text{(B-33)}$$

$$P_o = \frac{M s^2 y}{2A} \qquad \text{(B-34)}$$

provide the required relationships necessary for obtaining spool position, y, as a function of control pressure, P_c.

Neglecting the feedback path, the linear equations become

$$\frac{W_o}{W_{oo}} = K_i \frac{P_i}{P_{io}} \qquad \text{(B-35)}$$

$$W_o = W_s + W_c - W_B - W_D - W_P \qquad \text{(B-36)}$$

$$\frac{P_o}{P_{oo}} = \frac{P_i}{P_{io}} + 2 K M_{too} M_{to} \qquad \text{(B-37)}$$

$$\frac{M_{to}}{M_{too}} = \frac{\mathscr{A}}{\mathscr{A}_o} - \frac{W_s + W_c}{W_{so} + W_{co}} \qquad \text{(B-38)}$$

$$W_D = \frac{P_{oo} A s y}{RT} \qquad \text{(B-39)}$$

$$\frac{W_c}{W_{co}} = \left[1 + K_c \frac{P_{oo}}{P_{co}}\right] \frac{P_c}{P_{co}} - K_c \frac{P_o}{P_{co}} \qquad \text{(B-40)}$$

$$\frac{\mathscr{A}}{\mathscr{A}_o} = \left[1 + K_m \frac{P_{oo}}{P_{co}}\right] \frac{P_c}{P_{co}} - K_m \frac{P_o}{P_{co}} \qquad \text{(B-41)}$$

$$W_P = \frac{V}{k\,RT}\, s\, P_o \tag{B-42}$$

$$\frac{W_s}{W_{so}} = -K_s \frac{P_o}{P_{so}} \tag{B-43}$$

$$P_o = \frac{M s^2 y}{2A} \tag{B-44}$$

$$W_{oo} = W_{co} + W_{so} \tag{B-45}$$

Solving for y/P_c:

$$W_{oo} K_i \frac{P_i}{P_{io}} = W_{so}\left[1 + K_s \frac{P_{oo}}{P_{so}}\right]\frac{P_s}{P_{so}} - W_{so} K_s \frac{P_o}{P_{so}} + \ldots$$

$$\ldots + W_{co}\left[1 + K_c \frac{P_{oo}}{P_{co}}\right]\frac{P_c}{P_{co}} - W_{co} K_c \frac{P_o}{P_{co}} + \ldots$$

$$- \frac{P_{oo} A s y}{RT} - \frac{V}{k\,RT}\, s\, P_o \tag{B-46}$$

$$\frac{P_o}{P_{oo}} = \frac{P_i}{P_{io}} = \frac{\phi}{\phi_o} - 2K M_{too}^2 \left(\frac{W_s + W_c}{W_{so} + W_{co}}\right) \tag{B-47}$$

$$\frac{P_o}{P_{oo}} = \frac{P_i}{P_{io}} + 2K M_{too}^2 \frac{\phi}{\phi_o} + \frac{2K M_{too}^2 W_{so} K_s P_o}{(W_{so} + W_{co})\, P_{so}} - \ldots$$

$$\ldots - \frac{2 K M_{too}^{2} W_{co}}{W_{so} + W_{co}} \left[1 + K_c \frac{P_{oo}}{P_{co}}\right] \frac{P_c}{P_{co}} + \ldots$$

$$\ldots + \frac{2 K M_{too}^{2} W_{co} K_c P_o}{(W_{so} + W_{co}) P_{co}} \qquad \text{(B-48)}$$

$$\frac{\mathscr{d}}{\mathscr{d}_o} = \left[1 + K_m \frac{P_{oo}}{P_{co}}\right] \frac{P_c}{P_{co}} - K_m \frac{P_o}{P_{co}} \qquad \text{(B-49)}$$

$$P_o = \frac{M}{2A} s^2 y \qquad \text{(B-50)}$$

$$\frac{P_o}{P_{oo}} = \frac{P_i}{P_{io}} + 2 K M_{too}^{2} \left[1 + K_m \frac{P_{oo}}{P_{co}}\right] \frac{P_c}{P_{co}} - 2 K M_{too}^{2} \frac{K_m P_o}{P_{co}} + \ldots$$

$$\ldots + \frac{2 K M_{too}^{2} W_{so} K_s P_o}{(W_{so} + W_{co}) P_{so}} - \frac{2 K M_{too}^{2} W_{co}}{(W_{so} + W_{co})} \left[1 + K_c \frac{P_{oo}}{P_{co}}\right] \frac{P_c}{P_{co}} + \ldots$$

$$\ldots + \frac{2 K M_{too}^{2} W_{co} K_c P_o}{(W_{so} + W_{co}) P_{co}} \qquad \text{(B-51)}$$

$$P_o = \frac{M}{2 A} s^2 y \qquad \text{(B-52)}$$

$$\frac{P_i}{P_{io}} = \frac{W_{so} K_s P_o}{W_{oo} K_i P_{so}} + \frac{W_{co}}{W_{oo} K_i} \left[1 + K_c \frac{P_{oo}}{P_{co}}\right] \frac{P_c}{P_{co}} + \ldots$$

$$\ldots - \frac{W_{co} K_c P_o}{W_{oo} K_i P_{co}} - \frac{P_{oo} A s y}{RT W_{oo} K_i} - \ldots \left[\frac{V}{W_{oo} k RT K_i}\right] s P_o$$

(B-53)

$$\frac{P_o}{P_{oo}} = \frac{W_{so} K_s P_o}{W_{oo} K_i P_{so}} + \frac{W_{co}}{W_{oo} K_i P_{co}}\left[1 + K_c \frac{P_{oo}}{P_{co}}\right] P_c - \frac{W_{co} K_c P_o}{W_{oo} K_i P_{co}} - \cdots$$

$$\cdots - \frac{P_{oo} A_s y}{RT W_{oo} K_i} - \frac{V}{W_{oo} k RT K} + \cdots 2 K M_{too}^2 \left[1 + K_m \frac{P_{oo}}{P_{co}}\right] \frac{P_c}{P_{co}}$$

$$- \frac{2 K M_{too}^2 K_m P_o}{P_{co}} + \cdots \frac{2 K M_{too}^2 W_{so} K_s P_o}{(W_{so} + W_{co}) P_{so}}$$

$$- \frac{2 K M_{too}^2 W_{co}}{(W_{so} + W_{co})} \left[1 + K_c \frac{P_{oo}}{P_{co}}\right] \frac{P_c}{P_{co}} + \cdots \frac{2 K M_{too}^2 W_{co} K_c P_o}{(W_{so} + W_{co}) P_{co}}$$

(B-54)

$$P_c \left\{ \frac{W_{co}}{W_{oo} K_i P_{co}} \left[1 + K_c \frac{P_{oo}}{P_{co}}\right] + \frac{2 K M_{too}^2}{P_{co}} \left[1 + K_m \frac{P_{oo}}{P_{co}}\right] + \cdots \right.$$

$$\left. \cdots + \frac{2 K M_{too}^2 W_{co}}{(W_{so} + W_{co}) P_{co}} \left[1 + K_c \frac{P_{oo}}{P_{co}}\right] \right\} =$$

$$P_o \left\{ \frac{1}{P_{oo}} + \frac{W_{so} K_s}{W_{oo} K_i P_{so}} + \frac{V s}{W_{oo} k RT K_i} + \cdots + \frac{2 K M_{too}^2 K_m}{P_{co}} \right.$$

$$- \frac{2 K M_{too}^2 W_{so} K_s}{(W_{so} + W_{co}) P_{so}} + \frac{W_{co} K_c}{W_{oo} K_i P_{co}} + \cdots$$

$$\left. \cdots + \frac{2 K M_{too}^2 W_{co} K_c}{(W_{so} + W_{co}) P_{co}} \right\} \frac{P_{oo} A_s y}{R W_{oo} K_i T}$$

(B-55)

NOTE: Using (B-55) for $y = 0$, $V s = 0$ (static case), $W_{Bo} = 0$,

$$W_{oo} = W_{co} + W_{so}, \quad 2 K M_{too}^2 = 1$$

$$\frac{P_c}{P_{co}} = \frac{P_o}{P_{oo}}$$

Therefore there is not pressure gain, thus P_c must swing slightly more than the required P_o swing.

Let coefficient of $P_c = C_1$

Let coefficient of $P_o = C_2$ (all terms except s term).

$$C_1 P_c = \frac{C_2 M}{2A} s^2 y + \frac{M V s^2}{2A W_{oo} kRT K_i} + \frac{P_{oo} A s y}{RT W_{oo} K_i} \quad (B-56)$$

To verify the analysis experimentally, a spring-restrained vortex-operated spool was tested. It's dynamic response to a step input was obtained for comparison with the predicted response.

The equations are modified to cover a spring-restrained case. In addition, only one side of the spool was pressurized. Appropriate changes are made.

From Figure B-2

$$A P_o + F = Ms^2 y + K^1 y . \quad (B-57)$$

A true step input in P_c could not be obtained; hence, a step in F was used by forcing the spool over and releasing it.

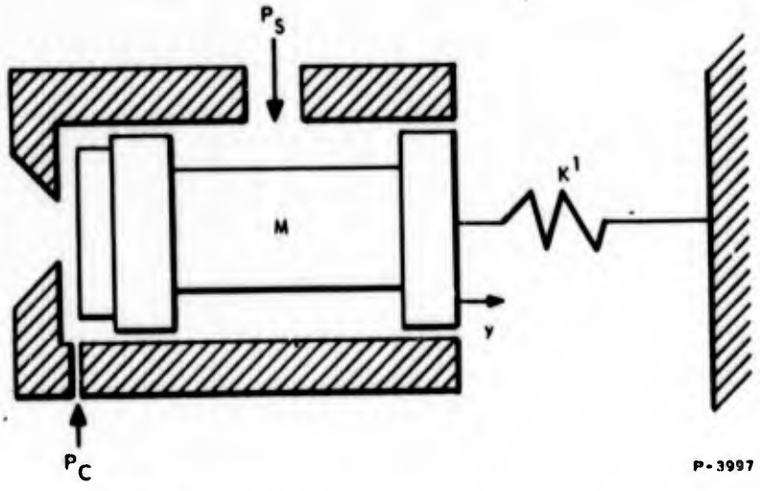

Figure B-2 - Spring Restrained Vortex Spool

The transfer function for y/F with $P_c = 0$ from equations (B-56) and (B-57) is

$$\frac{y}{F} = \frac{\dfrac{C_2}{A} + \dfrac{V_s}{A\,W_{oo}\,kRT\,K_i}}{\dfrac{MV}{A\,W_{oo}\,kRTK_i}\,s^3 + \dfrac{C_2 M}{A}\,s^2 + \left(\dfrac{W\,K^1}{A\,W_{oo}\,K_i\,RTk} + \dfrac{P_{oo}\,A}{RT\,W_{oo}\,K_i}\right)s + \dfrac{C_2 K^1}{A} + \dfrac{W_{Bo}\,\delta}{W_{oo}\,K_i}} \qquad \text{(B-58)}$$

It will be shown later that the lead term in the numerator can be neglected because its time constant is very very small. Proceeding without this term and letting W_{Bo} be zero.

$$\omega_{Ns}^2 = \frac{A^2 P_{oo}\,k}{MV} + \frac{K^1}{M} = \omega_N^2\left(1 + \frac{\omega_s^2}{\omega_N^2}\right) \qquad \text{(B-59)}$$

where

$$\omega_N^2 = \frac{A^2 P_{oo}\,k}{MV} \qquad \text{(B-60)}$$

and

$$a\,\omega_{Ns} = \frac{C_2 W_{oo}\,kRT\,K_i}{V} \qquad \text{(B-61)}$$

$$\beta\,\omega_{Ns} = \frac{\dfrac{C_2 K^1}{A}}{\dfrac{P_{oo}\,A}{RT\,W_{oo}\,K_i}\left[1 + \dfrac{V\,K^1}{A^2\,k\,P_{oo}}\right]}$$

$$\beta\,\omega_{Ns} = \frac{a\,\omega_{Ns}\,\omega_s^2}{\omega_N^2\left(1 + \dfrac{\omega_s^2}{\omega_N^2}\right)} \qquad \text{(B-62)}$$

$$\frac{\beta}{a} = \frac{\omega_s^2}{\omega_N^2 + W_s^2} \qquad \text{(B-63)}$$

Figure B-3 shows the vortex operated spool and a beam spring on the opposite end. Steps were introduced by deflecting the beam and quickly releasing it.

The vortex dimensions are

$A_c = 0.00140 \text{ in}^2$

$A_e = 0.00784 \text{ in}^2$

$A = 0.784 \text{ in}^2$

$M = 4.56 \times 10^{-4} \text{ lb-sec}^2/\text{in}$

m = mass of beam spring = $2.44 \times 10^{-4} \text{ lb-sec}^2/\text{in}$

$V = 0.101 \text{ in}^3$ (preset by chamber length of 0.100 in.)

$K^1 = 1670 \text{ lb/in.}$

The effective mass of a beam spring is 1/2 the total mass so the system mass is

$$4.56 + \frac{2.44}{2} = 5.78 \text{ lb-sec}^2/\text{in.}$$

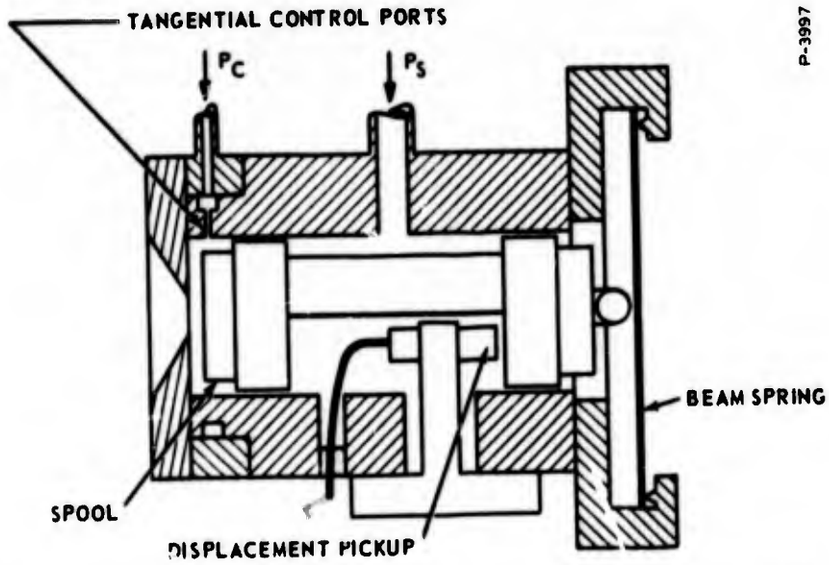

Figure B-3 - Spring-Restrained Vortex-Operated Spool Test Fixture

$$P_o = P_{ie}^{KM_{too}^2} \tag{B-64}$$

In order to determine the constant K a curve of P_{oo}, the steady-state chamber pressure versus the supply pressure for constant control pressure, was obtained. This curve is presented in Figure B-4 at the expected operating control pressure.

From the reference

$$\frac{W_{co}}{W_N} = \frac{A_c}{A_e} \frac{P_{co}}{P_{eo}} f_1 \left(\frac{P_{oo}}{P_{co}} \right) \tag{B-65}$$

$$\frac{W_{so}}{W_N} = \frac{A_s}{A_e} \frac{P_{so}}{P_{eo}} f_1 \left(\frac{P_{oo}}{P_{so}} \right) \tag{B-66}$$

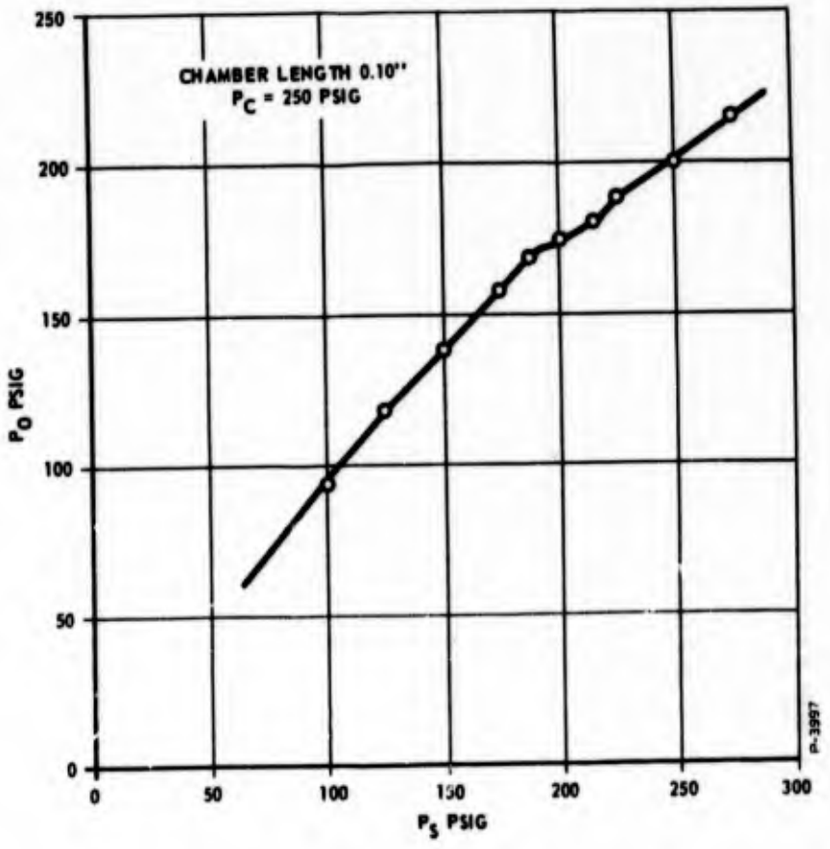

Figure B-4 - One Inch Vortex Servovalve Pressure Characteristics

$$\frac{W_{oo}}{W_N} = \frac{W_{co}}{W_N} + \frac{W_{so}}{W_N} = C_d \frac{P_i}{P_e} f_1\left(\frac{P_e}{P_i}\right) \qquad \text{(B-67)}$$

Test data with $P_{co} = 0$ gives

$P_{so} = 215$ psia

$P_{oo} = P_{io} = 150$ psia

from equation (B-66) and (B-67)

$$A_s = A_e \frac{150\,(1)}{215\,(0.93)} = 0.750\, A_e \,.$$

For the case of Figure B-4 where $P_c = 265$ psia

$$\frac{W_{co}}{W_N} = \frac{0.0014}{0.00785} \frac{265}{14.6} f_1\left(\frac{P_{oo}}{P_{co}}\right) = 3.24\, f_1\left(\frac{P_o}{P_c}\right) \qquad \text{(B-68)}$$

and

$$\frac{W_{so}}{W_N} = 0.051\, P_{so}\, f_1\left(\frac{P_{oo}}{P_{so}}\right) \qquad \text{(B-69)}$$

Using equations (B-67),(B-68),and (B-69) with the data of Figure B-4, the normalized characteristic curve of $\frac{W_{oo}}{W_N}$ versus $\frac{P_{oo}}{P_{eo}}$ can be obtained. Figure B-5 is a plot of this curve.

$$\mathscr{A} = M_{too} \frac{W_{oo}}{W_N} \qquad \frac{W_{oo}}{W_N} = \frac{P_{io}}{P_{eo}} f_1\left(\frac{P_{eo}}{P_{io}}\right) \qquad \text{(B-70)}$$

but $f_1\left(\frac{P_{eo}}{P_{io}}\right)$ for sonic ratios is 1;

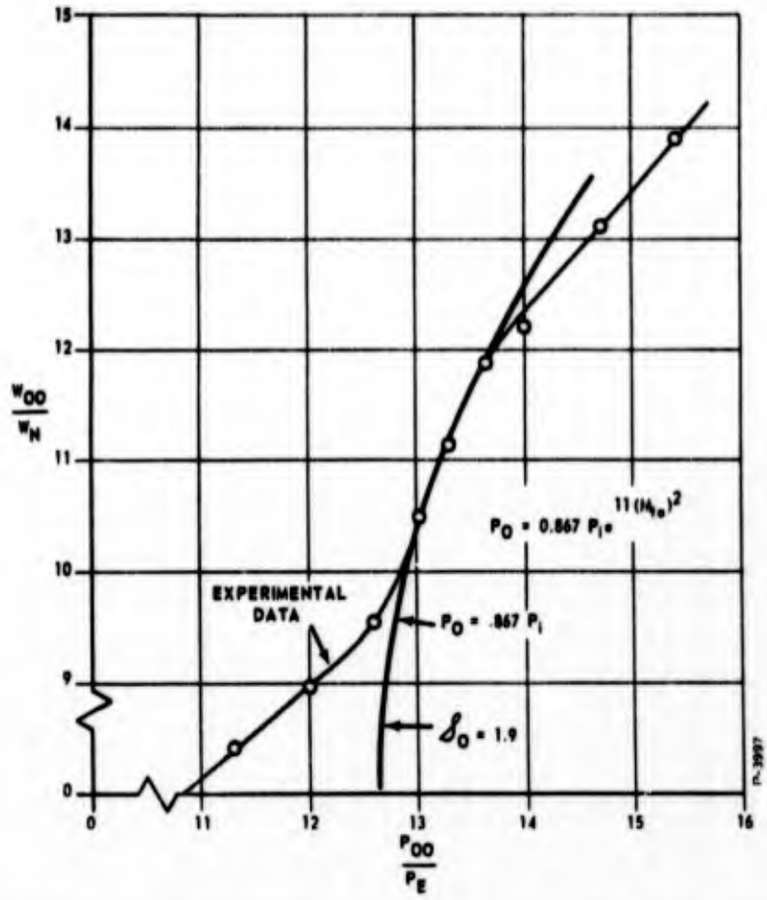

Figure B-5 - Characteristic Curve for One Inch Vortex Operated Servovalve

thus this equation (B-64) becomes

$$\frac{P_{oo}}{P_e} = \frac{W_{oo}}{W_N}\, e^{K \frac{\delta^2}{\left(W_{oo}/W_N\right)^2}}$$

also

$$\frac{W_{co}}{W_{oo}} = M_{too}\, \frac{f_1\left(\frac{P_{oo}}{P_{co}}\right)}{f_3\left(\frac{P_{oo}}{P_{co}}\right)} \qquad \text{(B-71)}$$

at the operating point

$$M_{too} = \frac{2.92\,(0.58)}{11.14\,(0.90)} = 0.170$$

$$\mathscr{S} = (0.170)\,(11.14) = 1.90$$

By trial and error the characteristic curve's slope can be obtained by letting K = 11; however, an additional constant K_1 is required in equation (B-71) to make its curve coincide with the experimental curve. The final form of equation (B-65) becomes

$$P_{oo} = K_1 P_{io} e^{K (M_{too})^2} \qquad \text{(B-72)}$$

where $K_1 = 0.867$ and K = 11. This curve is also shown in Figure B-7. The constant K_1 does not enter the linearized analysis and only applies to steady-state characteristics.

C. EXPERIMENTAL RESULTS

An experimental step response was obtained for the following conditions

$$P_c = 265 \text{ psia}$$

$$P_s = 215 \text{ psia}$$

$$P_o = 185 \text{ psia}$$

$$\omega_N^2 = \frac{(0.785)^2(1.4)(185)\,10^4}{(0.101)(5.78)} = 2.73 \times 10^6$$

$$\omega_s^2 = \frac{1680}{5.78} = 2.91 \times 10^6$$

$$\omega_{Ns}^2 = 2.73 \left[1 + \frac{2.91}{2.73}\right] = 5.64 \times 10^6$$

$$\omega_{Ns} = 2370 \text{ rad/sec} = 380 \text{ cps}$$

$$\frac{\alpha}{\beta} = \frac{2.91}{2.73 + 2.91} = \frac{1}{0.516}$$

$$K_m = -\frac{f_3'\left(\frac{P_{oo}}{P_{co}}\right)}{f_3\left(\frac{P_{oo}}{P_{co}}\right)} = \frac{1.8}{0.71} = 2.77$$

$$K_s = -\frac{f_1'\left(\frac{P_{oo}}{P_{so}}\right)}{f_1\left(\frac{P_{oo}}{P_{so}}\right)} = \frac{2.1}{0.71} = 2.96$$

$$K_c = \frac{f_1'\left(\frac{P_{oo}}{P_{co}}\right)}{f_1\left(\frac{P_{oo}}{P_{co}}\right)} = \frac{0.80}{0.93} = 0.086$$

$$K_i = 1$$

and from equations (B-67), (B-68) and (B-69)

$$\frac{W_{co}}{W_{oo}} = 0.275 \qquad \frac{W_{so}}{W_{oo}} = 0.722$$

$$M_{too} = 0.275\left(\frac{0.65}{0.93}\right) = 0.193$$

$$2KM_{too}^2 = 22(0.193)^2 = 0.820$$

$$P_{oo}C_2 = 1 + (0.722)(0.296)(0.862) + (0.820)(2.77)(0.698) - \ldots$$

$$\ldots - (0.820)(0.722)(2.96)(0.862) + (0.275)(0.86)(0.698) - \ldots$$

$$\ldots - (0.820)(0.275)(0.86)(0.698)$$

$$P_{oo}C_2 = 2.90$$

$$\omega_N = \frac{(0.53)(0.00785)(14.6)}{\sqrt{530}} = 0.0035$$

$$W_{oo} = 10.79\,(0.0035) = 0.0380 \text{ lb/sec}$$

$$\omega_{Ns} = \frac{2.90(0.0380)(1.4)(53.3)(12)(530)}{(0.101)(185)} = 3000$$

$$\alpha = \frac{3000}{2370} = \underline{\underline{1.30}}$$

$$\beta = \underline{\underline{0.700}} \qquad \frac{1}{\omega_{Ns}} = 0.000422 \text{ sec} .$$

Repeating the calculations for another case, where

$$P_c = 400 \text{ psia}$$

$$P_s = 315 \text{ psia}$$

$$P_o = 275 \text{ psia}$$

we obtain,

$$\alpha = 1.10$$

$$\beta = 0.450$$

$$\omega_{Ns} = 2640 \qquad \frac{1}{W_{Ns}} = 0.000380 \text{ sec} .$$

Checking the assumption that the lead term can be neglected, the time constant for Case I becomes

$$\left(1 + \frac{V}{C_2 W_{oo} kRT K_i}\right) s = \left(1 + \frac{0.1}{2.8(0.054)(1.4)(53.3)(12)(530)}\right) s = \left(1 + 0.0000014\, s\right)$$

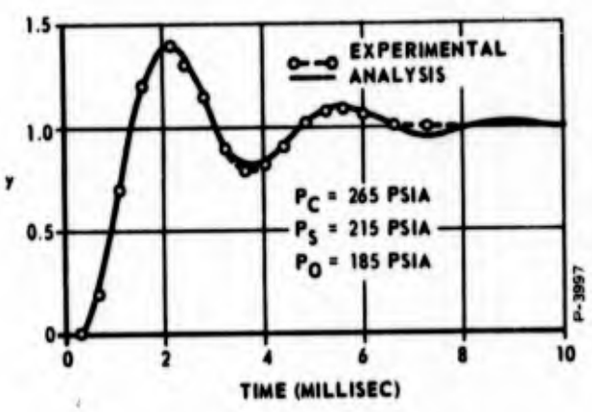

Figure B-6 - Spring Restrained Vortex Spool Response Comparing Experimental Data with the Analysis

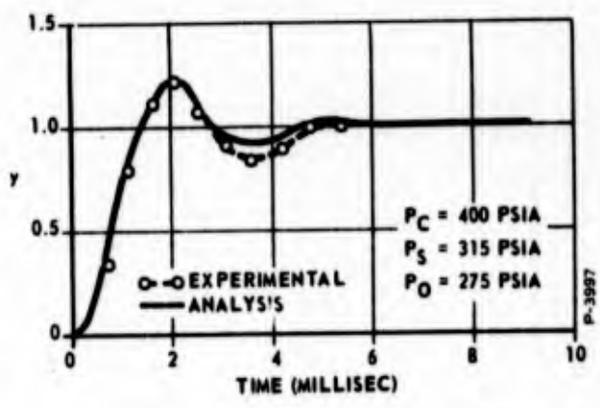

Figure B-7 - Spring Restrained Vortex Spool Response Comparing Experimental Data with the Analysis

D. CONCLUSIONS

Standard third-order dynamic response plots are shown in Figures B-6 and B-7 or the two cases above along with the experimental responses obtained from oscilliscope traces. The agreement as can be seen is excellent. The analysis can be assumed to cover the small signal range adequately. Having verified the analysis, we now proceed to obtain the closed loop value equations.

From equations (B-17), (B-18), (B-19), (B-20), (B-32) and (B-33)

$$\frac{P_i}{P_{io}} = -\left[\frac{W_{so}K_s}{W_{oo}K_iP_{so}} + \frac{W_{co}K_c}{W_{oo}K_iP_{co}} + \frac{W_{fo}K_f}{W_{oo}K_iP_{fo}}\right]P_o + \ldots$$

$$\ldots + \frac{W_{co}}{W_{oo}K_i}\left(1 + K_c\frac{P_{oo}}{P_{co}}\right)\frac{P_c}{P_{co}} + \frac{W_{fo}}{W_{oo}K_i}\left(1 + K_f\frac{P_{oo}}{P_{fo}}\right)\frac{P_f}{P_{fo}} + \ldots$$

$$\ldots + \frac{V_l}{W_{oo}K_ikRT}\,sP_o - \frac{P_{oo}A}{W_{oo}K_iRT}\,sy \qquad \text{(B-73)}$$

also from equations (B-26) and (B-27)

$$\frac{P_i}{P_{io}} = \frac{P_o}{P_{oo}} - 2KM_{too}^2\frac{\mathscr{A}}{\mathscr{A}_o} + 2KM_{too}^2\frac{W_s + W_e + W_f}{W_{oo}} \qquad \text{(B-74)}$$

substituting equations (B-17), (B-18), (B-19) and (B-73) into (B-74)

$$\frac{W_{fo}}{W_{oo} K_i}\left(1+K_f \frac{P_{oo}}{P_{fo}}\right)\frac{P_f}{P_{fo}} + \frac{W_{co}}{W_{oo} K_i}\left(1+K_c \frac{P_{oo}}{P_{co}}\right)\frac{P_c}{P_{co}} =$$

$$\left[\frac{W_{so} K_s}{W_{oo} K_i P_{so}} + \frac{W_{co} K_c}{W_{oo} K_i P_{co}} + \frac{W_{fo} K_f}{W_{oo} K_i P_{fo}} + \frac{1}{P_{oo}}\right] P_o + \frac{V_1}{W_{oo} K_i kRT} s P_o + \ldots$$

$$\ldots + \frac{P_{oo} A}{W_{oo} K_i RT} s y - 2 K M_{too}^2 \left[\frac{1}{1+f}\left(1+K_{m_c}\frac{P_{oo}}{P_{co}}\right)\frac{P_c}{P_{co}} - \ldots\right.$$

$$\ldots - \frac{1}{1+f}\left(K_{m_c}\frac{P_o}{P_{co}}\right) + \frac{f}{1+f}\left(1+K_{m_f}\frac{P_f}{P_{fo}}\right)\frac{P_f}{P_{fo}} - \ldots$$

$$\left.\ldots - \frac{f}{1+f}\left(K_{m_f}\frac{P_o}{P_{fo}}\right)\right] + 2 K M_{too}^2 \left[-\frac{W_{so} K_s}{W_{oo} P_{so}} P_o - \ldots\right.$$

$$\ldots - \frac{W_{co} K_c}{W_{oo} P_{co}} P_o - \frac{W_{fo} W_f}{W_{oo} P_{fo}} P_o + \left(1+K_c \frac{P_{oo}}{P_{co}}\right)\frac{P_c}{P_{co}}\frac{W_{co}}{W_{oo}} + \ldots$$

$$\left.\ldots + \left(1+K_f \frac{P_{oo}}{P_{fo}}\right)\frac{P_f}{P_{fo}}\frac{W_{fo}}{W_{oo}}\right] \quad . \qquad \text{(B-75)}$$

From a flow balance on the feedback line

$$W_f = W_s' - W_n \qquad \text{(B-76)}$$

and from equations (B-19), (B-23), and (B-24)

$$\frac{P_f}{P_{fo}}\left[W_{fo}\left(1+K_f\frac{P_{oo}}{P_{fo}}\right) + W_{no} + W_{so}' K_s' \frac{P_{fo}}{P_{so}}\right] + \ldots$$

$$\ldots + K_f W_{fo} \frac{P_o}{P_{fo}} = W_{no}\, \delta y \quad . \qquad \text{(B-77)}$$

Collecting terms in equations (B-75) and (B-77) gives

$$C_1 \frac{P_c}{P_{co}} = \left[\frac{C_3}{P_{oo}} - \frac{C_2 W_{fo} K_f}{C_4 P_{fo}}\right] P_o + \frac{V}{W_{oo} K_i kRT} s P_o + \ldots$$

$$\ldots + \frac{C_2 W_{no}}{C_4} \delta y + \frac{P_{oo} A}{W_{oo} K_i RT} s y \quad . \qquad \text{(B-78)}$$

The steady-state pressure gain is given by

$$\left.\frac{P_o}{P_c}\right|_{ss} = \frac{C_1/P_{co}}{\frac{C_3}{P_{oo}} - \frac{C_2 W_{fo} K_f}{C_4 P_{fo}}} \qquad \text{(B-79)}$$

where $y = 0$

where

$$C_1 = \frac{W_{co}}{W_{oo}} \left(1 + K_c \frac{P_{oo}}{P_{co}}\right)\left(\frac{1}{K_i} - 2KM_{too}^2\right) + \frac{2KM_{too}^2}{1+f}\left(1 + K_{m_c} \frac{P_{oo}}{P_{co}}\right)$$

(B-80)

$$C_2 = \frac{W_{fo}}{W_{oo}} \left(1 + K_f \frac{P_{oo}}{P_{co}}\right)\left(\frac{1}{K_i} - 2KM_{too}^2\right) + \frac{2KM_{too}^2}{1+f}\left(1 + K_{m_f} \frac{P_{oo}}{P_{fo}}\right)$$

(B-81)

$$C_3 = 1 + \left[\frac{W_{so} K_s P_{oo}}{W_{oo} P_{so}} + \frac{W_{co} K_c P_{oo}}{W_{oo} P_{co}} + \frac{W_{fo} K_f P_{oo}}{W_{oo} P_{fo}}\right]\left[\frac{1}{K_i} - 2KM_{too}^2\right] + \ldots$$

$$\ldots + 2KM_{too}^2 \left[\frac{1}{1+f} K_{m_c} \frac{P_{oo}}{P_{co}} + \frac{f}{1+f} K_{m_f} \frac{P_{oo}}{P_{fo}}\right] \qquad \text{(B-82)}$$

$$C_4 = W_{fo}\left(1 + K_f \frac{P_{oo}}{P_{fo}}\right) + W_{no} + W_{so}' K_s' \frac{P_{fo}}{P_{so}'} \quad . \qquad \text{(B-83)}$$

Substitution of equation (B-34) in equation (B-78) gives

$$C_1 \frac{P_c}{P_{co}} = \left[\frac{VM}{2 W_{oo} K_i kRT A} s^3 + \left(\frac{C_3}{P_{oo}} - \frac{C_2 W_{fo} K_f}{C_4 P_{fo}} \right) - \cdots \right.$$

$$\left. \cdots - \frac{M}{2A} s^2 + \frac{P_{oo} A}{W_{oo} K_i RT} s + \frac{C_2 W_{no} \delta}{C_4} \right] y \ . \qquad \text{(B-84)}$$

The third-order factors α, β and ω_{Ns} are given by

$$\omega_{Ns}^2 = \frac{2 A^2 k P_{oo}}{MV}$$

$$\alpha \omega_{Ns} = \left[\frac{C_3}{P_{oo}} - \frac{C_2 W_{fo} K_f}{C_4 P_{fo}} \right] \frac{W_{oo} K_i kRT}{V} \qquad \text{(B-85)}$$

$$\beta \omega_{Ns} = \frac{C_2 W_{no} W_{oo} K_i RT \delta}{C_4 P_{oo} A} \qquad \text{(B-86)}$$

E. DYNAMIC DESIGN FACTORS

A 5/8-inch spool valve with a stroke of ± 0.015 inch was designed using the equations developed in the last section. Initial fixed dimensions chosen were,

Button area A	-	0.306 sq in
Vortex exit hole area A_e	-	0.00196 sq in
Vortex chamber volume	-	0.03 cu in
Control and feedback port area	-	equal
Spool mass	-	0.00043 lb-sec^2/in
Supply area	-	0.00118 sq in

along with a ram chamber quiescent pressure of 215 psia.

The natural frequency of the valve becomes

$$\omega_{Ns}^{2} = \frac{(2)(0.306)(1.4)(215)}{(0.00043)(0.030)} = 4{,}210{,}000$$

$$\omega_{Ns} = 2060 \text{ rad/sec} = 328 \text{ cps} .$$

Maximum flow gain of the vortex pilot stage is desired and set by adjusting the constant $2 K K_i M_{too}^2$ equal to one (1). Since the exit hole is sonic and K_i is equal to 1, M_{too}^2 must be set at 0.1179. Assuming the supply orifices to be choked, the constants in equations (B-79) and (B-84) become,

$$C_1 = \frac{1}{1+f}\left(1 + K_{m_c}\frac{P_{oo}}{P_{co}}\right)$$

$$C_2 = \frac{f}{1+f}\left(1 + K_{m_f}\frac{P_{oo}}{P_{fo}}\right)$$

$$C_3 = 1 + \frac{1}{1+f} K_{m_c}\frac{P_{oo}}{P_{co}} + \frac{f}{1+f} K_{m_f}\frac{P_{oo}}{P_{fo}}$$

$$C_4 = W_{fo}\left(1 + K_f\frac{P_{oo}}{P_{fo}}\right) + W_{no} .$$

Substitution of the known quantities into these and the remaining equations of the analysis section enables one to obtain α and β. For example,

$$P_i = \frac{215}{e^{0.5}} = 130 \text{ psia}$$

$$\frac{P_{io}}{P_{eo}} = \frac{130}{14.7} = 8.86 = \frac{W_{oo}}{W_N}$$

$$\mathscr{J}_o = M_{too} \frac{W_{oo}}{W_N} = (0.1179)\ (8.86) = 1.036$$

$$A_c = A_f$$

$$\mathscr{J}_o = \frac{A_c}{A_e P_e} \left\{ P_{co} \left(f_3 \frac{P_{oo}}{P_{co}}\right) + P_{fo} \left(f_3 \frac{P_{oo}}{P_{fo}}\right) \right\}.$$

Choosing a control area of 0.0002 square inch and setting $P_{co} = P_{fo}$ results in

$$P_{co} = P_{fo} = 248 \text{ psia}$$

also

$$\frac{W_{no}}{W_{fo}} = \frac{A_{no}}{A_f f_1 \left[\frac{P_{oo}}{P_{fo}}\right]}$$

and for a 0.040-inch nozzle, a gain $\mathscr{J}$ of 30 and a ramp angle of 5 degrees

$$A_{no} = \frac{\pi\ (0.040)(0.0872)}{30} = 0.000365 \text{ sq in}$$

$$\frac{W_{fo}}{C_4} = \frac{1}{7.08}$$

$$C_1 = 3.53$$

$$C_2 = 3.53$$

$$C_3 = 7.05$$

$$K_f = 3.8$$

$$a\omega_{Ns} = \left\{ \frac{7.05}{215} - \frac{3.53(3.8)}{248(7.08)} \right\} \frac{(0.0053)\ (1.4)(640)(530)}{(0.030)} = 2120$$

$$a = 1.03 .$$

Similarly,

$$\beta = 0.523$$

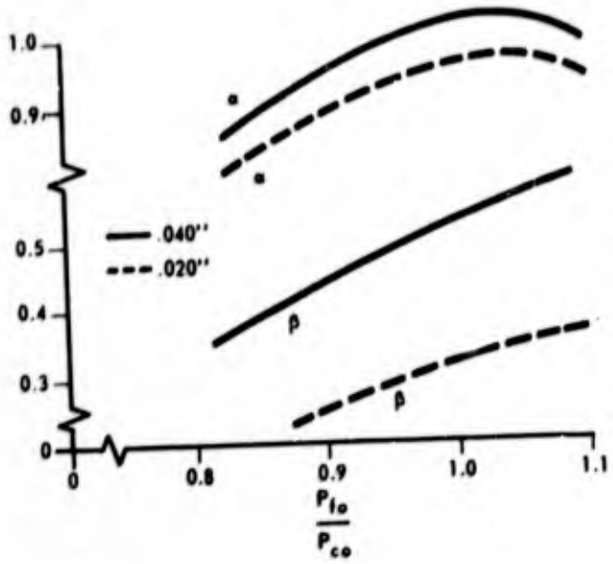

Figure B-8 - α and β as a Functions of P_{fo}/P_{co}

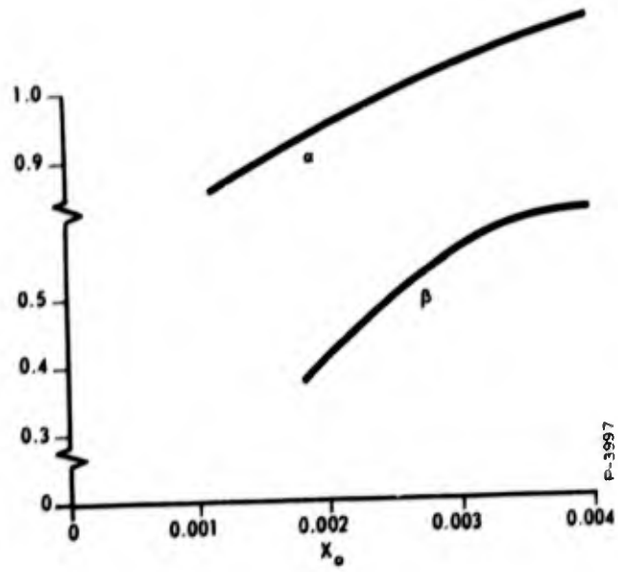

Figure B-9 - α and β as a Function of Nozzle Position

Figure B-8 is a plot of how α and β vary with changes in the ratio of P_f to P_c for two different nozzle sizes. Figure B-9 is a plot of α and β as a function of gain for a constant ratio of P_c/P_f - 1. The above two curves are for a total control port area to exit area ratio of 1:5. Increasing the control port area will reduce the control pressure ratios, adding further damping, while decreasing the area results in less damping.

A summary of the final design values is listed below:

Exit hole dia.	- 0.050 in
Control area	- 0.0002 sq in
Feedback area	- 0.0002 sq in
Feedback supply orifice	- 0.010 in
Supply land clearance	- 0.0006 in
Chamber Length	- 0.050 in

Static Design Factors

From equation(B-79,) the static ram chamber gain is

$$\left.\frac{P_o}{P_c}\right|_{ss} \frac{\frac{3.56}{263}}{\frac{6.58}{215} - \frac{3.01(5)}{235(8.61)}} = 0.590$$

From equation (B-84)

$$\left.\frac{y}{P_c}\right|_{ss} = \frac{\frac{C_1}{P_{co}}}{\frac{C_2 W_{no} \delta}{C_4}} = \frac{\frac{3.56}{263}}{\frac{(3.01)45}{2.70}} = \frac{1}{3720}$$

and for

$y = 0.015$ in

$P_c = 0.015(3,720) = 56$ psi.

Thus, the differential pressure across the spool will be

$$2(56)(0.590) = 66 \text{ psid}$$

for a full stroke error.

Chamber pressure (quiescent)	= 200 psig
Control pressure (quiescent)	= 250 psig
Feedback pressure (quiescent)	= 220 psig
Control pressure gain	= 7.5 psid/0.001 in travel
Ram chamber pressure gain	= 4.4 psid/0.001 in error .

BLANK PAGE

Unclassified
Security Classification

DOCUMENT CONTROL DATA - R&D

(Security classification of title, body of abstract and indexing annotation must be entered when the overall report is classified)

1. ORIGINATING ACTIVITY (Corporate author) The Bendix Corporation, Research Laboratories Div. 20800 Ten and One-Half Mile Road Southfield, Michigan 48075	2a. REPORT SECURITY CLASSIFICATION Unclassified 2b. GROUP N/A

3. REPORT TITLE

Synthesis of a Fluidic Flight Control System

4. DESCRIPTIVE NOTES (Type of report and inclusive dates)

Final Report (April 1964 - August 1966)

5. AUTHOR(S) (Last name, first name, initial)

Taplin, Lael B.
Verge, Kenneth W.
Datwyler, Walter F.

6. REPORT DATE	7a. TOTAL NO. OF PAGES	7b. NO. OF REFS
November 1966	Approx. 200	

8a. CONTRACT OR GRANT NO.	9a. ORIGINATOR'S REPORT NUMBER(S)
AF 33(615)-1492 b. PROJECT NO. 8266 c. Task No. 822605 d.	Report No. 3340 9b. OTHER REPORT NO(S) (Any other numbers that may be assigned this report) AFFDL-TR-66-184

10. AVAILABILITY/LIMITATION NOTICE This document is subject to special export controls and each transmittal to foreign governments or foreign nationals may be made only with prior approval of the Air Force Flight Dynamics Laboratory (FDCL) Wright-Patterson Air Force Base, Ohio 45433.

11. SUPPLEMENTARY NOTES	12. SPONSORING MILITARY ACTIVITY
	Air Force Flight Dynamics Laboratory Research and Technical Division Wright-Patterson Air Force Base, Ohio

13. ABSTRACT

A program was conducted to investigate the feasibility of synthesizing a fully-pneumatic fluidic flight control system for advanced vehicle applications. A pitch axis flight stabilization system was developed to determine feasibility and to indicate achievable performance.

The system approach selected for investigation utilizes a novel pulsating vortex rate sensor, jet digital signal processing elements, and orifice-volume analog frequency shaping network, and a complete integrated rotary position servo. The position servo consists of analog vortex and venjet amplifiers, a novel vortex servovalve, a fluidic position transducer, and a rotary actuator. All components and subsystems required were designed and developed into integrated configurations suitable for operation on 1000°F air in a 1000°F environment.

Functionality was demonstrated for all components and subsystems and for the complete integrated system. the position servo operated excellently with air supply and environmental temperatures in the tested range from 70°F to 1000°F. Operation of the rate sensing componentry was limited to several hundred degrees F. Basic designs exist for all functional components and subsystems required. Subsequent effort can be directed to design refinement for enhanced performance, temperature capability and packaging as desired.

DD FORM 1 JAN 64 1473

Unclassified
Security Classification

Unclassified

Security Classification

KEY WORDS	LINK A		LINK B		LINK C	
	ROLE	WT	ROLE	WT	ROLE	WT
Flight Control Flight Stabilization Systems Vortex Rate Sensors Control Components Fluidics Fluerics						

INSTRUCTIONS

1. ORIGINATING ACTIVITY: Enter the name and address of the contractor, subcontractor, grantee, Department of Defense activity or other organization *(corporate author)* issuing the report.

2a. REPORT SECURITY CLASSIFICATION: Enter the overall security classification of the report. Indicate whether "Restricted Data" is included. Marking is to be in accordance with appropriate security regulations.

2b. GROUP: Automatic downgrading is specified in DoD Directive 5200.10 and Armed Forces Industrial Manual. Enter the group number. Also, when applicable, show that optional markings have been used for Group 3 and Group 4 as authorized.

3. REPORT TITLE: Enter the complete report title in all capital letters. Titles in all cases should be unclassified. If a meaningful title cannot be selected without classification, show title classification in all capitals in parenthesis immediately following the title.

4. DESCRIPTIVE NOTES: If appropriate, enter the type of report, e.g., interim, progress, summary, annual, or final. Give the inclusive dates when a specific reporting period is covered.

5. AUTHOR(S): Enter the name(s) of author(s) as shown on or in the report. Enter last name, first name, middle initial. If military, show rank and branch of service. The name of the principal author is an absolute minimum requirement.

6. REPORT DATE: Enter the date of the report as day, month, year; or month, year. If more than one date appears on the report, use date of publication.

7a. TOTAL NUMBER OF PAGES: The total page count should follow normal pagination procedures, i.e., enter the number of pages containing information.

7b. NUMBER OF REFERENCES: Enter the total number of references cited in the report.

8a. CONTRACT OR GRANT NUMBER: If appropriate, enter the applicable number of the contract or grant under which the report was written.

8b, 8c, & 8d. PROJECT NUMBER: Enter the appropriate military department identification, such as project number, subproject number, system numbers, task number, etc.

9a. ORIGINATOR'S REPORT NUMBER(S): Enter the official report number by which the document will be identified and controlled by the originating activity. This number must be unique to this report.

9b. OTHER REPORT NUMBER(S): If the report has been assigned any other report numbers *(either by the originator or by the sponsor)*, also enter this number(s).

10. AVAILABILITY/LIMITATION NOTICES: Enter any limitations on further dissemination of the report, other than those imposed by security classification, using standard statements such as:

(1) "Qualified requesters may obtain copies of this report from DDC."

(2) "Foreign announcement and dissemination of this report by DDC is not authorized."

(3) "U. S. Government agencies may obtain copies of this report directly from DDC. Other qualified DDC users shall request through _____."

(4) "U. S. military agencies may obtain copies of this report directly from DDC. Other qualified users shall request through _____."

(5) "All distribution of this report is controlled. Qualified DDC users shall request through _____."

If the report has been furnished to the Office of Technical Services, Department of Commerce, for sale to the public, indicate this fact and enter the price, if known.

11. SUPPLEMENTARY NOTES: Use for additional explanatory notes.

12. SPONSORING MILITARY ACTIVITY: Enter the name of the departmental project office or laboratory sponsoring *(paying for)* the research and development. Include address.

13. ABSTRACT: Enter an abstract giving a brief and factual summary of the document indicative of the report, even though it may also appear elsewhere in the body of the technical report. If additional space is required, a continuation sheet shall be attached.

It is highly desirable that the abstract of classified reports be unclassified. Each paragraph of the abstract shall end with an indication of the military security classification of the information in the paragraph, represented as *(TS)* *(S)*, *(C)*, or *(U)*.

There is no limitation on the length of the abstract. However, the suggested length is from 150 to 225 words.

14. KEY WORDS: Key words are technically meaningful terms or short phrases that characterize a report and may be used as index entries for cataloging the report. Key words must be selected so that no security classification is required. Identifiers, such as equipment model designation, trade name, military project code name, geographic location, may be used as key words but will be followed by an indication of technical context. The assignment of links, rules, and weights is optional.

Unclassified

Security Classification